Probing SU(N)-symmetric orbital interactions with ytterbium Fermi gases in optical lattices

Francesco Scazza

München 2015

Probing SU(N)-symmetric orbital interactions with ytterbium Fermi gases in optical lattices

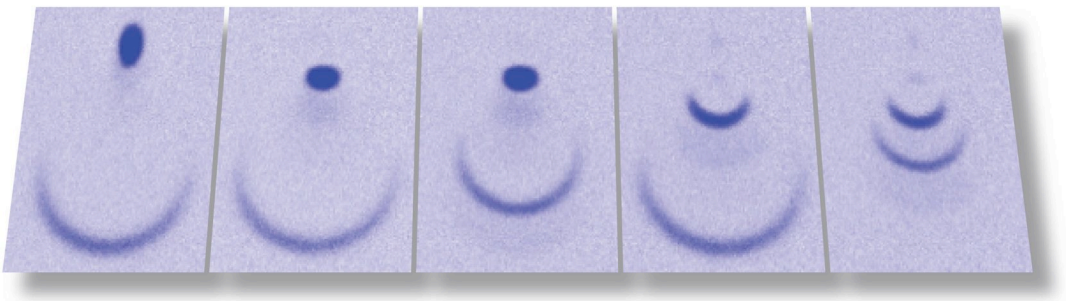

Dissertation an der Fakultät für Physik
Ludwig-Maximilians-Universität München

vorgelegt von

Francesco Scazza

aus Gallarate (Italien)

München, den 08. Januar 2015

Tag der mündlichen Prüfung: 23. Februar 2015

Erstgutachter: Prof. Immanuel Bloch

Zweitgutachter: Prof. Wilhelm Zwerger

Weiter Prüfungskommissionsmitglieder: Prof. H. Weinfurter, Prof. W. Zinth

Zusammenfassung

In dieser Arbeit wird die Erzeugung und Untersuchung wechselwirkender Ytterbium-Quantengase mit zwei elektronischen Orbitalen in optischen Gittern präsentiert. Entartete Fermigase aus Ytterbium oder anderen erdalkaliähnlichen Elementen wurden in jüngster Zeit als Modellsysteme für orbitale Phänomene in der Festkörperphysik herangezogen, wie z.B. die Kondoabschirmung, schwere Fermionen und kolossalen magnetischen Widerstand. Für diese Gase wurde des Weiteren eine hohen SU(N) Symmetrie vorhergesagt, die aus der starken Entkopplung des Kernspins resultiert, und die Erzeugung neuer exotischer Aggregatzustände ermöglicht.
Das SU(N) Hubbard-Modell mit zwei Orbitalen sowie interorbitaler Spinaustauschwechselwirkung lässt sich mit Hilfe der beiden niedrigsten (meta-)stabilen elektronischen Zustände realisieren, welche dabei die Rolle der Elektronen aus unterschiedlichen Orbitalen eines Festkörpers einnehmen. Die Wechselwirkungen in einer entarteten Mischung verschiedener Spinzustände von ^{173}Yb mit zwei Orbitalen werden durch die Anregung in den metastabilen Zustand in einem zustandsunabhängigen Gitter untersucht. Alle Streukanäle für die zwei Orbitale werden charakterisiert und die SU($N = 6$)-Symmetrie wird innerhalb der experimentellen Unsicherheiten nachgewiesen. Von herausragender Bedeutung ist der Nachweis einer sehr starken Spinaustauschwechselwirkung zwischen den zwei Orbitalen, wobei der dazugehörige Austauschprozess anhand dynamischen Ausgleichs der Spinpolarizierung zwischen verschiedenen Orbitalen beobachtet wird. Ermöglicht wird dies durch die Implementierung präzisionsspektroskopischer Verfahren sowie die vollständige, kohärente Kontrolle der Besetzung des metasabilen Zustandes. Die Verwirklichung eines SU(N)-symmetrischen Gases mit Spinaustauschwechselwirkung, des grundlegenden Bausteins für orbitalen Quantenmagnetismus, ist ein entscheidender Schritt in Richtung der Simulation von wichtigen Vielteilchenmodellen, wie dem Kondo-Gittermodell.

Abstract

This thesis reports on the creation and investigation of interacting two-orbital quantum gases of ytterbium in optical lattices. Degenerate fermionic gases of ytterbium or other alkaline-earth-like atoms have been recently proposed as model systems for orbital phenomena in condensed matter, such as Kondo screening, heavy-Fermi behaviour and colossal magnetoresistance. Such gases are moreover expected to obey a high SU(N) symmetry, owing to their highly decoupled nuclear spin, for which the emergence of novel, exotic phases of matter has been predicted.

With the two lowest (meta-) stable electronic states mimicking electrons in distinct orbitals of solid materials, the two-orbital SU(N) Hubbard model and its spin-exchange inter-orbital interactions are realised. The interactions in two-orbital degenerate mixtures of different nuclear spin states of ^{173}Yb are probed by addressing the transition to the metastable state in a state-independent optical lattice. The complete characterisation of the two-orbital scattering channels and the demonstration of the SU($N = 6$) symmetry within the experimental uncertainty are presented. Most importantly, a strong spin-exchange coupling between the two orbitals is identified and the associated exchange process is observed through the dynamic equilibration of spin imbalances between ensembles in different orbitals. These findings are enabled by the implementation of high precision spectroscopic techniques and of full coherent control of the metastable state population. The realisation of SU(N)-symmetric gases with spin-exchange interactions, the elementary building block of orbital quantum magnetism, represents an important step towards the simulation of paradigmatic many-body models, such as the Kondo lattice model.

Contents

Introduction

In the early days of quantum mechanics, the efforts of many physicists were focused on understanding the behaviour of the individual microscopic constituents of the world, such as electrons, photons and atoms. Following the progress of quantum field theory and catalysed by pioneering experimental observations, e.g. the discovery of superconductivity [1], an increasing interest has been directed towards the quantum description of the condensed phases of matter, consisting of large collections of interacting atoms or molecules. An accurate modelling of such quantum many-body systems is in general extremely challenging: including all degrees of freedom of the constituents and their relations is ineffective, owing to the high complexity of real materials. The typical approach in condensed-matter physics is precisely the opposite: one attempts to simplify the system as much as possible, formulating minimal models which include only few crucial degrees of freedom necessary to recreate the observed physical behaviour. Yet such models are the result of several assumptions and approximations; therefore, their ability to provide a correct description of the system's key properties needs to be verified. In many cases, the inclusion of apparently unimportant aspects, such as the presence of anistropies, disorder or impurities, can strongly influence the emerging physics.

The direct experimental investigation of real materials is the natural setting for validating a certain model's predictions. As an example, when the renowned BCS theory of superconductivity was proposed [2], it was able to quantitatively reproduce the key experimental evidences, establishing itself as the paradigmatic framework to describe superconductivity phenomena. However, several systems exist for which the entirety of the observations cannot yet be explained by an elementary model. The reasons are twofold: first of all, even seemingly simple theoretical models are frequently not exactly solvable, making it difficult to extract predictions about the macroscopic properties of materials in certain parameter regimes; secondly, the intrinsic complexity and inaccessibility of condensed-matter systems prevents a direct experimental validation of models at the microscopic scales.

Such a situation exists in the case of high-T_c cuprate superconductors [3, 4]: despite already having technological applications, they lack a consistent theory describing all observed features. The model believed to embrace the physics of high-T_c superconductivity within a minimal description, i.e. the repulsive Fermi-Hubbard model of electrons in solids [5], has withstood the theorists' persisting efforts for decades and its connection to experimental signatures has been elusive. Likewise, many further unsolved puzzles in condensed-matter physics still remain, e.g. concerning the existence of non-abelian anyonic excitations in superconductors [6] and fractional quantum Hall systems [7].

A widening of perspectives has gradually occurred over the past two decades: matter has no longer to be solely analysed by probing its intricate structure and by dissecting it. Thanks to the development of extraordinary experimental techniques in the fields of

atomic physics, photonics and nanotechnology, fully tailored quantum systems can be created and their microscopic degrees of freedom can be controlled and probed to a great extent. This new paradigm can be profitably exploited to engineer artificial matter with disparate properties and applications, imitating nature to some degree, yet in principle without any restriction. However, this is just one way of looking at the possibilities offered by synthetic matter.

As Feynman first pointed out in 1981 [8], one could engineer a controllable quantum system and use it to emulate another physical system by mimicking its evolution. In order for this to work, the simulator must behave and evolve just like the original system that one wishes to replicate. Feynman's vision brought to light the concept of a quantum simulator [9]. After more than 20 years, quantum simulators are now within experimental reach [9–13] and can already be used to produce physical realisations of certain many-body models that we are unable to solve or simulate with classical computers. Ideally, a quantum simulator needs to be a fully controllable and accessible system, so that models can not only be implemented, but accurately probed over a broad range of parameters. Quantum simulators hold great promise for the investigation of the connection between the features of real materials and the proposed models, and could provide in the near future significant advances in condensed-matter physics and beyond. The gained knowledge may then in turn be exploited to develop new synthetic materials, enhancing or suppressing specific effects.

Quantum simulation with ultracold atomic gases

The greatest difficulties in condensed-matter theory arise from the inclusion of strong inter-particle correlations, induced by interactions, and their interplay with quantum statistics. In solid materials the correlations between electrons moving through a crystal lattice are mediated by their Coulombian repulsion from one another and their attraction to the negatively charged ions. Treating electrons as approximately non-interacting succeeds in describing many properties of solids, e.g. the conductivity and the specific heat of metals in their normal phase. Yet it is really the correlated behaviour of interacting electrons that gives rise to a whole lot of fascinating quantum phenomena, ranging from magnetism to superconductivity.

It is largely owing to the simplicity and the tuneability of their interactions that ultracold atomic gases recently emerged as a powerful system to simulate strongly-correlated electron materials in a defect-free environment [12, 14]. In particular, ultracold atoms are especially suited to investigate collective behaviour, such as quantum phase transitions and critical phenomena, owing to the large number of particles that can be controlled in comparison to other quantum simulators [9]. In order to uncover the quantum nature of the particles, extremely low temperatures close to a nanokelvin are required due the low density of dilute atomic gases produced in the laboratories, many orders of magnitude lower than the typical electron density in solids. Decades of advances in laser cooling techniques with alkali atoms [15] enabled the celebrated achievement in 1995 of Bose-Einstein condensation (BEC) [16, 17], where a macroscopic number of atoms occupy the same quantum state, followed by Fermi degeneracy shortly after [18]. Such breakthroughs marked the beginning of the thriving field of ultracold atom physics. Cold atom research aimed

initially at revealing the single-particle coherence effects induced by quantum statistics, but the field rapidly expanded and developed towards the investigation of atomic interactions. A wealth of novel techniques were introduced, devoted to efficiently manipulate and probe ultracold atomic ensembles [14]. Many experiments succeeded in observing quantum effects induced by strong inter-atomic correlations, achieving for instance a detailed understanding of the BEC-BCS crossover in Fermi gases [14, 19] (and references therein).

At very cold temperatures, inter-atomic interactions that are typically moderate in bare trapped gases can be made to dominate the equilibrium properties and the dynamics of the system. Two possibilities exist to effectively tune interactions: Feshbach resonances and optical lattice potentials. On the one hand, Feshbach resonances offer a method for directly adjusting the strength of interactions [20]. Conversely, optical lattices enhance interaction effects mainly through the reduction of kinetic energy: in a periodic potential, the kinetic energy becomes bounded in distinct energy bands, which can be made arbitrarily narrow by increasing the lattice potential depth. Hence, the dominating energy scale is set by the interactions, increased on the contrary by the lattice confinement.

After Jaksch et al. pointed out in 1998 that ultracold atoms trapped in a lattice potential accurately implement the Hubbard model [21], the observation of the superfluid to Mott insulator transition in the first experimental realisation of the Bose-Hubbard model [22] demonstrated the ability of accessing the strongly-correlated regime through optical lattices. Optical lattice potentials represent nowadays a fundamental tool in cold atom physics [14, 23]. During the past decade, an exceptional variety of phenomena and phases have been revealed in optical lattices, such as Tonks-Girardeau gases [24, 25], correlated tunnelling and superexchange processes [26–28], fermionic superfluid pairing [29], fermionic band insulators [30] and Mott insulators [31, 32], to mention but a few. Lattice potentials can be further used to effectively alter the dimensionality of the system, by confining atoms very tightly along one or more directions, and to emulate the diverse crystal symmetries found in nature, which crucially influence the electronic properties of solid-state materials [33–36].

The enormous capability of ultracold atoms as model systems to study condensed-matter Hamiltonians has already been extensively demonstrated and further advances could lead to quantum simulations addressing new open problems in condensed-matter physics. On the one hand, large efforts are focused on developing innovative ways of controlling many-body states and analysing their properties and correlations, often with no analogues in condensed-matter experiments, e.g. spatial noise interferometry [37, 38], high-precision spectroscopy [39–41] and lattice single-site-resolved imaging [42, 43] and addressing [44]. In this respect, probing the out-of-equilibrium dynamics can also contribute to the theoretical understanding of the realised models [45]. On the other hand, the complexity of the attainable many-body models is rapidly increasing to include a larger variety of quantum phenomena and regimes, for instance with the recent realisation of strong artificial magnetic fields [46, 47]. In the same direction, the exploration of innovative quantum systems such as cold polar molecules, magnetic and Rydberg atoms with their long-range dipolar interactions became a central subject, witnessing important advances in the last years [48].

Taking advantage of atoms' internal degrees of freedom also permits to expand the pos-

sibilities for quantum simulation and stimulated recently a growing interest in several new atomic species, alternative to the widely studied alkali elements. In addition, such richer quantum systems may enable discoveries stretching beyond naturally occurring physical behaviour, including the realisation of novel synthetic phases of matter. Amongst others, the atomic species belonging to the class of so-called alkaline-earth-like atoms with two valence electrons gained special attention, specifically with elements as calcium, strontium and ytterbium. Such atoms internal structure does not only crucially determine the laser cooling strategy required to bring the ensembles to the quantum degenerate regime, but especially the kind of many-body models that can be implemented and the available manipulation and investigation tools.

Alkaline-earth-like atoms

Alkaline-earth-like elements have been primarily employed in the recent past as powerful frequency standards: their atomic structure includes low-lying metastable electronic levels and the associated ultranarrow optical transitions posses a remarkable intrinsic precision at the level of 10^{-18}. Since the realisation of the first alkaline-earth-based optical lattice atomic clock [49], many lattice clock systems around the world were assembled and currently represent the most precise existing frequency standards, surpassing even the performance of single-ion atomic clocks [50, 51]. Alongside their use in quantum metrology, alkaline-earth-atoms were brought to the attention of the cold atom community already more than 10 years ago, when the first bosonic isotope of ytterbium was cooled to degeneracy by the group of Y. Takahashi in Kyoto [52]. Their tremendous potential for quantum simulation was then realised [53–55], shortly after they were proposed as a promising system for quantum computation in optical lattices [56–59]. The more complex internal structure of alkaline-earth-like atoms compared to alkali atoms could provide a platform to implement so far inaccessible many-body phenomena, based on orbital interactions [55, 60, 61], enlarged symmetries [55, 62, 63] and strong effective gauge fields [64].

In the last years, various isotopes of alkaline-earth-like species have been brought to quantum degeneracy [65–71] and a fermionic Mott insulating state has already been reported [72]. Such progress inspired in turn numerous theoretical proposals regarding quantum simulation with these atoms. Amongst them, in particular the fermionic ^{87}Sr and ^{173}Yb are promising candidates for the quantum simulation of strongly-correlated phases, owing to the strength of their interactions and their nuclear spin properties [55, 63].

The above-mentioned fermionic isotopes possess a high nuclear spin, which is strongly decoupled from the electronic degrees of freedom due to the absence of electronic angular momentum, and permits the emergence of a high, unique symmetry of interactions. This enlarged symmetry, termed SU(N) from the mathematical group used to describe it, is predicted to have drastic effects on the properties of nearly any interacting fermionic many-body state [63]; such effects have already been experimentally studied in one dimension [73]. An assortment of states with fascinating properties, such as exotic spin liquids with topological order [62, 63], could be realised using Mott insulators of alkaline-earth-like atoms, having (yet) no known analogue in nature [53–55]. Moreover, the realisation of a system exhibiting an enlarged SU($N > 2$) symmetry is of interest outside the field of many-body physics with cold atoms, e.g. in quantum chromodynamics, where the SU(3)

group is central to describe the origin of forces between quarks [74].

The existence of long-lived metastable states is a unique feature of alkaline-earth-like atoms and its applications stretch far beyond the use of the associated ultranarrow transitions, which represent a very powerful spectroscopic tool in the context of ultracold gases. Most importantly, the lowest-lying metastable state can be used as an effective second ground state in the system, opening up unprecedented possibilities to realise condensed-matter models based on the interaction of electrons in distinct orbitals [55, 60, 61]. These models are used to describe a large class of materials, e.g. heavy-fermion compounds [75–77], transition-metal oxides with orbital degeneracy [78] and manganese oxide perovskites [79].

A fundamental ingredient for the establishment of a new many-body toolbox based on ultracold alkaline-earth-like atoms is the possibility of implementing highly symmetric spin interactions, which lead to strong many-body correlations between the particles. In particular, by adopting two distinct electronic states in combination, a special type of inter-atomic interactions can be realised, namely a direct spin exchange between atoms in different electronic states – or different orbitals, how they are often called in analogy to electrons in solids. Orbital spin-exchange interactions lie at the heart of various quantum phenomena in condensed matter, ranging from Kondo screening and heavy-Fermi behaviour to magnetism, colossal magnetoresistance and beyond [76, 79, 80]. Moreover, they can give rise to unconventional superconductivity [81, 82]. Fermionic alkaline-earth-like atoms could unquestionably contribute to the ongoing investigation of these phenomena, specifically by realising the physics of the Kondo lattice model in a controllable fashion [55, 60, 61] through the use of tuneable state-dependent optical lattice potentials and of novel spectroscopic addressing and probing techniques.

This thesis

The main subject of this thesis is the experimental implementation of a controllable quantum gas of fermionic ytterbium (^{173}Yb) for the study of SU(N)-symmetric inter-orbital interactions, and especially spin-exchanging interactions, in optical lattices. A Fermi gas with adjustable spin and orbital degrees of freedom is obtained by optical manipulation of the internal states of the atoms, achieving most importantly a full coherent control of the lowest metastable state population. The implementation of specific experimental techniques for cooling and trapping ytterbium atoms, through which the quantum degenerate regime of both bosonic and fermionic samples is reached, is an important part of the work reported herein. This involves the conception and development of the entire experimental apparatus, including an ultrastable laser system for addressing the transition to the metastable state. The elementary spin interactions between the two lowest electronic state of ^{173}Yb were spectroscopically probed and characterised, also demonstrating their SU($N = 6$) symmetry within the experimental uncertainty. The real-time evolution of the spin distribution of an initially imbalanced state, induced by a large spin-exchange coupling strength, was directly observed. This in turn enabled a comparison between the strength of the spin-exchange process and other unfavourable inelastic processes in the system, strongly supporting the feasibility of many recent theoretical proposals for the quantum simulation of orbital magnetism. Although a state-independent lattice has

been adopted for all experiments presented in this work, the reported results become particularly relevant in relation to currently ongoing projects in our experiment, based on many-body physics in state-dependent lattice potentials.

Outline

This thesis is organised as follows.

In Chapter 1, we review the general properties of alkaline-earth-like atoms, with particular emphasis on the peculiarities which made them recently object of a great attention. We explain the basics of their internal structure and discuss their consequences in the context of ultracold atomic gases in optical lattices. After recalling the theory of scattering at low temperatures, we elaborate on the emergence of the SU(N) symmetry of atomic interactions and present the SU(N) Fermi-Hubbard model. We furthermore introduce interactions between different (meta-) stable electronic states, termed inter-orbital interactions, and elucidate the mechanism behind the occurrence of inter-orbital spin-exchange interactions. In the last part, after a short digest of orbital magnetism in condensed matter, we illustrate a selection of prospects in quantum simulation with alkaline-earth-like atoms, focusing particularly on the Kondo lattice model and the SU(N) Heisenberg model, which are amongst the near-future goals of our experiment.

In Chapter 2, we summarise the atomic, nuclear and scattering properties of ytterbium, stressing the important effects of these on the cooling strategy towards degeneracy. We successively present the implemented cooling procedure, which includes the Zeeman slowing, the laser cooling in a narrow-line magneto-optical trap and the evaporation in a crossed far off-resonant dipole trap. Finally, we report on the production of degenerate bosonic (^{174}Yb) and fermionic (^{173}Yb) quantum gases and on their loading into a three-dimensional optical lattice.

In Chapter 3, we present the experimental apparatus. We detail the vacuum assembly and the optical setup surrounding the chamber where the atomic gases are trapped, manipulated and detected, reporting recent upgrades as well. We describe the cooling and trapping laser systems and finally present in detail the clock laser system employed for the excitation to the metastable electronic state.

Chapter 4 is devoted to the description of the experimental techniques which allow the nuclear spin state control and detection with ^{173}Yb, respectively obtained through a narrow-line optical pumping scheme and an optical Stern-Gerlach separation method. We briefly address the absence of spin relaxation in the ground state, thereby setting an upper bound estimate for the SU(N) symmetry breaking of ground-state collisions.

Chapter 5 prepares the ground for the presentation of the main results on SU(N) symmetric, spin-exchange interactions in Chapter 6. The excitation to the metastable state through the associated ultranarrow optical clock transition in an optical lattice is presented. Furthermore the effect of an external magnetic field are clarified and precision spectroscopic measurements of the clock differential Zeeman shift in ^{173}Yb are presented. In the following part, a simple model for inter-orbital interactions in a three-dimensional optical lattice is deduced and the relevance of a small SU(N) symmetry breaking for many-body physics is discussed.

In Chapter 6, we present the detailed investigation of interactions in the two lowest electronic states of ^{173}Yb. We first describe our spectroscopic characterisation of inter-

orbital interactions in the lattice and thereby report on the quantitative analysis of the scattering properties of the two-orbital system consisting of the two electronic states. A very strong on-site spin-exchange coupling is found, representing by far the dominant energy scale in a deep three-dimensional lattice. We further address the demonstration of the SU(N)-symmetric nature of all two-orbital interaction channels. We then proceed by presenting the direct observation of spin-exchanging dynamics in an array of tightly-confined two-orbital ensembles. The system is initialised in a strongly spin-imbalanced state and a fast equilibration towards equilibrium is revealed, induced by the strong spin-exchange coupling strength. We conclude by reportin our characterisation of the inelastic losses and discuss the feasibility of recent experimental proposals based on the coexistence of the two electronic states in a lattice.

In the final Chapter of this thesis we summarise the main results and provide an outlook on possible near-future experiments, prevalently focused towards the exploration of orbital many-body physics and quantum magnetism.

Publications

The main results of this thesis have been published in the following reference:

F. Scazza, C. Hofrichter, M. Höfer, P. De Groot, I. Bloch and S. Fölling. *Observation of two-orbital spin-exchange interactions with ultracold SU(N)-symmetric fermions.* Nature Phys. **10,** 779–784 (2014).

The following research articles have also been published during the course of this thesis:

B. Chalopin, F. Scazza, C. Fabre and N. Treps. *Multimode non-classical light generation through the optical-parametric-oscillator threshold.* Phys. Rev. A **81,** 061804(R) (2010).

B. Chalopin, F. Scazza, C. Fabre and N. Treps. *Direct generation of a multi-transverse mode non-classical state of light.* Opt. Express **19,** 4405–4410 (2011).

CHAPTER 1

Alkaline-earth-like atoms: properties and applications

The designation *alkaline-earth-like* (AEL) atoms includes all chemical elements in the second group of the periodic table (Be, Mg, Ca, Sr, Ba, Ra), as well as those d-block (Zn, Cd, Hg) and f-block (Yb, No) transition metals which have all complete internal shells and a complete outer s-shell with two electrons. The atomic properties of AEL species are largely determined by the two s-shell valence electrons, in a similar way as for Helium: the electronic states are separated into two manifolds with total electronic spin $S = 0$ and $S = 1$, respectively. For symmetry reasons, the optical coupling between states belonging to the two manifolds is to a first approximation forbidden. The internal structure and the optical transitions that are available for cooling and manipulating trapped AEL atoms are radically different from the ones used for the more conventional alkali elements, and introduce some new exciting possibilities. Owing to these, in the last few years, ultracold AEL atoms have attracted considerable theoretical interest in the context of quantum information processing [56, 58, 59, 83] and quantum many-body physics [53–55, 60, 61, 64, 84, 85]. In particular, ultracold ensembles of AEL atoms trapped in optical lattices hold promise for the neutral-atom implementation of yet unexplored condensed-matter models of strongly correlated quantum phenomena [55, 60, 61]. Alongside the intense theoretical efforts, several research groups around the world[1] have been setting up laboratory experiments with very diverse goals, attempting to explore the novel applications and the fascinating prospects that were devised.

In this Chapter, we will introduce the fundamental properties of AEL atoms, providing the necessary notions for subsequently describing the main experimental applications of cold atomic ensembles. We start here by reviewing the electronic and nuclear properties of AEL atoms, which are responsible for the presence of long-lived metastable states and for the angular momentum decoupling between the nucleus and electronic cloud. After introducing the theory of ultracold collisions, we discuss the emergence of SU(N) symmetry in Fermi gases of AEL atoms. We also generalise the treatment of interactions to an additional internal degree of freedom, represented by the presence of two (meta-) sta-

[1] At the moment of writing this manuscript, experiments adopting ultracold Yb have been assembled in Munich, Kyoto, Tokyo, Hamburg, Düsseldorf, Florence, Turin, Paris, Bangalore, Washington, Boulder and Seattle, whereas experiments adopting ultracold Sr were realised by groups in Amsterdam, Innsbruck, Florence, Paris, Tokyo, Houston and Boulder.

ble electronic states, and derive the two-orbital SU(N)-symmetric Hubbard model, which describes interacting AEL atoms in a periodic lattice potential. We then proceed by describing some proposed experimental applications for cold AEL atoms, stemming from the above-mentioned uncommon features. The simultaneous control of the spin and the orbital degree of freedom of the atoms leads to very exciting possibilities for the simulation of condensed-matter phenomena based on the interplay between the two analogous properties of strongly correlated electrons in solids. For instance, the implementation of the Kondo lattice model, the Kugel-Khomskii model and the SU(N) Heisenberg model with ultracold gases of AEL atoms have been proposed [54, 55, 60, 61]. We will illustrate different prospects in the field of quantum simulation of orbital and SU(N) magnetism, elaborating on the experimental feasibility of the proposed models and on the possibility of accessing their intriguing regimes.

1.1 Distinctive features of alkaline-earth-like atoms

In this Section we will give a brief overview of the main distinctive properties and prominent features which are common to all alkaline-earth-like atoms. We will specifically describe the three crucial attributes which inspire novel research prospects with AEL atoms, namely the existence of long-lived metastable states, the spin-independence of inter-atomic collisions and the possibility of engineering versatile state-dependent optical potentials.

1.1.1 Basic atomic properties

Most of the atomic properties of AEL atoms arise from their distinctive two-valence-electron level structure [86]. The two outer electrons can arrange in a spin singlet ($S = 0$), as in the ground state ($^1\mathrm{S}_0$), or in a spin triplet ($S = 1$). All lower-lying electronic levels can thus be separated in two manifolds, categorised by having either total electronic spin $S = 0$ or $S = 1$. All transitions which couple electronic states in the singlet manifold to states in the triplet manifold (or vice versa) are generally very narrow, owing to the fact that in the dipole approximation spin-flipping transitions ($\Delta S \neq 0$) are forbidden [86]. A finite dipole coupling between the ground state and the triplet states arises exclusively from a small mixing between triplet and singlet electronic states, induced by spin-orbit and hyperfine interactions [86]. One example of such narrow transitions is the $^1\mathrm{S}_0 \rightarrow ^3\mathrm{P}_1$ transition, which can be used for Doppler cooling the atomic samples down to very cold temperatures on the order of $10\,\mu$K or below, allowing the efficient direct loading of an optical dipole trap. More complex all-optical schemes exploiting this narrow transition were also devised, leading for instance to the improved rapid production of degenerate AEL atomic gases [87]. Another peculiarity of AEL atoms is the wavelength range of the optical transitions which are employed for laser cooling and manipulating the state of the atoms: they all lie in the visible range of the electromagnetic spectrum, as opposed to the transitions used in alkali atom experiments, which are typically found in the near-infrared range. Designing and assembling stable high-power laser sources at visible wavelengths

poses more difficulties compared to near-infrared sources, because of the lack of laser gain media systematically covering the visible spectrum (although a rapid technological development is gradually filling the gaps). On the other hand, visible light transitions present some advantages, e.g. the reduced diffraction limit associated with lower wavelengths used for imaging and the naked-eye visibility of coloured laser light which facilitates laser alignment.

A striking peculiarity of AEL atoms is the presence of metastable, long-lived excited electronic states in the triplet manifold, namely the $^3P_0$ and the $^3P_2$ states, which are very weakly coupled to the ground state. The transitions connecting such states to the ground state have extremely low linewidths of 10 mHz at most, associated with state lifetimes of tens of seconds to even hundreds of seconds for the lightest AEL elements (see e.g. Ref. [88] for a summary). Such transitions are often termed *ultranarrow*, as they are more than a factor of 10^8 narrower than typical optical transitions with linewidths on the order of 1 to 10 MHz. In particular, the $^1S_0 \rightarrow ^3P_0$ transition is usually denominated the *clock* transition, for it is frequently used in single-ion and optical lattice atomic clocks [89, 90]. The tremendously high Q-factor above 10^{17} of the clock transition in fermionic AEL has indeed empowered the implementation of the currently most stable and precise atomic clocks in the world [50, 51, 90]. Such a narrow transition represents in itself a very powerful experimental resource, since it can be used as a precise spectroscopic probe in the study of ultracold gases. Spectroscopic investigation of many-body states based on narrow transitions has indeed been already applied to bosonic Mott insulators [39, 40, 91] and tightly confined gases [92–95]. Furthermore, the existence of the metastable $^3P_0$ state opens up unique possibilities for the investigation of complex or even novel strongly-correlated quantum phases with cold atoms in optical lattices, as we will describe in the last part of this Chapter. This long-lived state can be used as a second stable electronic state and indeed represents a new precisely controllable degree of freedom for cold atomic systems. More details about the metastable state and transition will be presented in Section 1.1.2.

Another remarkable feature of AEL atoms is the strong decoupling between the nuclear spin and the electronic angular momentum, which is expected for all states with $J = 0$ and assures the independence of collisional properties from the nuclear spin orientation [55, 96] (see Section 1.1.4).

1.1.2 Metastable states and ultranarrow transitions

The very long lifetimes of the $^3P_0$ and the $^3P_2$ excited states is caused by the lack of a strong dipole coupling to the ground state (or to any other state[2]). In particular, the $^1S_0 \rightarrow ^3P_0$ transition is doubly-forbidden in dipole approximation [97], as it connects two states with zero total electronic angular momentum ($J = 0$) aside by requiring a spin flip ($S = 0 \rightarrow S = 1$). However, in fermionic isotopes with non-zero nuclear spin ($F = I \neq 0$), a mixing between the $^3P_0$ and the other triplet states $^3P_1$ and $^3P_2$ is induced by the hyperfine interaction, which couples states with different total electronic angular momentum J but

[2] The $^3P_0$ state is in fact the excited electronic state with the lowest energy.

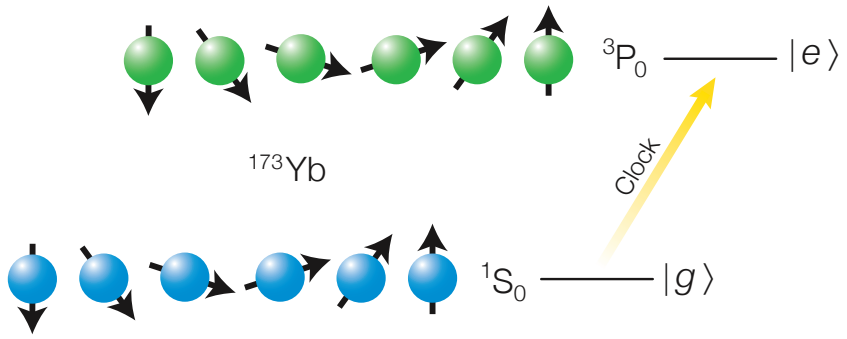

Figure 1.1 – An illustration of fermionic alkaline-earth-like atoms most remarkable features, through the example of ^{173}Yb. Two electronic states can be simultaneously used for experiments: the ground state $|g\rangle = {}^1S_0$ (blue) and the metastable state $|e\rangle = {}^3P_0$ (green) (see Section 2.1.2). They can be coherently coupled to each other owing to an ultranarrow optical clock transition (see Chapter 5). Moreover, different nuclear spin states are available (I=5/2 for ^{173}Yb). The nuclear spin can be manipulated and detected (see Chapter 4), and most importantly it is preserved throughout collisions, owing to the decoupling between nuclear spin and electronic angular momentum.

same total atomic angular momentum F. The $^3P_1$ state has in turn a small mixing with the strongly dipole-allowed $^1P_1$ state (see Section 2.1.2 for details concerning ytterbium) and this results in a finite transition dipole element of the $^1S_0 \rightarrow {}^3P_0$ transition [96]. A finite dipole coupling can also be artificially created for the bosonic isotopes by quenching the metastable state through a strong magnetic field [98, 99] or through high-intensity σ-polarised light [100], much like what the nuclear spin does in the case of fermionic isotopes. In this way, the eigenstates are perturbed and a small admixture between the $^3P_0$ and the $^3P_1$ is generated.

In addition to the innovative prospect of using the $^3P_0$ state for the quantum simulation of orbital magnetism, which will be discussed in Section 1.3, several other applications of the clock transition can be conceived. For example, owing to the long lifetime of the metastable state, the proposed schemes for engineering a coherent coupling between two or more internal states of alkali atoms via two-photon Raman dressing can be adapted to the use of a direct single-photon dressing on the clock transition. As no spontaneous emission processes would occur during typical experimental time scales eliminating any heating mechanism, such a one-photon dressing would be extremely convenient when large couplings are desirable, such as for spin-orbit coupling realisations [101, 102]. Moreover, spatially varying couplings could be implemented by modulating the intensity profile of the clock laser beam. Along this line, methods to generate strong artificial magnetic fields and gauge fields with AEL atoms have been proposed [46, 64, 84].

We also note that the metastable state possesses a zero total electronic angular momentum ($J = 0$) and it is therefore fairly insensitive to external magnetic fields, which couple only to its nuclear magnetic moment of the order of the nuclear magneton, yielding a sensitivity below a kHz/G. This insensitivity to magnetic fields of both the ground and the metastable states is a clear advantage over other atomic species in the context

of optical frequency standards [90] and atomic interferometry [103]. The insensitivity to external field fluctuations is moreover beneficial when the two lowest electronic states of AEL atoms and their nuclear spin states are used to implement qubit systems for quantum information processing, as envisioned in several proposals [56, 59, 83, 104, 105] and already exploited in CQED setups [106]. As we will explain later, the lack of electronic angular momentum in this state is also important for quantum simulation, as it is responsible for the decoupling of the nuclear spin from collisional processes.

1.1.3 State-dependent optical potentials

Dipole potentials

Optical potentials have become an absolutely central tool for the study of ultracold quantum gases [107]. Optical trapping potentials are based on the almost purely dispersive interaction between atoms and light detuned from the frequency of the atomic transitions. An atomic dipole moment is induced by the interaction of atoms with a rapidly oscillating electromagnetic radiation[3], and this moment interacts in turn with the light electric field [97]. By shaping the intensity profile of far off-resonant laser beams, optical potentials for confining the atoms can be engineered. Such potentials are greatly flexible and can be precisely tailored, in order to confine atomic samples on length scales ranging from below a single wavelength of the trapping light to hundreds of micrometers.

The induced atomic dipole moment $\mathbf{d}$ is proportional to the dynamic polarisability of the atom $\alpha(\omega)$, $\mathbf{d} = \alpha(\omega)\mathbf{E}$, where $\mathbf{E}$ is the (complex) electric field with frequency ω and amplitude E_0. By time-averaging the interaction energy between the radiation field and the induced dipole moment $\Delta E \propto -\mathbf{d}\cdot\mathbf{E}$ over the fast oscillating terms, one obtains the so-called AC-Stark shift (often simply named light shift). Treating this interaction perturbatively to the lowest non-vanishing order (second order) results in the AC-Stark shift [97, 107]:

$$V(\mathbf{r},\omega) = -\frac{1}{2\epsilon_0 c}\mathrm{Re}[\alpha(\omega)]\, I(\mathbf{r}) \tag{1.1}$$

where $I(\mathbf{r}) = 2/(\epsilon_0 c)|E_0(\mathbf{r})|^2$ and we have explicitly added the dependence on spatial coordinates $\mathbf{r} = (x, y, z)$. The conservative dipole force results from the spatial variation of the light shift:

$$\mathbf{F}(\mathbf{r},\omega) = -\nabla V(\mathbf{r}) = \frac{1}{2\epsilon_0 c}\mathrm{Re}[\alpha(\omega)]\,\nabla I(\mathbf{r}) \tag{1.2}$$

From Eq. (1.2), it can be understood how a suitably tailored intensity profile can be exploited to confine the atoms in a potential minimum or to exert a force on them.

The dynamic polarisability of a certain atomic state can be given explicitly considering all other electronic levels of the atom [97]. We refrain from recalling this here, as a two-level system approximation is sufficient in order to illustrate the working principle of dipole traps and optical lattices. Nevertheless, all electronic levels have to be included for a quantitatively accurate estimation of the state AC polarisability (see Appendix A). The

[3] If the wavelength of the radiation is comparable to the size of the atom, higher multipole moments need to be included, however this is not the case for light fields.

AC-Stark shift of the state $|\alpha\rangle$ can be given to a first approximation by considering the contribution of a single excited state $|\alpha'\rangle$ [107]:

$$V_\alpha(\mathbf{r},\omega) = -\frac{3\pi c^2}{2\omega_0^3}\left(\frac{\Gamma}{\omega_0-\omega}+\frac{\Gamma}{\omega_0+\omega}\right) I(\mathbf{r}) \simeq \frac{3\pi c^2}{2\omega_0^3}\left(\frac{\Gamma}{\Delta}\right) I(\mathbf{r}) \tag{1.3}$$

where ω_0 is the $|\alpha\rangle \rightarrow |\alpha'\rangle$ transition frequency and Γ is the transition linewidth. The last approximate equality holds in the so-called rotating wave approximation, which is accurate only for small detunings $\Delta = \omega - \omega_0 \ll \omega_0$. On the other hand, the two-level system approximation is justified only when one transition is largely predominant, i.e. when Γ/Δ is much larger for the $|\alpha\rangle \rightarrow |\alpha'\rangle$ transition than for any other transition, which is often not the case in typical experimental conditions (see Section 5.1.1). From Eq. (1.3) one can see how the sign of the light detuning from the dominant transition frequency determines the sign of the potential experienced by the atoms: a positive and a negative detuning will generate a repulsive and an attractive dipole potential, and atoms will be repelled by or attracted to the intensity maxima, respectively. Usually the Gaussian profile of red-detuned laser beams is used to create approximately harmonic dipole traps [108, 109] (for more details see Appendix A). However blue-detuned beams are successfully adopted as well to engineer specific potentials, e.g. quasi two-dimensional traps [110] or "box" potentials [111, 112].

As atoms are exposed to a light field, also the dissipative process associated with light absorption and spontaneous re-emission into dipole radiation needs to be considered. Absorption is described by the imaginary part of the polarisability [97, 107]:

$$\Gamma_{\mathrm{sc}}(\mathbf{r},\omega) = \frac{1}{\hbar\epsilon_0 c}\mathrm{Im}[\alpha(\omega)]\, I(\mathbf{r}) \tag{1.4}$$

In the two-level and rotating wave approximations the scattering rate Γ_{sc} for the state $|\alpha\rangle$ is given as [107]:

$$\Gamma_{\mathrm{sc}}(\mathbf{r}) \simeq \frac{3\pi c^2}{2\hbar\omega_0^3}\left(\frac{\Gamma}{\Delta}\right)^2 I(\mathbf{r}) \tag{1.5}$$

Photon scattering events described by Eq. (1.5) cause atoms to gain recoil-induced kinetic energy, which is much larger than the typical thermal energy in the trap. Heating and atom escape from the trap are induced, and photon scattering should thus be reduced as much as possible.

When the trapping of atoms in a single electronic $|\alpha\rangle$ state is necessary, a large detuning Δ from the dominant transition(s) can be adopted to minimise the photon scattering in Eq. (1.5). A suitable potential depth can yet be achieved through high light intensity I (see (1.3)), limited only by the availability of laser power. When the simultaneous trapping of two distinct species is necessary, e.g. two electronic states of the same atom, the trapping light should be far off-resonant while still producing a sufficiently large Stark shift for both species, often making the choice of wavelength less straightforward. Before we address the scenario of simultaneous trapping of two electronic states, let us specifically introduce optical lattice potentials, which are a key ingredient for quantum many-body physics with ultracold atomic gases [14, 23] and have many other applications, ranging from atomic clocks [49, 89] and quantum information [113–116] to matter-wave diffraction [103].

Optical lattices

Optical lattice potentials are of particular importance in the context of quantum simulation of condensed-matter models [23], as they allow to access the strongly-correlated regime by enhancing atomic interaction effects and to emulate the crystalline structure of solid materials. Usually all potentials exhibiting a discrete translational symmetry or a set of discrete translational symmetries are denoted as lattice potentials. The single-particle physics of atoms trapped in such lattices can be described using the Bloch theorem, which applies to any periodically-repeating structure [117, 118]. In addition to enabling the study of lattice systems in an almost defect-free environment, deep optical lattices can be used to probe physics in dimensions $D < 3$ by tightly confining atoms along one or more directions [24, 42, 43, 119].

A one-dimensional periodic potential can be created by aligning two counter-propagating laser beams at the same wavelength λ, which interfere and create a sinusoidally modulated intensity pattern. Usually, this is practically realised by aligning a single laser beam with its waist at the atoms position and retro-reflecting it off a mirror so that it travels back on itself, generating a standing-wave pattern with a $\lambda/2$-periodicity: $I(\mathbf{r}) = 4I_0(\mathbf{r})\cos^2(kx)$, where $\mathbf{k} = \frac{2\pi}{\lambda}\hat{x}$ is the laser wave vector and $I_0(\mathbf{r})$ is the intensity profile of the beam.

For the models and the experiments presented in this thesis, a three-dimensional square lattice potential is adopted. In order to produce this, three retro-reflected beams at the same wavelength λ, aligned in orthogonal directions, can be combined. The additional interference terms in the crossing region are suppressed by using beams with mutually orthogonal polarisations and by detuning them from one another by a frequency

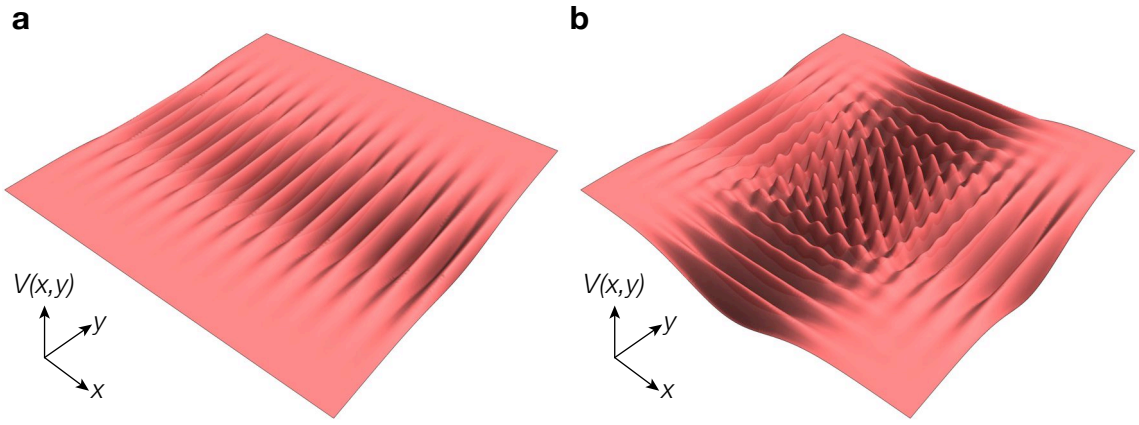

Figure 1.2 – Optical lattice potentials for red-detuned laser beams (not to scale). (a) A single retro-reflected beam along the x-axis interferes with itself and creates a one-dimensional array of potential wells. A confinement along the y-direction is also present owing to the Gaussian intensity profile of the lattice beam. (b) A two-dimensional square lattice potential is generated by crossing two retro-reflected beams with the same frequency and orthogonal polarisations. In real lattice potentials, a much greater number of lattice sites is available in the crossing region, as the size of the generating beams is much larger compared to their wavelength than in the illustration.

greater than the laser spectral width. More complex lattice geometries, i.e. characterised by translational symmetries that differ from the simple cubic one, can be created by interfering laser beams from different directions and possibly not orthogonally aligned to each other [33, 35, 36]. The potential experienced by the atoms in a three-dimensional square lattice can be written as:

$$V_{\text{lat}}(\mathbf{r}) = V_x(\mathbf{r})\cos^2(kx) + V_y(\mathbf{r})\cos^2(ky) + V_z(\mathbf{r})\cos^2(kz) \tag{1.6}$$

where $V_\mu(\mathbf{r})$ are given by the light shift in Eq. (1.3) with $I_\mu(\mathbf{r}) = 4\,I_{0\mu}(\mathbf{r})$. For red-detuned light, the potential minima are located at the anti-nodes of the standing-wave intensity pattern. By using laser beams with a Gaussian intensity profile, a spatial variation of the lattice potential depths $V_\mu(\mathbf{r})$ is present. However, the variation is typically significative only along the directions orthogonal to μ, e.g. $V_x(\mathbf{r}) \simeq V_{0x}\, I_{0x}(0, y, z)/I_0$ (see Fig. 1.2(a)). The lattice depth $V_{0\mu}$ along each direction is usually expressed in units of recoil energy of the lattice laser $E_r = \frac{\hbar^2 k^2}{2M}$, with M being the mass of the atom. The transversal variation of the potential is weak over the lattice wavelength scale (see Appendix A), yet it is fundamental to confine samples in optical lattices without additional trapping beams [107]. When distinct one-dimensional lattice potentials are combined in orthogonal directions, the confining potential produced by the Gaussian profile of each beam is aligned along the direction of propagation of another beam: the total potential along each direction is therefore given by the sum of a periodic lattice and a slowly-varying confinement (see Fig. 1.2(b) and Fig. A.2), and the periodicity of the homogenous lattice potential is removed.

Motion in a periodic potential: tight-binding Hamiltonian

Non-interacting, fermionic or bosonic atoms in a three-dimensional lattice potential are described by the Hamiltonian $\hat{H}_0 = \mathbf{p}^2/(2M) + V_{\text{lat}}(\mathbf{r})$, which can be written in second quantisation:

$$\hat{H}_0 = \int d^3r\, \hat{\psi}^\dagger(\mathbf{r}) \left(-\frac{\hbar^2}{2M}\nabla^2 + V_{\text{lat}}(\mathbf{r}) \right) \hat{\psi}(\mathbf{r}) \tag{1.7}$$

where $\hat{\psi}^\dagger(\mathbf{r})$ ($\hat{\psi}(\mathbf{r})$) is the field operator that creates (annihilates) a particle at position $\mathbf{r}$. For a homogenous lattice potential, this Hamiltonian can be diagonalised in the basis of the so-called Bloch waves, obtained by applying the Bloch theorem for particles moving in a periodic potential [117, 118]. Bloch waves are characterised by their crystal momentum or quasimomentum $\mathbf{q}$, which is restricted to the first Brillouin zone, i.e. $-k < q \leq k$ [118]. The energies of Bloch waves are clustered in continuous energy bands called Bloch bands, which are separated by energy gaps (see Fig. A.3). However, Bloch waves are strongly delocalised and are not suited to describe local effects, such as inter-atomic short-range interactions. A different basis can be constructed, composed by localised wave functions within each Bloch band, called Wannier functions [118] (see Appendix A for an explicit derivation). Wannier functions are as localised as possible around the positions of the lattice potential minima, usually denoted as *lattice sites*. They form a suitable orthonormal basis to treat contact interactions in a lattice, as we will see in the following Section, or to account for an additional confinement underlying the lattice potential (see Appendix B).

For typical experimental conditions, the Hamiltonian in Eq. (1.7) can be simplified by restricting the description to the lowest Bloch band and by applying the so-called tight-binding approximation, which can be done in the Wannier basis. To start with, in the limit of sufficiently deep lattices and ultralow temperatures, all energy scales become small compared to the energy gap to the first excited band, and only the lowest Bloch band is occupied. Secondly, we can neglect the tunnel coupling between Wannier states associated with non-neighbouring lattice sites, which is a good approximation for lattice depths exceeding $5\,E_r$ [14, 21]. This approximation is justified as the overlap between Wannier functions centred around non-neighbouring lattice sites becomes negligible for increasing lattice depths[4] (see Fig. A.4).
We now expand the field operators in Eq. (1.7) in terms of lowest-band Wannier operators:

$$\hat{\psi}(\mathbf{r}) = \sum_j w_j(\mathbf{r})\,\hat{c}_j \tag{1.8}$$

where $w_j(\mathbf{r})$ is the lowest-band Wannier function centred around lattice site j, and $\hat{c}_j^\dagger$ ($\hat{c}_j$) creates (annihilates) an atom localised at site j. For identical fermions, $(\hat{c}_j^\dagger)^2 = 0$, which ensures the application of the Pauli principle. Within the aforementioned approximations, the Hamiltonian of non-interacting atoms in a lattice potential takes now a very simple form:

$$\hat{H}_0 = -J \sum_{\langle i,j \rangle} \hat{c}_i^\dagger \hat{c}_j \tag{1.9}$$

where the $\langle\,\rangle$ brackets indicate that the sum runs only over neighbouring lattice sites. The tunnel coupling J is given by:

$$J \equiv J_{\langle i,j \rangle} = \int d^3r\, w_i^*(\mathbf{r}) \left(-\frac{\hbar^2}{2M}\nabla^2 + V_{\text{lat}}(\mathbf{r}) \right) w_j(\mathbf{r}) \tag{1.10}$$

and the value of J is independent of the specific pair of neighbouring lattice sites $\langle i,j \rangle$ in an isotropic cubic lattice. For non-cubic lattices, the tunnelling is anisotropic and different tunnelling coefficients must be specified for the different directions. J has an approximately exponential dependence on the lattice depth V_0 [14] and can therefore be experimentally varied over order of magnitudes by tuning the lattice beam intensities. In the following Section, we will extend the Hamiltonian (1.9) to describe fermionic atoms in different spins and electronic states, and especially to include interactions between them.

State-dependent potentials for alkaline-earth-like atoms

As already stated, the dipole potential experienced by an atom in the presence of detuned light depends entirely on its internal state. Thanks to the presence of metastable states, optical state-dependent potentials represent an exceptional tool in quantum gases experiments with AEL atoms [56]. We will discuss now the essential aspects of such potentials for AEL atoms and clarify the relevance of different alternative configurations for possible

[4] Similarly, in next Section, we will neglect off-site contact interactions, which depend on the absolute square overlap of Wannier functions.

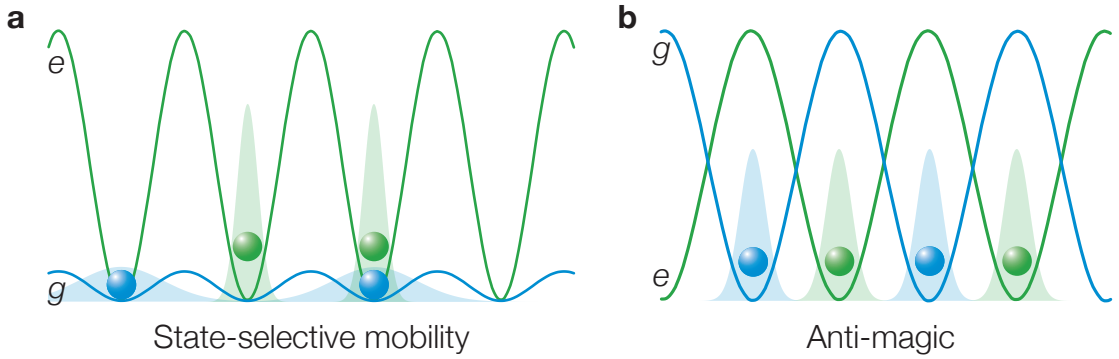

Figure 1.3 – State-dependent optical lattices for $|g\rangle$ (blue) and $|e\rangle$ (green) states of AEL atoms. The solid lines represent the light-induced potentials, whereas the coloured regions depict the atomic wave functions. (a) A state-selective lattice induces different localisation for the two states. The $|g\rangle$ state has a large tunnelling coupling and is therefore mobile, while the $|e\rangle$ state is localised in deep lattice sites. The minima of the potentials coincide, and atoms in different states can therefore be found on the same lattice site. (b) An anti-magic lattice generates two shifted but identical sub-lattices for the $|g\rangle$ and $|e\rangle$ states. Tunnelling between the two sub-lattices can be coherently driven using the clock transition.

applications. State-dependent potentials for cold atoms are actually not a new concept: spin state-dependent optical lattices based on polarisation schemes were already proposed and implemented for quantum information processing purposes [113–116, 120]. Furthermore, one can create hyperfine state-dependent potential for alkali atoms simply by employing laser light close-detuned to the D1 and D2 transitions, which results in different light shifts for the $F = 1$ and $F = 2$ ground states. However, substantial heating is caused in this way by the photon scattering. Let us henceforth denote the two electronic states $^1S_0$ and $^3P_0$ respectively as $|g\rangle$ and $|e\rangle$. One can already expect from Eq. (1.3) that the light shift created by a beam at a certain frequency ω will in general be different for $|g\rangle$ and $|e\rangle$ atoms, depending on the detuning from the relevant transitions for each of the two states (for details about the frequency dependence of the light shifts in ytterbium see Section 5.1.1). Using two (meta-) stable electronic states separated by an energy in the optical range grants a considerable advantage: state-dependent light shifts can be generated by light that is far-detuned with regard to transitions from both states [56]. One can therefore engineer state-specific optical potentials without sacrificing low photon scattering rates. Moreover, as the AC-Stark shift of the $|g\rangle$ and $|e\rangle$ states widely varies across the range of optical frequencies (see e.g. Fig. 5.1), a multitude of different relative potential depths can be tailored.

We will now summarise the most relevant of all possible relations between the two state polarisabilities. The first special scenario is found when the two states experience exactly the same AC-Stark shift, i.e. $\alpha_g(\omega_m) = \alpha_e(\omega_m)$, experiencing thus identical light potentials; the light frequencies (wavelengths) for which this is realised are called *magic*[5]. Magic-wavelength lattices are a crucial tool for precision spectroscopy of cold gases and

[5]We actually mean only the real part of the polarisability $\alpha_{g,e}(\omega)$. The associated imaginary parts follow a completely different behaviour, with maxima at the respective electronic transition frequencies.

for the operation of AEL-based optical lattice clocks, which represent a strong prospect for new absolute frequency standards and for a re-definition of the SI second [49, 89, 90]. In general, optical potentials induce line shifts and broadening of optical ultranarrow transitions like the clock transition in AEL atoms. However, at the magic wavelengths the second-order differential light shift is exactly cancelled, increasing dramatically the attainable precision of the clock frequency interrogation with trapped atoms [90, 121, 122]. Magic wavelengths between ground and short-lived excited states are also used in cavity quantum electrodynamics to obtain long trap lifetimes of single atoms inside the cavity, through preventing heating and decoherence caused by jumping between different trapping potentials while the transition is probed [123]. A magic lattice for ytterbium was used in the experiments presented in this thesis [124] and a detailed discussion of precision spectroscopy in such a lattice is found in Chapter 5.

The opposite scenario, where the two polarisabilities are equal in magnitude but have opposite signs, i.e. $\alpha_g(\omega_{am}) = -\alpha_e(\omega_{am})$, happens at *anti-magic* frequencies (wavelengths). As illustrated in Fig. 1.3(b), anti-magic lattice potentials trap the $|g\rangle$ and $|e\rangle$ atoms in separate sublattices, whose sites are located at the nodes and the anti-nodes of the standing-wave intensity pattern. These lattices can find applications based on state-selective forces, e.g. to spatially separate atoms in the two states [125]. Their use was proposed in combination with dressing of the $|g\rangle$ and $|e\rangle$ states through near-resonant clock light to implement sub-wavelength lattices [57] and as a key ingredient of optical flux lattices [84]. Clock spectroscopy in an anti-magic lattice could also be employed to study next-neighbour interactions between the two electronic states trapped in different sub-lattices. Moreover, tunnelling between the adjacent sites of the two sub-lattices can be coherently assisted by driving the clock transition, and this could be exploited for engineering strong artificial magnetic fields and even non-abelian gauge fields for neutral atoms [46, 64]. As another interesting prospect, spatially separate potentials for the two electronic states would allow the implementation of photoemission spectroscopy on the clock transition, in analogy to the radio-frequency photoemission spectroscopy implemented in alkali atom ultracold gases [126]. A momentum-conserving transfer to the metastable state trapped in a different location out of the ground state ensemble could be employed just like the radio-frequency transfer to a weakly interacting spin state.

In general, state-selective lattices with largely dissimilar depth for the two states can be realised, as depicted in Fig. 1.3(a), leading to state-dependent tunnelling amplitudes and Hubbard interactions (see Section 1.3). Perfectly state-selective lattices, generating a potential exclusively for one of the two electronic states, were initially suggested as transport lattices in a quantum computation scheme with AEL atoms [56]. Such lattices have been subsequently proposed for the study of renowned condensed-matter models based on the interaction between electrons occupying orbitals with different degrees of mobility or between electrons and localised impurities [55, 60, 61], e.g the Kondo lattice model [127] and the Kugel-Khomskii model[128]. We will specifically address the realisation of orbital magnetism with AEL atoms in state-dependent optical lattices in Section 1.3.
Moreover, lattices tuned to near-resonant frequencies to the clock transition were proposed for novel quantum computing schemes with AEL atoms [104] and for the realisation of optical flux lattices to generate strong effective magnetic fields [84]. As a final applica-

tion, techniques which were proposed and demonstrated in species-dependent potentials [129] could be extended to the case of state-dependent trapping, e.g. entropy exchange between the two states [130].

1.1.4 Nuclear spin and angular momentum decoupling

We have already mentioned that fermionic AEL isotopes possess a non-zero nuclear spin I, which is semi-integer owing to the odd-numbered atomic mass. On the contrary, all bosonic AEL atom isotopes possess a zero nuclear spin ($I = 0$). The reason for this becomes clear by considering that a total even number of electrons, given by the complete filling of the electronic shells, forces the number of protons and neutrons as well to be even for a bosonic atom. In nuclei with even number of protons and neutrons, usually named even-even nuclei, the pairing interaction between identical nucleons induces them to anti-align their spins, leading in this way to a zero nuclear spin.

Due to the absence of electronic angular momentum in the ground and in the lowest metastable state, the nuclear spin degree of freedom is the only angular momentum degree of freedom of the atom. For all states with $J = 0$ the total atomic angular momentum is thus simply $F = |\mathbf{J} + \mathbf{I}| = I$. This situation enables a strong decoupling between the nuclear spin and the electronic cloud: the spin is protected inside the nucleus and to a large degree it is not affected by the physics happening at the electronic cloud distance scale. This has a striking consequence concerning the atomic collisional properties, since in general nuclei can affect collisions only through hyperfine coupling to the electron angular momentum, aside from Pauli exclusion [20].

During a collision, two atoms come to be at very short distance, where molecular electronic states are coupled to the independent states of the colliding atoms. Those molecular states which dominate in collisions between atoms with $J = 0$ also have a zero projection $\Omega = 0$ of the total electronic angular momentum along the molecular axis. As a consequence, the nuclear spin is largely decoupled from the electronic state also during a collision, and can only couple very weakly to molecular states with non-zero angular momentum, which could lead to spin-changing processes [55]. Spin-changing processes are therefore expected to be completely suppressed over typical experimental time scales, with the nuclear spin being substantially immune to collisions. In addition, direct magnetic dipole-dipole coupling between the nuclear spins of two atoms is completely negligible even for inter-particle distances as small as few nanometers.
In conclusion, all collisional properties between atoms in states with $J = 0$ are expected to be largely independent of the nuclear spin. We will see in the following Section how this leads to the emergence of a high and unusual SU(N) symmetry in the interaction potential, where $N \leq 2F + 1$.

1.2 Two-orbital SU(N)-symmetric Fermi gases

Interactions play a crucial role in experiments with ultracold gases: it is largely owing to interactions that cold atoms emerged as quantum simulators of strongly-correlated phe-

nomena. In addition, they are essential for the creation of quantum degenerate samples, as they enable evaporative cooling. In dilute ultracold atomic ensembles, interactions are predominantly mediated by binary inter-atomic collision processes. Two-body atomic scattering processes are in general quite complicated, as the electronic wave functions get massively distorted when the two atoms find themselves at short relative distances. However, for the low temperatures $T < 1\,\mu$K which are typical in experiments, many simplifications can be applied. In this Section we will first briefly recall the theoretical description of scattering at low temperatures, focusing especially on the case of fermions with a spin degree of freedom. We will thereby introduce the s-wave scattering length and briefly discuss collisions between high-spin fermions, i.e. with spin higher than one-half. We will then discuss the emergence of the SU(N) symmetry of collisions for AEL atoms and derive the Hamiltonian for an interacting atomic ensemble trapped in an optical lattice, i.e. the so-called SU(N) Fermi-Hubbard model. We will finally extend the treatment of interactions to the presence of an additional internal degree of freedom, in order to provide a Hamiltonian describing interactions in a two-orbital gas, i.e. a gas containing atoms in both $|g\rangle$ and $|e\rangle$ states.

1.2.1 Interactions in an ultracold gas

In dilute atomic gases, i.e. with inter-particle spacing much larger than the inter-atomic potential range, interactions result almost exclusively from elastic binary collisions. We will initially neglect inelastic collisions, which can play a big role at high densities or when internal state relaxation processes are available [131]. The precise character of the binary interaction potentials critically depends on the inter-atomic distance $r = |\mathbf{r}|$; when two atoms come at short distance, several elastic and inelastic collision channels become available, associated with the different molecular potentials, that depend on the states of the two atoms and couple different incoming and outgoing states [20]. Nevertheless, in order to describe elastic scattering at very low energies, it is not necessary to know the precise shape of the molecular potentials.

Elastic scattering at low energies

Elastic collisions do not modify the relative kinetic energy of the colliding atoms, but can redistribute momentum between the atoms. For a given inter-atomic scattering potential $V(\mathbf{r})$ with characteristic range r_0, the relative asymptotic ($r \gg r_0$) wave function after the scattering can be written as [117]:

$$\psi(\mathbf{r}) = e^{i\,\mathbf{k}\cdot\mathbf{r}} + f(\mathbf{k},\mathbf{k}')\frac{e^{ikr}}{r} \tag{1.11}$$

where $\mathbf{k}$ and $\mathbf{k}'$ are respectively the wave vectors of the incoming and outgoing wave and $f(\mathbf{k},\mathbf{k}')$ is the scattering amplitude. Assuming the inter-atomic potential is spherically symmetric, which is in usual atomic gases a very good assumption, the scattering amplitude can be expanded into spherical harmonics [117]:

$$f(\mathbf{k},\mathbf{k}') = f(\theta) = \sum_{l=0}^{\infty}(2l+1)\,e^{i\delta_l}\,\sin\delta_l\,P_l(\cos\theta) \tag{1.12}$$

where θ is the scattering angle between $\mathbf{k}$ and $\mathbf{k}'$, δ_l is the phase shift acquired by the partial wave with angular momentum l and P_l are the Legendre polynomials. By integrating the square modulus of the scattering amplitude over solid angles, we can also obtain the total scattering cross section [117]. For distinguishable particles we can write:

$$\sigma_{\mathrm{el}} = \frac{4\pi}{k^2} \sum_l (2l+1) \sin^2(\delta_l) \tag{1.13}$$

At the typical temperatures of ultracold atomic samples, where the low energy limit applies ($k \to 0$), only the spherical wave $l = 0$ (s-wave) contributes to the scattering. More specifically, for potentials vanishing fast enough at large r, the phase shifts $\delta_l \propto k^{2l+1}$ as k tends to 0 and it can be shown that the scattering amplitude is given by [117]:

$$f(\theta) \underset{k\to 0}{=} -\frac{1}{a^{-1} + ik} \tag{1.14}$$

where a is called the the s-wave scattering length. In order to understand the physical meaning of a, let us take $r \gg r_0$ and write the asymptotic wave function:

$$\psi(\mathbf{r}) \underset{k\to 0}{\propto} \frac{r-a}{r} \tag{1.15}$$

The intercept of $r\,\psi(\mathbf{r})$ (the radial part of the wave function) equals $-a$ at $r = 0$, i.e. the asymptotic wave function intercept coincides with the s-wave scattering length. The scattering potential shifts thus the asymptotic wave function: a positive scattering length effectively corresponds to a repulsive interaction whereas a negative one reproduces an attractive interaction.
In the s-wave regime, the scattering cross section is simply given by:

$$\sigma_{\mathrm{el}} \underset{k\to 0}{=} 4\pi a^2 \tag{1.16}$$

We note finally that the spatial part of the two-body wave function is symmetric for even l and antisymmetric for odd l, as a consequence of the Legendre polynomials parity. Two identical fermions can therefore only interact via odd partial waves and do not interact in the s-wave scattering regime, whereas fermions in distinct internal states are allowed to interact via s-wave collisions.

In conclusion, the low-energy scattering between two atoms can be entirely described by the scattering length a, irrespective of how complicated the close-range potential might be. However, calculating the scattering length from first principles is a very complicated task and requires a detailed knowledge of the inter-atomic potentials. The scattering length a needs therefore to be determined experimentally for each element and isotope.

Interaction pseudo-potential

Since the low-energy scattering of two atoms is just characterised by the scattering length a, it is possible to model collisions by using any desired short-ranged potential yielding that scattering length. The scattering amplitude in Eq. (1.14) is exactly reproduced by constructing an s-wave pseudo-potential $U(r)$, called the Fermi contact potential [132]:

$$V(\mathbf{r}) = \frac{4\pi\hbar^2}{M} a\, \delta(\mathbf{r}) \tag{1.17}$$

When interactions are strong enough to significantly distort the relative two-particle wave function at $r \to 0$ and produce some non-regular contribution at $r = 0$, the contact potential needs to be regularised [133], replacing the Dirac delta with $\delta(\mathbf{r})\frac{\partial}{\partial r}r$. It should be kept in mind that the pseudo-potential (1.17) is a zero-range potential, in the sense that it does not account at all for the range r_0 of the real inter-atomic potential, so it fails for $k > 1/r_0$.

We can now write the interaction Hamiltonian between fermionic atoms with different spins, in second quantisation:

$$\begin{aligned}\hat{\mathcal{U}} &= \frac{1}{2}\sum_{mm'}\int d^3r\, d^3r'\, \hat{\psi}^\dagger_m(\mathbf{r})\,\hat{\psi}^\dagger_{m'}(\mathbf{r})\,V(\mathbf{r}-\mathbf{r}')\,\hat{\psi}_{m'}(\mathbf{r}')\,\hat{\psi}_m(\mathbf{r}') \\ &= \frac{4\pi\hbar^2 a}{M}\frac{1}{2}\sum_{mm'}\int d^3r\,\hat{\psi}^\dagger_m(\mathbf{r})\,\hat{\psi}^\dagger_{m'}(\mathbf{r})\,\hat{\psi}_{m'}(\mathbf{r})\,\hat{\psi}_m(\mathbf{r})\end{aligned} \tag{1.18}$$

where $\hat{\psi}^\dagger_m(\mathbf{r})$ ($\hat{\psi}_m(\mathbf{r})$) creates (annihilates) an atom with spin projection m at position $\mathbf{r}$, and satisfies: $\left\{\hat{\psi}_m(\mathbf{r}), \hat{\psi}^\dagger_{m'}(\mathbf{r}')\right\} = \delta_{mm'}\,\delta(\mathbf{r}-\mathbf{r}')$.
We will use this expression to later obtain the Hamiltonian of interacting fermionic AEL atoms in a lattice potential.

Inelastic collisions

We have so far only addressed the elastic scattering of atoms. However, inelastic collisions can also be significative, especially when internal state relaxation processes are available, converting atoms' internal energy into kinetic energy. The excess kinetic energy induces heating of samples, and can moreover cause atom losses: atoms can escape the trap by acquiring a kinetic energy larger than the trap depth. In the absence of internal relaxation processes, only two inelastic processes are available: vacuum background collisions and three-body recombinations. Vacuum background collisions, i.e. collisions with the background gas in the vacuum system, can be made insignificant by achieving a sufficiently low background pressure, so that their contribution during time scales on the order of seconds is negligible (see e.g. Fig. 3.4). On the other hand, three-body recombinations, i.e. processes in which two atoms form a weakly-bound state and a third atom carries away their binding energy, become relevant only for strongly interacting atoms and high densities, since the induced density loss rate scales approximately as $\propto n^2 a^4$ [131, 134] in comparison to $\propto n a^2$ for elastic scattering (see Eq. (1.22) below). Moreover, three-body collisions in the s-wave scattering regime are completely suppressed in a two-component Fermi gas, due to Pauli exclusion.

Most experiments in this thesis are performed using two-spin Fermi gases, yet including an additional internal degree of freedom, namely the electronic state. Atoms may then change their electronic state throughout a collision, in which case they escape the trap pair-wise due to the large acquired energy. We will now briefly discuss such two-body loss processes, which play an important role in the experiments presented in Section 6.2. Let us consider fermionic atoms in different internal states $|\alpha\rangle$ and $|\alpha'\rangle$, e.g. spin or electronic states, so that they are free to collide. Inelastic collisions causing atom losses can

be described by a two-body loss rate coefficient $\beta_{\alpha\alpha'}$ [135, 136]:

$$\dot{n}_\alpha(t) = -\beta_{\alpha\alpha'}\, n_\alpha(t)\, n_{\alpha'}(t) \tag{1.19}$$

where n_α is the mean density of the α component.

An imaginary part of the scattering length can be introduced by setting $a = A - iB$, in order to account for two-body inelastic processes which reduce the elastic scattering channel amplitude [137, 138]. The elastic and inelastic cross sections in the low-energy limit are then given by:

$$\sigma_{\text{el}} = 4\pi(A^2 + B^2), \qquad \sigma_{\text{inel}} = \frac{4\pi}{k}B \tag{1.20}$$

The elastic and inelastic collision rate constants γ_{el} and β_{inel} are related to the cross sections $\sigma_{\text{el, inel}}$ by the thermal averages [131, 138]:

$$\gamma_{\text{el}} = \frac{2\hbar}{M}\langle k\,\sigma_{\text{el}}\rangle_{\text{th}}\,, \qquad \beta_{\text{inel}} = \frac{2\hbar}{M}\langle k\,\sigma_{\text{inel}}\rangle_{\text{th}} \tag{1.21}$$

By inserting Eqs. (1.20) into these, we obtain:

$$\gamma_{\text{el}} = \frac{8\pi\hbar}{M}(A^2 + B^2)\langle k\rangle_{\text{th}}\,, \qquad \beta_{\text{inel}} = \frac{8\pi\hbar}{M}B \tag{1.22}$$

where k_B is the Boltzmann constant. Assuming inelastic collisions directly lead to pair losses, we can write the loss rate coefficient $\beta_{\alpha\alpha'}$ introduced above as:

$$\beta_{\alpha\alpha'} = -\frac{8\pi\hbar}{M}\text{Im}[a_{\alpha\alpha'}] \tag{1.23}$$

where $a_{\alpha\alpha'}$ is the scattering length between two atoms in internal state $|\alpha\rangle$ and $|\alpha'\rangle$. As an example, for a initial balanced density $n_\alpha = n_{\alpha'} = 10^{14}$ atoms/cm^3, a one-second lifetime results from a two-body rate coefficient $\beta_{\alpha\alpha'} = 10^{-14}$ cm^3/s. We finally note in particular that the inelastic scattering rate (in three dimensions) is independent of temperature. We will use this results in the last part of Chapter 6, in the context of inelastic collisions involving metastable state atoms.

Optical Feshbach resonances

Magnetic Feshbach resonances provide a powerful and widely used technique to tune the scattering length over a large range of values in alkali atomic ensembles [20]. Unfortunately, magnetic Feshbach resonances cannot be used to tune the interactions in atomic states lacking magnetic electronic structure, as it is the case for the ground and the metastable state of AEL atoms with $J = 0$. Nevertheless, the use optically-tuned Feshbach resonances (OFR) was proposed [138–140] and successfully demonstrated with ytterbium [141] and strontium [142]. The principle of OFR is to induce a coupling between a colliding pair of atoms and an excited molecular bound state through laser light tuned in the vicinity of a photoassociation resonance [139]. In AEL atoms, this comes with the beneficial availability of narrow photoassociation transitions associated with the singlet-triplet electronic transitions like the $^1S_0 \rightarrow {}^3P_1$, which can be employed to minimise

the photon scattering-induced heating and losses [140]. It should be noted, however, that the induced coupling to an excited state with $J \neq 0$ breaks the decoupling of nuclear spin and electronic angular momentum (see Section 1.1.4). p-Wave OFR were also suggested and recently implemented, with possible future applications in probing unconventional fermion superfluidity [143, 144]. An additional possibility with interesting prospects is the engineering of a spatially-varying scattering length by tailoring the intensity profile of the photoassociation laser beam [145].

1.2.2 SU(N) symmetry of interactions

We already anticipated that the decoupling between the nuclear spin and the electronic angular momentum leads to the emergence of SU(N) symmetry. After recalling the usual SU(2) symmetric description of systems with a spin degree of freedom associated with three-dimensional spin rotations, we will analyse the description of interactions between fermions with a spin higher than 1/2. Within this framework, we will then discuss the extension to SU(N) symmetry.

A many-particle system is said to possess a symmetry if its observable behaviour is invariable under certain transformations of a degree of freedom of its constituents. Symmetries can be continuous, such as the translational symmetry of a homogenous system in free space, or discrete, such as the translational symmetry of a system trapped in a periodic potential. Continuous symmetries are described by symmetry groups which in quantum mechanics are unitary groups, i.e. groups of unitary operators which preserve the norm of state vectors and therefore probabilities. A central example is the symmetry under three-dimensional rotations, which is described by the different (irreducible) representations of the rotation group $\mathcal{R}(3)$ and are identified by the integer (or half-integer) values of the angular momentum (or spin) operator F [117, 146]. The half-integer spin representations of $\mathcal{R}(3)$, also called SO(3), are actually double-valued representations of the group: to any rotation R correspond two distinct matrices differing by a sign. Strictly speaking these are representations of the SU(2) group, which is a universal cover of $\mathcal{R}(3)$. Although SU(2) and $\mathcal{R}(3)$ are therefore not isomorphic, we can safely consider the representations of SU(2) as double-valued representations of $\mathcal{R}(3)$ [117]:

$$U_R(\hat{\mathbf{n}}, \theta) = \exp\left(-i\,\mathbf{F}\cdot\hat{\mathbf{n}}\,\theta\right) \tag{1.24}$$

with $F = 1/2,\ 1,\ 3/2,\ \ldots$.

For a system of non-interacting spin-F fermions[6] (F is half-integer) the Hamiltonian usually possesses a SU(2) symmetry, i.e. is invariant under three-dimensional rotations U_R, given that terms breaking the spherical symmetry are absent. Symmetry-breaking terms include for instance couplings of the spin to an external magnetic field or vector AC-Stark shifts in optical potentials [97]. The symmetry induces an energy level degeneracy of order $2F+1$, because the Hamiltonian, $\mathbf{F}^2$ and F_z commute with each other and can be diagonalised simultaneously. States with different values of m_F, the projection of the spin

[6] The notation is suggestive, i.e. the total atomic angular momentum plays for fermionic atoms the role of the spin F. States with distinct F are eigenstates of the hyperfine interaction between the electronic angular momentum and the nuclear spin.

on the quantisation axis, have thus the same energy and we say that F and m_F are *good* quantum numbers[7]

Interactions between fermions with a spin degree of freedom

Let us now consider binary interactions between ultracold fermions, as they were introduced in the previous Section. When an atomic spin degree of freedom is present, the quantum mechanical exchange interaction causes the inter-atomic potential to depend strongly on the total spin of the colliding atomic pair [20, 147]. This gives rise for example to the splitting between the singlet and the triplet potentials for atoms with spin-1/2 electronic spin [20]. As atoms approach each other, the exchange interaction energy of the overlapping electron clouds increases and it becomes comparable to the individual atom hyperfine interaction energies. Therefore, the individual F and m_F are no more good quantum numbers at short inter-particle distances. However, another SU(2) symmetry is present, associated with the rotational invariance of the inter-atomic potential. The generators of this symmetry are the components of the total angular momentum of the collision. In the ultracold s-wave scattering regime, where the orbital angular momentum of the colliding pair is zero, the angular momentum of the collision is then equivalent to the internal angular momentum of the pair $\mathbf{F}_{\text{pair}}$ [8]. As a consequence, the internal angular momentum of the pair and its projection on the quantisation axis are conserved throughout collisions[9].

The interaction pseudo-potential introduced in Eq. (1.17) applies to single-component bosons and spin-1/2 fermions only, and has to be generalised for spinor condensates or higher-spin fermionic gases [148, 149]. The pseudo-potential for a pair of spin-F fermions can be written as:

$$V'(\mathbf{r}) = \frac{4\pi\hbar^2}{M} \sum_{\substack{F_{\text{pair}}=0 \\ \text{even}}}^{2F-1} a_{F_{\text{pair}}} \mathcal{P}_{F_{\text{pair}}} \delta(\mathbf{r}) \tag{1.25}$$

where $F_{\text{pair}} = 0, 2, \ldots, 2F-1$ is the modulus of the total spin of the pair, $\mathbf{F}_{\text{pair}} = 2\mathbf{F}$, and $\mathcal{P}_{F_{\text{pair}}}$ is the projection operator onto the states with total spin F_{pair}. Due to quantum statistics, only even values of F_{pair} are allowed [147]. Under particle exchange, the two-particle wave function of spin-F particles changes by a factor of $(-1)^{2F}$ and the spin wave function changes by a factor $(-1)^{2F+F_{\text{pair}}}$. For s-wave collisions the spatial wave function is symmetric, and we must therefore have $(-1)^{2F} = (-1)^{2F+F_{\text{pair}}}$, so that F_{pair} must be even[10]. From Eq. (1.25) it is clear that a total $(2F+1)/2$ scattering lengths $a_{F_{\text{pair}}}$ are

[7] Strictly speaking, these are good quantum numbers only at zero magnetic field, but it is reasonable to use them in the regime of weak fields as well (Zeeman regime), when the hyperfine interactions dominate over the effect of the magnetic field. If $F = I$ (hyperfine interaction is completely absent), $F = I$ and $m_F = m_I$ are good quantum numbers at any magnetic field.

[8] The symmetry can thus be described by the $(2F_{\text{pair}}+1)$-dimensional representations of SU(2), and the total symmetry group is SU(2) $\otimes$ SU(2) $\otimes \cdots \otimes$ SU(2), for all allowed values of F_{pair}.

[9] We are neglecting here spin-orbit coupling through the short-range molecular potentials, which can induce dipolar relaxation converting internal to orbital angular momentum. In that case, the atom pair can leave the collision with e.g a d-wave outgoing wave function by changing its internal angular momentum.

[10] Note that this requirement holds for both bosons and fermions.

in general necessary to describe all the available s-wave collision channels. The many possible relations among the various scattering lengths lead to a variety of spin orderings in the many-body ground state of such systems, even in bulk, yielding to very rich many-body phase diagrams [74, 147, 150–152].

To clarify the effect of collisions on the spin degree of freedom of the separated atoms, we may look at the coupling between different single-atom spin orientations caused by the interaction. Let's consider as an initial state of a separated atomic pair the factorised state: $|F,m_1\rangle \otimes |F,m_2\rangle$. The coupling to a different spin combination $|F,m_3\rangle \otimes |F,m_4\rangle$ through the interaction potential can be written as:

$$\begin{aligned}
&\langle F,m_3|\langle F,m_4|V'(\mathbf{r})|F,m_1\rangle|F,m_2\rangle = \\
&= \sum_{F_{\text{pair}}=0}^{2F-1} \sum_{M_{F\text{pair}}=-F_{\text{pair}}}^{F_{\text{pair}}} \langle F,m_3\,;F,m_4|V'(\mathbf{r})|F_{\text{pair}},M_{F\text{pair}}\rangle \left\langle F_{\text{pair}},M_{F\text{pair}}\,\middle|\,F,m_1\,;F,m_2\right\rangle \\
&= \frac{4\pi\hbar^2}{M}\delta(\mathbf{r}) \sum_{F_{\text{pair}}} \sum_{M_{F\text{pair}}} a_{F_{\text{pair}}} \left\langle F,m_3\,;F,m_4\,\middle|\,F_{\text{pair}},M_{F\text{pair}}\right\rangle \left\langle F_{\text{pair}},M_{F\text{pair}}\,\middle|\,F,m_1\,;F,m_2\right\rangle
\end{aligned} \tag{1.26}$$

From Eq.(1.26) one can see how all scattering channels F_{pair} with non-vanishing Clebsch-Gordan coefficients $\left\langle F,m_F\,;F,m_F'\,\middle|\,F_{\text{pair}},M_{F\text{pair}}\right\rangle$ on the initial and final states contribute to this coupling. Therefore in general, when atoms with definite spin projections undergo collisions, different spin states become populated owing to the interference of the different scattering channels with coupled spin F_{pair} [153]. Most importantly, no spin combination will then be stable during collisions, with the exception of the combinations of marginal states $|F,m_F=\pm F\,;F,m_F'=\pm F\mp 1\rangle$.

Emergence of SU(N) symmetry

There is one very special case where the interactions described by the pseudo-potential in Eq. (1.25) possess a symmetry that can be much higher than the $\otimes_{(2F+1)/2}$ SU(2) discussed above. We have already illustrated how fermionic AEL atoms in the ground state possess only a nuclear spin degree of freedom, which is completely decoupled from the electronic cloud owing to the absence of hyperfine interactions. Moreover, the metastable $^3\text{P}_0$ state also possess a vanishing hyperfine interaction to leading order [96], and has thus strongly decoupled nuclear and electron degrees of freedom. As the spin dependence of inter-atomic potentials arises from the quantum exchange interaction of the electron clouds, interactions become largely spin-independent when no electronic angular momentum is present [55]. The influence of nuclear spins on the scattering process is therefore reduced simply to Pauli exclusion, and all the scattering lengths $a_{F_{\text{pair}}}$ are equal. Under such conditions, the interaction Hamiltonian will be invariant under all transformations belonging to the SU($N=2F+1$) group. This means that not only the pair angular momentum F_{pair} and its projection along the quantisation axis are conserved, but the spin projection of each fermion is now individually conserved, so that m_F becomes a good quantum number at any inter-atomic distance. The most evident consequence of this fact is the absence of

spin-changing collisions in a system with SU(N)-symmetric interactions.

SU(N) symmetry has consequences on the properties of practically every interacting fermionic many-body system [63]; in the last part of this Chapter, for instance, the existence of SU(N) magnetic order in optical lattices will be discussed. Moreover, the consequences of SU(N) symmetry are remarkable in many fields of physics beyond many-body physics with ultracold gases, e.g in quantum chromodynamics, where quarks confined in baryons and mesons interact by exchanging SU(3) gauge bosons known as gluons. The similarities between SU(N)-symmetric atomic gases and gauge theories have indeed already stimulated several studies [53, 74, 85, 154]. Most importantly, we will describe in detail in Section 4.3 and 6.1 how we could experimentally reveal this enlarged symmetry in the ^{173}Yb fermionic isotope.

In order to explain this scenario more precisely, let us write in the second quantisation formalism the interaction part of the Hamiltonian, associated with the pseudo-potential in Eq. (1.25). Setting $a_{F_{\text{pair}}} = a$ for $F_{\text{pair}} = 0, 2, \ldots, 2F-1$, we can write:

$$\begin{aligned}\hat{\mathcal{U}} &= \frac{4\pi\hbar^2 a}{M}\frac{1}{2}\sum_{mm'}\int d^3r\, \hat{\psi}^\dagger_m(\mathbf{r})\hat{\psi}^\dagger_{m'}(\mathbf{r})\hat{\psi}_{m'}(\mathbf{r})\hat{\psi}_m(\mathbf{r}) \\ &= \frac{4\pi\hbar^2 a}{M}\frac{1}{2}\sum_{m\neq m'}\int d^3r\, \hat{n}_m(\mathbf{r})\hat{n}_{m'}(\mathbf{r})\end{aligned} \tag{1.27}$$

where we have used the fermionic anti-commutation relations and we have introduced the density operators $\hat{n}_m(\mathbf{r}) = \hat{\psi}^\dagger_m(\mathbf{r})\hat{\psi}_m(\mathbf{r})$ of atoms with spin projection m. In Eq. (1.27) it is explicit how the spin degree of freedom does not influence the interaction other than via the Pauli exclusion principle, prohibiting contact interactions of identical fermions with $m = m'$. This Hamiltonian commutes with any spin-permutation operator acting on $(2F+1)$-dimensional spinors [55]:

$$\left[\hat{\mathcal{U}}, \hat{S}^s_q\right] = 0 \quad \forall\, s, q = -F, \ldots, F \tag{1.28}$$

$$\hat{S}^s_q = \int d^3r\, \hat{\psi}^\dagger_q(\mathbf{r})\hat{\psi}_s(\mathbf{r}) \tag{1.29}$$

If we consider now the full Hamiltonian H, including a kinetic energy term and any spin-independent optical trapping potential (i.e. with negligible vector light shift), it does also commute with all spin-permutation operators. As already noted, in particular this implies that the total population $N_m = \hat{S}^m_m = \int d^3r\, \hat{n}_s(\mathbf{r})$ of each spin state is conserved, as $\left[H, \hat{S}^s_s\right] = 0$. Another important consequence is that by initially preparing a smaller number of occupied spin states, i.e. $\hat{S}^m_m = 0$ for some m, the system will effectively behave like having a lower spin.

The spin-permutation operators defined above are the generators of the SU(N) group, and as SU(N) is a Lie group, its irreducible representations can be obtained using the Lie algebra of its generators [146]:

$$\left[\hat{S}^s_q, \hat{S}^p_n\right] = \delta_{sn}\hat{S}^p_q - \delta_{pq}\hat{S}^s_n \tag{1.30}$$

The Hamiltonian commutes with all generators of SU(N) and it is therefore SU(N) symmetric. Details about building the irreducible representations of the SU(N) group can be found e.g. in the Appendix A of Ref. [63].

In two and three dimensions, such a system is expected to behave as a SU(N) Landau Fermi liquid [53, 155, 156]. A significant deviation of the Fermi liquid properties depending on N is theoretically predicted [53, 156], and could be experimentally probed by measuring the equation of state [157], the quasi-particle excitation spectra and the effective mass [158] via Bragg scattering [73, 159] or relative spin population fluctuations [156]. In one dimension, where the analogue of the Fermi liquid is the Luttinger liquid [155] with its peculiar spin-charge separation [160], the SU(N) symmetry has already proven to yield unusual static and dynamic non-Luttinger liquid properties [73]. On the other hand, the Fermi liquid description holds only in the regime for which interactions do not cause any symmetry-breaking phase transition. Any Fermi liquid is indeed notably subject to a Fermi surface instability known as the Pomeranchuk instability, which could possibly lead to SU(N) symmetry breaking [53, 63, 156], and to the BCS instability [155, 161, 162]. Investigating such instabilities with SU(N) symmetric fermions is extremely appealing although it might not be currently within experimental reach, owing to the required temperatures and strong interactions [53, 63, 154, 163, 164]. In this respect, optical lattices can be conveniently used to enhance interaction effects and explore the role of SU(N) symmetry in the strongly correlated regime.

Interactions in a lattice: the SU(N) Fermi-Hubbard model

We have seen above how elastic binary collisions between ultracold high-spin fermion can be described by the generalised zero-range pseudo-potential (1.25), which reduces to the usual Lee-Huang-Yang pseudo-potential (1.17) if collisions are SU(N)-symmetric. In order to describe interactions between fermionic atoms in a periodic lattice potential, we rewrite the interaction Hamiltonian (1.27) in the lowest-band Wannier state basis[11], by expressing the field operators as $\hat{\psi}_m(\mathbf{r}) = \sum_j w_j(\mathbf{r})\,\hat{c}_{jm}$, where $\hat{c}^\dagger_{jm}$ creates an atom with spin m on the j-th site. The resulting interaction Hamiltonian is:

$$\begin{aligned}\hat{\mathcal{U}} &= \frac{4\pi\hbar^2 a}{M}\frac{1}{2}\sum_{mm'}\sum_{ijkl}\hat{c}^\dagger_{im}\hat{c}^\dagger_{jm'}\hat{c}_{km'}\hat{c}_{lm}\int d^3r\, w_i^*(\mathbf{r})\,w_j^*(\mathbf{r})\,w_k(\mathbf{r})\,w_l(\mathbf{r}) \\ &\simeq \frac{4\pi\hbar^2 a}{M}\frac{1}{2}\sum_{imm'}\hat{c}^\dagger_{im}\hat{c}^\dagger_{im'}\hat{c}_{im'}\hat{c}_{im}\int d^3r\,|w_i(\mathbf{r})|^4\end{aligned} \tag{1.31}$$

where the second equality holds in the tight-binding approximation, i.e. off-site interactions are neglected as Wannier functions are exponentially localised around lattice sites (see Fig. A.4). We define here the Hubbard interactions strength:

$$U = \frac{4\pi\hbar^2 a}{M}\int d^3r\,|w(\mathbf{r})|^4 \tag{1.32}$$

Using the fermionic operators anti-commutation relations, we can rewrite the Hamiltonian (1.31) in a manifestly SU(N)-symmetric form:

$$\hat{\mathcal{U}} = \frac{U}{2}\sum_i \hat{n}_i(\hat{n}_i - 1) \tag{1.33}$$

[11] There are situations in which a single-band description is not accurate. For example, very strong on-site interactions can couple the lowest Bloch band to higher bands [165]. We will discuss this case in Chapter 6, with regard to our interaction spectroscopic measurements.

with $\hat{n}_i = \sum_m \hat{c}^\dagger_{im}\hat{c}_{im}$ being the number operator of atoms on site i, irrespective of the spin.

We can now write the full Hamiltonian, including the kinetic energy and the lattice potential obtained in Section 1.1.3:

$$\hat{H}_{\mathrm{FH}} = -J \sum_{\langle i,j\rangle, m} \hat{c}^\dagger_{im}\hat{c}_{jm} + \frac{U}{2}\sum_i \hat{n}_i(\hat{n}_i - 1) \tag{1.34}$$

This Hamiltonian is known as the SU(N) Fermi-Hubbard model [53, 55, 72, 166]. The SU(N) symmetry is once again assured by the commutation with the SU(N) spin ladder operators, which we can write in terms of lattice fermionic operators:

$$\hat{S}^n_m = \sum_i \hat{S}^n_{im} = \sum_i \hat{c}^\dagger_{im}\hat{c}_{in} \tag{1.35}$$

The SU(N) Fermi-Hubbard model in Eq.(1.34) looks at a first glance identical to the standard spin-1/2 Fermi-Hubbard model (for a review, see e.g. Refs. [167, 168]): the high symmetry is hidden precisely in this simplicity, as opposed to the more complicated Hamiltonians describing high-spin fermions in optical lattices, due to the various interaction channels (see above). A remarkable consequence of the high symmetry is the modification of the finite-temperature properties of SU(N) Mott insulators in comparison to the SU(2) Mott insulator [72, 169, 170]. Moreover, the higher spin symmetry has a decisive effect on the phases of both the repulsive [163, 166, 170–173] and attractive Hubbard model [63, 74, 151, 163, 164, 174], where BCS pairing is hindered with more than two fermions required in order to form a singlet. However, the most striking consequences of SU(N) symmetry emerge in the low-energy spin physics within the Mott insulating regime. The resulting grounds states, ranging from valence-bond states to exotic spin liquids, could be experimentally probed with Mott insulators of AEL atoms, having no condensed-matter analogues; the quantum many-body phases expected to emerge from the SU(N) Heisenberg model will be summarised in Section 1.3. Experimental schemes exploiting the inherent SU(N) symmetry of AEL atoms interactions in a lattice have also been suggested to simulate U(N) and SU(N) lattice gauge theories [85], and to realise extra synthetic dimensions [175].

1.2.3 Inter-orbital interactions

The description of interactions in an ultracold ensemble was presented in Section 1.2.1. The s-wave collision channel largely dominates, as higher partial waves are strongly suppressed in the ultracold temperature regime, and a single s-wave scattering length a_{gg} is sufficient to characterise collisions between $|g\rangle$ atoms in any nuclear spin state, owing to the their SU(N) symmetric nature. By extending the system to a second orbital, represented by the supplementary electronic state $|e\rangle$, additional collision channels become available. Thanks to the decoupling of the nuclear spin in the $|e\rangle$ state, also inter-orbital and $|e\rangle$ state interactions are expected to exhibit SU(N) symmetry: only four s-wave scattering lengths are required to fully describe collisions between all spin and orbital state

combinations[12]. The scattering lengths a_{gg} and a_{ee} characterise the interactions between atoms in the same electronic orbital, respectively $|g\rangle$ and $|e\rangle$. Furthermore, atoms in different electronic states can collide through two scattering channels, associated with two possible electronic pair wave function: the scattering lengths a_{eg}^{+} and a_{eg}^{-} respectively describe collisions via the symmetric $(|eg\rangle + |ge\rangle)/\sqrt{2}$ and antisymmetric $(|eg\rangle - |ge\rangle)/\sqrt{2}$ channels. These are in general unequal due to the different molecular electronic states which connect to different states of the separated atomic pair.

Two-orbital interaction Hamiltonian

Having defined the necessary scattering lengths for all interaction channels in a two orbital ensemble, we can generalise the pseudo-potential (1.17) to:

$$V(\mathbf{r}) = \frac{4\pi\hbar^2}{M}\,\delta(\mathbf{r})\sum_X a_X \mathcal{P}_X \tag{1.36}$$

where $X = gg, eg^+, eg^-, ee$, and $\mathcal{P}_{\alpha\alpha} = |\alpha\alpha\rangle\langle\alpha\alpha|$ with $\alpha = g, e$, while $\mathcal{P}_{eg}^{\pm} = \frac{1}{2}(|eg\rangle \pm |ge\rangle)(\langle eg| \pm \langle ge|)$. In order to write the corresponding interaction Hamiltonian through the usual field operators, we need a little manipulation. The terms proportional to a_{gg} and a_{ee} in the sum represent the interaction between atoms in the same electronic state with different spins, and lead therefore to two standard intra-orbital interaction terms like Eq. (1.27) in the total Hamiltonian. To treat the two inter-orbital interaction terms, we use the pseudo-spin-1/2 algebra of the two-level system formed by the states $|g\rangle$ and $|e\rangle$ to rewrite the projectors $\mathcal{P}_{eg}^{\pm}$. We introduce the pseudo-spin operators of the two atoms $\hat{\mathbf{T}}_1$ and $\hat{\mathbf{T}}_2$, such that $\hat{T}^z|g\rangle = -\frac{1}{2}|g\rangle$ and $\hat{T}^z|e\rangle = \frac{1}{2}|e\rangle$. The associated ladder operators switch the electronic states, i.e. $\hat{T}^+|g\rangle = |e\rangle$ and $\hat{T}^-|e\rangle = |g\rangle$. The projection operators on the pseudo-spin triplet and singlet $\mathcal{P}_{eg}^{\pm}$ can be expressed as:

$$\mathcal{P}_{eg}^{+} = \frac{3}{4} + \hat{\mathbf{T}}_1 \cdot \hat{\mathbf{T}}_2 \tag{1.37}$$

$$\mathcal{P}_{eg}^{-} = \frac{1}{4} - \hat{\mathbf{T}}_1 \cdot \hat{\mathbf{T}}_2 \tag{1.38}$$

We can now use the relation:

$$\hat{\mathbf{T}}_1 \cdot \hat{\mathbf{T}}_2 = \frac{1}{2}(\hat{T}_1^+\hat{T}_2^- + \hat{T}_1^-\hat{T}_2^+) + \hat{T}_1^z\hat{T}_2^z \tag{1.39}$$

Noting that for both inter-orbital states we have

$$\hat{T}_1^z\,\hat{T}_2^z\,\frac{|eg\rangle \pm |ge\rangle}{\sqrt{2}} = -\frac{1}{4}\,\frac{|eg\rangle \pm |ge\rangle}{\sqrt{2}}, \tag{1.40}$$

we can write the two-atom inter-orbital interaction Hamiltonian:

$$\begin{aligned}\hat{V}_{eg}(\mathbf{r}_1 - \mathbf{r}_2) &= \frac{4\pi\hbar^2}{M}\,\delta(\mathbf{r}_1 - \mathbf{r}_2)(a_{eg}^{+}\,\mathcal{P}_{eg}^{+} + a_{eg}^{-}\,\mathcal{P}_{eg}^{-}) \\ &= \frac{4\pi\hbar^2}{M}\,\delta(\mathbf{r}_1 - \mathbf{r}_2)\left(\frac{a_{eg}^{+} + a_{eg}^{-}}{2} + \frac{a_{eg}^{+} - a_{eg}^{-}}{2}\,(\hat{T}_1^+\hat{T}_2^- + \hat{T}_1^-\hat{T}_2^+)\right)\end{aligned} \tag{1.41}$$

[12]The tiny admixture of the $^3P_0$ with the $^3P_1$ state, generated by the hyperfine interaction in the $^3P_0$ metastable state [96], slightly breaks the angular momentum decoupling, leading however to a spin dependence of the scattering lengths only below a percent level [55] (see Section 5.2.2).

In second quantisation, the pseudo-spin operator is $\hat{\mathbf{T}} = \sum_{m\alpha\beta} \hat{\psi}^\dagger_{\alpha m}(\mathbf{r})\, \boldsymbol{\sigma}_{\alpha\beta}\, \hat{\psi}_{\beta m}(\mathbf{r})$, where $\boldsymbol{\sigma}$ is the vector of Pauli matrices and $\alpha, \beta = g, e$, so that $\hat{\psi}^\dagger_{\alpha m}(\mathbf{r})$ creates an atom in state $|\alpha\rangle$ with spin m at position $\mathbf{r}$. The associated ladder operators are $\hat{T}^+ = \sum_m \hat{\psi}^\dagger_{em}(\mathbf{r})\hat{\psi}_{gm}(\mathbf{r}) = (\hat{T}^-)^\dagger$. Through these substitutions and the fermionic anti-commutation relations, we can obtain two inter-orbital interaction Hamiltonian terms, respectively denoted as *direct* and *exchange* interaction [55]:

$$\hat{\mathcal{V}}_{\mathrm{d}} = \frac{4\pi\hbar^2}{M}\frac{a^+_{eg} + a^-_{eg}}{2} \sum_{mm'} \int d^3r\, \hat{n}_{gm}(\mathbf{r})\, \hat{n}_{em'}(\mathbf{r}) \tag{1.42a}$$

$$\hat{\mathcal{V}}_{\mathrm{ex}} = \frac{4\pi\hbar^2}{M}\frac{a^+_{eg} - a^-_{eg}}{2} \sum_{mm'} \int d^3r\, \hat{\psi}^\dagger_{gm}(\mathbf{r})\, \hat{\psi}^\dagger_{em'}(\mathbf{r})\, \hat{\psi}_{gm'}(\mathbf{r})\, \hat{\psi}_{em}(\mathbf{r}) \tag{1.42b}$$

where constant terms proportional to the total number of atoms $N = \sum_m \int d^3r\, [\hat{n}_{gm}(\mathbf{r}) + \hat{n}_{em}(\mathbf{r})]$ have been dropped. The naming of the two interaction terms is suggestive of the close analogy between the problem of two SU(N)-symmetric interacting atoms with a pseudo-spin degree of freedom, represented here by the electronic state, and the problem of interacting particles with spin-1/2, such as alkali atoms with one valence electron.

Let us now analyse how orbital interactions relate to the nuclear spin degree of freedom. In a binary collision the two-body wave function of fermionic atoms must be anti-symmetric. Moreover, for zero-range interactions to occur, the spatial part of the two-body wave function has to be symmetric, so we restrict ourselves to this case and omit the explicit expression of the spatial state. Within the SU(N) symmetry the nuclear spin can still influence collisions through Pauli exclusion: two atoms in the same $|g\rangle$ or $|e\rangle$ state can only collide if they are in a different nuclear spin state, and in the SU(N)-symmetric case, the individual spins are preserved throughout the collision. Taking two spin states $m, m' = \uparrow, \downarrow$, the pair-spin wave function must be a singlet: the interacting states are $|gg\rangle \otimes |s\rangle$ and $|ee\rangle \otimes |s\rangle$, with $|s\rangle = (|\uparrow\downarrow\rangle - |\downarrow\uparrow\rangle)/\sqrt{2}$.
On the other hand, considering two atoms in different electronic and spin states, two possible combinations are allowed to interact, respectively via the symmetric and anti-symmetric channel:

$$|eg^+\rangle = (|eg\rangle + |ge\rangle)/\sqrt{2} \otimes |s\rangle \tag{1.43a}$$

$$|eg^-\rangle = (|eg\rangle - |ge\rangle)/\sqrt{2} \otimes |t\rangle \tag{1.43b}$$

with $|t\rangle = (|\uparrow\downarrow\rangle + |\downarrow\uparrow\rangle)/\sqrt{2}$. Atoms in different electronic states but with identical spin can also collide, but only via the anti-symmetric channel a^-_{eg}, associated with the two-body states $(|eg\rangle - |ge\rangle)/\sqrt{2} \otimes |\uparrow\uparrow\rangle$ and $(|eg\rangle - |ge\rangle)/\sqrt{2} \otimes |\downarrow\downarrow\rangle$. Therefore, inter-orbital scattering happens via the symmetric channel a^+_{eg} in the spin singlet state and via the anti-symmetric channel a^-_{eg} in the spin triplet states. The most important fact here is that the exchange interaction in Eq. (1.42b) results in an energy difference between the spin singlet and triplet, being effectively a spin-spin interaction[13]. This is the essential principle

[13] Whereas the direct interaction is only density-dependent, and therefore does not break the singlet-triplet degeneracy.

at the basis of simulating orbital magnetism with AEL atoms, as we will see explicitly in the following Section.

Two-orbital SU(N) Fermi-Hubbard model

As discussed in Section 1.1.3, it is possible to engineer lattice potentials with the same periodicity but different depths for the $|g\rangle$ and $|e\rangle$ states, due to the distinct dynamic polarisabilities of the two states, as depicted in Fig. 1.3. We will consider now therefore AEL atoms in a state-dependent but spin-independent[14] optical lattice potential.

Using the two states Wannier basis, we can rewrite the field operators as $\hat{\psi}_{\alpha m}(\mathbf{r}) = \sum_j w_{j\alpha}(\mathbf{r})\hat{c}_{j\alpha m}$, with $\hat{c}^\dagger_{j\alpha m}$ creating an atom in state $|\alpha\rangle$ with spin m on site j. By applying the tight-binding approximation and dropping constant terms, we obtain the so-called two-orbital SU(N) Fermi-Hubbard model [59]:

$$\begin{aligned}\hat{H}_{\mathrm{2FH}} = &-J_g \sum_{\langle i,j\rangle,m} \hat{c}^\dagger_{igm}\hat{c}_{jgm} - J_e \sum_{\langle i,j\rangle,m} \hat{c}^\dagger_{iem}\hat{c}_{jem} + \frac{1}{2}\sum_{i\alpha} U_{\alpha\alpha}\hat{n}_{i\alpha}(\hat{n}_{i\alpha}-1) \\ &+ V\sum_i \hat{n}_{ig}\hat{n}_{ie} + V_{\mathrm{ex}} \sum_{imm'} \hat{c}^\dagger_{igm}\hat{c}^\dagger_{iem'}\hat{c}_{igm'}\hat{c}_{iem}\end{aligned} \tag{1.44}$$

where $\hat{n}_{i\alpha m} = \hat{c}^\dagger_{i\alpha m}\hat{c}_{i\alpha m}$ and $\hat{n}_{i\alpha} = \sum_m \hat{n}_{i\alpha m}$. The different Hubbard interaction strengths are defined as:

$$U_{\alpha\alpha} = \frac{4\pi\hbar^2}{M} a_{\alpha\alpha} \int d^3r\, |w_\alpha(\mathbf{r})|^4 \tag{1.45}$$

and

$$\begin{aligned} U^{\pm}_{eg} &= \frac{4\pi\hbar^2}{M} a^{\pm}_{eg} \int d^3r\, |w_e(\mathbf{r})|^2 |w_g(\mathbf{r})|^2 \\ V &= \frac{1}{2}(U^+_{eg} + U^-_{eg}) \\ V_{\mathrm{ex}} &= \frac{1}{2}(U^+_{eg} - U^-_{eg}) \end{aligned} \tag{1.46}$$

The exchange term proportional to V_{ex} is effectively an on-site inter-orbital spin interaction: the difference in the symmetric and antisymmetric inter-orbital interactions U^+_{eg} and U^-_{eg}, owing to fermionic anti-symmetrisation, lifts the interaction energy degeneracy between singlet and triplet spin states. Considering only two occupied spin states, we can readily find how an energy offset is induced between the on-site spin singlet $|eg^+\rangle$ and triplet $|eg^-\rangle$ states (see Fig.1.5):

$$\begin{aligned}\hat{\mathcal{V}}_{\mathrm{ex}}|eg^\pm\rangle &= V_{\mathrm{ex}} \sum_{mm'} \hat{c}^\dagger_{gm}\hat{c}^\dagger_{em'}\hat{c}_{gm'}\hat{c}_{em}|eg^\pm\rangle \\ &= -V_{\mathrm{ex}}\left(\hat{n}_{g\uparrow}\hat{n}_{e\uparrow} + \hat{n}_{g\downarrow}\hat{n}_{e\downarrow} + \hat{S}^+_g\hat{S}^-_e + \hat{S}^-_g\hat{S}^+_e\right)|eg^\pm\rangle \\ &= \pm V_{\mathrm{ex}}|eg^\pm\rangle\end{aligned} \tag{1.47}$$

[14] Vector and tensor light shifts can be made negligible by using linearly polarised light [96, 122].

where $\hat{S}^{\pm}$ are the spin ladder operators. We note also that for $V_{\mathrm{ex}} > 0$, the triplet has the lowest energy indicating a *ferromagnetic* interaction, whereas for $V_{\mathrm{ex}} < 0$, the singlet has the lowest energy indicating an *anti-ferromagnetic* interaction. Spin singlet and triplet eigenstate superpositions, such as:

$$|eg\uparrow\downarrow\rangle = |e\uparrow\rangle|g\downarrow\rangle - |g\downarrow\rangle|e\uparrow\rangle = \frac{1}{\sqrt{2}}(|eg^{-}\rangle + |eg^{+}\rangle) \tag{1.48a}$$

$$|eg\downarrow\uparrow\rangle = |e\downarrow\rangle|g\uparrow\rangle - |g\uparrow\rangle|e\downarrow\rangle = \frac{1}{\sqrt{2}}(|eg^{-}\rangle - |eg^{+}\rangle) \tag{1.48b}$$

are driven by the exchange interaction to oscillate between each other at a frequency $\omega_{\mathrm{ex}}/2\pi = |V_{\mathrm{ex}}|/h$ [176], exhibiting a so-called *spin-exchange* dynamics.

Furthermore, the two-orbital Hamiltonian (1.44) remains SU(N) symmetric, as it commutes with the generalised spin-permutation operators defined by summing the operators (1.35) over the electronic states:

$$\hat{S}^{n}_{m} = \sum_{i} \hat{S}^{n}_{im} = \sum_{i\alpha} \hat{S}^{n}_{i\alpha m} = \sum_{i\alpha} \hat{c}^{\dagger}_{i\alpha m} \hat{c}_{i\alpha n} \tag{1.49}$$

which satisfy the SU(N) algebra in Eq. (1.30) and are therefore generators of SU(N). Particular parameter regimes in the general Hamiltonian (1.44) produce simpler effective Hamiltonians. Some of these reproduce well-known condensed-matter models, characterised by a partial or complete localisation of one of the two orbitals, e.g. the SU(2) Kondo lattice model [55, 60, 61, 76, 127, 177, 178] or the Kugel-Khomskii model [55, 128]. AEL atoms in optical lattices offer therefore new possibilities for the quantum simulation of models which are the object of current research in condensed-matter, being still far from well understood. Furthermore, the SU(N) symmetric extensions of such models could be investigated, which have no realisation in nature and could represent a valuable benchmark for large-N theoretical treatments [171, 179, 180].

1.3 Quantum simulation with AEL atoms

The quantum simulation of strongly-correlated electron materials with ultracold quantum gases has already proven to be a successful and versatile approach for understanding quantum many-body phenomena, complementing the direct probing of real condensed-matter systems [12]. A large number of experiments with ultracold gases make use of alkali atomic species, which are conveniently suited for laser cooling and magnetic trapping. More recently, the development of all-optical cooling techniques has permitted to cool alkaline-earth-like atomic gases as well to the degenerate regime [52, 65–71]. Such experimental achievements have motivated several theoretical proposals, which exploit the unique possibilities arising from the properties of AEL atoms and open the door to the observation of yet unexplored quantum phenomena with ultracold gases.

Two essential aspects particularly stimulate the research in the field of quantum simulation with AEL: (i) SU($N > 2$) symmetries can be implemented, owing to the highly decoupled and large nuclear spin of fermionic AEL isotopes and (ii) an additional internal degree of freedom is provided through the existence of the metastable state, which

may be used to emulate the orbital degree of freedom of electrons in solids and is moreover expected to obey the same symmetry as the ground state. In contrast, alkali atomic species were theoretically found to exhibit at most an exact SO(5) symmetry [150], that is a lower symmetry group than SU(3), and the experimental realisation of symmetries larger than SU(2) in alkali gases has so far been inaccessible. Furthermore, the possibilities offered by employing different ground hyperfine states of alkali atoms or different Bloch bands to mimic electrons in distinct orbitals of solid materials are quite restricted. Many theoretical proposals exploiting multi-band lattice, superlattice or spin-dependent lattice potentials have been put forward with the purpose of realising spin-exchange interactions with alkali atoms [83, 115, 181, 182]. Onsite spin-exchange interactions between two vibrational states on a lattice site have been successfully implemented and used for creating entangled bosonic atom pairs [116]. However, realisations of on-site spin-exchange based on excited vibrational states or on effective low-energy Hamiltonians are generally not compatible with a strong tunnelling coupling. Conversely, a large tuneability of the tunnelling is required to explore models relying primarily on the competition between spin-exchange and tunnelling. Such models include the Kondo lattice model [76, 127, 177, 178] and the Kugel-Khomskii model [79, 128, 183, 184], which were formulated to explain condensed-matter phenomena resulting from the magnetic interactions of electrons in different orbitals. Using the different stable electronic states of AEL atoms represent a viable alternative for the implementation of such models [59–61]. As we have illustrated in Section 1.2.3, thanks to the fermionic exchange symmetry arising from quantum statistics, spin-exchange interactions are inherently implemented through the dependence of the scattering properties on the electronic wave function. Another unique tool, yielding a novel degree of controllability for quantum simulation, is found in far off-resonant, state-dependent optical potentials, which are exclusively available in AEL species. The selective trapping of one of the two electronic states allows for the tuning of the relative effective masses of the two states in a lattice potential, emulating conduction electrons and localised electrons or impurities in real materials.

In this Section we will give an overview of the current prospects in quantum simulation with ultracold AEL gases. In particular we will introduce the Kondo lattice model and the SU(N) Heisenberg model [62, 166, 171], and focus the discussion on the theoretical insights possibly provided by their realisation in atomic systems. We will elaborate on the experimental implementation of the Kondo lattice model with AEL atoms trapped in a state-dependent optical lattice, discussing its requirements and its feasibility in different regimes. We will in particular describe which observables could be probed to reveal the distinctive hallmarks of Kondo lattice many-body physics, and discuss the preparation of the Hamiltonian through occupation number-selective clock excitation. We will conclude by addressing SU(N) magnetism in optical lattices and related experimental prospects with AEL atom Mott insulators.

1.3.1 Orbital magnetism in condensed matter

Seminal models such as the Fermi-Hubbard model [118, 168] are able to incorporate electron-electron correlations within a minimal description, and can be realised in a defect-free and fully controllable fashion using ultracold fermionic atoms in optical lattices. However, many interesting quantum phenomena arising in complex solid materials, e.g. some instances of magnetic ordering or unconventional superconductivity, stem from the interactions between electrons occupying distinct orbitals. Spin-spin interactions between electrons occur as a consequence of the quantum exchange interaction associated with Coulombian repulsion, and are usually termed spin-exchange interactions. Inter-orbital spin exchange was first introduced by Kondo in 1964, in order to explain what became later known as the Kondo effect, i.e. a logarithmic increase in the electrical resistivity of a material as the temperature is lowered [185]. Since then, the interplay of the electrons spin and orbital degrees of freedom was found to be central for explaining the properties of various strongly-correlated electron materials, such as heavy-Fermi materials, a class of inter-metallic compounds with 4f or 5f electrons (typically from Ce or U atoms) with extraordinarily massive quasiparticles [75, 76, 177], or colossal-magnetoresistive transition-metal oxides [78, 79, 184].

An intense research in heavy-fermion (HF) physics has been especially catalysed by the discovery of unconventional (i.e. non-BCS) superconductivity in HF compounds [186], with the list of HF superconductors growing considerably in recent years [82]. In particular, superconducting rare-earth compounds have been found to possess intriguing properties, e.g. $CeCoIn_5$ is a candidate realisation of the FFLO phase [187–189]. HF materials have also emerged as prototype systems for the investigation of quantum critical phenomena, due to the presence of a quantum critical point which separates a magnetically-ordered phase from a Fermi liquid phase at zero temperature [77, 80, 190]. An enormous theoretical effort has been devoted to the understanding of the physics in proximity of this quantum critical point, where a breakdown of Fermi liquid behaviour has been observed [191] and an exotic non-Fermi liquid (NFL) behaviour ensues from long-range, long-lived quantum fluctuations of the magnetic order parameter [76, 80, 192]. Moreover, the contiguity between anti-ferromagnetic ordering and superconductivity manifests itself in HF in its most essential form [77, 81, 82, 193]. The microscopic pairing mechanism which leads to HF superconductivity (the 'glue') is not yet understood, and recent measurements suggest that it could be of the same type of the one found in cuprates [194, 195], exhibiting a nodal d-wave pairing gap symmetry and a gap in the non-superconductive state very reminiscent of the mysterious pseudogap state of cuprates. New insights in HF physics, especially regarding the interplay between quantum criticality and superconducting order [77, 81, 193], would therefore provide an inestimable contribution to the understanding of other types of unconventional superconductors.

The Kondo lattice model

The Kondo lattice model (KLM) [76, 177] has established itself as the prominent model for explaining the physics of HF compounds and other magnetic materials, e.g. nickel and manganese perovskites. It essentially depicts a lattice of localised magnetic moments

interacting with a band of itinerant conduction electrons via spin-exchange (see Eq. 1.50). The KLM was initially proposed by Doniach [127] as a lattice version of the single-impurity Kondo model, and was first shown by Schrieffer and Wolff to emerge as an effective Hamiltonian in a certain limit ($U \gg V$) of the periodic Anderson model [196, 197].

It is widely accepted that the low-energy physics of HF and other magnetic compounds is based upon the competition between two types of interactions, the Kondo-exchange interaction and the Ruderman-Kittel-Kasuya-Yosida (RKKY) interaction [198–200], which are both incorporated in the KLM. Such interactions respectively promote a paramagnetic and a magnetically ordered ground state (see Fig. 1.4), which have been extensively studied in HF materials, along with the tuneable quantum phase transition connecting them [77, 193]. A detailed comprehension of those phases represent a major success of the anti-ferromagnetic KLM, and several studies clarified how the competition between the Kondo screening and the RKKY interaction accounts indeed for the emergence of very exotic fermionic liquids near the quantum critical point [77, 80, 193, 201]. However, the phase diagrams in dimensions $D > 1$, the associated phase transitions and especially the role of Kondo exchange regarding the properties of HF superconductors are still far from understood. Many open questions remain concerning HF physics in the regime where RKKY and Kondo exchange interactions have comparable strength in the vicinity of the quantum critical point [77, 81, 202, 203].

The ferromagnetic KLM has attracted considerable interest as well, owing to the discovery of colossal magnetoresistance (CMR) in manganese oxides with perovskite structure [79, 204, 205], which is the subject of current experimental research and might lead to novel technological applications in the field of spintronics. Interest in transition-metal oxides with anisotropic d-orbital electrons also prompted renewed attention towards the Kugel-Khomskii model [78, 128, 183], which is used to describe magnetic Mott insulators of such compounds, exhibiting CMR and high-temperature superconductivity. The Kugel-Khomskii model is a particular multi-band Hubbard model describing electrons in degenerate orbitals, and can be mapped in the strong-coupling limit ($U \gg J$) to a spin-orbital Hamiltonian [55, 79, 128], formally equivalent to the superexchange-based Heisenberg model [118, 206].

The fundamental physical process which gives rise to the Kondo effect and to RKKY interactions is the scattering between conduction electrons and localised magnetic impurities, which can result in complete spin-screening of the impurities. In the KLM this process is expressed as an on-site spin interaction [76, 177]. The KLM Hamiltonian describes a tight-binding band of conduction electrons $c^{\dagger}_{gim}$ interacting through direct spin-exchange with a lattice of magnetic moments represented by localised spins $\mathbf{S}_j$:

$$\hat{H}_{\mathrm{KLM}} = -J_g \sum_{\langle i,j\rangle\, m} \hat{c}^{\dagger}_{gim}\hat{c}_{gjm} - 2V_{\mathrm{ex}} \sum_j \hat{\mathbf{S}}_j \cdot \hat{\mathbf{s}}_j \tag{1.50}$$

where $\mathbf{s}_j$ is the spin density of the conduction electrons on site j: $\hat{\mathbf{s}}_j = \frac{1}{2}\sum_{mm'} \hat{c}^{\dagger}_{gjm}\, \boldsymbol{\sigma}_{mm'}\, \hat{c}_{gjm'}$. Reminding that $\hat{\mathbf{S}}_j \cdot \hat{\mathbf{s}}_j = \frac{1}{2}(\hat{S}^{+}_j \hat{s}^{-}_j + \hat{S}^{-}_j \hat{s}^{+}_j) + \hat{S}^{z}_j \hat{s}^{z}_j$, and by expressing also the localised moments

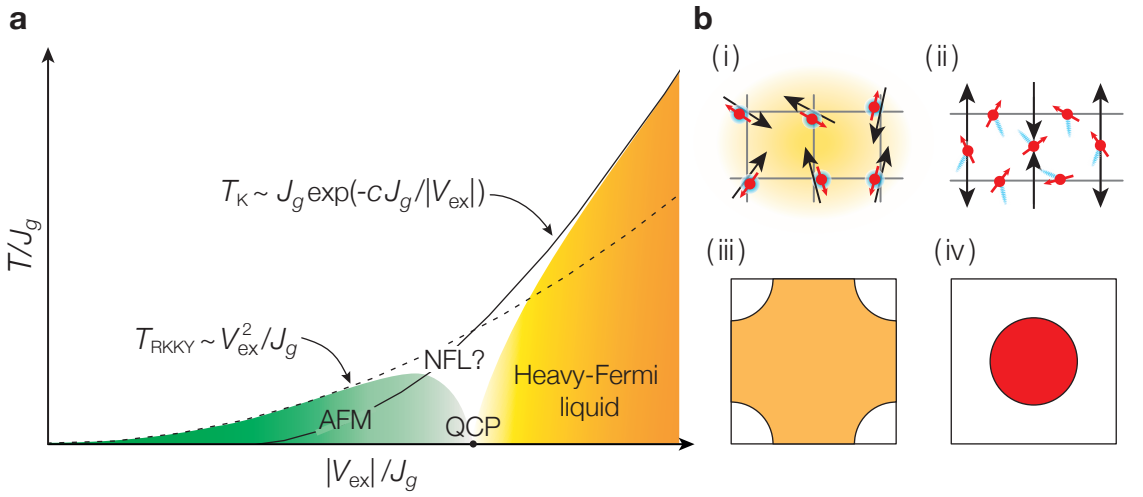

Figure 1.4 – (a) Doniach phase diagram of the anti-ferromagnetic Kondo lattice model. The two important temperature scales T_{RKKY} and T_K are respectively plotted as a dashed and solid line as a function of the coupling $|V_{\mathrm{ex}}|/J_g$. A Fermi liquid with large effective mass quasiparticles (HFL) is obtained in the strong coupling regime, where $T_K > T_{\mathrm{RKKY}}$. Conversely, a phase with anti-ferromagnetic order of the localised spins is obtained for $T_K < T_{\mathrm{RKKY}}$. A quantum critical point (QCP) separates these two phases at zero temperature, and non-Fermi liquid (NFL) behaviour is predicted to arise in the transition region. However, the physics close to the QCP is still the object of theoretical debate. (b) Illustrative representation of the Kondo lattice HFL and magnetically ordered states. In the HFL (i) conduction electrons bind to the localised moments, forming isolated Kondo singlets. The HFL is distinguished by a large Fermi surface (ii) resulting from the hybridisation between conduction electrons with the localised spins. In the weak exchange regime, the localised spins magnetically order (iii) and the small Fermi surface (iv) of conduction electrons is restored.

$\hat{\mathbf{S}}_j$ in terms of fermionic operators $\hat{c}^\dagger_{ejm}$, we can rewrite Eq. (1.50) as:

$$\hat{H}_{\mathrm{KLM}} = -J_g \sum_{\langle i,j\rangle\, m} \hat{c}^\dagger_{gim}\hat{c}_{gjm} + V_{\mathrm{ex}} \sum_{jmm'} \hat{c}^\dagger_{gjm}\hat{c}^\dagger_{ejm'}\hat{c}_{gjm'}\hat{c}_{ejm} \tag{1.51}$$

where all constant terms were dropped. Even more than for the Hubbard model, the apparent simplicity of the KLM is totally misleading[15] and gives rise to a rich phase diagram, being amongst the most studied ones in condensed-matter. The absence of small parameters in the model makes perturbative approaches rather ineffective, and an extension from the physical SU(2) symmetry of spin-1/2 electrons to a SU(N) symmetric description has been used to introduce a perturbative parameter, namely $1/N$ [76, 179]. Strong correlations between separated conduction electrons are generated by the spin-spin exchange interaction: when an electron undergoes spin-exchange with one of the localised spins, its spin becomes correlated with the spins of electrons which have previously interacted with the same localised moment, as the state of this is determined by all the experienced exchange processes. Therefore, both conduction electrons become spin-correlated with one another (and so do localised moments), although they never interact directly.

[15] Quoting P.W. Anderson [207]: "I am indebted to a London Times article about Idi Amin for learning that in Swahili "Kondoism" means "robbery with violence". This is not a bad description of this mathematical wilderness of models; H. Suhl has been heard to say that no Hamiltonian so incredibly simple has ever previously done such violence to the literature and to national science budgets."

A useful understanding of the KLM physics is nevertheless provided by discussing the two limits of weak and strong coupling. In the strong-coupling limit, $|V_{\rm ex}| \gg J_g$, the conduction electrons become pinned to the localised spins via the so-called static Kondo screening, i.e. by forming spin singlets or triplets to lower their energy, depending on the sign of the spin-exchange coupling. In dimensions $D > 1$ and for anti-ferromagnetic coupling, this results below the Kondo temperature T_K in the formation of a heavy Fermi liquid[16] (HFL), namely a Fermi liquid possessing highly massive quasiparticles, arising from the hybridisation of conduction electrons and localised moments. Such heavy quasiparticles must be incorporated in the Fermi volume, as being part of the conduction-electron excitation spectrum, and generate a large Fermi volume, with a "large Fermi surface" at the quasiparticles location in momentum space [76, 210, 211]. In the anti-ferromagnetic KLM, the energy scale T_K associated with the Kondo singlet formation is given by, in analogy to the single-impurity Kondo temperature [76]:

$$k_B\, T_K \sim J_g \exp\left(-C\,\frac{J_g}{|V_{\rm ex}|}\right) \tag{1.52}$$

where C is a constant of order 1 and T_K is usually termed Kondo temperature.

By increasing the tunnelling J_g of the conduction electrons, an effective magnetic interaction between the localised moments is mediated by second-order exchange processes, named Ruderman-Kittel-Kasuya-Yosida (RKKY) interaction [198–200]. According to its second-order scattering character, the RKKY interaction typical energy scale is given by:

$$k_B\, T_{\rm RKKY} \sim \frac{V_{\rm ex}^2}{J_g} \tag{1.53}$$

RKKY interactions are responsible for the instability of the HFL state at intermediate couplings $V_{\rm ex} \sim J_g$, when $T_{\rm RKKY} \approx T_K$, and favour magnetic ordering in the weak coupling regime $V_{\rm ex} < J_g$ of the localised spins (see the Doniach phase-diagram in Fig. 1.4). The HFL and the RKKY-induced magnetic ordered phases feature radically different conduction properties, which are brought to an extreme for half-filling of conduction electrons, where the exchange-dominated state develops into the so-called Kondo insulator [178, 212, 213].

1.3.2 The Kondo lattice with alkaline-earth-like atoms

The KLM in Eq. (1.51) is exactly reproduced by the two-orbital Fermi-Hubbard Hamiltonian (1.44) in the limit of $U_{ee} \gg J_e$ and $U_{gg} \ll J_g$, and with only two spin states occupied, as was first pointed out in Ref. [55]. The large interaction U_{ee} guarantees a strong localisation of the $|e\rangle$ atoms in a half-filled insulating state as long $T \ll U_{ee}$, whereas a large tunnel coupling J_g ensures the mobility of the $|g\rangle$ atoms. In order to fulfil these demands, independent lattice potentials for the two electronic states have to be engineered (see Fig. 1.3(a)), so as to independently tune the tunnel coupling of each state. We will clarify

[16] The onset of local Kondo screening with decreasing temperature is found already at the single-impurity Kondo temperature $T_K^{(1)}$ [208], but the HFL state only ensues below the energy scale associated with the Fermi-liquid coherence [209].

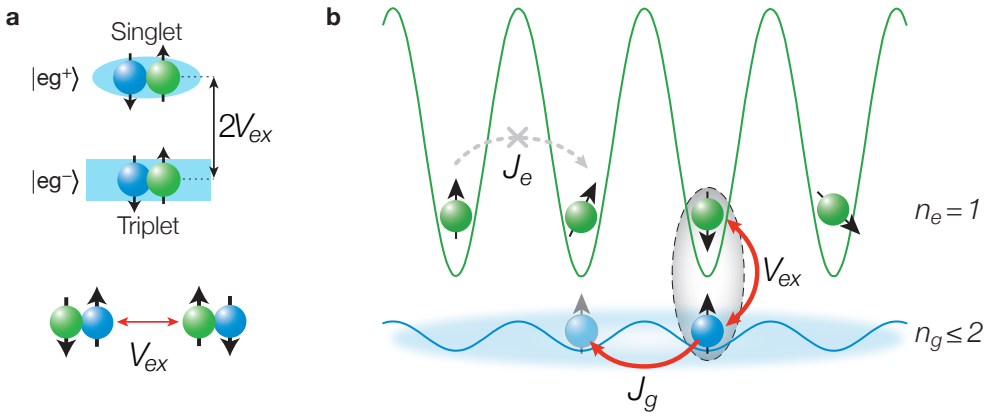

Figure 1.5 – (a) The exchange coupling ensues as a consequence of the different inter-orbital interaction energies in the spin singlet and triplet channels. Such coupling is responsible for the elementary spin-exchange process of polarised two-particle states, which are superpositions of the spin singlet and triplet: an isolated e-g atomic pair undergoes spin-exchange oscillations if prepared in a polarised spin state. (b) Illustration of the Kondo lattice model (KLM) implementation with AEL atoms in a state-dependent optical lattice. The on-site exchange interaction V_{ex} between mobile particles and localised spins competes with the tunnelling J_g of mobile particles. The SU(N) symmetry of interactions can be used to explore the physics of KLM beyond spin-1/2, but is also vital for interactions not to populate spin states out of the desired subset, typically with $N = 2$. The suppression of $|e\rangle$ state atoms tunnelling is essential to prevent strong on-site lossy collisions between distinguishable $|e\rangle$ atoms. Ideally, the interaction U_{gg} between $|g\rangle$ state atoms is much smaller than both J_g and V_{ex}.

how such a state-dependent lattice can be realised for ytterbium in Section 5.1.1. Under these conditions, we can neglect terms in Eq. (1.44) proportional to U_{gg} and J_e and we can moreover discard terms proportional to U_{ee} and to the direct interaction V, which are zero and constant, respectively, for a homogeneous half-filling of $|e\rangle$ atoms.

In practice, the filling of the $|e\rangle$ orbital can be fixed to to $n_{je} = 1$ for all j by performing an occupation number-selective clock excitation on a band insulator inside a sufficiently deep state-dependent optical lattice (see Fig. 1.6 below), without the demand of $T \ll U_{ee}$. The $|e\rangle$ atoms must be selected to play the role of the localised magnetic moments in the KLM, since they would otherwise suffer strong lossy collisions (see Section 6.3). A sketch of the KLM Hamiltonian realisation with AEL atoms in a lattice is displayed in Fig. 1.5. An optical lattice emulation of the KLM is therefore a concrete prospect, provided only that a sufficiently large inherent exchange coupling V_{ex} is found in the proposed AEL isotopes, and could help addressing the notable theoretical challenges concerning the quantum phase transition in the KLM. We also note that, by populating more than two spin states at the same time, the SU($N > 2$)-symmetric generalisation of the SU(2) KLM could be realised [179, 180], i.e.:

$$\hat{H}'_{\mathrm{KLM}} = -J_g \sum_{\langle i,j\rangle\, m} \hat{c}^{\dagger}_{gim}\hat{c}_{gjm} - V_{\mathrm{ex}} \sum_{jmn} \hat{S}^{n}_{jm}\hat{s}^{m}_{jn} \tag{1.54}$$

where the SU(N) spin-permutation operators were defined in Section 1.2, offering e.g. the intriguing possibility of exploring HFL and Kondo insulator physics at varying $N \geq 2$. As we

will see in Chapter 6, a large ferromagnetic SU(N)-symmetric spin-exchange strength was measured in ^{173}Yb [124, 176] making this isotope very attractive for the implementation of exchange-based two-orbital models like the KLM. On the other hand, the exchange strength in fermionic ^{171}Yb still requires to be determined and might be revealed of antiferromagnetic type. A weaker ferromagnetic exchange coupling was moreover found in ^{87}Sr [214].

Phases and observables of the Kondo lattice model

Let us now discuss how the different predicted phases of the KLM could be prepared, accessed and observed. First of all, in order to prepare the required uniform half-filling of $|e\rangle$ atoms, a number-selective state preparation is necessary. Atoms on doubly occupied lattice sites can be separately addressed on the clock transition owing to their interaction shift, which can be increased (if required) by applying a strong magnetic field up to a value equal to the direct interaction strength V (see Section 5.2.1 and Fig 5.14). The excitation light is shone along the direction of a deep magic lattice and the applied Rabi frequency should be large compared to the tunnelling coupling in any direction, i.e. $\Omega \gg J_g$, so that atom pairs stay localised during the excitation. For a two-spin Fermi gas of $|g\rangle$ atoms loaded into a combined lattice-harmonic potential with a chemical potential above the upper edge of the first band (see Fig B.3), a central band-insulating core is formed with $n_g = 2$ [31]. After one $|e\rangle$ atom has been prepared on all doubly occupied sites, a central region with $n_e = 1$ is therefore created. For very cold temperatures, this core can extend nearly to the edge of the cloud [31]. However, it is in general beneficial

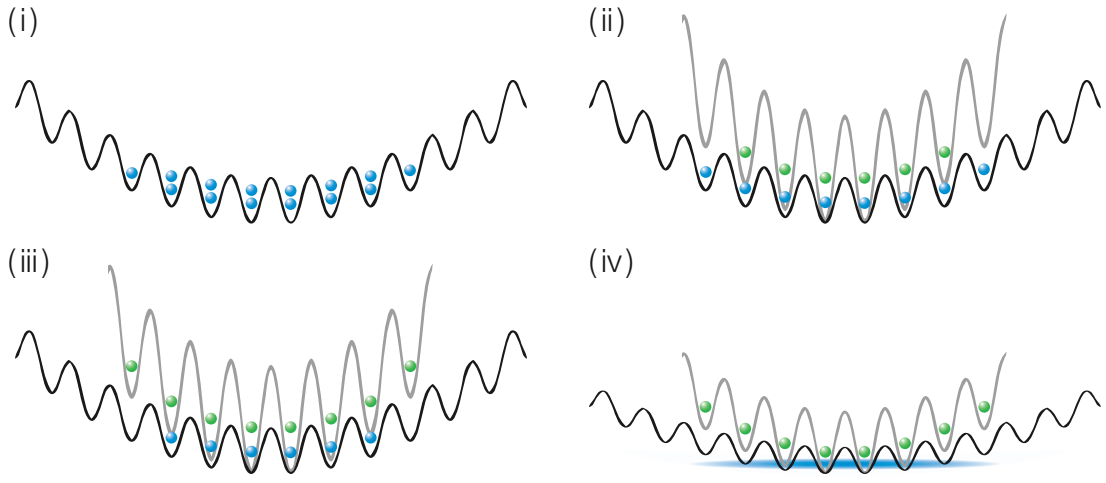

Figure 1.6 – Experimental sequence for the preparation of the KLM Hamiltonian in a state-dependent lattice. (i) A band-insulating core with unit filling is created by loading ground state atoms in a sufficiently deep optical lattice. (ii) One atom on each doubly occupied lattice site is excited by a clock π-pulse resonant with the interaction-shifted transition. (iii) Atoms on singly occupied lattice sites at the margins of the cloud are also excited by a resonant clock π-pulse. (iv) The state-dependent lattice potential is lowered to obtain the desired tunnelling coupling J_g.

to also excite atoms on singly occupied sites located at the margin of the cloud. A uniform lattice of localised impurities should indeed be present, entirely covering the density distribution of the mobile particles, considering that the Kondo physics reveals itself mostly in a modification of the properties of the conduction particles, as compared to their normal free-Fermi or Fermi-liquid behaviour. Conduction particles which do not experience the spin-exchange interaction at the edges would effectively hinder the observation of exchange-induced effects, especially when the atomic ensemble is globally probed. After the state preparation is complete, different J/V_{ex} regimes of the KLM can be investigated by adiabatically ramping down the state-dependent lattice to the desired value of J_g, yet providing enough localisation of the $|e\rangle$ state (which might also be enhanced by interactions). The harmonic confinement provides in this conditions an intrinsic variation of the filling factor for the $|g\rangle$ atoms that are set free to tunnel. By varying the lattice depth and consequently the $|g\rangle$ state bandwidth, or the harmonic confinement, the filling factor can be adjusted [30, 31]. The proposed preparation sequence is summarised in Fig. 1.6.

The temperature requirements for observing different phases of the KLM seem in general quite convenient, compared to their analogues in the case of magnetic super-exchange interactions [27, 28]. The KLM is therefore a promising candidate for the observation of long-range strongly correlated states with ultracold fermionic gases in optical lattices. We will discuss here the example of the anti-ferromagnetic KLM, which is the most widely studied in the condensed-matter community. The heavy-Fermi liquid phase predicted for $J_g < V_{\mathrm{ex}}$ should indeed be observed already at temperatures $T < T_K$, where $T_K \sim V_{\mathrm{ex}}/k_B$ when V_{ex} and J_g are of the same order (see Eq. (1.52)). On the other hand, lower temperatures $T < T_{\mathrm{RKKY}} \propto V_{\mathrm{ex}}^2/J_g$ are necessary to access the magnetically ordered phase predicted for $J_g > V_{\mathrm{ex}}$ and governed by the RKKY interaction energy scale [55, 76]. With realistic maximum allowed tunnelling rates e.g. for ytterbium of 300-400 Hz, we have $T_{\mathrm{RKKY}} \sim 10\,\mathrm{nK}$, which should be experimentally accessible with $T \lesssim 0.1\,T_F$ considering typical Fermi temperatures before the loading to the lattice around $T_F \sim 50 - 100\,\mathrm{nK}$ [215, 216]. An efficient way to ensure tolerant temperature demands is to adopt the largest allowed tunnelling J_g, providing however a sufficient $|e\rangle$ state localisation. The maximum attainable J_g is given the by the ratio between the two state light shifts, which should be as large as possible. The different phases of the KLM can then be accessed by varying the exchange coupling V_{ex}, which can be achieved by engineering a state-dependent potential reducing the spatial overlap between the $|g\rangle$ and $|e\rangle$ states [56]. The laser system for such a bi-chromatic lattice potential was already implemented in our laboratory and will soon be applied to the atoms, also to prepare individual two-dimensional tightly confined gases. Details about the laser system and the scheme for the state overlap reduction can be found in Ref. [125].

In the HFL phase, many observables displaying the main hallmarks of the Kondo screening physics are available. First of all, the effective mass of the $|g\rangle$ state atoms is heavily enhanced and this could be detected by analysing the centre-of-mass motion of the sample after a harmonic trap displacement [60, 61]. Similar measurements have been already realised in Fermi one-dimensional atomic gases [217, 218]. A possible difficulty could arise from a too small tunnelling coupling J_g as compared to the harmonic confinement offset between neighbouring lattice sites, which would inhibit dipole oscillations in

the harmonic trap by localising the states at the border of the cloud [92, 217]. Very low confinement frequencies should therefore be preferred.

Another strong signature of Kondo physics is the appearance of a completely insulating phase for filling $n_g = 1$, i.e. the so-called Kondo insulator. In this case, the harmonic trapping typical of cold atom experiments is an advantage, much alike for the observation of Mott insulator shells [40, 219], since the filling factor n_g varies radially across the trap. In the case of a two-dimensional system, high resolution imaging of local density in the lattice would directly allow for the observation of an insulating density plateau. Moreover, the Kondo insulator possesses a vanishing compressibility, which could be probed by trap compression measurements [31]. In addition, methods for probing or even directly imaging the density plateau exploiting the occupation-number-dependent clock interaction shifts are completely realistic [39], along the lines of the KLM state preparation. The occupation-number selective and spin-state selective clock excitation of ^{173}Yb atoms in a magic three-dimensional lattice is an important result of this work and will be reported in the Chapter 6.

A very notable feature which could be observed in atomic systems in a relatively simple way is the large Fermi surface in the HFL phase [61]. The momentum distribution and the Fermi surface in the lattice can be readily probed by the band mapping technique [30]. Strong fluctuations of the Fermi surface are expected when crossing the Kondo temperature T_K, due to the transition from a normal Fermi liquid to the HFL. Such an observation would establish a connection between the ideal Kondo lattice realised in atomic systems and heavy-fermion materials which are actively studied in condensed matter, for which large Fermi surfaces and their temperature-induced collapse were already observed [194, 220].

In the magnetically ordered phase, the detection of spin correlations is necessary. For this purpose, local [221] or global spin fluctuation measurements, and spatial noise interferometry [37] are the most powerful available tools. Moreover, proof-of-principle experiments of RKKY interaction-induced spin dynamics in isolated double-well potentials can be envisioned by employing optical superlattice potentials [27, 55]. We have briefly discussed how the crossover between the Kondo and the RKKY-dominated regimes is especially interesting, as the competition between these two type of interactions is expected to give rise to non-Fermi-liquid behaviour; accessing this regime with ultracold AEL atoms seems feasible.

We want to stress again the importance of a strong $|e\rangle$ state localisation, in order to prevent otherwise large two-body inelastic losses between distinguishable excited atoms (see measurements in Section 6.3), and the importance of a high-fidelity preparation of the $|e\rangle$ state ensemble in the lattice. A vital condition for probing both HFL behaviour and magnetic ordering is indeed the half-filling of the localised impurities. Only few theoretical studies exist of the so-called depleted KLM [222, 223], i.e. a KLM where some of the magnetic moments are randomly replaced by non-magnetic inactive impurities. The general indication is that a crossover from the HFL behaviour to a single-impurity Fermi liquid can occur already at very low impurities depletion, depending on the delocalised particles filling factor n_g. Such a crossover may hinder the observation of the typical signatures of local Kondo screening, such as the effective mass enhancement or the presence

of a Kondo insulator plateau in the in-situ density profile. The presence of a small number of holes in the localised particle density would also have consequences on the emergence of magnetic order. For a large number of holes, global magnetic ordering is primarily suppressed by the lack of (second-order) RKKY interactions. Preliminary theoretical studies indicate however that magnetic ordering in smaller domains could survive for a sizeable parameter range, as long as $T_{\mathrm{RKKY}} > T_K$ [223].

An additional complication might arise due to the finite interaction strength between $|g\rangle$ state atoms, which is significant also in very shallow lattices. A scenario with significant U_{gg} would be described by the so-called Kondo-Hubbard model [224, 225], which inherits features of both underlying models. Considering the case of ytterbium, if the ground state interactions in ^{173}Yb prove to be excessively strong, precluding the observation of KLM phases, the near absence of interactions in the ground state of the fermionic isotope ^{171}Yb [226] could be exploited to realise a fully exchange-dominated system. This isotope could moreover be interesting with regard to a possibly opposite sign of the exchange coupling.

We conclude this discussion by noting that, although not mentioned explicitly, the SU(N) symmetry of interactions is essential for the simulation of the spin-1/2 KLM, maintaining the system confined in a two-component subset of the spin manifold. Furthermore, by increasing the number of populated spin states above two, the experimentally unexplored SU(N) KLM may be investigated. The properties of the novel SU(N) HFL could be studied experimentally and further compared with large-N limit studies of the KLM [76, 179].

Direct optical hybridisation of orbital bands

A completely different possibility for delving into the physics of hybridisation between mobile and localised particles is the optical dressing of $|g\rangle$ and $|e\rangle$ states in a state-dependent lattice, which can be obtained by coherent coupling of the two electronic states. By tuning the clock light intensity and its detuning from resonance, one could freely control the coupling between a strongly dispersive energy band for the $|g\rangle$ state and a flat energy band for the $|e\rangle$ state, and their relative energy. A quasimomentum-dependent hybridisation of the two bands would be possible by choosing a Rabi frequency smaller than the $|g\rangle$ state bandwidth. Such a system would be of high interest for the study of impurity physics, as it realises a particular regime of the periodic Anderson model[17] [196]. Using Rabi frequencies well below the interaction clock shift and spin-polarised Fermi gases would be necessary in order to minimise the strong $|e\rangle$ state losses, which could however limit the attainable hybridisation strength.

1.3.3 SU(N) magnetism

A particularly interesting regime of the (single-orbital) SU(N) Hubbard model in Eq. (1.34) is the limit of large repulsive interaction, $U \gg J$. Deep in the Mott insulating phase at half-filling [31, 168], that model can be mapped at lowest perturbative

[17] Specifically, the high Coulomb-repulsion limit of the Anderson model is realised, where the on-site interaction term constrains the filling of the localised particles to $n_e = 1$.

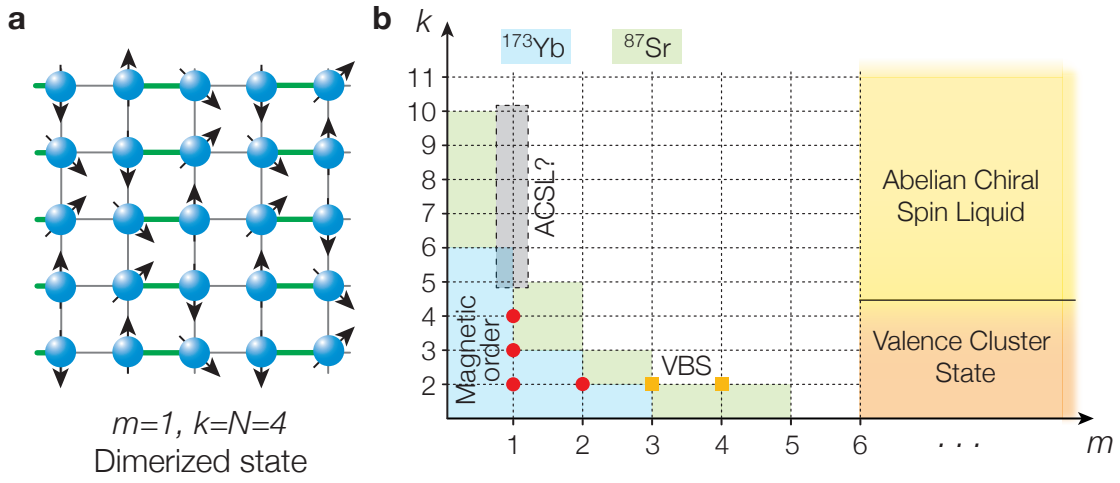

Figure 1.7 – (a) An illustration of the magnetically ordered state predicted for $N = k = 4$ and $m = 1$. Such a state spontaneously breaks translational and SU(4) symmetry, with a Néel-like order of spin dimers [227]. (b) The phase diagram of the square-lattice SU(N) Heisenberg model as a function of the inverse filling factor k and of the number of fermions per site m. Many different regimes are accessible using AEL atoms in two-dimensional optical lattices, and the $m = 1$, $k > 2$ Mott insulators are of particular interest. Magnetic order (red dots) is expected to persist up to $k = 4$ and $m = 2$, whereas for $k = 1$ and $m > 2$ valence bond states (VBS) are predicted (orange squares). For $k > 4$ and small m, no theoretical prediction is available and the possible existence of an abelian chiral spin liquid (ACSL) suggested by large-N studies provides an exciting prospect. The regions of the phase diagram accessible with ^{173}Yb and ^{87}Sr are shaded in different colours. The figure is an update of the one given in Ref. [62].

order (second order) to an effective SU(N) Heisenberg model [62, 166, 171], analogously to the SU(2) case [118, 206]:

$$\hat{H}_{\mathrm{H}} = \frac{2J^2}{U} \sum_{\langle i,j \rangle} \sum_{mn} \hat{S}^n_{im} \hat{S}^m_{jn} \tag{1.55}$$

where the on-site SU(N) spin operators were defined through Eq. (1.35).

The consequences of SU(N) symmetry are drastic, as spontaneous SU($N > 2$) symmetry breaking is in general less energetically favourable than SU(2) symmetry breaking. This is manifest in the extensive degree of degeneracy of the SU(N) classical ground states [54], in a similar way to what happens in frustrated magnets where magnetic order is unstable and spin liquids are favoured [228]. In the context of condensed-matter physics, almost only the SU(4)-symmetric Kugel-Khomskii spin-orbital model has been studied [78, 229, 230]. With the prospect of implementing higher symmetries through ultracold high-spin fermionic gases, SU($N > 2$) Heisenberg models have attracted much attention in the theoretical physics community and many studies were recently published [53–55, 62, 63, 163, 173, 227, 231–238]. A suppression of magnetic order at large N is predicted, accompanied by the emergence of exotic phases such as valence-bond and valence-cluster states, and even completely novel spin liquids with no analogues in nature [53–55, 62, 227, 233, 238]. Moreover, correlated magnetic states are expected to arise already at temperatures scales comparable to the super-exchange energy J^2/U

[55, 239, 240], which are under reach in ongoing experiments [63, 72, 73, 87, 124].

The crucial difference between SU(2) and SU(N) lattice spin models lies in the fact that more than two spins and thus more than two lattice sites are generally necessary to form a SU(N) singlet. Let us denote with k the minimum number of sites required to form a singlet, i.e. the inverse filling factor, and with m the number of fermions per lattice site, so that $N = m \times k$. m is in principle experimentally not restricted, however it is clear how $m = 1, 2$ represent the most feasible cases, as they can be realised by up to two-shells Mott insulators while avoiding three-body losses. k is restricted by $k \leq N/m$ where $N \leq 2F+1$ is the number of available nuclear spin states, with $N \leq 6$ for ^{173}Yb and $N \leq 10$ for ^{87}Sr (see Fig. 1.7(b)). Strong numerical evidences of ordered states on square lattices have been found for SU(3) [232] and SU(4) [227] Mott insulators, as represented in Fig. 1.7(a). On the other hand, it has been numerically shown that weak Neél order survives for $m = 2$ and $k = 2$ [173] and valence bond state (VBS) order appears for $m = 3, 4$ and $k = 2$ on a square lattice [173, 241] (see Fig. 1.7(b)). Large-N treatments of the 2D-Heisenberg model [54, 62] established the existence of Abelian chiral spin liquids (ACSL) and valence cluster states (VCS). Although the separation at $k > 4$ between those two phases has been determined [62], it is unknown to which value of m the chiral spin liquid phase extends. This is particularly exciting as the ACSL region may stretch as far as $m = 1$ and $k > 4$, which is experimentally accessible with AEL atoms (see Fig. 1.7(b)). The observation of the ACSL would be an extraordinary fulfilment, as such a state exhibits fractional statistics and topological order [54, 62], with spin-carrying gapless chiral edge states[18]. Topological order is so far exclusively realised in fractional quantum Hall liquids [242] and, very recently, in a kagome-lattice antiferromagnetic material [243]; no other known material is at present foreseen to possess a topologically ordered spin liquid ground state. The experimental realisation of AEL atom two-dimensional Mott insulators with $T \lesssim J^2/U$ is therefore of extreme interest for the observation of exotic spin states, which may have similarities to spin liquids in frustrated magnets [244] or possess no natural counterpart.

[18] By extending the model to include a second orbital, spin liquids with non-Abelian anyonic excitations are further predicted at large N [62].

CHAPTER 2

Creation of degenerate gases of ytterbium

In this Chapter, we present the fundamental properties of ytterbium and we give an overview of the experimental techniques which led to the production of ytterbium degenerate gases. Similar techniques have been successfully implemented in the last years by different research groups, leading to the production of degenerate gases of AEL atoms in several laboratories [52, 65–71, 87, 245–248]. After briefly introducing the physical and chemical properties of ytterbium, the electronic level structure with the experimentally relevant optical transitions is presented and the most important aspects of each transition are elucidated. The scattering properties in the ultracold regime are also summarised, with regard to both the ground and metastable states. We then address the typical cooling procedure employed to prepare ultracold gases of ytterbium, which are used to perform the experiments reported later in this work. The cooling strategy involves three distinct steps: Zeeman slowing of an atomic beam leaving the source, magneto-optical trapping of slowed atoms and successive evaporation in an optical crossed dipole trap. Depending on the choice of the isotope, Bose-Einstein condensation and Fermi degeneracy are achieved and some details are reported here. As a final part of this Chapter, the loading of such ultracold gases in a three-dimensional optical lattice and their characterisation with typical experimental techniques are presented.

2.1 Ytterbium essentials

Ytterbium (Yb) is is the fourteenth element in the lanthanide series with atomic number $Z = 70$. It is the last element in the f-block of the periodic table, meaning the 4f-shell is complete with 14 electrons. The full electronic configuration is thus [Xe] $4f^{14}$ $6s^2$. Owing to this complete f-shell, its electronic structure is mostly determined by the two valence electrons in the 6s-shell and its properties are therefore very similar to alkaline-earth atoms of the second group rather than to other rare-earth elements like erbium and dysprosium.

The discovery of ytterbium dates back to 1878, when the Swiss chemist Jean Charles Galissard de Marignac, while examining samples of gadolinite, found a new component in the earth then known as erbia, and he named it ytterbia [249]. The name was chosen due to Ytterby, the Swedish village close to where de Marignac found the new component

of erbium[1]. Marignac foresaw that ytterbia was a compound of a new element that he called *ytterbium* and in 1907 the chemists Georges Urbain, Carl Auer von Welsbach and Charles James independently separated ytterbia into two components: neoytterbia and lutecia [250]. Neoytterbia would finally become known as the element ytterbium, and lutecia would finally be known as the element lutetium. Nevertheless, the chemical and physical properties of ytterbium could not be determined with any precision until 1953, when the first almost pure sample of ytterbium metal was obtained.

2.1.1 Physical and chemical properties

Ytterbium is a rare-earth element. It is soft, malleable and ductile, and when pure it appears bright and silvery. Ytterbium metal slowly tarnishes, reacting with moisture in air, and it quickly oxidizes when dispersed in air and under oxygen. It has a density of $6.90\,\mathrm{g/cm^3}$ near room temperature [251]. With a melting point of 824 °C and a boiling point of 1196 °C, it has the smallest liquid range of all metals [250]. The melting and boiling points are significantly lower than those of the neighbouring elements in the periodic table (thulium and lutetium), mainly owing the closed-shell electron configuration of ytterbium, which causes only the two 6s electrons to be available for metallic bonding [251]. The temperatures required to produce a sufficient vapour pressure $\gtrsim 10^{-3}$ mbar, in order to provide the necessary atomic flux for experiments with degenerate gases, are very well below the melting point but however still quite high [252]. Temperatures between 400 °C and 500 °C are typical, and are fortunately still reachable by means of relatively uncomplicated oven setups (see Section 3.1.1). Ytterbium metal becomes highly reactive when brought into this temperature range and rapid chemical deterioration of silica glass has been reported [253]. Ytterbium is known to chemically bond to silica glass and (more weakly) to sapphire also at room temperature, so particular care has to be taken with vacuum viewports, which should not be exposed to the atomic vapour or to a direct flux without being heated.

Isotopes

Ytterbium is present in nature with seven stable isotopes: ^{168}Yb, ^{170}Yb, ^{171}Yb, ^{172}Yb, ^{173}Yb,^{174}Yb and ^{176}Yb [254]. The relative abundances and some fundamental properties of the different isotopes are summarised in Table 2.1. One exceptional feature of ytterbium, as opposed to many alkali and alkaline-earth-like atoms, is the presence of many isotopes with relatively high natural abundance. The two isotopes with non-zero nuclear spin, ^{171}Yb($I = 1/2$) and ^{173}Yb($I = 5/2$), are fermionic, whereas all other isotopes, including the most abundant ^{174}Yb, are bosonic and have zero nuclear spin ($I = 0$).

Ytterbium offers an extraordinary versatility, due to the wide choice of collisional properties (see Section 2.1.3) and of bosonic or fermionic statistics of the different isotopes. This is very attractive both for the production of quantum gases of a single isotope and for the study of ultracold interacting Bose-Bose, Bose-Fermi and Fermi-Fermi mixtures [66, 71, 255, 256]. The results which will be presented later in this work are almost

[1] In total, four elements were named after the village: ytterbium, yttrium, terbium and erbium

exclusively obtained by employing the fermionic ^{173}Yb isotope, which has the peculiarity of a nuclear spin larger than 1/2, strong repulsive interactions in the ground state (see Section 2.1.3) and the possibility of directly exciting the ground state to the lower $^3P_0$ metastable state owing to a weak intrinsic hyperfine interaction (see Section 2.1.2).

Isotope	Mass (u)	Abundance (%)	Nuclear spin I	Statistics	$\mu_I\,(\mu_N)$
^{168}Yb	167.933894	0.12	0	bosonic	
^{170}Yb	169.934759	2.98	0	bosonic	
^{171}Yb	170.936323	14.09	1/2	fermionic	+0.4919
^{172}Yb	171.936378	21.68	0	bosonic	
^{173}Yb	172.938208	16.10	5/2	fermionic	−0.6776
^{174}Yb	173.938859	32.03	0	bosonic	
^{176}Yb	175.942564	13.00	0	bosonic	

Table 2.1 – Nuclear properties of the seven stable isotopes of ytterbium. Naturally occurring abundances are taken from [254], while the atomic mass and the nuclear magnetic moment μ_I (incorporating the diamagnetic correction) are taken from [257].

2.1.2 Electronic properties

The electronic level structure of ytterbium reproduces the typical structure of alkaline-earth elements, which in turn partially resembles the one of Helium. This structure can be well described by the LS-coupling (Russell-Saunders coupling) scheme, where the total electronic spin angular momentum $\mathbf{S}$ and the total electronic orbital angular momentum $\mathbf{L}$ couple together to form the total electronic angular momentum $\mathbf{J} = \mathbf{S} + \mathbf{L}$. Each electronic level is then denoted by a term symbol $^{2S+1}L_J$ [86]. As already mentioned in Chapter 1, the two valence electrons can arrange in a spin singlet with total spin $S = 0$ or a spin triplet with $S = 1$, forming two separate level manifolds which are connected only by narrow optical transitions, usually termed *intercombination* transitions. These transitions would be completely forbidden as electric dipole (E1) transitions in the pure LS-coupling picture, owing to the spin selection rule $\Delta S = 0$; however, a significant mixing between the $^1P_1$ and the $^3P_1$ states is generated by spin-orbit interaction, as described later in more detail. This is a direct manifestation of the high Z of ytterbium, for which the LS-coupling scheme is a reasonably good approximation but not as good as for lighter alkaline-earth atoms as magnesium or calcium. This spin-orbit coupling indirectly enables in turn a decay channel from the $^3P_0$ to the ground state for the fermionic isotopes, due to the hyperfine interaction between the ^3P states originating from the non-zero nuclear magnetic moment. On the other hand, transitions within each of the two spin manifolds are broad and all the main transitions connecting the low-lying states to each other are in the visible region of the electromagnetic spectrum, which is typical of all AEL atoms. As we will describe in the following part of this Section, both type of transitions can be used for a number of applications, including laser cooling, state preparation, detection and repumping. A detailed scheme of the electronic level structure is shown in Fig. 2.1, where the most

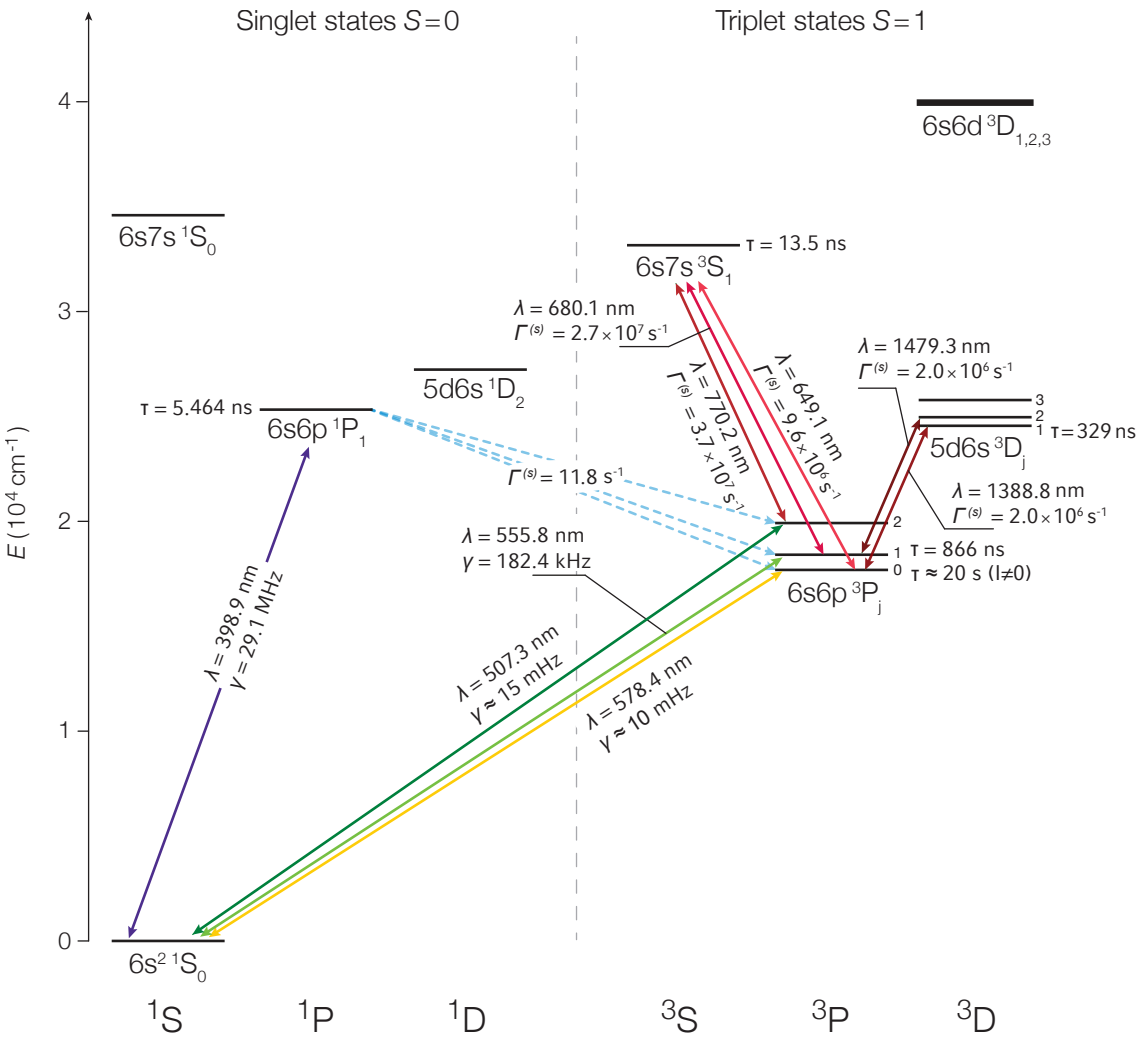

Figure 2.1 – Term diagram for the ytterbium electronic level structure. Optical transitions are illustrated as solid arrows connecting the different levels, with the corresponding wavelength indicated. Dashed lines indicate multi-photon decay channels. Lifetimes τ and radiative decay rates $\Gamma^{(s)}$ of the most relevant states are noted. For the closed transitions, natural linewidths $\gamma = \Gamma/(2\pi)$ are provided. The hyperfine structure of fermionic isotopes is omitted (see below for hyperfine splitting diagrams). State lifetimes are taken from Refs. [258] ($^1P_1$), [259] ($^3P_1$ and $^3D_1$), [260] ($^3P_0$) and [261] ($^3S_1$). The decay rate of the $^1P_1$ state to the triplet states is taken from Ref. [262], whereas other radiative decay rates are calculated from the transition dipole elements given in Ref. [261].

relevant states and transitions are indicated. A few essential parameters of the three most important transitions in ytterbium are summarised in Table 2.2.

One remarkable difference between ytterbium and alkaline-earth atoms is the presence of states with an electronic excitation from the 4f-shell of the core, which have to be described in the jj-coupling scheme. All these transitions should be taken into account for a correct theoretical prediction of the AC polarisability of each particular electronic state, although it complicates the calculation [263]. However, in practice, the ultimate option for safely ascertaining the differential polarisability between two states at a particular

Parameter	$^1S_0 \rightarrow {}^1P_1$	$^1S_0 \rightarrow {}^3P_1$	$^1S_0 \rightarrow {}^3P_0$
λ	398.9 nm	555.8 nm	578.4 nm
τ	5.464 ns	866.1 ns	$\gtrsim 20$ s ($I \neq 0$)
$\Gamma/(2\pi) = 1/(2\pi\tau)$	29.1 MHz	182.4 kHz	$\lesssim 10$ mHz
g_J	1.035	1.493	($J = 0$)
$I_{\mathrm{sat}} = \pi hc/(3\lambda^3\tau)$	59.97 mW/cm^2	0.139 mW/cm^2	$\lesssim 10$ pW/cm^2
$T_{\mathrm{D}} = \hbar\Gamma/(2k_{\mathrm{B}})$	699 μK	4.4 μK	–

Table 2.2 – A summary of some relevant parameters for the $^1S_0 \rightarrow {}^1P_1$, $^1S_0 \rightarrow {}^3P_1$ and $^1S_0 \rightarrow {}^3P_0$ transitions in ytterbium. λ and Γ denote the wavelength and the natural linewidth of the optical transition, τ and g_J are the lifetime and the Landé g-factor of the excited states. I_s is the saturation intensity of the transition and T_D is the transition associated Doppler temperature. Data for the three excited state lifetimes are respectively from Refs. [258–260].

wavelength is the experimental measurement of transition shifts [121]. Many of the f-shell excited states are found at large energies which are not accessible via single-photon excitations. Nevertheless, two-photon transition could still be troublesome in some cases, when choice of the wavelength is very limited or obligated (see Section 1.1.3). Some of the associated electronic transitions are in fact strongly coupled to the ground state [264], so particular care has to be taken with applications involving detuned high-power light, as these could cause substantial scattering. For example, considerable efforts have been devoted to measuring the influence of particular two-photon f-shell transitions which are found in proximity of the $^1S_0$-$^3P_0$ magic wavelength at 759.35 nm [121, 265].

The ground state

The ground state is the spin-singlet state $^1S_0$. Owing to the antiparallel alignment of the two s-shell valence-electron spins, it possesses zero total electronic angular momentum, $J = 0$. This in turn implies that, even for the fermionic isotopes with non-zero nuclear spin, no hyperfine structure is present in the ground state. The total angular momentum F is therefore entirely determined by the nuclear spin I, namely $F = I$. Bosonic isotopes have thus zero total atomic angular momentum and are entirely insensitive to magnetic fields. Amongst other consequences, the absence of any substructure in the ground state prohibits any sub-Doppler cooling mechanism [266]. On the other hand, for the fermionic isotopes, the Zeeman energy shift of the ground state sublevels in an external magnetic field B is simply given by:

$$\Delta_Z(B) = g_F m_F \mu_B B \tag{2.1}$$

where m_F is the nuclear spin projection along the field direction in units of $\hbar$. The Landé g-factor can be written as:

$$g_F = g_J \frac{F(F+1) - I(I+1) + J(J+1)}{2F(F+1)} + g_I \frac{F(F+1) + I(I+1) - J(J+1)}{2F(F+1)} \tag{2.2}$$

and the first term vanishes for $J = 0$. The total g-factor of the ground state is therefore given by the nuclear g-factor:

$$g_I = \frac{\mu_I}{\mu_B |I|} \tag{2.3}$$

where μ_I is the nuclear magnetic moment[2] and $|\mu_I| \sim |\mu_N|$ (see Table 2.1). As already mentioned in Section 1.1.4, due to μ_N being weaker then the Bohr magneton by a factor of ≈ 2000, the ground state of fermionic isotopes has a drastically reduced magnetic sensitivity as well, compared to atoms whose ground state has $J \neq 0$ (see inset of Fig. 2.5(b)).

The complete lack of hyperfine structure in the ground state manifold precludes the decay to different lower hyperfine states during the cooling. Consequently, a smaller number of lasers is required to carry out the cooling procedure, compared to alkalis which typically need repumping light during all stages of the laser cooling sequence. This characteristic of AEL species is moreover very desirable for a number of metrological applications [90, 96, 267], yet it has also some rather unfavourable consequences. First of all, magnetic trapping of ground-state atoms is extremely impractical, as magnetic gradients on a scale of 10^4 G/mm would be necessary, making all-optical methods the only viable solution for trapping and cooling to degeneracy. Magnetic Stern-Gerlach separation of the different nuclear spin states would also require enormously large field gradients and it is therefore not realistic: we will see in Chapter 4 how it is possible to achieve a nuclear spin-dependent and nearly uniform force by optical means.

The blue $^1S_0 \rightarrow {}^1P_1$ cooling transition

The dipole-allowed $^1S_0 \rightarrow {}^1P_1$ transition has a wavelength of 398.9 nm i.e. in the blue-violet visible range of the optical spectrum. Owing to its large linewidth it is mostly employed for initial slowing and magneto-optical trapping of atoms, and for absorption imaging as well (see Section 4.1). Its natural linewidth was measured with high precision [258] to equal $\Gamma_{\text{blue}} = 2\pi \cdot 29.13(3)$ MHz. This strong transition is almost closed, but a very weak radiative decay channel from the $^1P_1$ to the $^3P_{0,1,2}$ states is present. Atoms in the $^1P_1$ state decay to the triplet $5d6s\,{}^3D_{1,2}$ states, which in turn decay to the $^3P_{0,1,2}$ states[3] (see Fig. 2.1), respectively with lifetimes of 329 ns and 460 ns [259, 268]. Atoms in the $^3P_1$ state decay quickly back to the ground state, whereas the $^3P_{0,2}$ states are metastable (see below for more details). Atoms trapped in a MOT operating on the blue transition can therefore be lost when they get shelved in those states. This loss process can establish the ultimate limit on the number and the lifetime of trapped atoms in such a MOT [262, 269, 270]. In order to bring atoms back to the blue cooling cycle, optical repumping of the $^3P_{0,2}$ states to the $6s7s\,{}^3S_1$ state can be used [262] (see also below for more details on these repumping transitions). Such a repumping scheme can improve the lifetime and the maximum attainable number of atoms in a blue MOT by respectively 100% and 30%, but efficient cooling is still possible without any repumping light. For Zeeman slowing on the blue transition, the very weak decay path to the ^3P states poses no concern at all.

[2] The diamagnetic correction σ_d, accounting for shielding of external magnetic fields by the electronic cloud, is included in the values of μ_I given in Table 2.1.

[3] For details on each of the decay channels see Ref. [262].

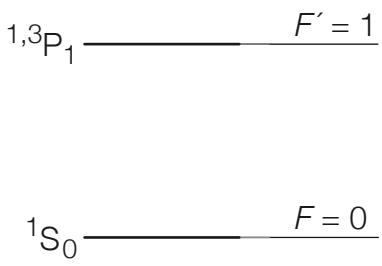

Figure 2.2 – Line structure of the $^1S_0 \rightarrow {}^1P_1$ and $^1S_0 \rightarrow {}^3P_1$ transitions for the bosonic isotopes of ytterbium. The lack of hyperfine interaction arises from the zero magnetic moment of the nucleus ($I = 0$).

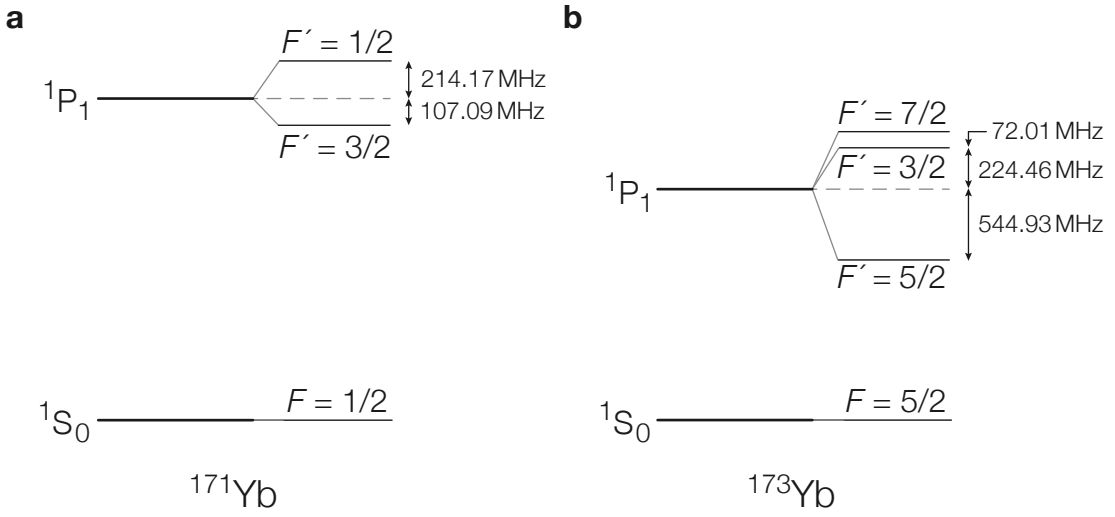

Figure 2.3 – Line structure of the $^1S_0 \rightarrow {}^1P_1$ transition for the fermionic isotopes of ytterbium: (a) ^{171}Yb and (b) ^{173}Yb. Hyperfine shifts are on the order of several hundreds of MHz. Shifts are relative to the respective transition centroids (see Table 2.3).

While only a single transition $F = 0 \rightarrow F' = 1$ is available for the bosonic isotopes, the hyperfine interaction in the fermionic isotopes with non-zero nuclear magnetic moment generates additional structure in the $^1P_1$ state. As the resulting hyperfine energy shifts (see Fig. 2.3) are comparable to the isotope shifts of the blue transition, the spectrum shows a succession of intertwined resonances from different isotopes. A precision measurement of the transition frequencies was reported in Ref. [271], where a complete characterisation of the spectrum is given. Isotope shifts are summarised in Table 2.3, given with respect to the transition frequency in ^{174}Yb : $\nu^{174}_{\text{blue}} = 751\,525\,987.761(60)$ MHz. Hyperfine splittings relative to transition centroids are indicated in the diagram in Fig. 2.3. Isotope and hyperfine shifts are significantly larger than the natural linewidth of the blue transition and addressing of individual isotopes or hyperfine states is therefore feasible. Selective slowing of different isotopes to load them in succession into a multi-frequency MOT is the most practical scheme for the production of cold isotope mixtures [66]. Addressing different hyperfine blue transitions with a suitable light polarisation can be em-

Isotope	$^1S_0 \rightarrow {}^1P_1$ shift (MHz)	$^1S_0 \rightarrow {}^3P_1$ shift (MHz)	$^1S_0 \rightarrow {}^3P_0$ shift (MHz)
^{168}Yb	1887.40	3655.13	n/a
^{170}Yb	1192.39	2286.35	n/a
^{171}Yb (centroid)	939.52	1825.72	1811.28164
^{172}Yb	533.31	1000.02	n/a
^{173}Yb (centroid)	291.52	555.78	551.53839
^{174}Yb	0	0	0
^{176}Yb	−509.31	−954.83	n/a

Table 2.3 – Isotope shifts of the $^1S_0 \rightarrow {}^1P_1$, $^1S_0 \rightarrow {}^3P_1$ and $^1S_0 \rightarrow {}^3P_0$ transitions in ytterbium. Shifts are taken respectively from Ref. [271], Ref. [272], and Refs. [122, 273, 274], and are relative to the ^{174}Yb absolute transition frequencies given in the text.

ployed to optically pump atoms into a subset of the nuclear spin states [71] (see also Section 4.2).

The green $^1S_0 \rightarrow {}^3P_1$ cooling transition

The $^1S_0 \rightarrow {}^1P_1$ transition wavelength is 555.8 nm, corresponding to a pale green colour, to whom the eye is extremely sensitive. It is essentially a closed transition and its natural linewidth is $\Gamma_{\text{green}} = 2\pi \cdot 182.4(4)$ MHz (deduced from Ref. [259]). The only decay path in addition to the one to the ground state is an extremely weak magnetic dipole (M1) transition to the $^3P_0$ state [275], which is entirely negligible for any of the applications reported in this work. A detailed characterisation of this transition for all isotopes was reported in Ref. [272]. Isotope shifts are summarised in Table 2.3, given with respect to the transition frequency in ^{174}Yb. The absolute transition frequency in ^{174}Yb is $\nu_{\text{green}}^{174} = 539\,386\,561(10)$ MHz. Hyperfine splittings relative to transition centroids are indicated in the diagram in Fig. 2.4. All the different resonances are well separated owing to the narrow natural linewidth of the transition.

This intercombination transition is strictly forbidden in the *LS*-coupling scheme. The reason why the $^3P_1$ state is in reality coupled to the ground state by a weak dipole transition lies in the magnitude of the spin-orbit interaction, which is not a small perturbation of the residual electrostatic interaction and mixes therefore the pure *LS*-coupling eigenstates [86]. Labelling the pure *LS* eigenstates as $|^1P_1^0\rangle$ and $|^3P_1^0\rangle$, one can write the eigenstates in the intermediate coupling regime by introducing a mixing[4] as (see e.g. [96]):

$$|^1P_1\rangle = \alpha|^1P_1^0\rangle + \beta|^3P_1^0\rangle \tag{2.4}$$

$$|^3P_1\rangle = \alpha|^3P_1^0\rangle - \beta|^1P_1^0\rangle \tag{2.5}$$

Only the pure *LS* eigenstate $|^1P_1^0\rangle$ is coupled to the ground state by an electric dipole transition, and therefore the $|^3P_1\rangle$ state inherits a dipole coupling because of $\beta \neq 0$. The

[4] The **J** operator commutes with the spin-orbit interaction operator H_{so}; the spin-orbit interaction generates thus a mixing only between states with the same J.

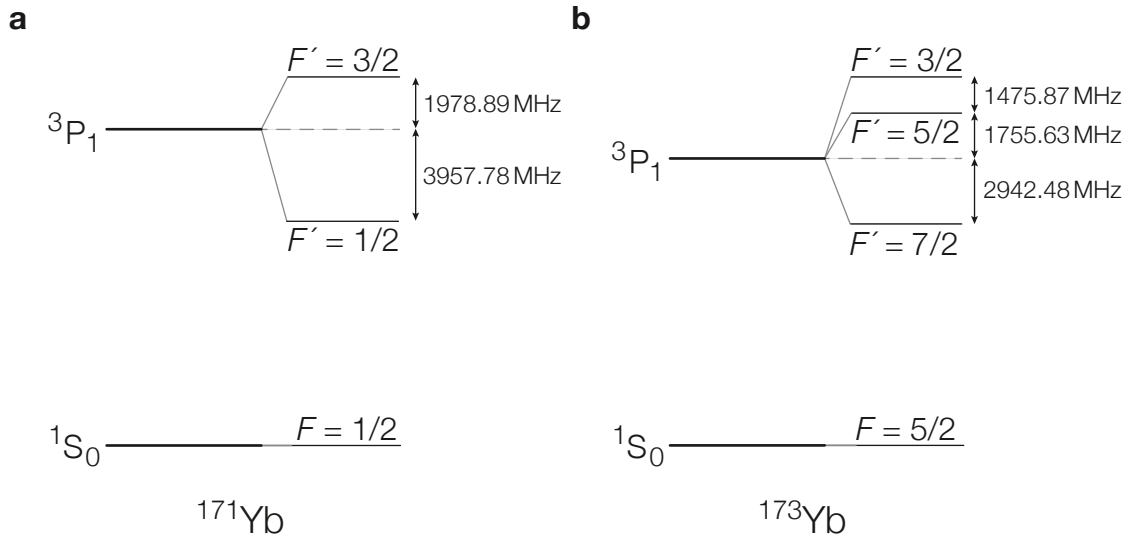

Figure 2.4 – Line structure of the $^1S_0 \rightarrow {}^3P_1$ transition for the fermionic isotopes of ytterbium: (a) ^{171}Yb and (b) ^{173}Yb. A strong hyperfine interaction generates shifts on the order of several GHz. Shifts are relative to the respective transition centroids (see Table 2.3).

coefficients α and β can be calculated through the measured lifetimes, since $\tau = C/(\nu^3 d^2)$, where d is the dipole matrix element of the transition [86]:

$$\frac{|\alpha|^2}{|\beta|^2} = \frac{\tau\left({}^3\mathrm{P}_1\right)\nu^3_{\mathrm{green}}}{\tau\left({}^1\mathrm{P}_1\right)\nu^3_{\mathrm{blue}}} \tag{2.6}$$

and by the normalisation relation $|\alpha|^2 + |\beta|^2 = 1$. Using the data given in Table 2.3, we obtain $|\alpha|^2 = 0.9834$ and $|\beta|^2 = 0.0166$.

Few fundamental parameters of the transition are reported in Table 2.2. A very low Doppler temperature $T_{\mathrm{D}} = 4.4\,\mu$K sets the minimum achievable temperature when laser cooling is performed on this narrow-line transition. The Doppler temperature is however still very well above the photon recoil temperature T_r =0.36 μK, which is not the case for lighter AEL species with even narrower intercombination transitions.

In the same way as for the blue transition, the hyperfine structure of the $^3P_1$ state is absent for the bosonic isotopes where only the transition $F = 0 \rightarrow F' = 1$ is available to use for optical cooling. For both fermionic isotopes on the other hand, the $F = I \rightarrow F' = F + 1$ transitions are used for MOTs and optical pumping (see Section 4.2), and they are sufficiently separated from other hyperfine transitions to be the dominant photon scattering channel even for a detuning of thousands of Γ_{green}.

The magnetic substructure of this transition also becomes important for magneto-optical trapping and optical pumping. The Landé factor g_F of an atom in the $^3P_1$ state depends of course on the total angular momentum F of the state under consideration (see Eq. (2.2)), and it is directly equal to the electronic Landé factor g_J for the bosonic isotopes; however, for any isotope, it is larger than the ground state g_F factor by about three orders of magnitude. The magnetic shift of the transition frequency is therefore essentially determined by the Zeeman shift of the excited state (see Fig. 2.5). In the case of

the bosonic isotopes, the standard MOT textbook configuration applies, with operation on a $J = 0 \rightarrow J' = 1$ transition. On the other hand, when hyperfine structure exists, a very unusual regime of MOT operation is established, where the magnetic shift of the transition goes from negative to positive for different m_F states (see Fig. 2.5(b)). This is the case for Yb fermionic MOTs and will be briefly discussed later in Section 2.2.2 (for a detailed explanation see e.g. Ref. [276]).

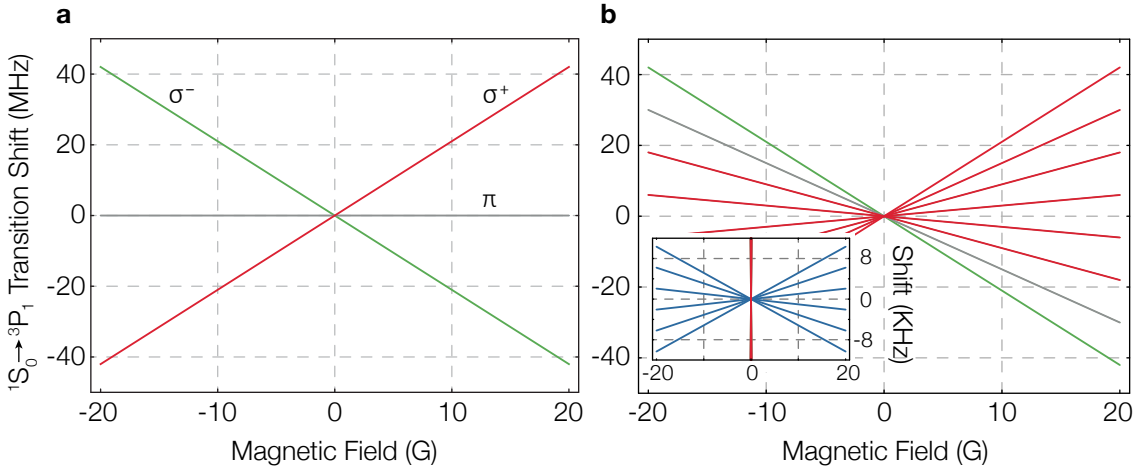

Figure 2.5 – Magnetic substructure of the $^1S_0 \rightarrow ^3P_1$ transition for (a) the bosonic and (b) the fermionic ^{173}Yb ($I = 5/2$) isotope of ytterbium. The Zeeman frequency shift of the transition changes sign with the sign of the m_F states, unlike usual MOT transitions in alkali atoms. Red, green and grey lines denote respectively σ^+, σ^- and π-transition frequencies. The inset of (b) shows the weak magnetic substructure of the ground state of ^{173}Yb, arising from a finite nuclear magnetic moment on the order of μ_N.

The yellow clock transition and the $^3P_0$ metastable state

The doubly-forbidden $^1S_0 \rightarrow ^3P_0$ transition has a wavelength of 578.4 nm, corresponding to an orange-yellow colour. The direct excitation of the clock transition has so far been achieved in three isotopes [122, 273, 274]. The absolute clock frequency transition in ^{174}Yb is 518 294 025.309 217 8(9) MHz [273] and the known isotope shifts are reported in Table 2.3. For fermionic isotopes, the tiny but non-zero dipole matrix element of the clock transition arises from the hyperfine interaction which couples states with the same F and causes thus a mixing between the $^3P_0$ state with the $^3P_1$ (F=I) state. This mixing and the consequent matrix element of the transition can be accurately estimated by relativistic many-body calculations [260, 265], yielding values for the natural linewidths of the clock transition $\Gamma_{\text{clock}} = 2\pi \cdot 7$ mHz in ^{173}Yb and $\Gamma_{\text{clock}} = 2\pi \cdot 6$ mHz in ^{171}Yb. Assuming a reasonable light intensity $I_0 = 4\,\text{W/cm}^2$, obtained for example by a beam waist $w_0 = 200\,\mu$m and a power $P_0 = 5$ mW, clock Rabi frequencies on the order of $\Omega \simeq 2\pi \cdot 2$ kHz are obtained.

In the bosonic isotopes, the metastable state decays to the ground state only via E1-M1 two-photon processes, and consequently its lifetime is much longer than in the fermionic isotopes, although exact values are not known. A finite dipole matrix element can be nevertheless induced by quenching the metastable state through a strong static magnetic

field [98, 99] or a strong laser field at the magic wavelength [100]. Through the magnetic field-induced coupling technique, Rabi frequencies on the order of $\Omega \simeq 2\pi \cdot 100\,\mathrm{Hz}$ can be obtained with a field of 100 G and the same light intensity assumed above [98].

The $^3\mathrm{P}_0$ metastable state has zero electronic angular momentum $J = 0$, like the ground state, and therefore no hyperfine structure is present either. In the fermionic isotopes, where a magnetic substructure is present, the Zeeman shift associated with each m_F state is given by Eqs. (2.1)-(2.3). However, due to the nuclear spin-induced mixing with the $^3\mathrm{P}_1$ state, the nuclear g-factor g_I of the metastable state is different from the one of the ground state. As a consequence, the various transitions $^1\mathrm{S}_0(F = 5/2, m_F) \rightarrow {}^3\mathrm{P}_0(F' = 5/2, m_F')$ experience a Zeeman shift $\Delta_Z = \mu_B B\,(g_I\,(m_F' - m_F) + \delta g\, m_F')$ where the differential g-factor was measured as $\delta g = h/\mu_B \cdot 112(1)\,\mathrm{Hz/G}$ (see Section 5.1.3). With typical clock Rabi frequencies on the order of 100 Hz, each nuclear spin state can thus be separately addressed in a magnetic field of just a few Gauss. We also note that the individual line strengths of the $^1\mathrm{S}_0(F = 5/2, m_F) \rightarrow {}^3\mathrm{P}_0(F' = 5/2, m_F')$ transitions are directly inherited from the $^1\mathrm{S}_0(F = 5/2, m_F) \rightarrow {}^3\mathrm{P}_1(F' = 5/2, m_F')$ transitions (see Appendix A).

As we will see in the last part of this thesis, addressing the clock transition of ^{173}Yb in a three-dimensional optical lattice allows for occupation-number-selective and spin state-selective excitation, owing to the interaction and the Zeeman clock shifts. This has important applications related to the preparation and the detection of many-body states in optical lattices. Atoms on singly or doubly occupied lattice sites can be made selectively and non-destructively dark to the imaging light and, with a sufficient optical resolution, could be imaged independently in-situ. Moreover, inter-orbital spin singlet and triplet can be distinguished from each other owing to their distinct interaction shifts (see Section 1.2.3), and on-site inter-orbital spin correlations could therefore be locally probed, with great use in the characterisation of orbital magnetic phases.

The $^3\mathrm{P}_2$ metastable state

The $^3\mathrm{P}_2$ state is also metastable, with a theoretical predicted lifetime $\sim 10\,\mathrm{s}$, which yet varies over the different hyperfine states with $F' = 1/2$, $3/2$, $5/2$ and $7/2$ due to the varying hyperfine mixing with the $^3\mathrm{P}_1$ state sublevels [260]. The dominant radiative decay channel in ytterbium is a magnetic dipole (M1) transition to the $^3\mathrm{P}_1$ state. Additional weak decay channels to other lower-lying $^3\mathrm{P}_0$ and $^1\mathrm{S}_0$ states are present, respectively of electric quadrupole (E2) and magnetic quadrupole (M2) type [260, 261]. In strong contrast to the $^3\mathrm{P}_0$ state, the $^3\mathrm{P}_2$ state exhibits a strong magnetic field sensitivity with a magnetic moment of $3\mu_B$, which is undesirable for optical frequency standards and precision spectroscopy. On the other hand, it represents a valuable resource as a readout state for quantum information processing with AEL atoms [105], since it could e.g. enable single-site-resolved addressing of atoms in an optical lattice in combination with a magnetic gradient [56, 58]. Indeed, spatially-resolved magnetic resonance imaging in an optical lattice using the $^1\mathrm{S}_0 \rightarrow {}^3\mathrm{P}_2$ transition has already been demonstrated [277].

The $^3P_0 \rightarrow {}^3S_1$ and $^3P_2 \rightarrow {}^3S_1$ repumping transitions

Several higher-lying states are available for the repumping of metastable state atoms to the ground state. Successive atom counting can then be achieved by means of either absorption imaging or MOT recapture followed by fluorescence detection. The strongly allowed $^3P_0 \rightarrow {}^3S_1$ and $^3P_2 \rightarrow {}^3S_1$ transitions (see Fig. 2.1) represent the most natural alternative, with their respective wavelengths 649.1 nm and 770.2 nm, conveniently located in a diode laser range, and their broad linewidth of approximately 12 MHz [278]. Both transitions have to be driven at the same time to achieve efficient repumping to the ground state via an intermediate decay to the $^3P_1$ state, owing to a branching ratio of the $^3S_1$ state of approximately 1:3:4 to the $^3P_{0,1,2}$ states [261]. The two repumping transition absolute frequencies in ^{174}Yb are $\nu_{\mathrm{rp0}}^{174} = 461\,868\,855(37)$ MHz and $\nu_{\mathrm{rp2}}^{174} = 389\,260\,412(24)$ MHz, and the isotope shifts are reported in Table 2.4 [278]. Two-photon Raman schemes exploiting these two transitions have also been suggested to coherently couple the two metastable states [56]. Another possibility for the detection of atoms in the $^3P_0$ state is the use of the $^3P_0 \rightarrow {}^3D_1$ transition at 1388.8 nm (see Fig. 2.1). With a branching ratio of approximately 60:3:1 of the $^3D_1$ state into the $^3P_{0,1,2}$ states [261, 262], this transition allows for ≈ 20 absorption cycles before the state become dark and could be used for direct absorption imaging. Alternatively, efficient repumping to the ground state by this transition can be attained via the intermediate decay to the $^3P_1$ state [122]. In our experiment, repumping of the metastable state of ^{173}Yb with an efficiency around 50% has been already achieved by driving the $^3P_0\,(F = 5/2) \rightarrow {}^3S_1\,(F' = 7/2)$ and $^3P_2\,(F = 9/2) \rightarrow {}^3S_1\,(F' = 7/2)$ transitions and will be presented in Ref. [279].

Isotope	$^3P_0 \rightarrow {}^3S_1$ shift (MHz)	$^3P_2 \rightarrow {}^3S_1$ shift (MHz)
^{170}Yb	−937	−968.3
^{171}Yb	−758	−751.6
^{172}Yb	−413	−425.3
^{173}Yb	−228	−229.3
^{174}Yb	0	0
^{176}Yb	392	425.7

Table 2.4 – Isotope shifts of the $^3P_0 \rightarrow {}^3S_1$ and $^3P_2 \rightarrow {}^3S_1$ transitions from Ref. [278]. Shifts are relative to the transition frequencies in ^{174}Yb given in the text.

2.1.3 Scattering properties

A complete characterisation of the scattering processes between ground state atoms in the s-wave regime has been reported in Ref. [226]. As we already discussed in Chapter 1, the collisional properties are independent of the nuclear spin, which is decoupled from the electronic degrees of freedom. The scattering lengths for all isotope combinations have been determined with great precision by means of two-colour photoassociation spectroscopy on the $^1S_0 \rightarrow {}^3P_1$ transition, which is particularly accurate owing to the absence of

Isotope	^{168}Yb	^{170}Yb	^{171}Yb	^{172}Yb	^{173}Yb	^{174}Yb	^{176}Yb
^{168}Yb	**252.0(34)**	117.0(15)	89.2(17)	65.0(19)	38.6(25)	2.5(34)	359.2(30)
^{170}Yb		**63.9(21)**	36.5(25)	-2.1(36)	-81.3(68)	-518.0(51)	-209.5(23)
^{171}Yb			**-2.8(36)**	-84.3(68)	-578(60)	-429(13)	141.6(15)
^{172}Yb				**-599(64)**	418(13)	200.6(23)	106.2(15)
^{173}Yb					**199.4(21)**	138.8(15)	79.8(19)
^{174}Yb						**104.9(15)**	54.4(23)
^{176}Yb							**-24.2(43)**

Table 2.5 – Scattering lengths (*s*-wave) in units of a_0 for ground state atoms of all ytterbium isotope combinations. Intra-isotope scattering lengths are highlighted in bold. Data are taken from Ref. [226].

hyperfine structure in the ground state. The measured *s*-wave scattering lengths are summarised in Table 2.5, and they can be seen to vary from large negative to large positive values with a wide choice of intermediate conditions. In the context of ultracold fermionic gases, we note especially the strong interactions between ^{173}Yb atoms, the almost vanishing interactions between ^{171}Yb atoms and the extremely strong interactions between atoms of the two isotopes, which can be exploited for the preparation of a Fermi-Fermi mixture via sympathetic cooling of ^{171}Yb atoms with ^{173}Yb atoms [71]. Furthermore, the two bosonic isotopes ^{174}Yb and ^{170}Yb are well suited for independent evaporative cooling. Thanks to the large variety of abundant isotopes and available interaction strengths, ytterbium is particularly suitable for the investigation of many-body physics with ultracold mixtures [66, 255].

Scattering between ground and metastable atoms

More recently, also the scattering properties between the two lower-lying $^1S_0$ and $^3P_0$ states in the fermionic isotopes[5] have been studied [124, 176, 280, 281]. Such studies are motivated on one hand by the strong interest in the $^3P_0$ metastable state as a resource for quantum simulation prospects, and on the other hand by the demand of collision shifts characterisation in optical lattice clocks [90]. The characterisation of the inter-orbital collisions in ^{173}Yb is an important part of this work and a detailed discussion on the determination of the scattering parameters is found in Chapter 6, together with the verification of their nuclear spin independence. We report here only the results for ^{173}Yb and ^{171}Yb, summarised in Table 2.6, extracted from the references indicated next to each value.
A very large symmetric-antisymmetric scattering length difference $\Delta a_{eg} = a_{eg}^{+} - a_{eg}^{-} \approx 3000\, a_0$ in ^{173}Yb has been confirmed by two independent studies [124, 176], indicating in turn a large exchange coupling between the two lower-lying electronic states of this isotope (see Eqs. (1.42b) and following). An evaluation of the exchange coupling in ^{171}Yb is unfortunately not yet available, as measurements on this isotope were so far performed in very low-density spin-polarised samples where only two *s*-wave scattering channels are

[5] In addition, the elastic and inelastic collisions between the ground state and the $^3P_2$ state have been studied in bosonic isotopes and the elastic interaction strengths were found to be magnetically tuneable [91].

Isotope	^{173}Yb	^{171}Yb
a_{gg}	199.4(21) [226]	−2.8(36) [226]
a_{eg}^{+}	3300(300) [176]	n/a
a_{eg}^{-}	219.5(29) [124]	−25(25) [281]
a_{ee}	306.2(106) [124]	n/a
β_{eg}^{+}	$3.9(16)\times10^{-13}$ [124]	$3(2)\times10^{-11}$ [280]
β_{eg}^{-}	$<3\times10^{-15}$ [124]	
β_{ee}	$2.2(6)\times10^{-11}$ [124]	$5(3)\times10^{-11}$ [280]

Table 2.6 – Scattering lengths (*s*-wave) in units of a_0 and inelastic loss rates in cm^3/s for the ^{1}S$_0$ and ^{3}P$_0$ states of the fermionic ytterbium isotopes. The reported inelastic rate coefficients β_{eg}^{+} and β_{ee} for ^{173}Yb were measured in quasi-2D ensembles (see Section 6.3 for more details). The inelastic rate coefficients β_{eg} and β_{ee} measured in ^{171}Yb contain also the contribution of *p*-wave collisions.

available [280, 281]. Given that interactions between ground state atoms of ^{171}Yb are practically absent, an experimental evaluation of the exchange process strength is of high interest, as ^{171}Yb could represent a completely exchange-dominated system.
Inelastic collisions were investigated as well in both isotopes (see the bottom rows of Table 2.6). In ^{173}Yb, as long as metastable atoms are kept isolated from each other, the system was found to be stable over the experimental time scales [124] (see Section 6.3). Similar studies have been also performed on ^{87}Sr [214, 282, 283], revealing a much smaller exchange coupling with $\Delta a_{eg} \sim 100\,a_0 \sim a_{gg}$, which makes this element rather unsuitable for realising exchange-dominated many-body systems, such as the Kondo lattice model.

2.2 All-optical cooling to degeneracy

In order to produce quantum degenerate gases of Yb, a procedure involving at least three stages of slowing-cooling is necessary. First, atoms out of a thermal beam are decelerated inside a Zeeman slower (ZS) working on the strong dipole-allowed ^{1}S$_0 \rightarrow ^1$P$_1$ transition, which is designed to slow them down to velocities of only a few m/s. Subsequently, the cooling starts by capturing the slow atoms in a magneto-optical trap (MOT) working on the narrow ^{1}S$_0 \rightarrow ^3$P$_1$ intercombination transition. After loading the MOT for a sufficient time, a suitable smooth variation of the different MOT parameters yields a sample with $N \approx 5\times10^7$ atoms at $T \simeq 20\,\mu$K, although the final density and temperature are dependent upon the chosen isotope. The third stage of cooling starts after loading the laser-cooled sample to a crossed optical dipole trap (ODT), where evaporative cooling is performed leading to quantum degeneracy. The different stages of the cooling procedure will be described in this Section, whereas technical details about the laser system and the optical setup can be found in Chapter 3. An illustration of the laser configuration used to cool and trap the atomic samples in the centre of the vacuum chamber is given in Fig. 3.6.

2.2.1 Zeeman slowing

Unlike many alkali atomic species, alkaline-earth-like (AEL) elements generally have a high melting point and a low vapour pressure and ytterbium is not an exception (see Fig. 3.3). High temperatures are therefore needed to produce a thermal atomic beam with sufficient flux, and Zeeman slowing is the usual approach to bring a large portion of atoms inside the capture velocity range of a MOT [15]. A clear advantage of AEL atoms over alkali species is the much lower Doppler temperature which can be achieved in MOTs thanks to narrow-line cooling on the intercombination line. This benefit however comes at a price: owing to the small natural linewidth of the intercombination transitions, such MOTs have very low capture velocities and appropriate measures have to be taken in order to provide efficient loading. The direct loading of an intercombination MOT is very desirable, in comparison to schemes with a first cooling stage in a MOT operating on the strong $^1S_0 \rightarrow ^1P_1$ transition followed by a transfer to a narrow-line MOT. For some AEL atomic species, e.g. strontium, the latter strategy is the only practicable option, as the $^1S_0 \rightarrow ^3P_1$ intercombination transition is simply too narrow for any other approach to work. For ytterbium on the other hand, direct loading of a green intercombination MOT can be implemented by a careful design of the ZS and considerable line broadening of the intercombination transition during the initial loading stage.

The ytterbium broad blue transition is very effective for slowing, offering a high scattering rate with consequently very short ZS setups ($L \sim 30\,\text{cm}$) and relatively large capture velocity, in comparison to standard alkali atom slowers with typical lengths $L \sim 1\,\text{m}$. Alternative approaches have been pursued as well, involving the use of dispenser sources in combination with a two-dimensional MOT, which make a ZS unnecessary [248]. However, we have chosen to implement a conventional atomic oven and a ZS, which can provide a sufficient flux of slow atoms to directly load a green intercombination MOT. In general, heated reservoir atomic sources have a longer lifetime in comparison to dispenser sources. Moreover, a ZS provides a rather isotope-independent performance by working on the stretched $^1S_0 \rightarrow ^1P_1$ transition, with the only demand of requiring a rather large light intensity $I_s \gtrsim I_{\text{sat}} = 60\,\text{mW/cm}^2$ to saturate such a broad transition (see Table 2.2). Although the ZS increases the longitudinal size of the vacuum system, the length of the narrow ZS tube is conveniently exploited to maintain a large pressure difference between the main vacuum chamber and the oven vacuum section (see Section 3.1 for more details).

We have opted for an increasing field ZS design. This configuration presents a key advantage compared to a decreasing field design due to the sudden change of the field at the end of the solenoid: the ZS light detuning to the resonance for atoms at rest is maximum for zero magnetic field. Consequently, a large detuning is present at the MOT location, which minimises the losses due to the ZS light radiation pressure on the cloud trapped in the intercombination MOT during the loading. Furthermore, atoms go quickly out of resonance at the exit of the slower; hence the radiation force abruptly decreases and the exit velocity of the atoms can be cleanly tuned by the ZS light detuning. An increasing field configuration is additionally less sensitive to laser frequency and intensity fluctuations, as the exit velocity is intrinsically less dependent on the ZS light parameters than for the decreasing field variant [284].

The ZS operates on a so-called *stretched* state transition: ${}^1\mathrm{S}_0\,(F, m_F = \pm F) \rightarrow {}^1\mathrm{P}_1\,(F' = F+1, m_{F'} = m_F \pm 1)$. The slowing light is circularly polarised and the excited state can only decay back to the original m_F state by emitting a circularly polarised photon. In the case of an increasing-field ZS, a negative (red) light detuning Δ_s is necessary to compensate the positive Doppler shift $\Delta\omega_D = k_s v$ of the atomic transition at the beginning of the slower ($k_s = 2\pi/\lambda_s$ is the wave vector of the ZS laser light, with $\lambda_s = 398.9\,\mathrm{nm}$, and v is the atom velocity). A negative Zeeman shift is therefore needed to bring into resonance the red detuned slower light, which must hence be σ^--polarised. The lack of hyperfine structure in the ground state of ytterbium is beneficial in this context: a single transition is available at any magnetic field, as no level crossings between different hyperfine level manifolds exist. No additional radiative decay channel is therefore present, except the extremely weak above-mentioned decay path from the ${}^1\mathrm{P}_1$ state to the triplet states (see Section 2.1.2). The transition frequency Zeeman shift in a field with magnitude B is given by:

$$\Delta\omega(B) = (g_{F'}\, m_{F'} - g_F\, m_F)\,\frac{\mu_B}{\hbar} B \simeq g_{F'}\, m_{F'}\,\frac{\mu_B}{\hbar} B\,, \tag{2.7}$$

where the approximation holds as $g_{F'}\left({}^1\mathrm{P}_1\right) \gg g_F\left({}^1\mathrm{S}_0\right)$ (see Eq. (2.2)). For the stretched transitions, $g_{F'} = g_{J'}/(I+1)$ and $|g_{F'}\, m_{F'}| \simeq 1$ for all isotopes up to corrections of order 10^{-2} (see Table 2.2 and Eq. (2.2)), and for the σ^--transition we can therefore write:

$$\Delta\omega^-(B) \simeq -\frac{\mu_B}{\hbar} B \tag{2.8}$$

The maximum Zeeman shift in the slower determines the minimum required light detuning Δ_s:

$$\mathrm{Min}\,|\Delta_s| = \left|\Delta\omega^-(B_{\max})\right| \tag{2.9}$$

which can be increased (in absolute value) to yield a positive exit velocity. The capture velocity v_c and the exit velocity v_f follow from the light detuning:

$$k_s v_c = -\Delta_s \tag{2.10}$$

$$k_s v_f = \Delta\omega^-(B_{\max}) - \Delta_s \tag{2.11}$$

The ZS beam detuning Δ_s can thus be used for the fine tuning of the atom exit velocity from the ZS, which is approximately their velocity when they reach the MOT location.

The coils in our ZS setup are designed to deliver a maximum magnetic field $B_{\max} \simeq 650\,\mathrm{G}$, which corresponds to $v_c \simeq 360\,\mathrm{m/s}$ and a light detuning $\Delta_s \simeq -2\pi \cdot 900\,\mathrm{MHz}$ (for details on the slower solenoid see Section 3.1.3). The ZS solenoid is 35 cm long, which is substantially longer than the minimum length $L_s \approx 25\,\mathrm{cm}$ required for operation at a light intensity $I_s = I_{\mathrm{sat}}$. The design is thus rather conservative: operation with a light power $P_s \approx 100\,\mathrm{mW}$ (corresponding to $I_s \approx 2I_{\mathrm{sat}}$ for a beam waist of $w_s = 5\,\mathrm{mm}$) is optimal but the performance is sufficient also at considerably lower light powers down to 60 mW, below which the loading rate of our MOT rapidly drops. The ZS beam size is decreasing along its path towards the oven source collimation section, in order to match the divergence of the atomic beam, and has a waist $w_{s0} \simeq 4\,\mathrm{mm}$ at the ZS input position and $w_{s1} \simeq 7\,\mathrm{mm}$ at the ZS output position.

Thermal beam velocity

In our experimental setup, an atomic beam of ytterbium is produced by heating atoms out of a reservoir through an array of collimation tubes (for details on the atomic oven system see Section 3.1.1). Additional transverse velocity selection is provided by a differential pumping tube section placed ahead of the ZS entrance flange, where by geometrical constraints the beam has a maximum full divergence of approximately 10 mrad. The distribution of velocities in the atomic beam along the direction of propagation must be taken into account, in order to design a ZS with an appropriate maximum capture velocity v_c and efficiently decelerate a significant portion of the velocity distribution. For a collimated atomic beam, the velocity along the beam axis is much larger than the transverse velocity. The distribution $P_{\mathrm{v}}(T)$ of longitudinal velocities v as a function of the reservoir temperature T can then be written as [285]:

$$P_{\mathrm{v}}(T) \simeq \frac{1}{2}\left(\frac{M}{Tk_B}\right)^2 v^3 \exp\left(-\frac{Mv^2}{k_B T}\right) \tag{2.12}$$

where M is the atomic mass of ytterbium and k_B is the Boltzmann constant. The typical temperature of operation of our atom source $T \sim 400\,^{\circ}\mathrm{C}$ leads to an average longitudinal velocity $\bar{v} \approx 340\,\mathrm{m/s}$. By integrating $P_{\mathrm{v}}(T)$ up to our design capture velocity $v_c = 360\,\mathrm{m/s}$, we estimate that $\sim 60\%$ of the beam velocity distribution is captured in the slower.

Slower magnetic-field design

In order to directly load the narrow-line green MOT, a very small exit velocity v_f from the ZS is necessary, due to the small capture velocity v_{MOT} of such a MOT. For very small final velocities, the transverse heating of the decelerated atoms due to the spontaneous re-emission of the blue ZS photons becomes important. The longitudinal and the transverse velocities become comparable at the end of the ZS, i.e. the slow atom beam acquires a large divergence angle when exiting the ZS. When leaving the ZS, the slowed atomic beam consequently expands very quickly to a size larger than the MOT capture region, determined by the MOT beam waist size.

In order to minimise the detrimental effect of a large beam divergence on the loading of the MOT, the distance between the exit location of the ZS and the centre of the MOT quadrupole B-field should be kept as short as possible. In our setup this is achieved by means of a specific design of the ZS last solenoid coil section and of the vacuum flange connecting the ZS tube to the main vacuum chamber (see Section 3.1 for the design details). A distance of just approximately 6 cm has to be traversed by the atoms to reach the centre of the MOT region. Additionally, the last ZS coil has a small diameter of just 18 mm and a thickness of 7 mm, in order to generate a very abrupt decay of the B-field magnitude in the direction of the MOT location. A semi-classical numerical simulation was performed to verify the effect of the transverse heating during the slowing, and theoretically estimate the loading rate of the MOT. We estimate a mean final transverse velocity $\bar{v}_f^T \simeq 1.8\,\mathrm{m/s}$ and expect that approximately 1% of the atoms entering the ZS tube are decelerated below a MOT capture velocity $v_{\mathrm{MOT}} = 8\,\mathrm{m/s}$ and reach the MOT centre within a region of radius $r_{\mathrm{MOT}} = 7\,\mathrm{mm}$. The observed loading rate of the MOT (see below) roughly matches

the expected values from the simulation, assuming an atomic flux $\Phi \approx 1 \times 10^{10}$ atoms/s entering the ZS for ^{174}Yb (see Eq. (3.2) and measured values).

Zeeman slowing of ^{173}Yb

An unfortunate coincidence leads to some complications when the ZS is tuned to operate on the ^{173}Yb isotope: the hyperfine transition $F = 5/2 \rightarrow F' = 5/2$ has a shift of -840 MHz from the ZS transition $F = 5/2 \rightarrow F' = 7/2$ (see Fig. 2.3). The design ZS detuning $\Delta_s = -2\pi \cdot 900$ MHz therefore tunes the light into near-resonance with the unwanted hyperfine transition for all atoms with a low velocity. When atoms leave the slower, they occupy the $^1S_0$ ($F = 5/2, m_F = -5/2$) state and they are dark to σ^--polarised light resonant to the $F = 5/2 \rightarrow F' = 5/2$ transition. On the other hand, as soon as they are captured in the MOT, cycling on the $^1S_0 \rightarrow ^3P_1$ transition pumps them to different m_F states. The ZS light then pushes them away from the MOT region by driving the $F = 5/2 \rightarrow F' = 5/2$ transition and all atoms are rapidly lost from the MOT.
As the ZS transition linewidth is power broadened by a factor of 1.5, one must necessarily increase or decrease the detuning substantially, to have several Γ_{blue} between the ZS light frequency and the $F = 5/2 \rightarrow F' = 5/2$ resonant frequency. In our setup, the solution which produced the best performance is a reduction of the light detuning to $\Delta_s = -2\pi \cdot 650$ MHz, equivalent to $\Delta(F = 5/2 \rightarrow F' = 5/2) \simeq 7\,\Gamma_{\text{blue}}$. This detuning corresponds to a reduced capture velocity $v_c \simeq 260$ m/s and a B-field maximum $B_{\max} \simeq 450$ G. The performance of the ZS is obviously worsened compared to other isotopes because of the lower ZS capture velocity, but still fully sufficient for loading the intercombination MOT to approximately a third of the maximum atom number attainable with ^{174}Yb (see Section 2.2.2). However, atoms trapped in the MOT experience a significant radiation force by the ZS light, owing to the reduced detuning from the main ZS transition and from the supplementary hyperfine transition. A considerable improvement in the operation of the MOT is obtained by blocking the top part of the slower laser beam with a metal blade and by displacing the centre of the quadrupole B-field up by few millimetres, in order to minimise the overlap between the blue beam and the atomic cloud trapped in the MOT. The geometric shape of the ^{173}Yb cloud during the MOT loading is nonetheless largely influenced by the blue light beam.

2.2.2 Magneto-optical trapping on the intercombination transition

The green intercombination transition in ytterbium is almost perfectly closed and therefore well suited for magneto-optical trapping. Its natural linewidth is small, yet sufficiently strong to support an atomic cloud against gravity. The maximum achievable acceleration through photon scattering equals $\Gamma_{\text{green}}\,\hbar k/2M \approx 2\times10^3$ m/s^2, which is indeed much larger than the gravitational acceleration. For lighter AEL atoms with narrower intercombination lines, gravity can play a big role in MOTs, e.g. in strontium [276, 286, 287], or even preclude the possibility of narrow-line MOT. In the latter case, the only method to cool on the intercombination line is quenching the $^3P_1$ state with other shorter-lived states to increase the photon scattering rate, e.g. in calcium [288]. The first intercombination MOT

Cooling stage	Duration (s)	Detuning (Γ)	Intensity (I_{sat})	Gradient (G/cm)
Zeeman slowing	8	^{174}Yb: −31 ^{173}Yb: −22	∼ 2	n/a
MOT (loading)	8.25	−35	400	2.0
MOT (compression)	0.16	−7	0.1	9.5

Table 2.7 – A summary of the experimental parameters used for the different stages of the laser cooling.

for ytterbium was reported in 1999 by the Kyoto group [289] with direct loading from a ZS. Narrow-line laser cooling represents an interesting subject in its own right and has been extensively studied with strontium atoms [287, 290]; we will limit ourselves to a brief description and report our experimental conditions. The operation parameters for our MOT on the $^1S_0\,(F = I) \rightarrow {}^3P_1(F' = F + 1)$ transition are summarised in Table 2.7.

Capture velocity

An especially important parameter for the efficient loading of a narrow-line MOT is the capture velocity v_{MOT}, i.e. the highest velocity for which an incoming atom will be captured inside the MOT region. In order to estimate the actual capture velocity of the MOT, two trap parameters need to be specified: the size of the MOT region, determined by the laser beam waists w_{MOT}, and the quadrupole field gradient[6] A. The waist size of the MOT beams in our setup is $w_{MOT} \simeq 6\,\text{mm}$, that was chosen as a trade-off between a high intensity and a sufficient trap volume. Six independent MOT beams are used, with a power $P_{MOT} \simeq 60\,\text{mW}$ in each beam during the loading phase, equivalent to an intensity $I_{MOT} \simeq 400\,I_{sat}$.

The highest attainable MOT capture velocity is given by assuming that the light is constantly tuned to resonance while an atom traverses the entire MOT region. As $I_{MOT} \gg I_{sat}$, the radiation force at resonance is $\mathcal{F}_{max} \simeq \Gamma_{green}\,\hbar k_{MOT}/2$, with $k_{MOT} = 2\pi/\lambda_{green}$. By energy conservation we can write:

$$v_{MOT,\,max} = \left(\frac{2\hbar k_{MOT}}{M}\,\Gamma_{green}\,w_{MOT}\right)^{1/2} \simeq 8\,\text{m/s} \tag{2.13}$$

Such a moderate capture velocity is still compatible with the performance of our ZS, as for $v_f = 8\,\text{m/s}$ the slowed atom beam has a radius of approximately 1.4 cm at the MOT position, and a large portion of atoms is therefore hitting the MOT region. On the other hand, a capture velocity close to this upper limit needs to be achieved, by adopting a large MOT light detuning Δ_{MOT} and by power broadening the laser spectrum[7]. The power broadening assures that the cooling light is absorbed by the atoms located across the entire MOT region, as long as $|\Delta_{MOT}| \sim \Gamma_E = \Gamma_{green}\sqrt{1 + I_{MOT}/I_{sat}}$.

[6] Here, A denotes the gradient in the plane orthogonal to the MOT coils axis; in the usual anti-Helmholtz configuration, the axial gradient is simply twice as large.

[7] In our experiment, the transition power broadening provided by the high laser intensity turns out to be sufficient. In other experimental setups, the required broadening is realised by means of a frequency modulation of the MOT light (see e.g. [88, 289]).

In a one-dimensional configuration with a single beam directed against the incoming atom direction[8], we can write the resonance condition for an atom in the MOT at position x with velocity v:

$$k_{\mathrm{MOT}}\, v + \frac{\mu'}{\hbar} A x + \Delta_{\mathrm{MOT}} = 0 \tag{2.14}$$

where μ' is the magnetic moment of the excited state. $k_{\mathrm{MOT}}\, v$ and $\mu' A x/\hbar = g_{F'}\, m_{F'} \mu_B A x/\hbar$ are the Doppler and the Zeeman shifts of the cooling transition respectively (see Eq. (2.7)). For the stretched MOT transitions ${}^1\mathrm{S}_0\,(F, m_F) \rightarrow {}^3\mathrm{P}_1(F+1, m'_F = m_F \pm 1)$, $|\mu'| \simeq 1.5\mu_B$ for both bosonic and fermionic isotopes (see Eq. 2.2 and Fig. 2.5). With a detuning $\Delta_{\mathrm{MOT}} \simeq -1.7\,\Gamma_E = -35\,\Gamma_{\mathrm{green}}$ and a gradient of 2 G/cm (see Table 2.7), atoms entering the MOT are captured when their velocity is below[9] $v_{\mathrm{MOT}} = 5$ m/s, found by setting $x = -w_{\mathrm{MOT}}$ in Eq. (2.14). For an atom with velocity $v < v_{\mathrm{MOT}}$, the Doppler shift is exactly compensated by the light detuning and the Zeeman shift at some position $-w_{\mathrm{MOT}} < x < w_{\mathrm{MOT}}$ where the atom tunes into resonance with the cooling light and is then eventually decelerated to zero velocity. In order for the light to slow the atoms to rest, the field gradient A cannot be arbitrarily large: the decelerating radiation force of the MOT beams can never overcome its resonant value $\mathcal{F}_{\mathrm{max}}$. From Eq. (2.14) we can write:

$$\left|\frac{dv}{dx}\right| = \frac{\mu' A}{\hbar k_{\mathrm{MOT}}}, \qquad \frac{dv}{dx} = \frac{1}{v}\frac{dv}{dt} \leq \frac{\mathcal{F}_{\mathrm{max}}}{M v} \tag{2.15}$$

From this we obtain the maximum quadrupole gradient which can be used in order to capture atoms up to v_{MOT}:

$$A_{\mathrm{max}} = \frac{\hbar^2 k_{\mathrm{MOT}}^2}{2M} \frac{\Gamma_{\mathrm{green}}}{\mu'\, v_{\mathrm{MOT}}} \simeq 3.7\,\mathrm{G/cm} \tag{2.16}$$

Using a gradient $A < A_{\mathrm{max}}$ leads to a smaller capture velocity (see Eq. (2.14)), but it allows a larger trap volume, which is desirable to minimise light-induced atom losses and heating, and to maximise the overlap with the divergent ZS atom beam.

Loading of the bosonic MOT

The bosonic isotopes do not possess any magnetic substructure in the ground state and the MOT operates therefore on the two $F = 0 \rightarrow F' = 1$ stretched transitions with $\Delta m_F = \pm 1$. Due to the large detuning $|\Delta_{\mathrm{MOT}}| > \Gamma_E$, the cooling light is resonant with the atomic transition only in an ellipsoidal shell where the Zeeman shift balances the detuning, and atoms at the centre of the MOT are tuned out of resonance. The radius of the shell is given by $\hbar|\Delta_{\mathrm{MOT}}|/(\mu_{F'} A)$ and its thickness by $\hbar\Gamma_E/(\mu_{F'} A)$. For our parameters $A = 2.0$ G/cm (axial) and $|\Delta_{\mathrm{MOT}}| = 35\,\Gamma_{\mathrm{green}}$, the shell has a radius of 2.5 mm and a thickness of 1.5 mm,

[8] The usual experimental configuration involves two beams with an angle of 45° each to the direction of the incoming atoms velocity. The radiation forces from the two beams simply add up to $\sqrt{2}$ times the radiation force of each single beam. We moreover neglect the radiation force of the beams propagating in the same direction as the atoms, since their detuning adds up to the negative Doppler shift, tuning them out of resonance.

[9] In reality, the capture velocity is expected to be close to 7 m/s, as a considerable radiation pressure is provided also out of resonance owing to power broadening, down to a detuning of $-45\Gamma_{\mathrm{green}}$.

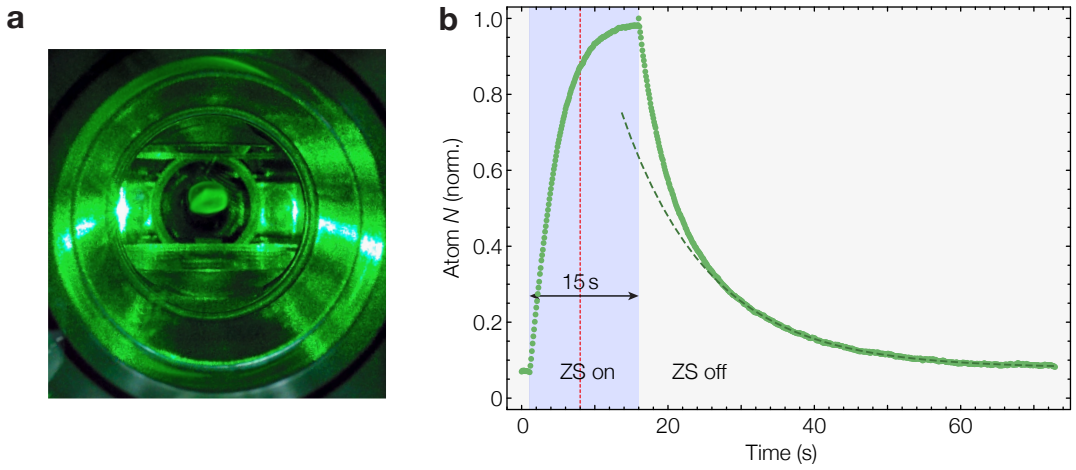

Figure 2.6 – (a) A photo of the bosonic MOT during the loading in a field gradient $A = 1.3\,\mathrm{G/cm}$ with $|\Delta_{\mathrm{MOT}}| = 35\,\Gamma_{\mathrm{green}}$. A dark region is clearly visible in the centre. (b) Loading and discharge of the bosonic MOT with $A = 2.0\,\mathrm{G/cm}$, $|\Delta_{\mathrm{MOT}}| = 35\,\Gamma_{\mathrm{green}}$ and $I_{\mathrm{MOT}} \simeq 400\,I_{\mathrm{sat}}$. After 15 s of loading, the atom number in the MOT reaches its steady-state value. A loading time of 8 s is used for the experiments reported in this thesis, marked by a red line. After turning off the ZS, the lifetime of the MOT is measured. Even at a low gradient, density-induced atom losses in addition to the exponential background losses are visible. The dashed line is an exponential fit for $t > 25\,\mathrm{s}$ to the detected fluorescence, yielding a lifetime of 12 s (at the date of this measurement, the vacuum background was $P \simeq 5 \times 10^{-10}$ mbar).

and the MOT characteristic hollow ellipsoid shape is visible by eye in ^{174}Yb (see Fig. 2.6(a)). The atom fluorescence detected during the loading and the successive discharge of the the ^{174}Yb MOT is shown in Fig. 2.6(b). A loading time of 8 s is used in typical experimental sequences, which allows to trap more than 70% of the steady-state MOT atom number[10] $N \approx 1 \times 10^9$, with a loading rate $\Phi_{\mathrm{MOT}} \approx 1 \times 10^8$ atoms/s.

Loading of the fermionic MOT

In ^{173}Yb, although the Zeeman splitting of the MOT transition is dominated by the Zeeman shift of the $^3\mathrm{P}_1$ state, a nuclear substructure is present in the ground state (see Eq. (2.7) and Fig. 2.5(b)). Due to the lower substructure, a fundamentally different operation of the MOT is realised for ^{173}Yb. First of all, the orientation of the field gradient in the MOT needs to match the orientation of the gradient in the ZS: atoms exit the σ^- slower in the $m_F = -5/2$ state and, in order to be decelerated and captured, they must absorb σ^--polarised light from the MOT beams countering their motion, resonant with the stretched transition [289]. Another consequence of the $m_{F'}$-dependent Zeeman shift is that the strength and even the orientation of the radiation forces in the MOT become m_F-dependent. Let us briefly explain why this is the case (a complete discussion can be found e.g. in Ref. [276]). With all lower m_F states populated, the light of one MOT beam at a given B-field strength can be seen by the atoms as resonant, red-detuned, or blue-detuned depending on the

[10] The loaded atom number is calibrated via MOT fluorescence detection with a small NA and the given value N should therefore be taken only as a rough estimate.

value of m_F and on the light polarisation (see Fig. 2.5(b)). For a given light detuning, the different m_F states are therefore tuned to resonance by the Zeeman shift at different locations. Along the x direction, for $B = Ax$, each state with $m_F > 0$ ($m_F < 0$) is tuned to resonance with the σ^+-polarised and σ^--polarised MOT beams at two locations $x > 0$ ($x < 0$). The σ^+-polarised (σ^--polarised) beam coming from $x < 0$ ($x > 0$) pushes the atoms towards $x = 0$ only when they are located at $x < 0$ ($x > 0$), and pushes them otherwise outwards[11]. A stable steady-state operation of the MOT is nevertheless guaranteed by the favourable transition strength difference between the $\sigma^\pm$-polarised transitions (see Appendix A). An average restoring force is generated in this way over many absorption processes, yet the force in the fermionic MOT is reduced compared to the bosonic MOT. Furthermore, as every m_F state is resonant at a different distance from the MOT centre, the characteristic geometric shell-like structure of the ^{174}Yb MOT is not observed in the ^{173}Yb MOT.

The optimal loading performance of the ^{173}Yb MOT is obtained by displacing the quadrupole field centre and the beam centres by ≈ 4 mm above the ZS beam. A maximum atom number $N \approx 3 \times 10^8$ can be loaded in $t \simeq 20\,s$, corresponding to about a third of the bosonic MOT steady-state atom number. The MOT alignment and loading parameters are however optimised to achieve the largest atom number after a time of 8 s, and further fine-tuned to yield the highest transfer efficiency to the dipole trap.

Compression and cooling of the MOT

After the loading is completed, the ZS light and all magnetic coils except the MOT quadrupole coils are turned off. At the same time, the current in the MOT coils is changed to compensate for the switch-off of the ZS compensation coils and ensure a sufficient field gradient. The MOT is held in this configuration for 200 ms in order for all parasitic fields to have completely decayed, before the compression phase is started so as to complete the transfer into the dipole trap.

The compression phase is aimed at greatly increasing the density of the MOT while drastically reducing its temperature, in order to achieve the highest possible transfer efficiency to the optical dipole trap. The field gradient, the light detuning and the light power are varied in 60 ms to reach their respective final values $A = 9.5$ G/cm, $|\Delta_{\mathrm{MOT}}| \simeq 7\,\Gamma_{\mathrm{green}}$ and $I_{\mathrm{MOT}} \simeq 0.1 I_{\mathrm{sat}}$. Simultaneously, the dipole trap beams are turned on, so that atoms are cooled into and inside the trap. The MOT light is eventually turned off after 100 ms of additional cooling in these conditions. We note here that the MOT parameters in this last cooling stage are optimised exclusively to maximise the number of atoms loaded into the dipole trap after the MOT has been turned off. At the end of the cooling stage, our typical ^{173}Yb samples contain $N \simeq 5 \times 10^7$ atoms at a temperature of $T \simeq 20\,\mu$K, measured by time-of-flight absorption imaging. The final temperatures are slightly higher in ^{174}Yb samples with $T \simeq 30\,\mu$K, which matches the expected Doppler temperature at a detuning $|\Delta_{\mathrm{MOT}}| \simeq 7\,\Gamma_{\mathrm{green}}$, consistently with the absence of Sisyphus cooling in the bosonic isotopes [266]. The sample size is narrower in the vertical direction, with an aspect ratio around

[11] In conventional MOTs, like the bosonic ytterbium MOT or alkali atom MOTs, only the σ^+-polarised (σ^--polarised) beam is tuned to resonance by the field gradient for $x < 0$ ($x > 0$).

3:1, due to the MOT quadrupole field anisotropy as well as to the effect of gravity, which becomes important when the light intensity is drastically decreased at the end of the cooling. A compressed MOT volume on the order of $5 \times 10^{-4}\,\mathrm{cm}^3$ leads to a mean density $n \approx 10^{11}\,\mathrm{atoms/cm}^3$. The final attainable temperature in the high-density regime is very likely limited by heating due to the reabsorption of photons and by inelastic light-induced collisions [131]. Lower temperatures, down to $T \simeq 15\,\mu\mathrm{K}$, can indeed be reached using smaller samples and a smaller detuning, resulting however in an overall reduction of the atom number loaded into the dipole trap.

In order to transfer the atoms from the compressed MOT into the dipole trap, the spatial overlap in the vertical direction must be maximised. For this purpose, the vertical position of the compressed MOT is adjusted to exactly match the position of the dipole trap beam via an additional homogenous B-field. This vertical offset field can be finely regulated by changing the current in a thin coil, wound concentrically to one of the MOT coils.

2.2.3 Optical crossed dipole trap

Due to the unfeasibility of magnetic trapping of ytterbium, the optical dipole trap has to be directly loaded from the MOT. It is preferable in this condition to use a crossed dipole trap, consisting of one very intense horizontal beam and a weaker vertical beam intersecting at the position of the potential minimum. The main contribution to the trapping potential is given by the horizontal beam, which supports the atoms against gravity and largely dominates the trap depth. The vertical beam increases the confinement along the horizontal beam propagation axis, which would be otherwise too weak to sustain the evaporative cooling to degeneracy.

In our setup, the crossed optical dipole trap (ODT) is formed by two laser beams at a wavelength $\lambda_{\mathrm{DT}} = 1064\,\mathrm{nm}$. The first beam (HDT beam) is aligned horizontally and travels at a small angle from one of the MOT beams. The second beam is instead nearly vertically aligned, with an angle of approximately 20° to the z-axis (see Fig. 3.6). The geometric configuration of our crossed ODT is shown in Fig. 2.7. The HDT beam has an elliptic profile, and it is focused onto the atoms with a horizontal waist size $w_{\mathrm{HDT\,h}} = 17\,\mu\mathrm{m}$ and a vertical waist size $w_{\mathrm{HDT\,v}} = 90\,\mu\mathrm{m}$. Differently, the VDT has a circular profile, with a waist size of $w_{\mathrm{VDT}} = 190\,\mu\mathrm{m}$. Both ODT beams are turned on at the beginning of the MOT compression stage, and atoms are therefore continuously loaded into the trap, as soon as a good spatial overlap is attained and their temperature drops below the trap depth threshold. With a HDT beam power $P_{\mathrm{HDT}} \simeq 11\,\mathrm{W}$ and VDT beam power of $P_{\mathrm{VDT}} \simeq 1\,\mathrm{W}$, we obtain an initial trap depth $V_0 \simeq 170\,\mu\mathrm{K}$. We achieve a transfer efficiency from the MOT of approximately 20%, corresponding to $N \simeq 10^7$ atoms remaining in the ODT after 1 s of hold time at the initial trap depth.

Before describing the evaporation sequence, we briefly explain the main reasons for the use of a horizontal elliptic beam instead of a circular one, especially since the ODT is directly loaded from the MOT. First of all, as the shape of the MOT is anisotropic, a good spatial overlap is obtained by using a beam with a similar aspect ratio. Moreover, during the evaporation atoms leave the trap predominantly along the vertical direction assisted

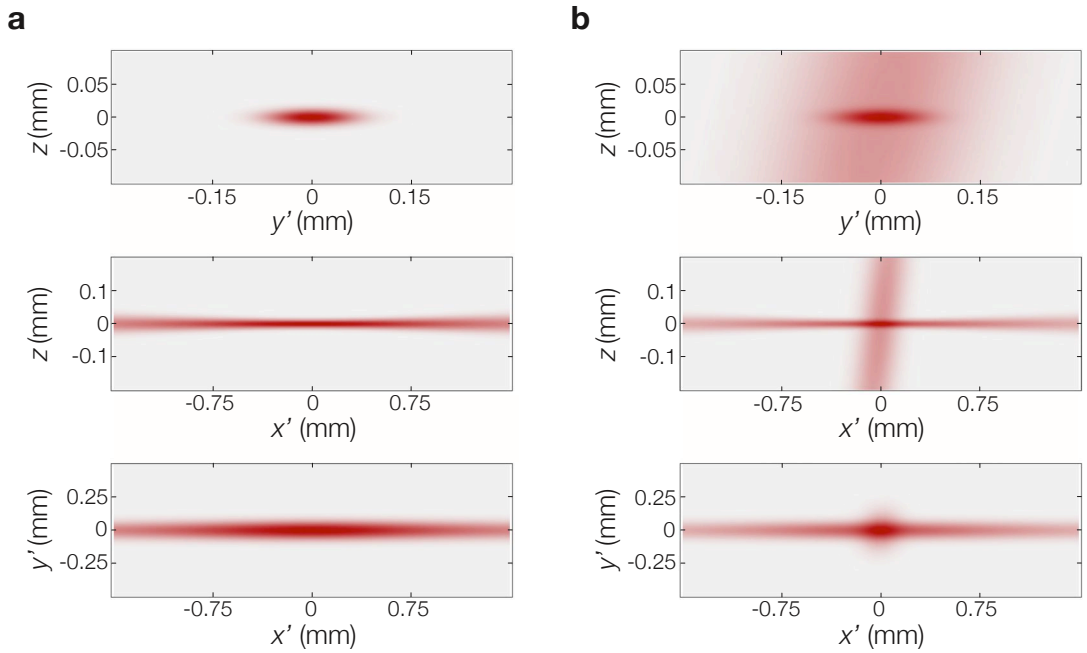

Figure 2.7 – Dipole trap potential profiles along the three spatial directions with $P_{\mathrm{HDT}} = 0.5\,\mathrm{W}$ and $P_{\mathrm{VDT}} = 7\,\mathrm{W}$ (gravity is not included). Here, x' and y' indicate respectively the axis of propagation of the HDT beam and the horizontal axis orthogonal to x'. (a) Trap potential generated by the HDT beam alone. (b) Trap potential generated by both beams crossed at the origin.

by gravity, and a tight vertical confinement is beneficial. Once an atom leaves a collision with a large kinetic energy, a high vertical trap frequency helps expelling it as quickly as possible, before it can release its energy again to the rest of the gas via further collisions. Therefore, the vertical trap frequency should ideally be large compared to the gas mean collision rate.

On the other hand, a very tight vertical confinement produces an increase of the sample density, and should be counterbalanced by a looser transverse confinement to avoid three-body losses. Since the elastic collision rate scales as $\propto n\,a^2$ with the density n, while the three-body loss rate scales as $\propto n^2\,a^4$ [131, 134], the optimal initial density depends on the scattering properties of the atoms. With our large initial atom numbers $N \sim 10^7$ and the rather strong interactions of ^{173}Yb (see Table 2.5), it is desirable to start with a large trap volume and a moderate mean trap frequency [87, 276]. The density (and therefore the collision rate) can eventually be enhanced during the evaporation under the influence of the VDT beam, in order to enhance the evaporation. For a given power and trap depth, an elliptic beam represents the best trade-off between a large initial trap volume and sufficiently high trap frequencies.

Evaporation in the crossed dipole trap

With our trap geometry and the beam powers reported above, we obtain the trap frequencies $\omega_v = 2\pi \cdot 1.67\,\mathrm{kHz}$ in the vertical, $\omega_t = 2\pi \cdot 315\,\mathrm{Hz}$ in the transversal (horizontal) and $\omega_a = 2\pi \cdot 19\,\mathrm{Hz}$ in the axial (horizontal) direction, corresponding to a mean trap

frequency $\bar{\omega} = (\omega_v\,\omega_t\,\omega_a)^{1/3} = 2\pi \cdot 215\,\mathrm{Hz}$. The naming refers to the HDT beam directions. The evaporation starts with a hold time of 1 s in the ODT after the MOT has been turned off, during which the density in the central region increases considerably due to damping of the in-trap collective motion. Subsequently, the power of the HDT beam is exponentially decreased in approximately 14 s to a value of $P_{\mathrm{HDT}} \simeq 350\,\mathrm{mW}$, which can be adjusted to vary the final atom number. At the same time, the power in the VDT beam is increased up to $P_{\mathrm{VDT}} \simeq 3\,\mathrm{W}$ to partially compensate the rapid decrease in the axial trap frequency and maintain an adequate collision rate. Owing to the effect of the VDT beam, the horizontal trapping geometry becomes more and more isotropic as long as the evaporation progresses. During the last 5 s of evaporation, the VDT beam power is ramped to reach its final value, producing the desired final axial trap frequency ω_a. The redistribution of power between the two dipole beams during the evaporation is achieved by means of a rotating motorised wave-plate, which varies the power splitting between the two beams at the laser source. A smaller VDT beam would allow to speed the evaporation by increasing the collision rate, but would reduce the trap volume and the trappable atom number N. We recently reduced the VDT beam size to $w_{\mathrm{VDT}} = 130\,\mu\mathrm{m}$ with the goal of producing smaller but colder degenerate samples, exploiting the considerably larger attainable trap frequencies, especially in the last part of the evaporation. Typical trap frequencies after the evaporation are $(\omega_a, \omega_t, \omega_v) = 2\pi \cdot (8(1), 27(1), 220(5))\,\mathrm{Hz}$, obtained with $P_{\mathrm{HDT}} \simeq 0.5\,\mathrm{W}$ and $P_{\mathrm{VDT}} \simeq 1\,\mathrm{W}$, or $(\omega_a, \omega_t, \omega_v) = 2\pi \cdot (10(2), 41(3), 375(10))\,\mathrm{Hz}$, obtained with $P_{\mathrm{HDT}} \simeq 1\,\mathrm{W}$ and $P_{\mathrm{VDT}} \simeq 1.5\,\mathrm{W}$ (see Fig. 2.7 and measurement in Fig. 2.8). The final gas can be made almost completely isotropic by using a final $P_{\mathrm{VDT}} \simeq 7\,\mathrm{W}$, which yields an axial frequency $\omega_a \simeq 23\,\mathrm{Hz}$. Such a pancake-shaped trap geometry is optimal to load only a small number of sites in the vertical optical lattice (see below).

2.2.4 Degenerate gases of ytterbium

By means of the evaporation sequence described above, quantum degenerate gases of both ^{174}Yb and ^{173}Yb can be produced. These two isotopes are the most practical for the production of Bose-Einstein condensates and degenerate Fermi gases respectively, owing to their large natural abundances and their large positive ground state scattering lengths (see Table 2.5). The atom number N in the final degenerate gas can be tuned by slightly changing the final HDT beam power and by decreasing the initial HDT beam power, in order to initially load a smaller sample into the ODT. In the following, a brief summary of typical parameters of our Bose-Einstein condensates (BEC) of ^{174}Yb and degenerate Fermi gases (DFG) of ^{173}Yb are presented. To conclude this Chapter, we illustrate the loading of the degenerate gases into a three-dimensional magic optical lattice.

Bose-Einstein condensation

The first condensation of ^{174}Yb in our experimental setup has been achieved with a different trap geometry from the one described above. The trap geometry has been subsequently adapted to the production of Fermi gases and to the use of the VDT beam as an additional variable confinement applied while atoms are trapped into the optical lattice. For this

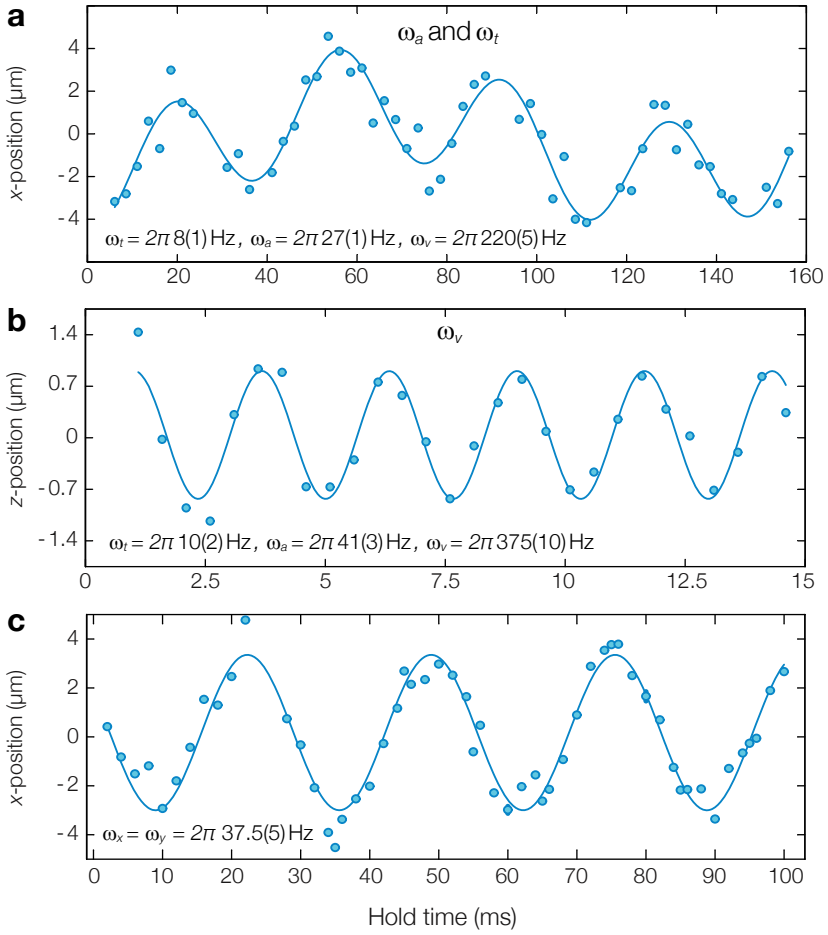

Figure 2.8 – Confinement frequency measurements. The sloshing motion of a Fermi gas in the trap is excited by a sudden small trap displacement. The centre-of-mass position of the cloud after a short TOF is recorded over time and the fitted oscillation frequencies are given in the corner. (a)-(b) Crossed dipole trap frequencies with (a) $P_{\mathrm{HDT}} \simeq 0.5$ W and $P_{\mathrm{VDT}} \simeq 1$ W, and (b) $P_{\mathrm{HDT}} \simeq 1$ W and $P_{\mathrm{VDT}} \simeq 1.5$ W. (c) Confinement frequencies in the vertical optical lattice with a depth $V_z = 50\,E_r$. The measured position along the x-axis in (a) and (c) is affected by both the axial and the transverse motion (see optical setup in Fig. 3.6).

reason, the ODT volume and the evaporation ramp are not optimised for the production of BECs of ^{174}Yb and by adjusting it larger BECs could be attainable.

The last stage of the transition from a thermal gas of ^{174}Yb to a nearly pure BEC is displayed in Fig. 2.9. The condensate fraction in the gas is estimated by a two-dimensional combined Gaussian-parabolic fit. A final atom number just below $N \simeq 2 \times 10^5$ in the condensate is reached, clearly exhibiting the characteristic parabolic Thomas-Fermi density distribution and anisotropic expansion behaviour. The ODT trap frequencies at the moment of the release are as in Fig. 2.8(a), implying a much tighter confinement in the vertical direction than in the horizontal ones. This leads to the observed broader momentum distribution along the vertical axis. The observed aspect ratio is further explained by the presence of strong interactions with $a \simeq 105\,a_0$ during the expansion, which broaden the cloud especially along the x-direction, i.e. the one characterised by the narrow momentum distribution.

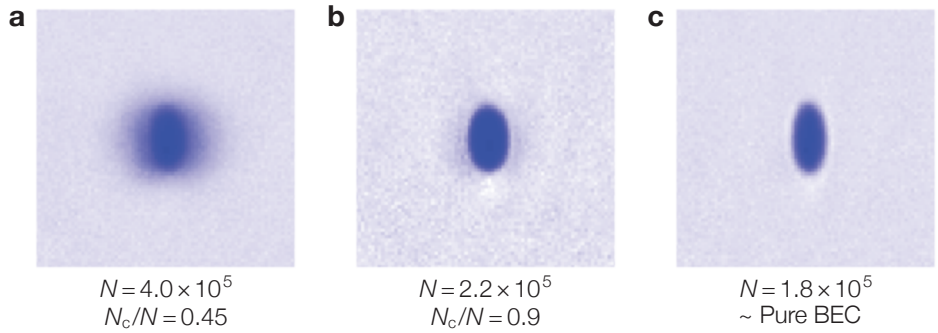

Figure 2.9 – Bose-Einstein condensation of ^{174}Yb. (a)-(c) Time-of-flight absorption images for different values of the final HDT beam power when the gas is released. (c) The condensate fraction N_c/N reaches nearly unity below $N \simeq 2 \times 10^5$ atoms, with no thermal component visible.

Degenerate Fermi gases

Efficient evaporative cooling to degeneracy of individual fermionic atomic species is only possible by using a mixture of internal states (without resourcing to sympathetic cooling with another isotope or species). In this respect, ^{173}Yb is well suited for direct evaporation in a spin mixture, with a total of six nuclear spin states and a large scattering length $a \simeq 200\, a_0$.

The final attainable temperature is nevertheless limited by the so-called Pauli blocking of evaporation. At temperatures well below degeneracy $T \lesssim 0.5 T_F$, with T_F being the Fermi temperature of the gas (see Appendix B for an expression of T_F and more details on Fermi gases), the occupation of trap states becomes dense below the Fermi energy. As atoms can only scatter into unoccupied final states due to Pauli exclusion, the scattering rate is gradually reduced when the gas temperature decreases below T_F. Evaporative cooling is based on the continuous thermalisation of the gas while the trap depth is lowered, and becomes very inefficient below Fermi degeneracy. In order to compensate the lack of thermalisation in the last stage of the evaporation to Fermi degeneracy, the trap depth reduction needs to be slowed down. However, technical heating effects, background losses or three-body losses[12] eventually limit the minimum evaporation speed. Due to Pauli blocking, when the regime of insufficient thermalisation is reached, one observes a characteristic halt in the cooling, and the reduced temperature T/T_F remains constant even if the trap depth and the atom number are further reduced. A larger number of spin states is beneficial in this respect, providing a higher collision rate due to the larger number of available scattering channels.

Time-of-flight (TOF) absorption images (see Section 4.1.1 for a description of the imaging process) of ^{173}Yb gases below Fermi degeneracy are displayed in Fig. 2.10, together with Thomas-Fermi fits to their momentum distribution. The momentum distribution of an ideal Fermi gas in a harmonic trap is isotropic, independent of the trap geometry, and this is reflected in the free expansion [19]: for long expansion times $t \gg 1/\bar{\omega}$ the cloud exhibits an aspect ratio approaching unity. This is however true only in the collisionless

[12] Three-body loss processes in a Fermi gas are possible only if a number of spin components larger than 2 is used, due to Pauli exclusion.

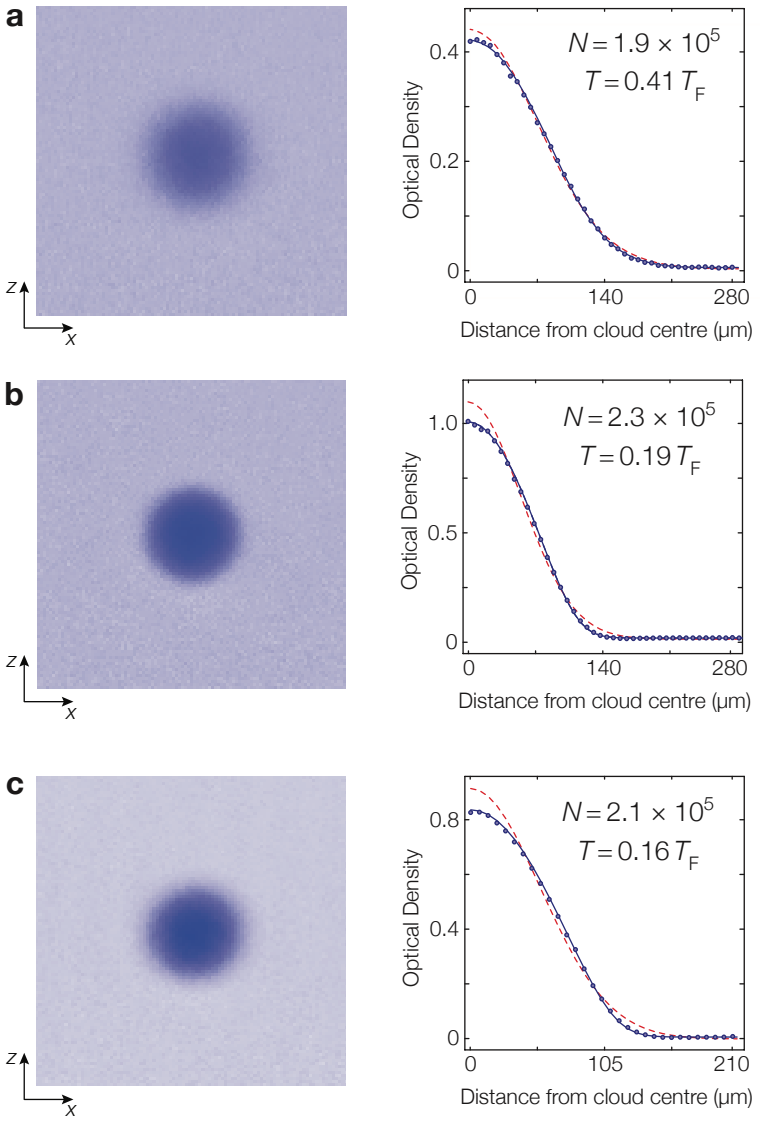

Figure 2.10 – Degenerate Fermi gases of ^{173}Yb with six spin states. (a)-(c) The momentum distribution is detected after a 30 ms time of flight by absorption imaging. The azimuthally integrated momentum distribution is also shown, together with the result of two-dimensional Thomas-Fermi and Gaussian fits to the data. N denotes the total atom number in the cloud. For the lowest temperatures $T < 0.2\ T_F$ (b) and (c), the deviation of the data from the Gaussian profile is clearly noticeable.

expansion regime, whereas with strong interactions and a collision rate $\Omega_{\text{coll}} > \bar{\omega}$ the expansion is anisotropic, due to kinetic energy redistribution between the different directions of propagation [19]. With our final trap geometry $\bar{\omega} \gtrsim 2\pi\cdot 35\,\text{Hz}$ and typical densities $n \approx 5 \times 10^{12}\,\text{atoms/cm}^3$, the expansion is expected to be approximately collisionless, with $\Omega_{\text{coll}} = n\,\gamma_{\text{el}} \approx 2\pi \cdot 6\,\text{Hz} < \bar{\omega}$, calculated using Eq. (1.22). For low final VDT power however, the axial trap frequency ω_a is smaller than the collision rate and slight expansion anisotropies are observed.

In order to determine T/T_F from the detected momentum distributions, a two-dimensional fit to the column density of the gas with a Thomas-Fermi density function is performed and the gas fugacity is extracted (see Appendix B). Large gases with up

to $N \simeq 2 \times 10^5$ atoms at a minimum of $T/T_F \simeq 0.16$ can be attained by evaporating a six-spin mixture, whereas slightly higher temperatures are obtained if optical pumping is performed early in the evaporation to only populate two of the spin states (for spin-state preparation via optical pumping see Section 4.2).

Loading into an optical lattice

All experiments presented in the last Chapters of this thesis were performed with fermionic atomic samples trapped in an optical lattice tuned to the magic wavelength $\lambda_m = 759.35\,\text{nm}$ between the $^1S_0$ and the $^3P_0$ states (see Section 5.1.1). A three-dimensional cubic lattice is generated by retro-reflecting three laser beams. The vertical lattice beam is aligned to the z axis, whereas the two horizontal lattice beams are aligned at ±45° from the atomic beam propagation axis. For consistency with the labelling of the ODT axes, we will label here the two horizontal lattice axes as $x' = (x-y)/\sqrt{2}$ and $y' = (x+y)/\sqrt{2}$. A clear illustration of the beam orientation around the main vacuum chamber is given in Fig. 3.6. The horizontal lattice beams have an elliptic intensity profile with a horizontal waist size $w_{\text{L1 h}} = w_{\text{L2 h}} = 190\,\mu\text{m}$ and a vertical waist size $w_{\text{L1 v}} = w_{\text{L2 v}} = 40\,\mu\text{m}$, while the vertical lattice beam has a circular profile with a waist size of $w_{\text{L3}} = 130\,\mu\text{m}$. In order to avoid unwanted interference in the intersection region, the horizontal lattice beams are frequency detuned from each other by 160 MHz, whereas the vertical lattice beam is detuned by 190 MHz and 30 MHz from the two horizontal beams.

The atoms are usually first loaded into the vertical lattice with a depth $V_z \sim 50\,E_r$, which is done by smoothly ramping up the power of the vertical lattice beam in 200 ms and at the same time decreasing the VDT and the HDT beam powers to zero. This procedure minimises the extension of the gas in the vertical direction, by reducing the number of occupied vertical lattice sites compared to a direct three-dimensional lattice loading. Details about the density distribution after the loading to the vertical lattice can be found in Appendix B. The delay time between the ramp-up of the vertical lattice beam and the ramp-down of the HDT beam is adjusted to minimise the cloud motion and the heating during the loading procedure. The heating produced by a not fully adiabatic lattice transfer can be characterised by reloading the atoms into the ODT and performing a TOF imaging of their momentum distribution. After optimising the beam alignment, the ramp durations and the delay times, we attain a minimum increase in temperature $T \approx 0.1 T_F$ after the double transfer procedure with ^{173}Yb. The main source of such heating is to date still unclear, but the final temperature does not depend on the hold time inside the lattice and we can therefore exclude technical heating from the lattice laser beams.

Subsequently, the two horizontal lattices are ramped up in 200 ms and the desired final lattice depth configuration is reached. The depth of the lattice potential along each direction can be independently calibrated by the standard parametric heating technique. The lattice beam intensity is modulated and the frequency of the parametric excitation to second excited Bloch band is determined by detecting the associated heating through TOF imaging directly out of the lattice. By comparing the measured resonance frequency to the calculated band structure one can deduce the actual lattice depth. Additionally, the

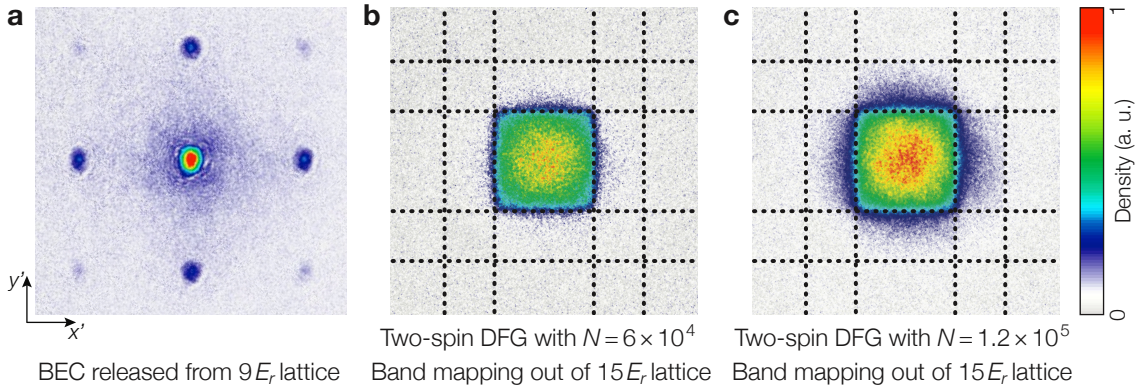

Figure 2.11 – (a) Density distribution after 20 ms TOF of a ^{174}Yb condensate, released from a 3D lattice potential with a depth $V_h = 9\,E_r$ along the horizontal directions. The central peak of atoms with momentum $q = 0$ and the higher order lattice peaks are clearly visible. (b)-(c) Two-spin Fermi gases of ^{173}Yb with different total atom number, released from a 3D lattice potential using a band mapping technique. The lattice depth before the release is $V_h = 15\,E_r$ along the horizontal directions. For $N = 6 \times 10^4$ atoms (b) only very small higher band occupations are visible, whereas for a higher atom number (c) more than 10% of the atoms occupy excited bands.

confinement given by the Gaussian intensity profile of the red-detuned lattice beams is characterised by means of centre-of-mass oscillations, as in the case of the dipole trap (see Fig. 2.8(c)). For vertical lattice depths $V_z = 35\,E_r$, $42\,E_r$ and $50\,E_r$, isotropic horizontal confinements with respectively $\omega_x = \omega_y = 2\pi \cdot 33.5(10)$ Hz, $2\pi \cdot 35.5(10)$ Hz and $2\pi \cdot 37.5(5)$ Hz are measured. The geometry of the lattice beams is such that the confinement in the horizontal plane is entirely dominated by the vertical lattice potential depth, owing to the smaller waist size of the vertical lattice beam in the horizontal direction and to the small vertical waist size $w_{\mathrm{L1\,v}}$, $w_{\mathrm{L2\,v}}$ of the horizontal lattice beams. As a result of their elliptic profile, the horizontal beams require a much lower power to generate a certain potential depth, compared to the vertical beam, and do not contribute substantially to the confinement in typical configurations with depths $V_{x'} \sim V_{y'} \leq V_z$.

Absorption images collected after a TOF out of the three-dimensional lattice are shown in Fig. 2.11, with an abrupt release of a ^{174}Yb condensate in panel (a) and a band mapping release of ^{173}Yb Fermi gases in panels (b)-(c). The BEC exhibits the characteristic diffraction pattern owing to phase coherence in the horizontal lattice with depth $V_h = 9\,E_r$, with diffraction peaks spaced by $2\hbar k$. For deeper lattices the superfluid to Mott transition can be observed, marked by the disappearance of the off-site coherence of the BEC [22]. Conversely, as Fermi gases do not exhibit any off-site phase coherence at any lattice depth, a band mapping technique is used to inspect the state of the gas in the lattice. With two populated spin states and total atom numbers $N \gtrsim 6 \times 10^4$, atoms start occupying higher bands (see Section 4.1.1 for a description of the band mapping technique).

We will now briefly address the reason why higher-band occupation are indeed expected already at low atom numbers for a Fermi gas of heavy atoms such as ytterbium. Let us initially consider the loading of a free-space Fermi gas into a homogenous lattice potential. When the loading procedure starts, the free-particle parabolic dispersion relation starts developing energy gaps. In one dimension, the first band gap immediately

opens up around an energy equal to E_r. In two and three dimensions, energy gaps open up only at finite depth and the energy along the edges of the first Brillouin zone is no longer constant, yet the situation is qualitatively similar: the free-momentum states with an energy below E_r occupy a central circular (2D) or spherical (3D) region of the first Brillouin zone with diameter $2\hbar k$, filling a large part of its volume.

As the lattice depth is gradually increased, the state energies adiabatically transform and cluster into energy bands. All free-momentum states with an energy below E_r eventually finish up in the first Bloch band, whereas states with a higher energy transform into higher band states. The scenario is approximately equivalent when the lattice potential is combined with an underlying harmonic confinement. While the lattice depth is increased, the reduction of the bandwidths gradually localises the higher-energy eigenstates in each band at the edges of the cloud [92, 291, 292] (see also Appendix B). The states with an initial energy above E_r transform into lowest-band states localised at the wings of the cloud only for a close to perfect adiabatic transfer. In practice, a large portion of states with an energy above E_r finish up occupying higher-band states located in the centre of the harmonic potential, which have an energy as large as the lowest-band states located at the wings [291]. Therefore, in order not to generate any higher bands population during the loading within a finite loading time, the initial gas Fermi energy E_F must not exceed $E_r \simeq h \cdot 2\,\mathrm{kHz}$. Moreover, the finite gas temperature T generates finite state occupations even above E_F, with an energy width $\sim k_B T$. The onset of higher band occupations is thus expected at $E_F + k_B T \simeq E_r$. With our mean ODT frequency $\bar{\omega} \simeq 2\pi \cdot 40\,\mathrm{Hz}$ at the moment of the lattice transfer and a temperature $T = 0.2\,T_F$, $E_F + k_B T = E_r$ for $N_s \simeq 1.5 \times 10^4$ atoms per spin component.

The onset of higher-band occupations is therefore expected at a total atom number $N = 1.5 \times 10^4$ or $N = 3 \times 10^4$ for a spin-polarised and a two-spin Fermi gas, respectively. While the observations are in fair agreement with this estimate in the spin-polarised case (see Fig. 5.7), for two-spin gases higher bands are nearly unpopulated below approximately 5×10^4 atoms (see Fig. 2.11(b)). This discrepancy can be attributed to the role of interactions during the loading, which reduce double occupancies in the trap centre as long as the interaction energy U is larger than the thermal energy in the lattice[13] [31, 167]. More accurate theoretical estimates would require a full numerical treatment of the loading procedure in the Fermi-Hubbard model. Moreover, the 200 ms lattice ramp time allows a portion of the ODT states above E_r to transform into lowest-band states during the first stage of the loading. We conclude this discussion by noting that, as the recoil energy scales like $E_r \propto 1/M$, very low trapping frequencies are desirable for heavy species such as ytterbium[14]. In this way the Fermi energy $E_F \propto \bar{\omega} N^{1/3}$ can be kept well below E_r for large atom numbers. Optical lattices with a short periodicity e.g. $\lambda = 532\,\mathrm{nm}$ are a possible alternative to increase E_r, however not in the presence of specific wavelength constraints related to the simultaneous trapping of the metastable state.

[13] The interaction between atoms in the lowest band equals $U \simeq h \cdot 1\,\mathrm{kHz}$ at $V_{x'} = V_{y'} = 4\,E_r$ and $V_z = 50\,E_r$. The interaction between atoms in different bands is lower, yet on the same order of magnitude.

[14] The trapping frequencies scale with $\omega \propto 1/\sqrt{M}$ and a heavy mass is therefore convenient to generate low trapping frequencies with a given trap depth.

CHAPTER 3

Experimental Setup

Since ytterbium atomic gases were initially brought to quantum degeneracy a decade ago [52], highly diverse machines have been assembled in several laboratories. Our experimental sequence is based on three stages of slowing and cooling, and was described in the previous Chapter. In this Chapter we will present the details of the experimental apparatus used to produce and study degenerate gases of ytterbium, which has been originally developed in the framework of this thesis. First, the vacuum and magnetic coil setups are described, followed by details about the optical setup of all laser beams sent through the main vacuum chamber. Subsequently, the laser system used to generate the necessary light beams at various wavelengths is delineated. In particular, special attention is devoted in the final Section to the description of the laser system for addressing the $^1S_0 \rightarrow {}^3P_0$ clock transition.

3.1 Vacuum system and magnetic field coils

The complete vacuum system is illustrated through the model given in Fig. 3.1. The mechanical design of the system itself, its supporting structure and the laser routing assemblies are optimised to be as stable as possible, while maintaining a sufficient degree of flexibility to align the different sections with each other and to avoid mechanical strains. The main vacuum chamber represent the central part of the experimental setup: atoms are cooled, trapped and detected inside the same octagonal steel chamber. For this reason, nearly every laser beam in our setup is pointed and focused to the centre of that chamber. Three optical tables are positioned at a short distance from one another in the laboratory: the vacuum vessel is supported by the central table (termed from now on the experiment table), while all laser systems are located on the two tables on its sides. Each optical table is isolated inside a temperature-stabilised enclosure (~ 0.1°C stability), also providing a constant downward air flow to maintain the surfaces free of dust.

The vacuum system is divided into three sections, characterised by different vacuum pressures: (i) the oven section, where the pressure reaches $P_1 \simeq 5 \times 10^{-9}$ mbar when the atomic source is set to the operation temperature, (ii) the second pumping chamber section with an intermediate UHV pressure $P_2 \simeq 3 \times 10^{-10}$ mbar and (iii) the UHV main chamber section with a pressure $P_3 \simeq 1 \times 10^{-11}$ mbar. The pressure in section (i) is dominated by the oven emission; a differential pumping tube of 11 cm length and 8 mm diameter is used to almost fully decouple the pressure of section (ii) from section (i). The three sec-

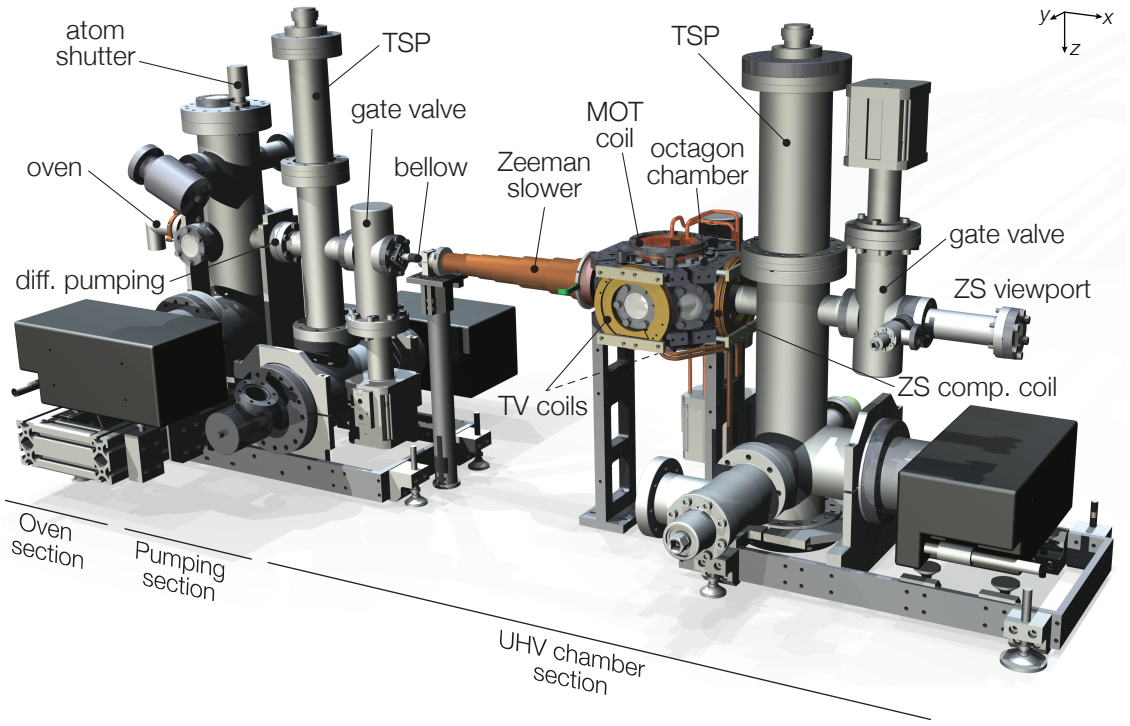

Figure 3.1 – CAD model of the experiment vacuum system. The entire vacuum vessel and its support structure are displayed, while all protective enclosures and optical assemblies are omitted. The three principal vacuum sections are labeled. The main octagonal UHV chamber provides good optical access by means of two large CF100 silica viewports on top and bottom and six CF40 silica viewports on the sides. The magneto-optical trap (MOT) coils are aligned along the z-axis, while the transverse (TV) coils are aligned along the y-axis. The Zeeman slower (ZS) residual field at the centre of the main chamber is canceled by the ZS compensation coil.

tions are equipped with independent 65 l/s ion pumps[1]; two titanium sublimation pumps[2] (TSP) are additionally installed in the UHV sections (ii) and (iii). A first pneumatic gate valve[3] separates sections (i) and (ii) from section (iii), and a second pneumatic gate valve separates the octagon chamber from the Zeeman slower viewport subsection. Such valves can be used to independently vent the single sections in order to perform maintenance operations, such as replenishing the atomic source reservoir, and can be electronically controlled in order to automatically close in case a vacuum leak is detected.

3.1.1 Atomic source and oven section

The vapour pressure of ytterbium is rather low, similarly to other AEL species, and high temperatures are required to provide the necessary vapour density for efficient operation of the Zeeman slower and the MOT. Our main oven is composed by a steel reservoir and a collimation section, as displayed in Fig. 3.2. The reservoir was filled with approximately

[1] Agilent Varian VacIon Plus 75 StarCell Ion Pump.
[2] Agilent Varian TSP Cartridge
[3] VAT all-metal CF40 gate valve Series 48

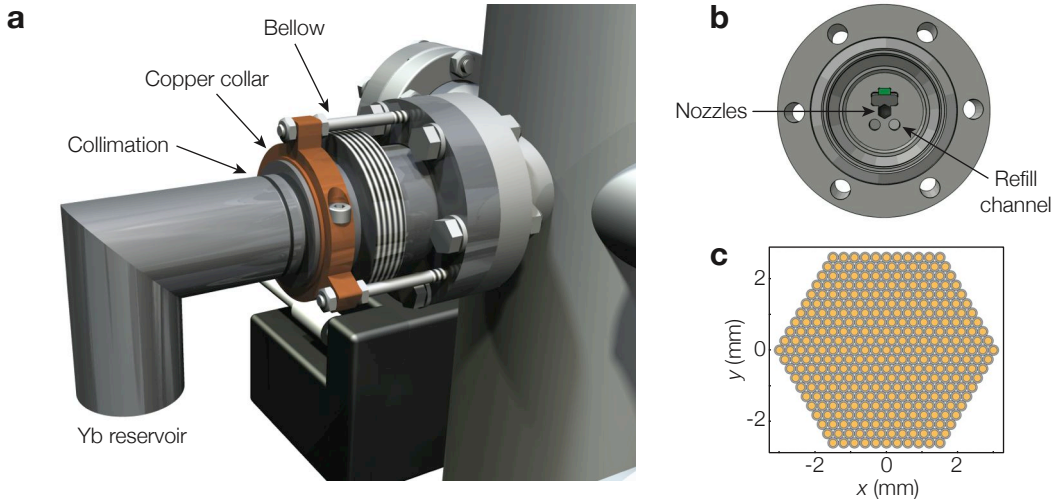

Figure 3.2 – Ytterbium atomic oven section. (a) A model of the oven section of the experiment. While the ytterbium reservoir flange is heated, a copper collar provides cooling to avoid large temperatures at the CF40 flange connection. The copper collar is placed just after the collimation tube array. Three alignment screws are used for pointing the atomic beam along the Zeeman slower axis, tilting the oven section around a non-rigid bellow connection. (b) A section of the collimation setup. Two screw holes allow for the filling of the reservoir and are during in-vacuum operation are plugged by two screws. (c) An illustration of the hexagonal array of collimation channels.

50 g of 99.99% pure ytterbium metal flakes and small pieces[4], which should suffice for several years of operation. The collimation section consists of an array of approximately 300 cylindrical channels with a length of 10 mm and a diameter of 200 μm, clamped with a hexagonal arrangement (see Fig. 3.2(c)). Employing such an array of channels, instead of a conventional set of two apertures, determines a considerable reduction of the amount of source material that is simply deposited in the first vacuum section, never returning to the source and never reaching the Zeeman slower [285]. Atoms exiting the oven with an excessive angle strike the channel walls and can leave again by either returning to the source or escaping along the channel direction. The longitudinal and transverse velocity distribution of atoms emerging from the collimation section is plotted in Fig. 3.3(b).

The reservoir can be heated by means of three separate sections of a coaxial resistive heater wire[5] wound around the elbow tube. N-type thermocouples are installed in each section, and three PID controllers regulate the current to each heater section to keep the temperature constant at the set value. The three sections are heated to different temperatures, differing by 20°C from one another, and the hottest temperature is reached just ahead of a circular copper heat sink, where the collimation section is located. In this way, permanent accumulation of solid ytterbium metal inside the collimation channels or nearby their entrance is avoided. The assembly is thermally insulated by means of several layers of a high-temperature insulation mat and enclosed inside an aluminium case, reaching up to the heat sink location.

In order to produce a sufficient flux, the ytterbium reservoir is heated to a temperature

[4]Chempur 903073 and 009508
[5]Thermocoax 2ZEI20/HT

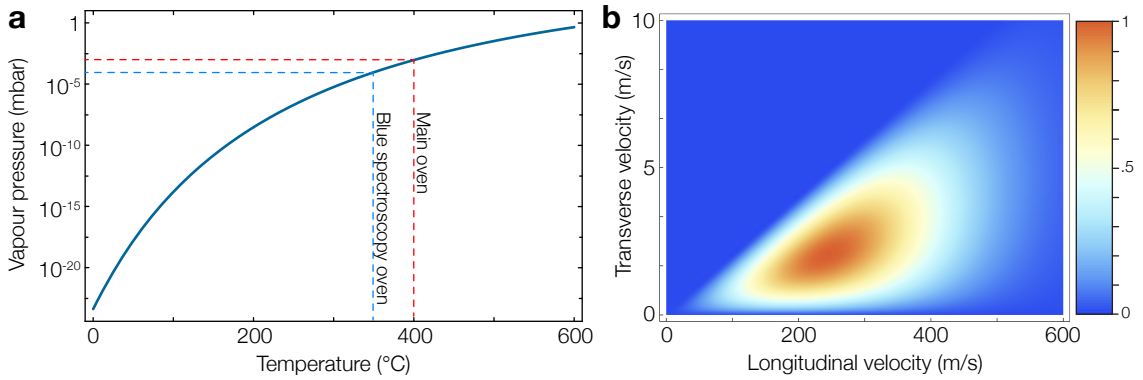

Figure 3.3 – (a) Ytterbium vapour pressure as a function of temperature. The temperatures of operation of our main ytterbium oven and spectroscopic cell are indicated by dashed lines. (b) Longitudinal and transverse velocity distribution for the thermal atomic beam collimated out of the oven. The distribution is obtained by random sampling of an initial Maxwell-Boltzmann distribution in combination with the divergence constraints given by the collimation channel array. Collisions and re-emission from the channel walls are neglected and they only contribute to the peripheral part of the atomic beam, which is blocked by subsequent physical constraints downstream in the vacuum system.

of 400 °C, yielding an average thermal velocity of $\simeq 290$ m/s. The regular temperatures of operation for the three heater sections are $T_1 = 400$°C at the reservoir, $T_2 = 420$°C at the the elbow and $T_3 = 440$°C at the collimation segment. The usual stand-by temperatures are 100°C lower. The expected atomic beam flux Φ out of the collimation channel array for a reservoir temperature T can be written as (see e.g. [285]):

$$\Phi(T) \simeq N_c \frac{\pi d^3}{12 l} n(T) \bar{v}(T) \tag{3.1}$$

where N_c is the total number of collimation channels, $n(T)$ is the Yb vapour density and $\bar{v}(T)$ is the thermal mean velocity inside the atomic source reservoir, l and d are respectively the length and the diameter of the cylindrical channels. For temperatures between 400 °C and 450 °C, the expected flux directly out of the collimation section is approximately between 2×10^{14} and 1×10^{15} atoms/s. The flux at the entrance of the Zeeman slower is reduced by a large factor, owing to additional physical constraints, namely a differential pumping tube with an aspect ratio of 4:100 and a subsequent 9 mm diameter bellow section close to the slower starting point. The expected flux Φ' at the entrance of the slower is given by [285]:

$$\Phi'(T) \simeq \frac{\pi d^2}{16} n(T) \bar{v}(T) N_c \frac{A'}{\pi L^2} \simeq 2 \times 10^{-3} \Phi(T) \tag{3.2}$$

where A' and L are the section and the distance from the oven of the limiting aperture. Light absorption measurements, performed using a beam resonant with the $^1S_0 \rightarrow {}^1P_1$ transition and directed orthogonally to the atomic beam, were used to estimate the flux ahead of the Zeeman slower, yielding values of $\Phi' \approx 2 \times 10^{11}$ atoms/s at 450 °C and $\Phi' \approx 8 \times 10^{10}$ atoms/s at 430 °C for ^{174}Yb, in good agreement with the design expectations.

Following the atomic beam after the collimation section, an atomic shutter is operated to interrupt the atomic flux after the MOT has been fully loaded. The vacuum lifetime

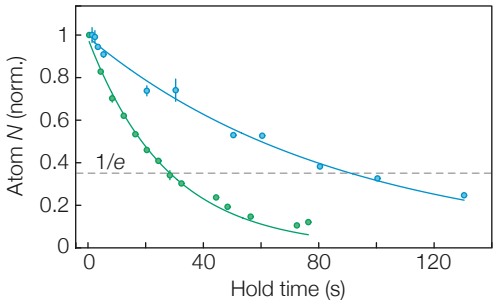

Figure 3.4 – Vacuum lifetime of a spin-polarised Fermi gas loaded into a 40 E_r deep three-dimensional optical lattice at 759 nm. The atom number N is monitored after a varying hold time in the lattice potential. The displayed data sets were collected respectively with the atomic beam shutter in close position (blue) and in open position (green) during the hold time. A difference in the gas lifetime is evident; a very long $1/e$ decay time of approximately 90 s is measured with the shutter blocking the atomic beam during the hold.

of degenerate gases is strongly affected by the presence of the atom beam (see Fig. 3.4), and it is therefore necessary to block the flux during every experimental cycle. For this purpose, a steel U-shaped blade is switched between the open and the closed position. A servo motor acts on the shaft holding the shutter blade, which is fixed to a magnetic rotary feedthrough.

3.1.2 UHV section

Zeeman slower section

The UHV section begins with the Zeeman slower (ZS) tube, which is approximately 45 cm long. The ZS solenoid has a length of 35 cm and it is wound around a 28 mm diameter steel tube. It is concentrically aligned with the ZS vacuum tube, yet in no direct contact to the vacuum vessel, in order to prevent the heat dissipated during operation from affecting the vacuum system temperature. The ZS section vacuum tube is rather narrow and acts as a differential pumping stage. Its inner section is tapered, with an opening angle of $\simeq 10$ mrad matching the atomic beam divergence from the oven collimation section; the

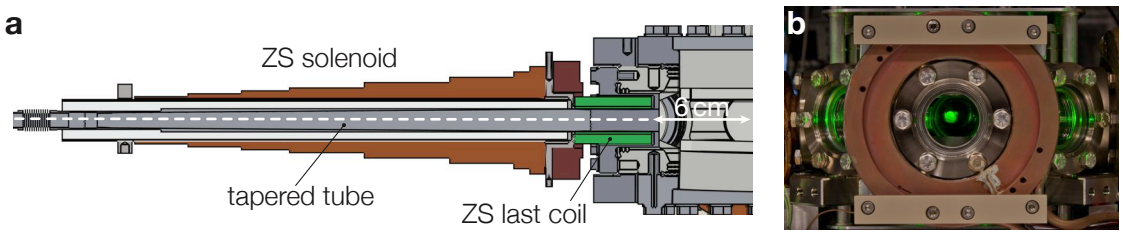

Figure 3.5 – (a) A half-section view of the Zeeman slower (ZS) assembly. The ZS solenoid consists of separate coils, grouped in three segments, marked with different colours. The last high-current coil (green) is partially inserted into the flange connecting the ZS vacuum tube to the main chamber. The inner section of the ZS tube is conical and its opening angle is roughly equal to the divergence angle of the atomic beam. (b) A photo of the main chamber seen from the side, with one of the transverse (TV) coil mounts in the front. The green ytterbium MOT fluorescence is clearly visible in the centre of the chamber.

diameters at the ZS input and output are 9 mm and 14 mm, respectively. A narrow bellow with 9 mm diameter and a CF10 flange connect the ZS tube to a gate valve, neutralising the mechanical stress at this narrow conjunction. On the other side, the ZS tube is attached to the main chamber through a custom-made CF40 flange, which is recessed into the chamber itself: the last coil of the ZS solenoid is placed at a distance of just 6 cm from the centre of the main chamber (see 3.5(a)). Such a short distance between the ZS exit position and the MOT position allows the ZS to operate with an estimated exit velocity of only approximately 7 m/s.

Main chamber

The vacuum chamber where all experiments take place is a stainless steel spherical-octagon chamber by Kimball Physics, with eight CF40 flange connections on the sides and two CF100 connections on top and bottom (see Fig. 3.7 for a close-up section view). The inner surface of the chamber has been additionally treated with a non-evaporable getter (NEG) coating with an activation temperature around 80°C, in order to increase the vacuum pumping rate around the most critical locations in the apparatus. Two large-area silica CF100 viewports are installed on the top and on the bottom of the chamber; the bottom viewport is tilted by a few degrees to prevent laser reflections between the two viewports from interfering. The main chamber is connected to the rest of the vacuum vessel through two CF40 flange connections: on one side the ZS tube is attached, while on the other side a large pumping chamber, equipped with a TSP and an ion pump, allows to reach a UHV pressure of 1×10^{-11} mbar. Six silica CF40 viewports are installed on the chamber sides, providing a good optical access in the horizontal plane as well. The chamber is independently supported from stainless steel pillars from the bottom and is the only part of the vacuum system which is rigidly connected to the optical table without any tuneable degree of freedom.

Zeeman slower viewport

During the MOT loading, the atomic beam impinges on a sapphire CF40 viewport, through which the ZS beam is aligned to counter the atomic beam. In order to avoid deposition of an ytterbium reflective layer on the inner sapphire surface after long periods of operation, the entire viewport assembly is stabilised to a temperature of 150°C. Such a temperature was verified to be sufficient for the deposited layer to evaporate again during the overnight oven stand-by. Sapphire was chosen as it is less sensitive to etching of aggressive materials in comparison to silica glass. A gate valve is nonetheless placed in between the ZS viewport subsection and the UHV pumping chamber, in order to allow the replacement of the viewport in case it becomes compromised by a permanent ytterbium coating.

3.1.3 Magnetic field coils

Uniform magnetic fields and gradients about the centre of the main chamber are generated by means of two pairs of coils: the magneto-optical trap (MOT) coils, aligned along

Coil pair	Windings	B/I (G A^{-1})	$\partial B/(\partial z\, I)$ (G cm^{-1} A^{-1})	$I_{\max}$ (A)
MOT	12	1.74	0.81	20
TV	13	0.25	0.059	100
MOT (new design)	43	6.22	2.56	250

Table 3.1 – Magnetic field coils: summary of the attainable fields and gradients. The number of windings and the magnetic-field amplitude per unit of current are provided in the first two columns. Additionally, the gradient $\partial B/\partial z$ refers to the gradient along the axial direction of the coil pair set to the anti-Helmholtz configuration, whereas $I_{\max}$ is the maximum design current for continuous operation.

the z-axis, and the transverse (TV) coils, aligned along the y-axis. Both coil pairs can be switched between the Helmholtz and the anti-Helmholtz configuration by means of MOSFET-based H bridges. The attainable field and gradients are summarised in Table 3.1. The TV coils are water-cooled through a circular copper mount to which they are glued with thermally conductive epoxy. Additional lower-current coils are used to produce offset fields, or to compensate the earth magnetic field and other stray fields. A typical magnetic field stability on the order of mG is achieved by using the current-regulated outputs of DC power supplies[6] with a relative stability below 10^{-4}. All coils can be quickly turned off by means of MOSFET switches, however eddy currents in the vacuum copper gaskets limit the effective field extinction time to a millisecond scale. Recently, we have replaced the MOT coils in our setup with a higher-current water-cooled coil pair capable of generating magnetic fields with an amplitude of more than 1 kGauss, while providing at the same time an improved optical access (see Section 3.2).

Zeeman slower coils

The ZS solenoid assembly consists of four independent coil segments. The first segment is composed by four layers of flat copper wire loops, that are wound in series around the ZS carrier tube with a progressively decreasing number of loops and are operated at a current of 5.4 A. Four additional layers of hollow core copper wire are superimposed on the first segment, forming a tapered second segment, and are operated at a current of 16.1 A. The hollow core wire is actively cooled by a constant water flow of ~ 0.5 l/min. To produce the required final peak field along with a steep cut-off, two adjacent higher-current cylindrical coils are placed nearby the main chamber. A first cylindrical coil with an inner diameter of 36 mm and a thickness of 21 mm is located just next to the main chamber. The last cylindrical coil has a small inner diameter of just 18 mm and a thickness of 7 mm and is almost fully inserted into a recessed custom-made CF40 flange (see Fig.3.5). Both coils are made of the same hollow core water-cooled wire and they are usually operated at a current of 36.0 A and 68.0 A, respectively, generating a field peak amplitude of approximately 450 G. Higher currents of up to 100 A in the last coil can be employed; however, a larger B-field results in a decrease of the MOT loading rate for ^{173}Yb, due to a supplementary hyperfine transition being tuned to resonance with atoms at zero velocity (see Section 2.2.1). The

[6] Delta Elektronika SM800-SM1500

solenoid operation currents are normally not changed when switching to ^{174}Yb, as the performance of the ZS with a maximum B-field of 450 G is amply sufficient. The residual Zeeman slower field at the position of the MOT is canceled by a ZS compensation coil, placed at the opposite side of the chamber, which is operated at a current of 37.5 A during the MOT loading and subsequently turned off. The TV coils are also used during the MOT loading in an anti-Helmholtz configuration to cancel the residual gradients generated by the ZS last coil and by the ZS compensation coil at the MOT location.

3.2 Optical setup

Experiments on the atomic samples take place only in the octagonal UHV chamber, and therefore all laser beams for cooling, trapping, manipulating and detecting the atoms are sent towards the centre of it. Three large non-magnetic honeycomb optical breadboards are installed on the sides of the chamber assembly, hosting the optical elements for the horizontal beam paths. Additional mounts for routing the laser beams along the vertical axis are placed under and over the chamber. A layout of the optical setup surrounding the main chamber is displayed in Fig. 3.6.

Horizontal setup

The majority of the beams propagate within the horizontal x-y plane. The four horizontal MOT beams (1-4) at 556 nm are transported to the experiment table by distinct single-mode polarisation-maintaining (PM) fibre. The fibre output beams are travelling through orientable compact assemblies of optical elements for beam shaping and polarisation alignment (denoted as MOT guns). They are collimated and aligned at an angle of 90° from one another; the counter-propagating beams are superimposed having the appropriate circular polarisation.
Three beams at 399 nm are aligned along the y-axis and at ±45° from it (along the lattice axes), and each of them impinges on a CCD camera for absorption imaging measurements. Dichroic mirrors are used to superimpose them on other beams and separate them again. A blue-light optimised Andor iXon and two AVT Manta G-046 cameras are used along the y-axis and the two lattice axes, respectively. The CCDs on the lattice axes can be used for imaging the atoms or inspecting the alignment of the horizontal lattice beams, while the Andor CCD is predominantly used for TOF imaging.
The horizontal dipole trap (HDT) beam at 1064 nm, emerging from a PM crystal fibre and collimated using an air-spaced triplet lens, is sent through spherical and cylindrical telescopes for elliptic beam shaping and through an achromatic doublet lens, which focuses it to the MOT location. The horizontal lattice beams (L1 and L2) at 759 nm are out-coupled from single-mode PM fibres through aspheric collimators and are similarly aligned through cylindrical telescopes and achromatic doublets, focusing them to the same position as the HDT beam. The lattice beams are retro-reflected by means of identical short-pass dichroic mirrors with an edge wavelength of 650 nm. The L2 beam is first superimposed to and then separated from the HDT beam through a long-pass and a short-pass dichroic beam-splitter respectively, with edge wavelengths around 900 nm. Finally, the Zeeman slower

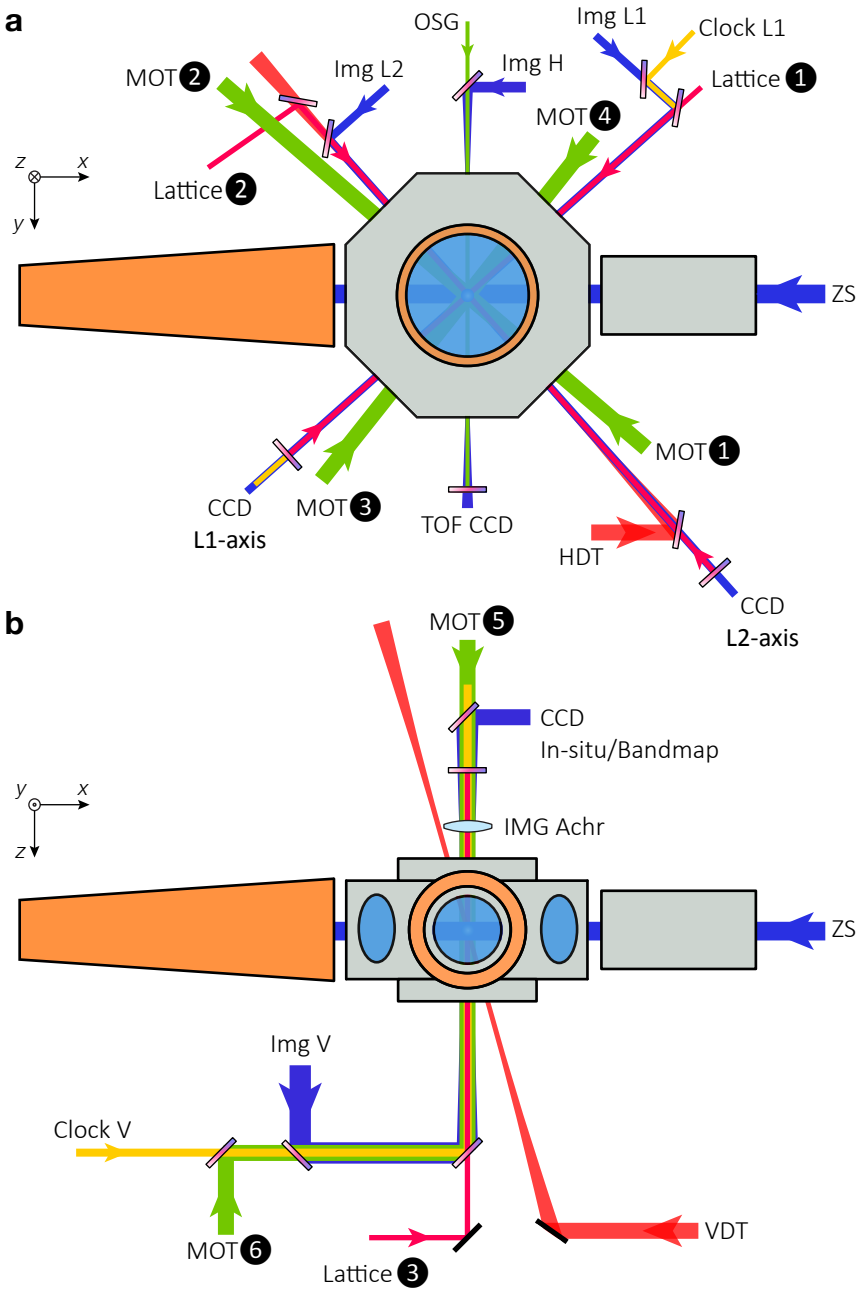

Figure 3.6 – Illustration of the optical setup: (a) the *x*-*y* plane and (b) the *x*-*z* plane (see the text for a brief description of the beam paths). The various colours denote the following wavelengths: 399 nm (blue), 556 nm (green), 578 nm (yellow), 759 nm (magenta) and 1064 nm (red). Nearly all optical elements are omitted for clarity; the dichroic combiners used to superimpose different laser beams on the same path are shown for clarity.

(ZS) beam at 399 nm, the optical Stern-Gerlach (OSG) beam at 556 nm and the clock excitation beam at 578 nm emerging from single-mode PM fibres are aligned through beam-shaping and polarisation-adjusting optical elements and they are focused using standard spherical lenses. Prior to entering the vacuum chamber, the clock beam is overlapped with the L1 beam path by means of a dichroic combiner.

Vertical setup

Nearly all laser beams entering the vacuum chamber from above or below propagate along the vertical axis, with the only exception of the vertical dipole trap (VDT) beam which crosses the HDT beam with an angle of approximately 20° to the vertical axis. The counter-propagating vertical MOT beams (5-6) are shaped and steered by MOT guns identical to the horizontal MOT guns, which are supported by independent mounts fixed to the horizontal breadboards. The VDT beam, emerging from a PM crystal fibre and collimated by a triplet lens, is sent through shaping optics mounted on the bottom face of one of the horizontal breadboards and is focused to the atom position by means of an achromatic doublet. The vertical lattice beam (L3) is travelling from the output of a single-mode PM fibre through an aspheric collimator and a spherical telescope, before being focused to the atoms position through an achromatic doublet. It is retro-reflected by a dichroic filter placed inside a vertical linear assembly of optical elements mounted on top of the vacuum chamber, which includes an achromatic doublet with a focal length $f = 75\,\mathrm{mm}$ for absorption imaging. The upward propagating MOT beam, an imaging beam and a clock laser beam are superimposed to each other by dichroic mirrors and are deflected up by an additional dichroic combiner placed below the UHV chamber, where they are overlapped to the L3 beam. The imaging beam is split off by a dichroic mirror and impinges on a Manta G-145 CCD camera, typically used for in-situ and band mapping images. The focus positions of the HDT, the VDT and the L3 beams can be very precisely aligned by means of motorised mirror mounts [7] with an angular resolution below $1\,\mu\mathrm{rad}$.

The dipole trap, the lattice and the clock excitation beam intensities are actively stabilised with a bandwidth around 100 kHz by monitoring a small portion of the light on the experiment table and regulating the RF driving power to AOMs placed on the laser tables ahead of the fibre in-coupling.

Recent upgrades

All experiments described in this thesis have been performed using the optical setup summarised above. Very recently, we have installed a new optical assembly above the UHV chamber. It consists of a high-resolution imaging lens quadruplet[8] with a focal length $f = 67\,\mathrm{mm}$, a retro-reflecting dichroic mirror for the L3 beam, a dichroic beam-splitter for diverting off the vertical imaging beam and a compensation lens for the downward-propagating MOT beam. The objective position along the z-axis can be precisely adjusted by means of a translational stage, whereas the retro-reflecting dichroic can be aligned using a motorised custom-made mirror mount. This vertical optical setup has been installed in conjunction with new high-current z-axis coils, capable of delivering large B-fields above kG. The new coils are designed to be operated with a constant maximum current of 250 A, owing to the large cooling power provided by a constant water flow inside the copper mounts to which they are glued. The attainable fields and gradients are

[7] New Focus 8821 and 8816.

[8] The quadruplet objective was designed by Lens Optics with a numerical aperture $NA \simeq 0.37$ and a nominal resolution of approximately $0.8\,\mu\mathrm{m}$ at 399 nm. The lenses design includes a compensation of the spherical aberrations caused by the 8 mm thick viewport glass substrate.

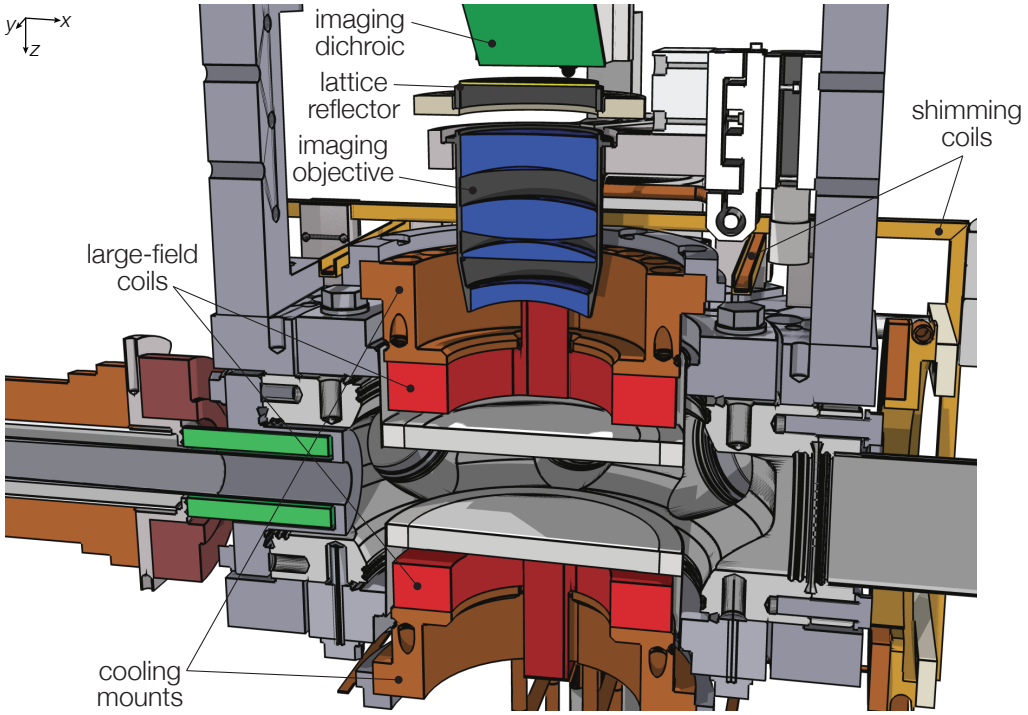

Figure 3.7 – An illustration of the newly installed vertical optical setup together with the z-axis large-field coil pair. A half-section along the x-z plane is displayed, where the essential optical elements are visible along the supporting structure fixed to the upper surface of the UHV chamber. New rectangular shimming coils for earth field compensation and offset fields generation are also shown.

given in Table 3.1. A section view of the newly installed setup is sketched in Fig. 3.7.

3.3 Laser system

In this Section we will summarise the technical aspects of the various laser setups, which were developed in the context of this thesis and are used to perform the experiments presented therein. First, the two laser systems generating the light for laser cooling and resonant manipulation or detection of the atoms, namely the blue and the green laser systems, are described. Secondly, the two infrared laser sources providing high-power outputs for the optical dipole trap and the magic-wavelength lattice are briefly illustrated. Finally, the clock excitation laser system is presented in some detail in a dedicated Section. Additional laser sources for generating a state-dependent bi-chromatic lattice potential and for the repumping of metastable state atoms have also been already implemented and are described in Refs. [125, 293]. Supplementary details about the stability of the clock laser can be found in Appendix C.

3.3.1 Blue laser system

The blue laser system produces the necessary light power at 399 nm for the operation of the Zeeman slower and for the imaging beams. A schematic of this laser system is dis-

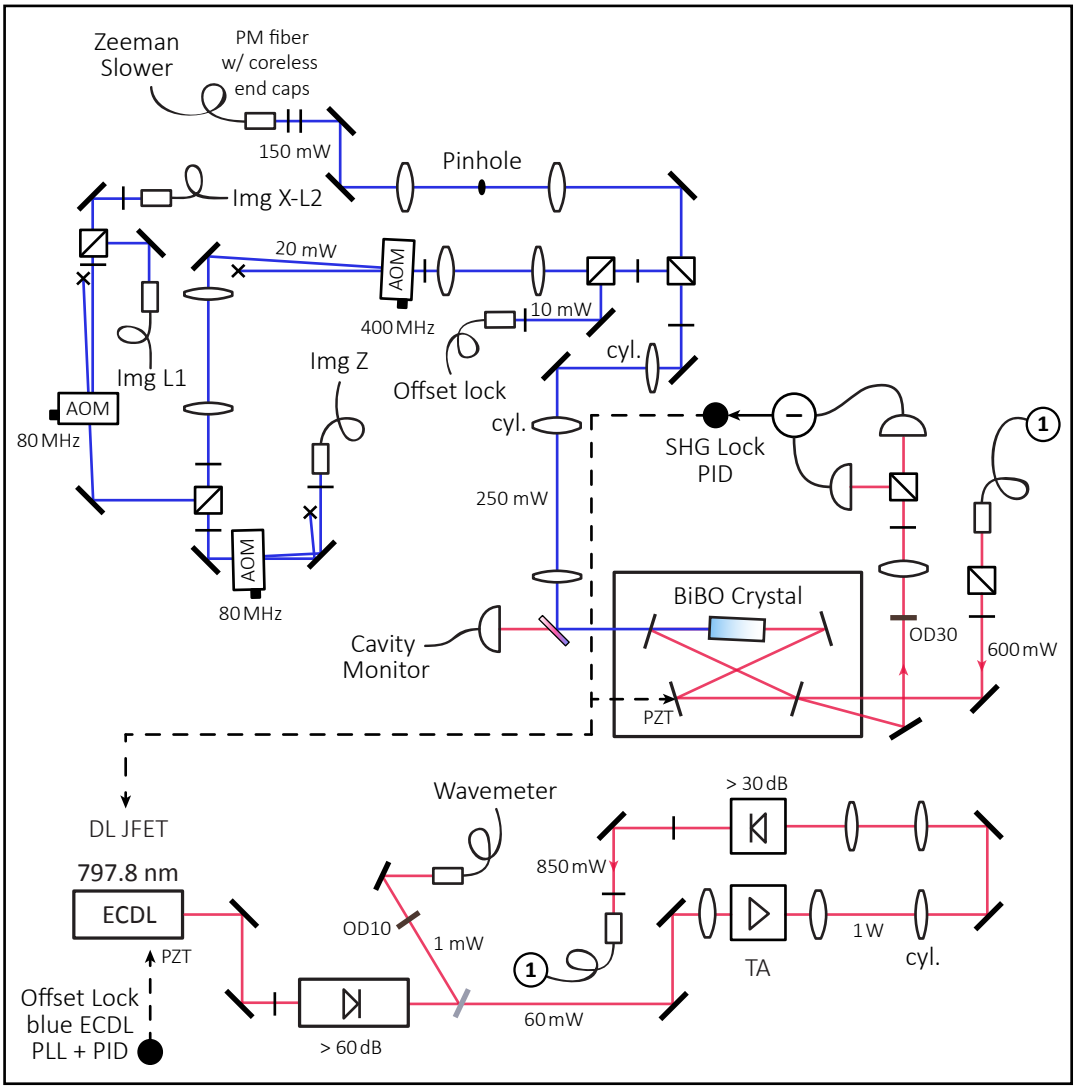

Figure 3.8 – A schematic of the blue laser system. Three main blocks can be recognised: the infrared laser source at 797.8 nm, the SHG bow-tie cavity for frequency doubling to 399 nm and the distribution optics, which deliver the light with the necessary power and detuning for use in the experiment. The fibres are labeled by their final destination on the experiment table (see Fig. 3.6). Dashed lines denote the control signals from PID controllers in the lock feedback loops.

played in Fig. 3.8. The primary laser source is an external-cavity diode laser (ECDL)[9] at 798 nm, emitting 60 mW of light power and seeding a tapered amplifier (TA) chip[10], housed in a custom-made cooling mount. The TA amplifies the infrared light power to approximately 1 W. The beam is then sent through a short optical fibre, in order to decouple the alignment of the first part of the laser setup from the one of the following second-harmonic generation (SHG) cavity. The output of the fibre is polarisation aligned

[9]The ECDL setup is custom-built using an Eagleyard EYP-RWE-0840 diode in a linear cavity, formed by the diode emitting surface and a semi-transparent mirror. The frequency selectivity is provided by a tilted thin etalon.

[10]Eagleyard EYP-TPA-0795.

and in-coupled into a bow-tie SHG cavity with a finesse around 100. The light is frequency up-converted to 399 nm with an efficiency around 40% using a 10 mm long, angle phase-matched non-linear BiBO crystal, generating approximately 250 mW of blue light. The cavity length is locked to resonance by means of the Hänsch-Couillaud technique [294], mainly acting on a piezoelectric stack mounted behind one of the cavity mirrors. Additionally, the short-term cavity fluctuations are tracked by regulating the ECDL frequency through a fast small-amplitude diode current modulation[11].
Light at the output of the cavity is shaped by cylindrical and spherical telescopes and divided into several paths for different applications. The largest portion of the light power is polarisation-aligned, mode-cleaned and coupled to a high-power optical fibre[12] with coreless end caps, preventing power-induced long-term damage of the fibre surfaces (which is a common issue with short ultraviolet-visible wavelengths already above 100 mW). Another smaller portion of the power is frequency shifted by +480 MHz using AOMs[13] and used for absorption imaging or ground state atom removal. The AOMs do not need to entirely produce the required detuning between the ZS light and the $^1S_0 \rightarrow {}^1P_1$ resonance, as the ECDL frequency can be rapidly varied during the experimental cycle by means of an offset frequency lock (see below). A small fraction of the light is in-coupled to a fibre, which transports it to a separate breadboard, where the frequency offset lock setup is located.

Offset frequency lock to the atomic reference

In order to lock the frequency of the diode laser at 798 nm to the atomic transition frequency, an offset lock scheme was implemented. A second ECDL emitting directly at 399 nm, based on a low-power laser diode[14], is frequency locked to the ytterbium atomic transition by means of FM saturation spectroscopy in an ytterbium vapour cell. A schematic of the frequency lock setup is shown in Fig. 3.9, while a detailed description of the spectroscopic cell and of the FM spectroscopy lock to the atomic reference can be found in Ref. [295]. Part of the stabilised 399 nm low-power ECDL light is made to interfere with frequency-doubled light from the main blue laser breadboard. The two beams impinge on a 1.5 GHz fast AC coupled photodiode[15], which detects their beat note frequency. The fast photodiode signal is amplified and sent to a PLL circuit, where it is divided to lower frequencies and compared to a stable RF source. The PLL output signal is then fed as an error signal to a PID controller, which adjusts the frequency of the 798 nm ECDL by regulating the voltage to a piezoelectric element varying the laser cavity length. In this way, the beat note is stabilised to the RF source and the main ECDL absolute frequency is locked to the atomic resonance with an adjustable offset. A PLL capture range exceeding a GHz allows for large sudden variations of the beat lock frequency with rapid re-locking during the experimental cycle. When working with ^{173}Yb, we typically lock the 399 nm ECDL frequency to the $^1S_0 \rightarrow {}^1P_1$ transition of ^{176}Yb. At the beginning of the cycle,

[11] The gate voltage of a JFET in parallel to the laser diode is adjusted within its linear response range.
[12] AMS Technologies QPMJ-A3HPC-400-3
[13] Gooch&Housego 47400-.3-.4-LTD-XQ (quartz - 400 MHz) and Crystal Tech. 3080-125 (TeO_2 - 80 MHz)
[14] Nichia NDV1413
[15] Newport 818-BB-20

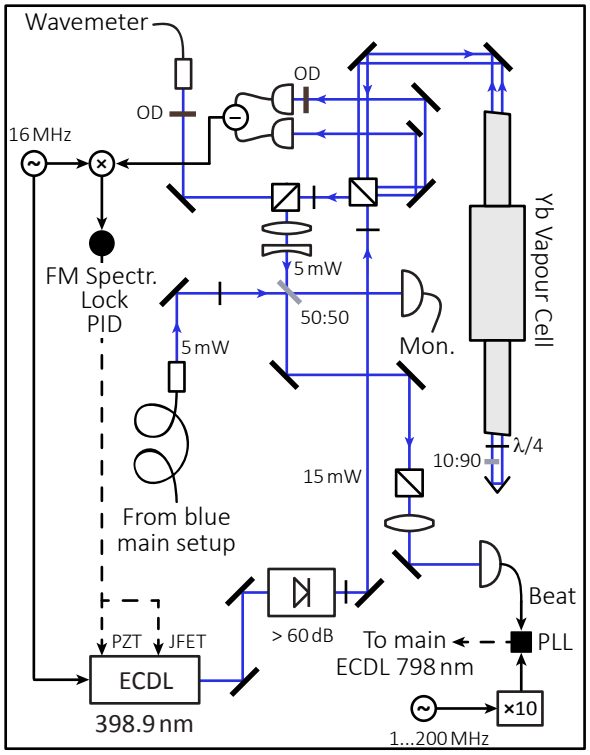

Figure 3.9 – A schematic of the blue laser lock system. A low-power ECDL at 399 nm is locked to the atomic transition frequency using FM spectroscopy. The frequency stabilised light is made to interfere with a small portion of light from the frequency-doubled blue primary source. The frequency of the primary ECDL at 798 nm source is regulated to produce a constant beat note with the low-power blue ECDL. The frequency offset between the two laser can be externally controlled.

the beat note is stabilised to the frequency difference of approximately 450 MHz between the ^{173}Yb ZS operation frequency and the ^{176}Yb resonance[16]. As soon as the ZS light is shuttered off, after the MOT loading, the beat set frequency is changed to bring the imaging beams into resonance with the ^{173}Yb transition. As a frequency shift of +480 MHz is produced by AOMs, the offset frequency is tuned to approximately 620 MHz to cover the total 1.1 GHz shift between the ^{176}Yb and ^{173}Yb transitions. The offset locking method is very versatile, as in principle it allows to tune the laser to any desired frequency during the experimental cycle, with a switching speed currently limited by the ECDL piezo bandwidth.

3.3.2 Green laser system

The green laser systems generate the light required for the operation of the MOT, of the optical pumping sequence and of the OSG spin separation. An overview of this laser setup is given in Fig. 3.10. The primary laser source is an Yb-doped fibre laser[17] emitting at 1112 nm, with an intrinsic linewidth around 100 kHz and an output power around 2 W. The output of the fibre laser is polarisation-aligned and injected into an bow-tie SHG cavity

[16] The ZS detuning is $\Delta_s \simeq -650$ MHz from the $^1S_0\,(F = 5/2) \rightarrow {}^1P_1\,(F' = 7/2)$ resonance in ^{173}Yb
[17] Menlo Systems Orange One

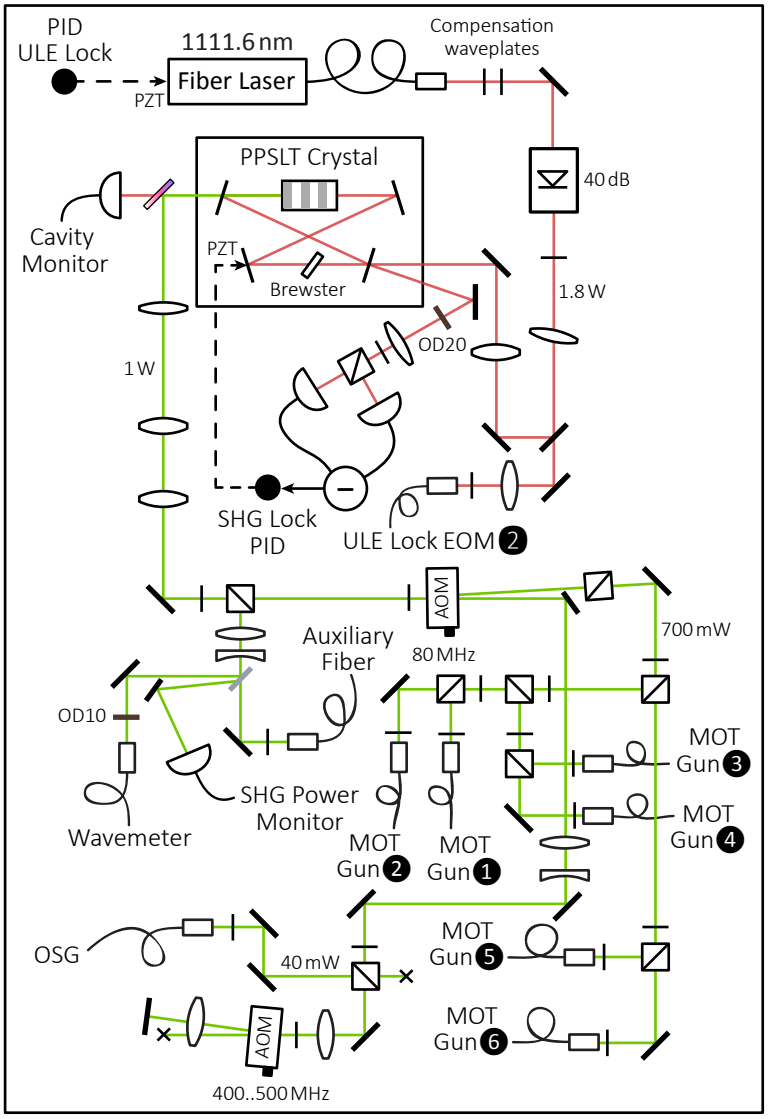

Figure 3.10 – A schematic of the green laser system. The infrared laser source output at 1112 nm is injected into the SHG bow-tie cavity for frequency doubling to 556 nm, followed by various optical elements used to distribute the light for the MOT and the OSG beams. The fibres are labeled by their final destination on the experiment table (see Fig. 3.6). Dashed lines denote the control signals from PID controllers in the lock feedback loops.

with a finesse of approximately 20, relying on a 20 mm long PPSLT crystal for frequency up-conversion to 556 nm. As for any other doubling cavity in our laser system, the cavity length is locked to resonance using the Hänsch-Couillaud technique, just by regulating in this case the voltage to a piezoelectric element that displaces one of the cavity mirrors. An SHG efficiency exceeding 50% is achieved, yielding a green output power around 1 W. The green beam travels then through beam-shaping optics and through a 80 MHz AOM[18], which is used to switch the MOT beams and regulate their intensity. Six independent PM single-mode fibres are used to transfer the MOT light to the experiment table. A portion of

[18] Crystal Tech. 3080-125

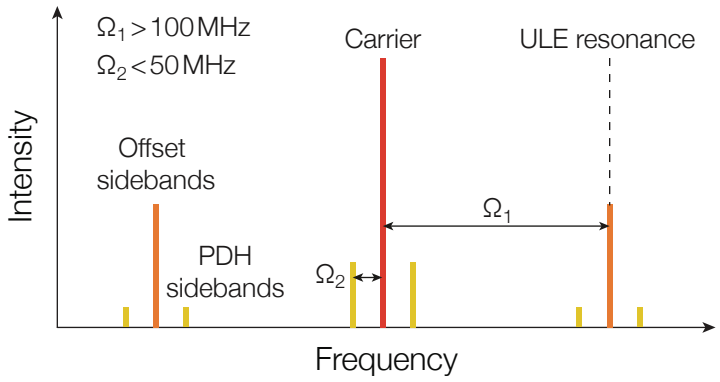

Figure 3.11 – Generation of double laser sidebands by a fibre-coupled EOM for PDH lock with a frequency offset. High-frequency sidebands with $\Omega_1 > 100$ MHz (orange) are created, in order to serve as carriers for lower-frequency PDH lock sidebands with $\Omega_2 < 50$ MHz (yellow). One of the high-frequency sidebands is locked to a resonance of the ULE cavity, so that the laser carrier (red) is stabilised and its absolute frequency remains close to the atomic resonance. The frequency Ω_1 can be varied, in order to accurately tune the laser detuning to the atomic resonance. This scheme is adopted for the stabilisation of both the green and the clock lasers.

the AOM zero-order beam is exploited for producing the OSG beam, which is detuned by +850 MHz with a double passage through a high-frequency AOM[19], resulting in a power of approximately 40 mW coupled into a PM single-mode fibre.

Cavity reference lock

The frequency of the green light is frequency stabilised by locking the fibre laser to a cavity reference with a finesse $\mathcal{F} = 1.08(8) \times 10^4$ at 1112 nm, exhibiting a linewidth of 140 kHz and a day-scale frequency stability around 4 kHz (see Fig. 3.16). This ultrastable ULE resonator is briefly described below in the context of the clock laser stabilisation and presented in more detail in Ref. [296]. In order to lock the fibre laser to the cavity reference, a small amount of infrared light is collected and transferred to a separate breadboard where the resonator is placed (see Fig. 3.16). The light addressed to the resonator is sent through a custom-made fibre-coupled EOM from Jenoptik with a 5 GHz bandwidth, which is driven by two stable RF sources to generate a double set of sidebands (see Fig. 3.11). One of the high-frequency sidebands is locked to the resonator by means of the Pound-Drever-Hall (PDH) technique (see Fig. 3.16), with a PID controller regulating the voltage to a piezoelectric element installed in the fibre laser, so as to tune its frequency (the PDH lock system is fully described in the above-mentioned Ref. [296]). The fibre laser frequency is therefore stabilised to the resonator with an adjustable frequency offset, which can be electronically set during each experimental cycle. By suitably adjusting the sideband spacing, the laser carrier detuning from the resonance can be varied. Moreover, controlled frequency sweeps can be carried out, with a speed limited only by the servo bandwidth of the PDH lock. The dynamic frequency adjustment is exploited both for the compression

[19] Brimrose TEF-500-100-399

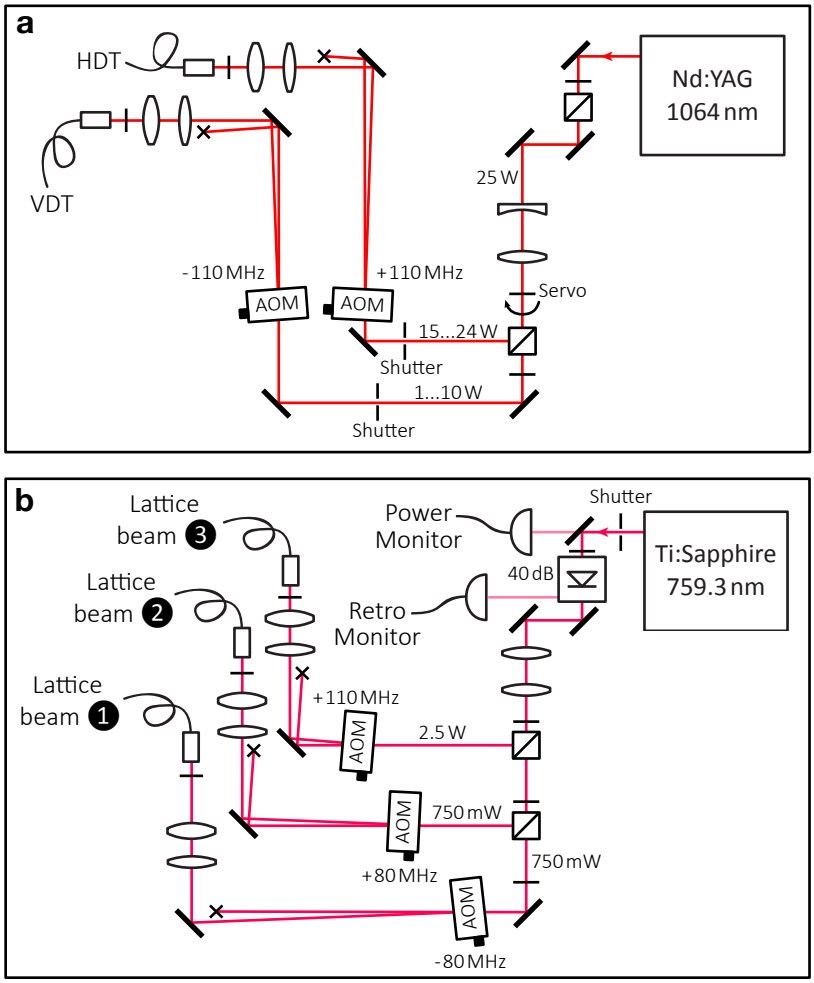

Figure 3.12 – (a) A schematic of the ODT laser source. Two high-power beams are shaped, frequency-shifted and coupled into large mode-area fibres carrying the light to the experiment. The power distribution between the HDT and VDT beams can be varied by remotely controlling the servo motor rotating a half wave-plate in the beam path ahead of the splitting PBS. (b) A schematic of the optical lattice laser source. Three beams are coupled into different fibres after being frequency-shifted for avoiding undesired interference between distinct lattice beams. The shifting AOMs are also used for power control and stabilisation of the lattice beams.

stage in the MOT and for multi-pulses optical pumping sequences (see Section 4.2).

3.3.3 Dipole trap and optical lattice laser sources

An overview of the optical dipole trap (ODT) and lattice laser setups is given in Fig. 3.12. The source producing the high-power ODT beams is a 25 W Nd:YAG laser[20]. The output of the laser is polarisation filtered, resized with a spherical telescope and subsequently split into separate paths corresponding to the two ODT beams. The power ratio between the beams can be remotely controlled by means of a motorised rotating half wave-plate, allowing a continuous power re-distribution during the evaporation, which increases the power of the VDT beam while the HDT beam power is decreased. Both beam paths are

[20] Innolight Mephisto

equipped with high-power laser shutters[21] and large-crystal quartz AOMs[22]. The two AOMs deflect the respective beams in opposite directions and are thus used both for preventing unwanted interferences at the ODT crossing region and for power stabilisation and regulation of the two ODT beams. The beams are coupled into high-power large mode-area fibres[23] with a length of 5 m, which are capable of transmitting optical powers of approximately 13 W at most before Brillouin scattering sets in.

The source for the creation of the three-dimensional optical lattice is a Ti:Sapph ring laser[24], capable of delivering approximately 5 W of power at 759 nm. The laser resonator has an intrinsic long-term frequency stability of 1 GHz, which is amply sufficient for our current experiments. A setup for locking the laser to a cavity reference has been nevertheless implemented, and will be exploited in the future for bi-chromatic lattice setups requiring higher stability [125]. Similarly to the ODT laser system, the main laser output is divided into three beams and sent through AOMs[25] for preventing interference between distinct lattice beams and for their power control and stabilisation. The beams are then coupled into three PM single-mode pure silica fibres. The alignment of the lattice retro-reflection on the experiment table can be optimised by maximising the amount of light which is back-coupled to the optical fibre. For this purpose, this light is collected by a photodetector placed on the side port of the optical isolator input PBS, where the back-propagating light is diverted off the principal beam path.

3.4 Clock excitation laser system

The laser system for the excitation of the ultranarrow $^1S_0 \rightarrow {}^3P_0$ clock transition is one of the crucial parts of the entire experimental setup. In order to manipulate the population of the metastable state in a coherent fashion and with a high degree of control, a laser with an adequately long coherence time and sufficient power is essential. This is necessary for realising and probing the two-orbital many-body Hamiltonians described in Chapter 1. In particular, a very high frequency resolution is necessary for probing interaction clock shifts and exploiting such shifts for occupation number-selective excitation in a three-dimensional lattice.

However, prior to the measurements presented in Chapter 6, the interaction properties of the metastable state were still largely unknown along with the exact magnitude of the associated clock shifts. At the time of designing and assembling the clock laser setup, typical interaction shifts were expected to be on the order of kHz. Consequently, we initially constructed a laser system capable of delivering a sub-kHz narrow output with a relatively high power of approximately 20 mW at the clock wavelength 578 nm, corresponding to attainable clock Rabi frequencies above 10 kHz for a waist of $\sim 100\,\mu$m. We subsequently discovered through our early clock shift measurements that a higher resolution close to 10 Hz would be highly desirable, owing to clock shifts between different interaction chan-

[21] NMLaser LST4WBK2
[22] Crystal Tech. 3080-198
[23] NKT Photonics LMA-PM-15
[24] Sirah-Spectra Physics Matisse TS
[25] Crystal Tech. 3080-125 and 3110-120

nels being on the order of only few hundreds of Hz. The clock laser system underwent thus a continuous improvement process, which is still ongoing. The setup presented here is the one used for the measurements reported in this thesis and is capable of achieving an atomic absorption linewidth as low as approximately 40 Hz, corresponding to a relative short-term stability below 10^{-13}. The laser system consists of two main blocks: (i) the laser source and (ii) the ultrastable high-finesse cavity reference. In the following we will describe these parts, with particular focus on the locking system which stabilises the frequency of the laser source to the cavity reference. When the laser source is locked to the cavity reference, the long-term resonator stability is transferred to the laser and the linewidth of the laser is narrowed. Details about the short-term and long-term stability of the clock laser can be found in Appendix C. A detailed treatment of our ultralow-expansion (ULE) cavity design, of its mechanical and thermal properties, and of a large part of the frequency lock setup can be found in Ref. [296].

3.4.1 Laser source

As the only available laser sources emitting at 578.4 nm are dye lasers, which are expensive and troublesome to maintain, we opted to frequency double an infrared laser source at 1156.8 nm in a dedicated second-harmonic generation cavity. A high-power laser diode[26], delivering a 200 mW single-mode output, represented the most flexible and cost-effective solution. In this respect, narrow-line (sub-Hz) diode-based laser sources have already been implemented (see e.g. [297]). The diode is assembled in a standard ECDL (External-Cavity Diode Laser) Littrow configuration [298]. Its main distinctive characteristic is the long ($\sim$ 10 cm) external cavity (see Fig. 3.13(a)), which reduces the linewidth of the ECDL cavity and leads to a rather narrow output linewidth well below 100 kHz before the laser is locked to any reference. The initial linewidth of the laser output is estimated through a frequency noise measurement in a diagnostic Fabry-Perot cavity with a linewidth of 2 MHz. The power spectral density (PSD) linewidth can be deduced from the frequency spectral noise density through integration below the so-called β-separation line [299]. An earlier version of the laser source in our setup adopted a standard cm-long external cavity setup and is described in [296]. While the initial laser linewidth and the thermal stability were improved from one revision to the next, the power output and the characteristic frequency response to current modulation are largely equivalent. Furthermore, the new laser source is insulated from external sound and thermal fluctuations by a sealed case, whose sides consist of 3 mm lead-rubber layers glued to steel plates.

By locking to the ultrastable cavity reference, the infrared laser linewidth is narrowed down to a 20 Hz level and its absolute frequency is stabilised against long-term drifts. This is achieved by means of a fast Pound-Drever-Hall lock system, which will be presented below. The laser frequency is stabilised with a 800 kHz-high servo bandwidth through an AOM operating at a central frequency of 120 MHz (see also Appendix C). A slower laser frequency compensation is actuated by a piezo element adjusting the ECDL cavity length, which can easily counteract frequency deviations as large as several tens of MHz and allows the AOM to operate around its central frequency.

[26] Innolume GC-1156-TO-200

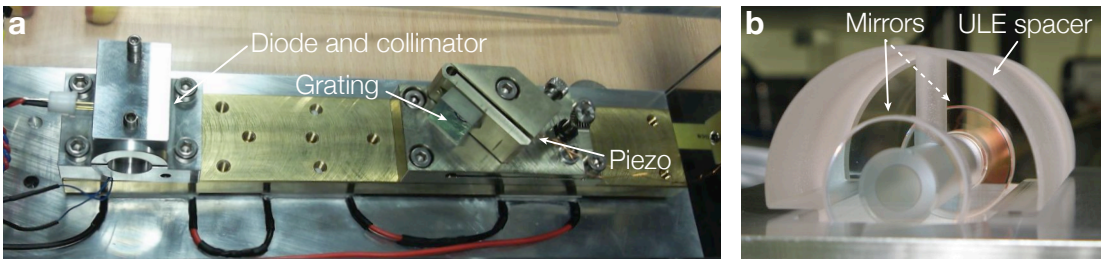

Figure 3.13 – (a) A photo of the ECDL laser source, with the long cavity formed between the diode emitting surface and the ruled diffraction grating. The cavity elements are fixed to a brass plate, which is temperature stabilised by two thermo-electric elements exchanging heat with a large aluminium base block. A piezoelectric actuator can finely tune the cavity length by tilting the grating mount. (b) A photo of the horizontal-design ULE cavity before its placement into the vacuum vessel. Two ULE glass mirrors are optically contacted on a 10 cm long ULE glass spacer. The spacer shape is optimised for minimising the effect of mechanical solicitations on the cavity length [296].

The stabilised infrared laser output at 1156.8 nm is then frequency doubled to 578.4 nm through a SHG bow-tie cavity analogous to the one adopted in the 556 nm laser setup, based on a PPSLT non-linear crystal. The cavity SHG efficiency is approximately 25% when optimally aligned, yielding a typical output yellow light power of 20 mW. Like the other SHG cavities in our experiment, this cavity is locked to the laser frequency by means of the Hänsch-Couillaud technique. An important difference however is the presence of an additional fast piezo-electric transducer mounted behind one of the SHG cavity mirrors, which allows for cavity lock bandwidths of several tens of kHz without resorting to any laser-diode current fast regulation, as opposed to the case of the blue SHG cavity setup (see above). Modulation of the laser diode current compensating the short-term SHG cavity length fluctuations must necessarily be excluded in this case, as it would harmfully affect the laser frequency noise and compromise its short-term stability. The implementation of the SHG cavity and its locking scheme are described in detail in Refs. [296, 300]. The alignment of the SHG cavity is decoupled from the alignment of the first part of the infrared laser path by a short optical fibre (see Fig. 3.14). Prior to in-coupling into this fibre, a small portion of the light is collected for use in the ULE cavity lock section and for frequency monitoring via a wavemeter.

After the doubling, the beam travels through an AOM operating at 100 MHz, which is mainly used for stabilising the light intensity and shaping the clock light pulses applied to the atoms. The light is then transferred to the experiment table through a several meters-long optical fibre. The light intensity is actively stabilised by controlling the AOM driving power through a PID controller, using the signal from a photodiode that collects a small portion of the clock light at the fiber output. The noise introduced by vibrations and thermal fluctuations of the fibre can be eliminated through a standard fibre-noise cancellation system based on a beat-note stabilisation scheme. This noise canceller is shortly illustrated below and uses the same 100 MHz AOM as a transducer to correct the light frequency before the fiber (more details on its performance are given in Appendix C).

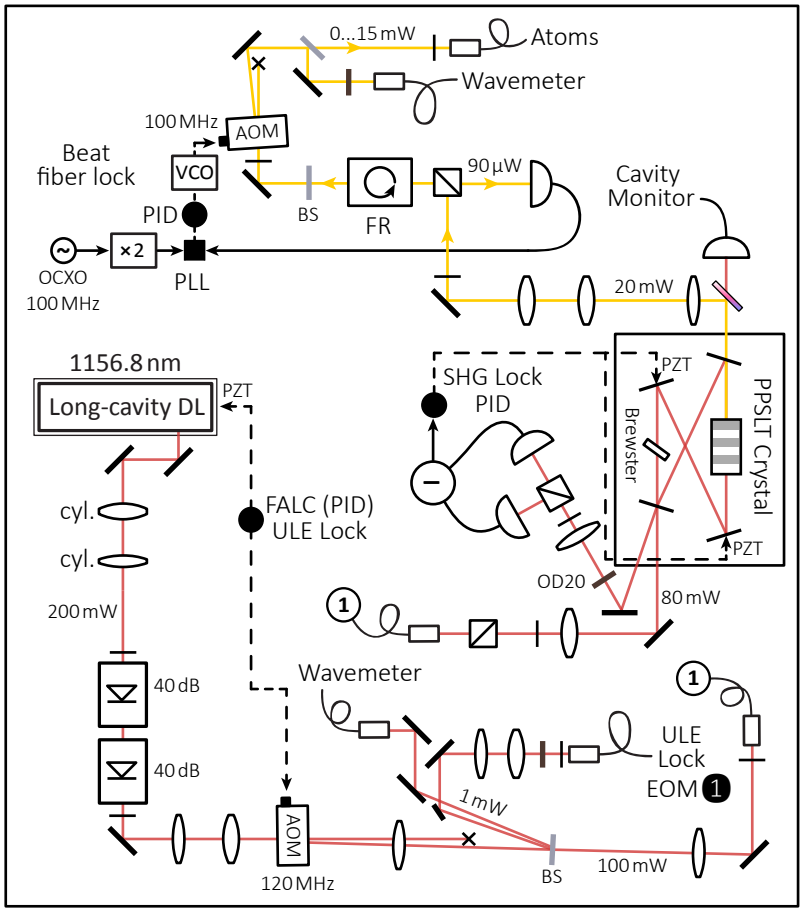

Figure 3.14 – A schematic of the clock laser source setup. The long-cavity ECDL at 1156.8 nm is frequency stabilised to a ULE reference resonator by acting on a piezo element mounted on the laser-cavity diffraction grating (slow feedback) and on a 120 MHz AOM placed downstream the laser beam (fast feedback). After beam shaping optics, two Faraday isolators are providing a large extinction ratio of unwanted feedback from the ULE cavity setup (see below). A beam sampler collects a small portion of the light for use in the ULE cavity lock section. The stabilised infrared light is injected into an PPSLT-based SHG bow-tie cavity, which converts up to 25% of the power to 578.4 nm, and is frequency locked to the laser by the Hänsch-Couillaud technique. After the frequency doubling, the light is transferred to the atoms after passing through a 100 MHz AOM, which is used for both fibre-noise cancellation and actively controlled pulse shaping (see text).

3.4.2 Ultrastable cavity setup

The ultrastable cavity used in our setup was designed by Advanced Thin Films and a suited vacuum vessel was provided by Stable Laser Systems, already equipped with the temperature sensors and foil heaters required for temperature stabilisation. The cavity assembly consists of two ultralow-expansion glass[27] (ULE) mirrors optically contacted to a 10 cm ULE spacer. The resonator has a plano-convex geometry, with the curved mirror radius of curvature $R_c = 50$ mm, and has a free spectral range of 1.5 GHz. The finesse of the resonator at 1156.8 nm was measured through a ring-down measurement to equal $\mathcal{F} = 8.46(6) \times 10^4$ [296], corresponding to a linewidth of 17.7(1) kHz.

[27] Corning Code 7972

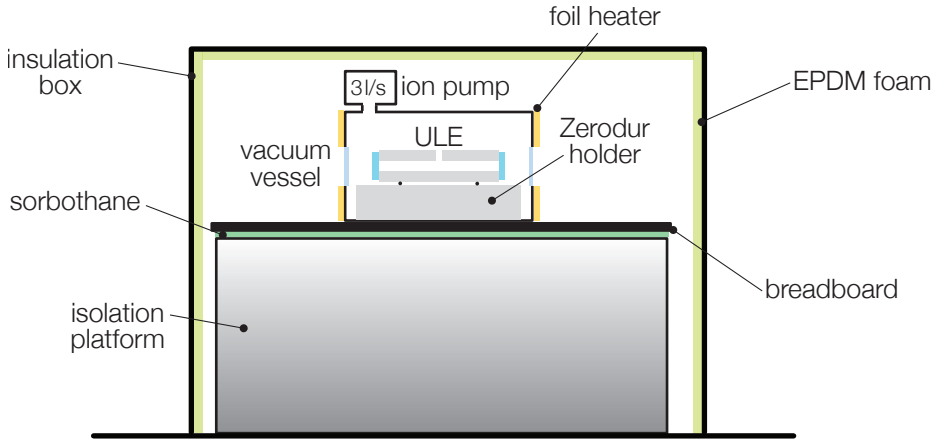

Figure 3.15 – An illustration of the ULE cavity setup with the various parts used to decouple the resonator mechanically and thermally from the surrounding environment (see text for details).

The spacer has a hollow cylindrical shape with two large rectangular cutouts on the bottom and a ventilation channel on the top (see Fig. 3.13(b)). The spacer shape is designed for operation of the resonator in a horizontal alignment. The resonator is placed on a rectangular holder[28] and is supported by Viton spheres placed at four points exactly located in order to minimise the effect of gravity and other mechanical perturbations which modify the resonator length l (and therefore the resonance frequency ν of its eigenmodes, as $\Delta\nu/\nu = \Delta l/l$) [296]. To give an idea of the required length stability corresponding to a relative frequency stability of 10^{-14}, the distance between the mirrors is not allowed to vary by more than approximately a proton radius. It is therefore fundamental to isolate the cavity from any external effect which cause a resonator length variation. We will hereafter refer to short-term and long-term stability of the resonator, respectively denoting the frequency stability within the time scale of a single experimental cycle ($\lesssim 1$ min) and extending over several experimental cycles ($\gtrsim 1$ min).

Resonator frequency fluctuations

Given the geometrical optimisation of the spacer, mechanical solicitations can nonetheless play a big role in both the short and long-term stability of the ULE cavity, depending on their characteristic frequency. For this reason, thorough countermeasures have to be taken to mechanically decouple the cavity from the surroundings. First of all, vacuum is used to largely insulate the cavity acoustically and thermally. Furthermore, the cavity vacuum-assembly, along with all injection and detection optics for the Pound-Drever-Hall scheme, are placed on an aluminium breadboard, positioned in turn on top of a high-performance passive vibration isolation platform[29], with a noise suppression of more than 50 dB above 20 Hz in all directions. A 8 mm layer of Sorbothane rubber is additionally placed between the platform and the breadboard. A sound and thermal insulation box

[28] The holder itself is made of Zerodur (Schott AG) glass, a glass ceramic with very low thermal expansion and high three-dimensional homogeneity.

[29] Minus K 100BM-1

enclosing the entire breadbord-platform apparatus is installed, whose aluminium walls are covered by an EPDM rubber-based foam[30], which suppresses sound waves above 500 Hz and reaches a damping factor of 30 dB at 5 kHz. The box and the vibration isolation platform are directly sitting on the air-floated laser optical table. In this way, dynamic mechanical perturbations are prevented as much as possible from reaching the cavity by either air or rigid connections.

Another source of short-term fluctuations is the variation of the refractive index inside the resonator, due to background pressure fluctuations. The vacuum vessel is kept at a pressure of 10^{-6} mbar by continuous operation of a compact 3 l/s ion pump[31]. The specified residual pressure fluctuations are of 10^{-7} mbar, which induce a variation of the refractive index and an associated frequency shift below the sought linewidth of 10 Hz.

The resonator stability is also affected by environment temperature variations, which cause its length to vary typically over temperature fluctuation time scales of several seconds. The effect of temperature fluctuations can be minimised by adopting thermally insensitive materials such as ULE and additionally implementing an accurate temperature regulation of the cavity. ULE is a titania-doped silicate glass with an extremely low thermal expansion minimum at a temperature T_0 which is close to room temperature. The exact value of T_0 depends on the concentration of titanium and is determined experimentally for our spacer to equal $T_0 = 26.3(1)$°C (see Appendix C). When the spacer is operated at the thermal expansion minimum T_0, the linear coefficient of thermal expansion vanishes and the temperature-induced relative variation of the cavity frequency retain only a quadratic dependence on T:

$$\frac{\Delta \nu}{\nu} = \alpha^{(2)} (T - T_0)^2 \lesssim 10^{-9}\,\mathrm{K}^{-2} (T - T_0)^2 \tag{3.3}$$

It is therefore essential to regulate the temperature of the cavity as close as possible to T_0 with high long-term stability to prevent drifts of the resonator frequency. For this reason, the temperature of the entire vacuum vessel is stabilised to $T_0 = 26.3$°C with fluctuations below 5 mK using a digital PID temperature controller[32], yielding a frequency stability at the CTE minimum of 5 Hz (see Appendix C). Two large-area resistive foil heaters regulate the temperature of the two vacuum viewport sides of the chamber and two 10 kΩ-thermistors sense the temperature in the centre of the chamber. As the electronic board of the temperature controller needs to drive a constant current above $1A$ to the foil heaters and its equilibrium temperature differs by some degrees from room temperature, it is stabilised itself by means of an identical temperature controller, to prevent thermoelectric voltage fluctuations affecting the regulation. As already mentioned, the apparatus including the resonator assembly and the necessary optical and electro-optical elements are isolated from the surrounding environment by an insulating box, which also substantially contributes in stabilising the air temperature around the vacuum vessel owing to the presence of a thick rubber-based foam layer. In addition, the two EOMs used to modulate the 1156.8 nm and 1111.6 nm beams in-coupled to the ULE cavity are placed inside this box. The temperature of a thick aluminium plate to which they are fixed is stabilised

[30] Paulstra Strasonic - 22 mm thickness
[31] Gamma Vacuum 3S
[32] Ing. Büro R. Tschaggelar (http://www.ibrtses.com/products/tec.html)

close to the equilibrium air temperature inside the box ($\sim 28^{\circ}$C) with fluctuations lower than 0.1°C; therefore, this also partly contributes to maintain the box inner temperature constant and independent from the outer temperature (22°C).

Temperature regulation of the resonator within 0.1°C from T_0 and with a stability below 5 mK allows for a long-term[33] frequency stability below 100 Hz (see Appendix C), which is sufficient for our requirements yet could be improved using a superior PID controller. In addition to the ULE spacer, also the ULE mirror substrates and their optical coating can expand or contract due to temperature variations. The mirrors expansion is included in our characterisation of the cavity thermal frequency shift, and their expansion is anyhow expected to partially compensate the expansion of the ULE spacer, i.e. when the mirror substrates expand the resonator length decreases and vice versa. On the other hand, the temperature of the optical coatings is mainly dominated by absorption of the light present in the cavity, which should be kept low in order to minimise the frequency offset between the "bright" and the "dark" cavity. Typical power dependent shifts for resonators with a finesse comparable to ours are on the order of 10 Hz/μW [301]. We inject approximately 10 μW into the resonator and the light power fluctuations are very well below μW: we expect therefore a steady-state absorption-induced constant shift on the order of 100 Hz and fluctuations well below 10 Hz. For lasers with sub-Hz short-term stability, the intensity-induced thermal noise of the mirrors becomes important as well [302, 303]; however it has a negligible contribution in our system with 10 Hz short-term stability. Even for a perfectly mechanically and thermally insulated resonator, a linear frequency drift caused by the ageing of the ULE spacer is present, which in our setup is measured to be 40 mHz/s (resulting in 80 mHz/s on the clock frequency-doubled light). Fortunately, this drift is constant in time and can be compensated with a feed-forward correction of the clock laser frequency, i.e. by shifting the frequency offset between the laser and the resonator linearly in time with the appropriate slope. In the following we will explain how the laser can be locked with an adjustable frequency offset to the cavity, inheriting its stability and reducing its linewidth.

3.4.3 Laser linewidth narrowing and absolute frequency stabilisation

Our infrared ECDL laser is locked to the ULE cavity by means of the Pound-Drever-Hall (PDH) technique [304, 305]. In atomic physics experiments, the PDH technique is ordinarily used to lock the average frequency of a laser to a cavity reference, in order to compensate for the drifts of the laser without affecting its linewidth. In order to shrink the laser linewidth, the phase of the laser needs to be locked: this can also be achieved using the PDH technique (in reflection) to lock the laser to a narrow reference cavity. A narrow cavity filters all the incoming laser high-frequency phase fluctuations thanks to its low-pass characteristic behaviour, acting as a flywheel. The PDH technique works in this regime prevalently as a phase lock between the laser light directed to the cavity and the light already stored in the cavity [304], effectively comparing the instantaneous laser

[33] The short-term (~ 10 s) stability of the temperature regulation is only known to be smaller than 5 mK, but it is plausibly below a mK.

phase with its historical average. In this way, laser linewidth reduction to values much smaller than the cavity linewidth itself becomes possible [306].

When implementing a tight PDH lock with the goal of narrowing the laser linewidth by several orders of magnitude, the demands on the control loop gain and bandwidth are quite exceptional. Ideally, one would like to reduce the frequency noise of the laser across the whole spectrum; practically, this is obviously impossible, owing to the finite bandwidth of the feedback loop. However, the frequency noise in different regions of the spectrum contributes very differently to the linewidth of a laser. It can be shown that only the high modulation index part of the frequency noise spectral density, i.e. the portion of spectrum where the amplitude of the noise is larger than its frequency, contributes substantially to the width of the power spectral distribution [299]. This has the important implication that, in order to shrink the laser linewidth, it is sufficient to suppress the laser frequency noise up to a frequency on the order of its initial linewidth [299], in our case 100 kHz[34]. The laser frequency noise can be maximally reduced to the lock detector noise level, and starting from 100 kHz, a very high gain of more than 80 dB is required to bring the linewidth below 10 Hz. On the other hand, for some high frequency the closed-loop transfer function will have a pole, i.e. the phase of the loop transfer function reaches 180°, making the loop unstable if the gain at this frequency is larger than unity. The bandwidth of the control loop needs therefore to be large enough for the gain to decrease from its high low-frequency value to 0 dB before the location of the pole. That explains the reason for implementing as fast as possible feedback loops for linewidth shrinking applications of the PDH technique: the bandwidth is not needed to compensate very high frequency noise components, which are rather unimportant, but mainly to push the position of the closed-loop pole as far as possible towards high frequencies and leave sufficient room for the closed-loop gain to decrease to 0 dB.

An implementation of the PDH lock to the ULE cavity of both our green and clock laser sources has been already described in Ref. [296]. However, important changes were subsequently implemented to improve the performance of the lock, mainly concerning the actuators which convert the PDH lock signals into a laser frequency correction. In particular, we initially attempted to exploit the ECDL current modulation as a fast regulation of the laser frequency, but this approach has shown itself to be ineffective to reach a laser linewidth below kHz. The frequency response of the laser diode to current modulation was found to be much slower than expected [296] and, although attempts were made to overcome such an issue by additional electronics, a different better-performing alternative was found, namely frequency regulation by a AOM with a sufficiently high modulation bandwidth. We will not describe the details of the control loop design and characteristics, which can be found in the above mentioned reference. The current optical setup in the vicinity of the ULE cavity is displayed in Fig. 3.16(a).

Our feedback loop comprises the standard four main blocks: the frequency detector, the controller, the transducers and the laser. The phase/frequency deviation detector consist of the ULE resonator along with the lock photodiode[35], detecting the modulated PDH

[34] A much lower frequency threshold in the order of a few kHz should actually suffice, considering that the laser noise spectral density decays with a characteristic 1/f dependence.

[35] Thorlabs PDA10CF

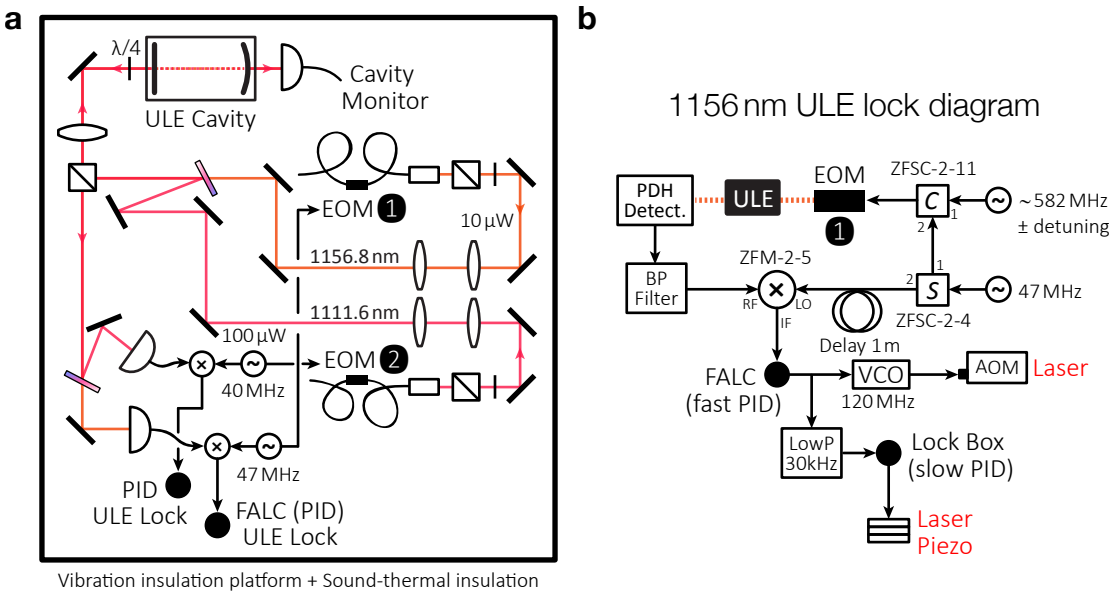

Figure 3.16 – (a) A schematic of the ULE resonator section of the laser system. Low-power beams at 1111.6 nm and 1156.8 nm are injected to the resonator, after being modulated in high-bandwidth fibre-coupled EOMs. These EOMs generate the high-frequency sidebands which are locked to the ULE cavity, allowing the laser carriers frequency to match the position of the atomic resonances; they moreover create the sidebands required for the operation of the PDH lock, at 40 MHz and 47 MHz respectively. Using a quarter wave-plate in front of the cavity input, the light reflected back from the cavity is diverted off the incoming beam path by a PBS and directed onto two fast photodetectors. The two laser wavelengths are combined and separated through angle-tuned dichroic beamsplitters. The detected signals are down-mixed and fed to PID controllers which regulate the respective laser frequencies via different transducers (see text and panel (b)). (b) Pound-Drever-Hall (PDH) frequency lock scheme for the 1111.6 nm clock laser. A power splitter (C) combines two stable RF-signals at 47 MHz and approximately 582 MHz to create a double set of sidebands, driving a fibre-coupled EOM placed in between the laser source and the ULE resonator setups. One of the high-frequency sidebands is locked to the ULE cavity thanks to its lower-frequency sidebands. Part of the 47 MHz RF-signal is sent to a mixer, in order to down-convert to lower frequencies the photodetector signal, carrying the information about the frequency deviation of the relevant laser sideband from the cavity resonance. The down-converted error signal, i.e. the PDH error signal, is fed to a fast PID controller (FALC). On one branch, this directly drives a VCO controlling an AOM which can implement fast laser frequency corrections. On another branch, the error signal is low-passed and fed to a slower PID controller which drives the piezo adjusting the ECDL cavity length.

error signal at 47 MHz, which is subsequently band-pass filtered, down-mixed to low frequencies, low-pass filtered and fed to the controller. The main controller is a commercial fast PID controller with a bandwidth of 10 MHz[36] and a maximum DC gain of 80dB; three separate integrator gain stages, acting on different frequency ranges, can be individually adjusted to produce the desired transfer function. An additional house-built PID controller with a low bandwidth of 30 kHz is placed in a cascade configuration after the fast PID controller, providing the necessary additional low-frequency gain. The ECDL frequency is regulated by two voltage-to-frequency transducers: (i) the piezo element varying the cavity length of the ECDL, by displacement of the diffraction grating and (ii) the AOM placed directly after the Faraday isolators on the infrared beam path (see Fig. 3.14), driven by

[36]Toptica FALC 110 - High-speed output

a in-house custom-made VCO with a modulation bandwidth exceeding 5 MHz. The high low-frequency gain provided by the two PID controllers in series allows the piezo actuator to compensate the largest frequency deviations, making the lock quite stable to external disturbances and letting the AOM operate around its central frequency of 120 MHz with maximum deviations on a MHz scale. A diagram of the PDH control loop is shown in Fig. 3.16(b).

As the frequency of the cavity resonances is fixed, the laser needs to be independently adjusted to the desired frequency while locked to the stability of the ULE cavity. To this end, it is not the laser carrier which is directly locked to the ULE resonator but a high-frequency sideband generated by a custom-made fibre-coupled EOM from Jenoptik with a bandwidth of 5 GHz, as depicted in Fig. 3.16 (see also Fig. 3.11. This EOM is used to create the offset sideband (located at approximately +582 MHz for ^{173}Yb), as well as the sidebands at ±47 MHz required for the PDH locking technique.

The position of the closed-loop pole, i.e. the lower bound for the time response of the circuit, is determined by the delay accumulated by the driving signal before reaching the light inside the AOM: the RF signal needs to travel to a transducer and subsequently propagate as a sound wave inside the crystal to finally reach the laser beam. We chose an AOM[37] with a 0.8 mm small crystal, to be able to efficiently act on a small beam, minimising the distance to the electrode; a beam waist of approximately 100 μm is adopted and the AOM is mounted on a translational stage to be able to displace it and precisely minimise the delay.

A servo bandwidth of approximately 800 kHz is achieved; this value is reached after the gain settings and the different integrator corner frequencies of the fast PID controller are optimised, by analysing the noise spectral density suppression with a network analyser (see Appendix C). Increasing the light power injected into the ULE cavity does not improve significantly the noise suppression, as an indication that the lock is not currently limited by the noise of the PDH photodiode.

The only way to directly characterise both the short-term and the long-term stability of the laser locked to the ULE cavity is to analyse its beat note with a laser possessing a comparable or superior stability[38]. Since neither a comparable laser or a frequency comb are provided in our laboratory, the laser performance is directly tested by atomic spectroscopy on the clock transition (see Chapter 5). It should be stressed that the important figure of merit for our experiments is indeed the atomic spectroscopy linewidth; a stability evaluation of the laser alone should only be considered as a way to address specific issues or test ongoing technical developments. A minimum spectroscopy linewidth of approximately 40 Hz was observed, indicating a stability of the infrared laser on the order of 20 Hz over several minutes, which is the time scale required to execute a complete spectroscopic measurement. The detuning of the laser can be varied only between one experimental cycle and the next, by varying the driving frequency to the fibre-coupled EOM; a single spectroscopy data point is then collected after each cycle by measuring the residual ground state atomic population.

[37] Crystal Tech. 3120-190

[38] Self-heterodyning is not a viable option as it would require thousands of kilometres of optical fibre delay line

This laser linewidth is most likely currently limited by sources of resonator frequency fluctuations which are not actively compensated, e.g. residual mechanical vibrations, or other optical effects such as etaloning between elements in the PDH lock beam path. Furthermore, the optical fibre carrying the light to the experiment table is a possible source of noise, which can deteriorate the short-term frequency stability at the atoms position. For this reason, a fibre-noise cancellation system is already implemented and is briefly illustrated below.
The long-term stability of the laser is satisfactory as well, and after compensation of the dominant frequency drift caused by ULE ageing, the resonance position does not shift by more than a kHz over a time span of several days. However, occasional shifts on the order of 100 Hz can be observed during the day, probably due to slow environment temperature and pressure variations, which influence the temperature regulation of the cavity assembly.

3.4.4 Excitation pulse shaping and fibre-noise cancellation

Clock excitation pulses for spectroscopy and coherent population transfer are created by regulating the RF power driving the 100 MHz AOM[39], acting on the frequency-doubled light (see Fig. 3.14). The pulse light intensity is monitored by a photodiode on the experiment table in the vicinity of the main chamber and is stabilised by a 100 kHz-fast PID controller, and square pulses as short as 10 μs can be reliably produced. A fibre-noise cancellation system (analogous to the one presented in Ref. [301]) has been implemented to suppress the light frequency fluctuations introduced by vibrations and temperature fluctuations while the light traverses the optical fibre to the experiment table. As illustrated in Fig. 3.14 (see also Appendix C), the light from of a retro-reflecting beam sampler placed before the AOM and the light from a retro-reflecting beam sampler placed on the other side of the fibre can be diverted off the forward light path by means of a Faraday rotator and a PBS. The two combined retro-reflections are made to interfere on a fast photodiode, which detects thus their beat note, centred around twice the AOM frequency. The frequency noise resulting from propagating back and forth through the fibre is consequently detected at 200 MHz as well. The beat signal can be locked to a stable RF source by a fast regulation of the driving frequency to the 100 MHz AOM. To this end, the beat signal is down-converted to low frequencies using a stable RF source into to a PLL circuit, which in combination with a PI controller regulates the frequency of a high-bandwidth VCO, driving the AOM. For details about the design of our PLL circuit, see e.g. [125]. This noise canceller is capable of eliminating the largest part of the fibre-introduced frequency fluctuations (see Appendix C). However, preliminary spectroscopic measurements indicate that this noise is currently not the limiting factor for the final linewidth of the clock laser, and simple open-loop operation with a 100 MHz stable RF source directly driving the AOM is presently preferred. The noise cancellation is expected nonetheless to become essential if laser linewidths closer to Hz-level are achieved in the future.

[39] Crystal Tech. 3100-125

CHAPTER 4

A SU(N)-symmetric Fermi gas with tuneable spin

As discussed already in Chapter 1, one main long-term purpose of the experiments presented in this work is the study of orbital and SU(N) quantum magnetism employing a Fermi gas of ^{173}Yb trapped in an optical lattice. With a total of six nuclear spin states, ^{173}Yb allows for the exploration of intriguing quantum many-body phases beyond the standard SU(2)-symmetric scenario. An essential requirement is however the ability of controlling the number of spin states that are present within the fermionic gas, in order to study the effect of varying N from 1 to a maximum of $2F+1=6$, where $F=I=5/2$ is the total atomic angular momentum of ^{173}Yb (for details about the atomic properties of ytterbium see Chapter 2). Moreover, for many applications related to the simulation of condensed-matter models which describe the behaviour of (spin-1/2) electrons, only two spin states in total need to be used. The flexible production of different single- and two-component Fermi gases is also beneficial for the investigation of two-orbital physics within minimal spin configurations, which result in a simpler description of the system with respect to the many-spin gas case.

For these reasons, the experimental techniques that lead to the manipulation and detection of the nuclear spin degree of freedom are of central importance in the context of quantum simulation with ^{173}Yb. In this Chapter, we will show how the different nuclear spin states of ^{173}Yb can be separately imaged and how arbitrary mixtures of spin states can be prepared by means of optical techniques. The consequent control over the spin degree of freedom in the ground state can also be extended through the coherent coupling to the metastable $^3P_0$ state, achieving control over a total of $2(2F+1)=12$ states (see next Chapter). Another important aspect in view of quantum simulation of SU(N)-symmetric models is the experimental demonstration of the SU(N) symmetry of atomic interactions in ^{173}Yb, which was so far only theoretically predicted. In particular, as we will see, SU(N) symmetry in the ground state results in the collisional stability of any arbitrary spin-state mixture over long time scales. This system is especially suited for the comparison between theory and experiment, since any isolated many-body state with N spin states occupied remains confined within the N-dimensional spin subspace.

4.1 Nuclear spin detection and manipulation

In this Section we will present the experimental technique for the detection of the spin degree of freedom in a fermionic ultracold gas of ytterbium. All techniques presented in this and the next Sections were obtained adopting ^{173}Yb, but could be directly implemented with an ultracold gas of ^{171}Yb. We start by briefly recalling the absorption imaging technique to then explain in detail the optical Stern-Gerlach nuclear spin detection scheme and the preparation of arbitrary spin-state mixtures through optical pumping on the green intercombination transition.

4.1.1 Absorption imaging

Absorption imaging is the most consolidated experimental technique for detecting the density distribution of cold atomic ensembles [14]. The concept behind this method is very simple: atoms absorb resonant laser light and their shadow can therefore be imaged on a CCD sensor array. A collimated beam resonant with a strong dipole transition, in our case the $^1\mathrm{S}_0 \rightarrow {}^1\mathrm{P}_1$ ($F = 5/2 \rightarrow F' = 7/2$) transition, is directed on the atomic sample, with a waist size much larger than the cloud extension. For low-intensity light, the beam is attenuated by the atomic sample following the Lambert-Beer law, as photons get absorbed and re-emitted in a random spatial direction. The reduction in the initial intensity profile $I_0(x,y)$ of a beam propagating along the z-axis through the atomic density distribution is given by:

$$I(x,y) = I_0(x,y) \exp\left(-\sigma_0 \int dz\, n(x,y,z)\right) \tag{4.1}$$

where σ_0 is the scattering cross section[1] of the atomic transition, which characterises the probability of absorption of a photon by an atom. The intensity therefore decreases exponentially as a function of the local density $n(x,y,z)$ of the atomic distribution integrated along the beam propagation direction, i.e. the column density of atoms. A CCD camera can be used to detect the imaged intensity profile of a beam at the location of the atomic sample. In a typical experimental sequence, two separate images are consecutively collected: a first image with the atoms present and absorbing the light, and a second reference image with no atoms present. Each pixel of the CCD camera, labeled by its coordinates in the (x,y)-plane, is therefore used to detect both the attenuated light intensity $I(x,y)$ and the initial light intensity $I_0(x,y)$. By combining these two signals, the column atomic density for each pixel can be retrieved:

$$n_{\mathrm{col}}(x,y) = -\frac{1}{\sigma_0} \ln\left(\frac{I(x,y)}{I_0(x,y)}\right) \tag{4.2}$$

A strong transition is preferably used for imaging as a high photon scattering rate is favourable: shorter light pulses give a superior performance with respect to time accuracy, provided that a sufficient signal to noise ratio is achieved by the CCD sensor. Absorption imaging can be used to obtain both the *in situ* density distribution, i.e. the density distribution of the atoms while trapped either in a crossed dipole trap or in an optical lattice,

[1] For low light intensity ($I \ll I_{\mathrm{sat}}$) and a closed stretched transition, $\sigma_0 = 3\lambda_0^2/2\pi$ [86, 97].

and their momentum distribution, by allowing them to freely expand for an adequate time of flight before the image is taken. A time-of-flight measurement is initiated by simultaneously switching off all trapping potentials and letting the cloud move only under the influence of gravity. In the absence of other potentials, the atomic distribution evolves according to its initial momentum distribution, and for a sufficiently long expansion time the initial size of the cloud can be neglected, so that the observed density distribution is directly representing the momentum distribution of the atoms. Momentum distributions obtained in this way are shown in Section 2.2.4, in the context of the production of degenerate gases of ytterbium.

Band mapping

The quasimomentum distribution of atoms trapped in an optical lattice can also be obtained by time-of-flight imaging, through the so-called band mapping technique [14, 30, 307, 308]. Atoms are released from the optical lattice by smoothly turning off the light potentials in order to avoid excitations to higher Bloch bands, however still quickly compared to the tunnelling dynamics in the lattice. All atoms follow therefore adiabatically the band structure during the lattice ramp-down, and the quasimomentum distribution of the desired initial state is mapped onto free-space momentum in an unambiguous way. The population of each Bloch band is mapped into the population of separate free-space Brillouin zones, as sketched in Fig. 4.1(a). In Fig. 4.1(b) the momentum distribution obtained by applying the band mapping technique on a very large gas of spin-polarised ^{173}Yb is shown, and atoms occupying several Brillouin zones are visible. Another image obtained by band mapping with a smaller two-spin degenerate Fermi gas of ^{173}Yb out of a lattice is shown in Fig. 4.2, where sections of the density distribution along the two horizontal directions are also shown.

In-situ imaging

In situ density profiles can be obtained through absorption imaging with a resolution limited only by the optical system used to carry the atoms image onto the CCD sensor. A high-resolution density detection constitutes a useful tool for probing local observables of atomic samples, such as local density fluctuations, which can reveal characteristic signatures of correlated many-body phases [219]. For that purpose, an imaging system with a resolution well below the typical cloud sizes of 10-100 μm is needed, and was recently implemented in our experimental setup. With an imaging wavelength of 399 nm, an imaging system with a numerical aperture NA ≈ 0.35 is sufficient for a resolution $r \lesssim 1\,\mu$m (see Section 3.2).

4.1.2 Nuclear spin state-sensitive imaging

Optical Stern-Gerlach scheme

The usual experimental technique for spatially separating atoms in different spin states is to apply a magnetic field gradient and let the atomic cloud fall under the influence of

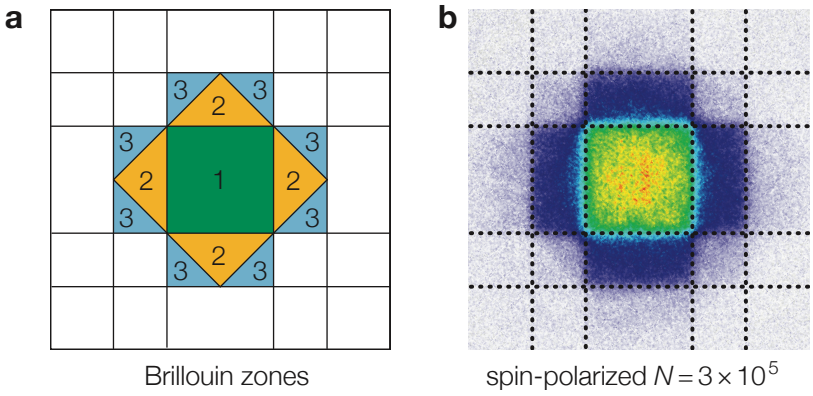

Figure 4.1 – Band mapping in an optical lattice. (a) Illustration of the first three Brillouin zones in the $x - y$ plane for a square lattice potential. The first Brillouin zone extends from $-\bar{k}$ to $+\hbar k$, where k is the lattice wave vector. (b) A spin-polarised gas of ^{173}Yb is loaded into a three-dimensional cubic optical lattice and the quasi-momentum distribution in the horizontal plane is imaged through the band mapping technique. The populations of different (excited) Bloch bands is mapped to population of distinct Brillouin zones in two dimensions. A large atom number $N = 3 \times 10^5$ and a temperature above degeneracy result in several Bloch bands to be populated. By integrating the atomic column density over the different rectangular regions, the population of the excited bands can be determined. A lattice ramp-down time around 2 ms is found to yield the best Brillouin zone distinguishability.

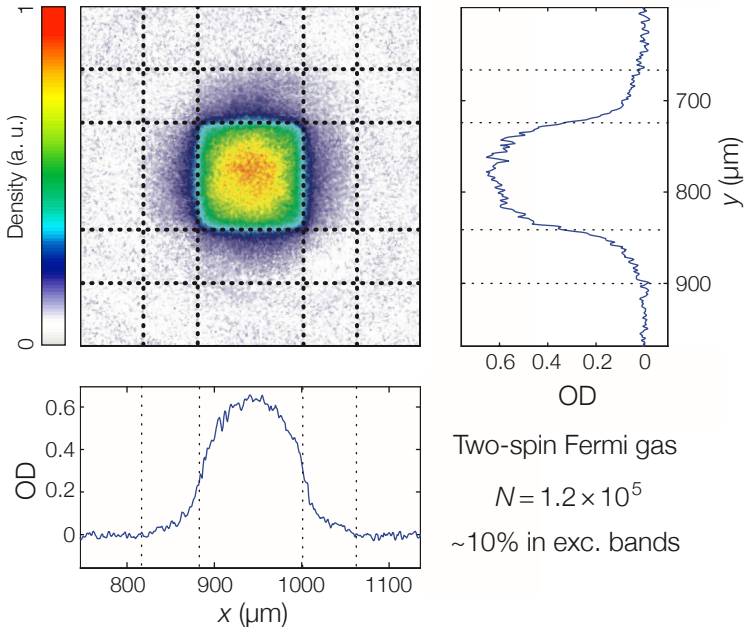

Figure 4.2 – Band mapping of a two-spin Fermi gas with a total atom number $N = 1.2 \times 10^5$ atoms and a temperature $T \simeq 0.25\, T_F$. The depth of the two horizontal lattices along x and y directions at the moment of the release is $V = 15\, E_r$ and a TOF of 20 ms is used. A fraction of approximately 10% of the population is found in the rectangular Brillouin zones along the two directions, indicating an equivalent population of the first excited Bloch bands.

the resulting state-dependent magnetic force. This technique exploits the Stern-Gerlach effect: when moving into a linearly varying magnetic field, atoms in different internal states will experience a constant force proportional to their magnetic moment [309]. After some time of flight, the atomic density distribution is divided in regions corresponding to the different states, which can then be imaged and counted independently. This scheme works quite simply for alkali atomic species and it is widely used to separate the different m_F states [109]. The m_F-dependent magnetic moment of the electronic ground state is large enough to obtain sufficient spacial separation with magnetic field gradients of a few G/cm, which are easily attainable. On the other hand, AEL atoms as ytterbium possess a nearly zero magnetic moment both in the ground and in the metastable state owing to the lack of electronic angular momentum, $J = 0$. In order for only the weak nuclear magnetic moment to provide a sufficient spatial separation, extremely large and hardly achievable magnetic field gradients would be required.

For this reason another method to implement an m_F dependent separation is used, so that a state-dependent force can instead be produced by optical means. One usually refers to such an implementation as optical Stern-Gerlach (OSG) scheme [71, 310, 311]. We first discuss the general operation principle of the OSG scheme on fermionic AEL atoms and subsequently describe our specific experimental implementation, which is illustrated in Fig. 4.4. The key ingredient for the OSG separation of an atomic cloud released from a trap is the application of a state-dependent optical dipole force. One way to generate a sufficiently strong force is shining a circularly polarised light beam closely detuned with respect to a dipole optical transition. The reason why the magnitude of such a dipole force is dependent upon the m_F state of the atoms is found in the nuclear spin and polarisation-dependent line strength of each transition within the magnetic substructure of any dipole transition. Details on how to calculate the line strengths are given in Appendix A.

In ^{173}Yb, the $^1\mathrm{S}_0\,(F, m_F) \rightarrow {}^3\mathrm{P}_1\,(F', m_F \pm 1)$ transition strengths vary by a large factor

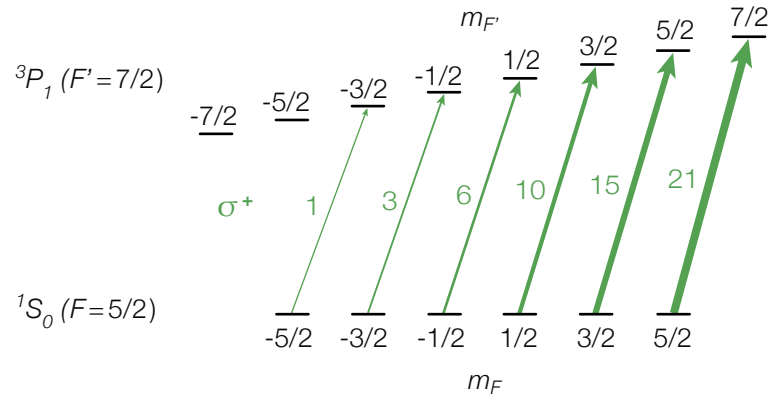

Figure 4.3 – Line strengths for the $^1\mathrm{S}_0\,(F = 5/2) \rightarrow {}^3\mathrm{P}_1\,(F' = 7/2)$ transitions with $\Delta m_F = +1$ (σ^+-polarised light). The strengths are normalised to the weakest allowed transition. A significant nuclear spin state-dependent force can be created by shining a circularly-polarised beam closely detuned to these transitions, as the dipole force experienced by each state depends on the line strength of the corresponding transition.

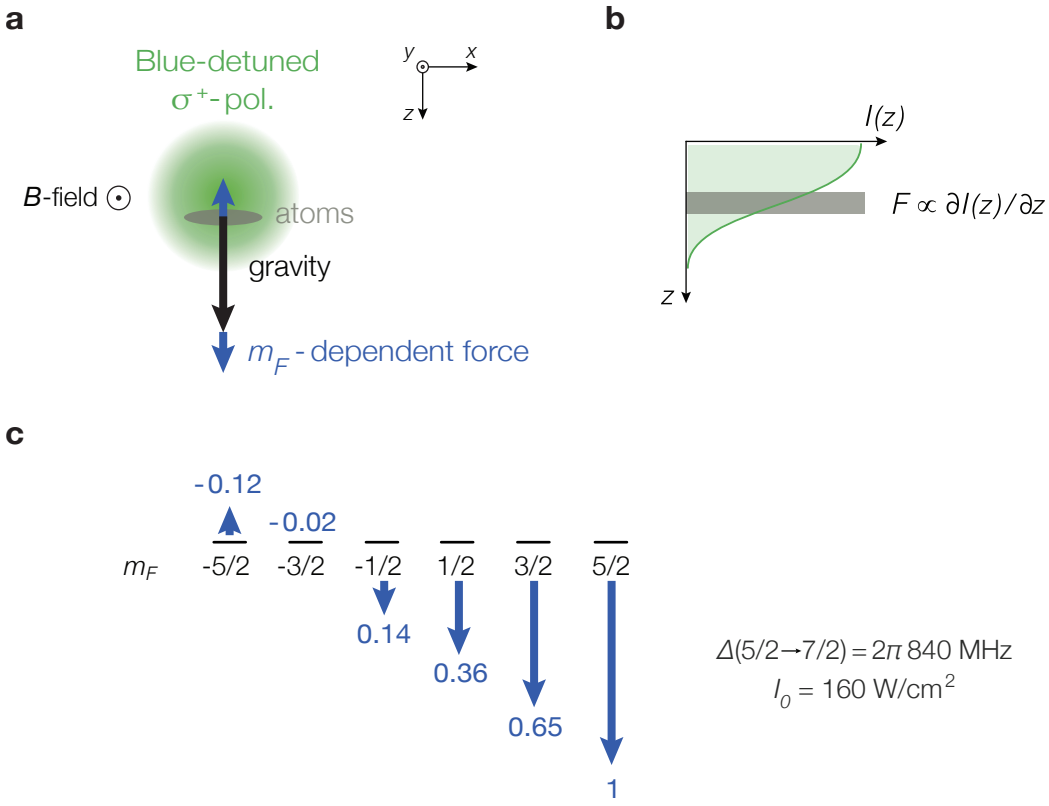

Figure 4.4 – Illustration of the operating principle of the optical Stern-Gerlach method. (a) A blue-detuned σ^+-polarised laser beam is aligned above the atomic cloud, in order to have its maximum intensity gradient at the cloud position in the trap. (b) A spin state-dependent dipole force proportional to the local light intensity gradient is produced, dominantly pointing downwards. (c) The resulting light forces on different spin states can be calculated for a given light detuning, polarisation and intensity. The (normalised) forces acting on different spin states are given, normalised to the maximum one.

across the different m_F states, as displayed in Fig. 4.3 for the $F = 5/2 \rightarrow F' = 7/2$ hyperfine transition with σ^+-polarised light (all line strengths of the different hyperfine transitions are given in Appendix A). As a consequence, the magnitude of the dipole potential obtained by shining on the atoms a circularly-polarised light beam closely detuned to this transition is monotonically dependent upon the m_F state (see Eq. (A.8)). The generated force is proportional to the optical intensity gradient applied to the atoms; it can be made approximately uniform by aligning the beam so as to present a linearly varying intensity over the atomic cloud, as depicted in Fig. 4.4(b). A blue detuning and a red detuning are suited for σ^+ and σ^--polarised light, respectively, so that the detuning is the smallest for the strongest m_F transition. In this way the force reduction due to the increasing detuning adds up to the effect of the decreasing line strengths, as visible from Fig. 4.3.

Experimental aspects

In our experimental setup, a gaussian circular beam with 40 mW of power at 556 nm is directed along the y-axis and is right-circular polarised (see Fig. 4.4(a)). A uniform magnetic field of 4 G is applied also along the y-axis, in order to provide a quantisation axis such that the light only couples to the σ^+ transitions. The OSG beam is focused at the atomic cloud position with a waist $w_0 \simeq 75\,\mu$m, with its centre displaced above the cloud by approximately half a waist size. The frequency detuning of the beam from the $^1S_0\,(F = 5/2) \rightarrow {}^3P_1\,(F' = 7/2)$ is positive: $\Delta_{5/2} \simeq 2\pi \cdot 840$ MHz. On the other hand, the detuning from the $^1S_0\,(F = 5/2) \rightarrow {}^3P_1\,(F' = 5/2)$ and $^1S_0\,(F = 5/2) \rightarrow {}^3P_1\,(F' = 3/2)$ hyperfine transitions is negative and respectively equal to $\Delta_{5/2} \simeq -2\pi \cdot 3.9$ GHz and $\Delta_{3/2} \simeq -2\pi \cdot 5.4$ GHz. The influence of the two further red-detuned transitions is not negligible and it actually gives a favourable contribution, as it generates a significant up-pushing force on the $m_F = -5/2$ state which helps in separating it entirely from the $m_F = -3/2$ state. All the resulting forces in such a configuration are depicted in Fig. 4.4(c), calculated taking into account the line strengths of the three different hyperfine transitions in ^{173}Yb for σ^+-polarised light (see Appendix A). The forces have a very weak dependence upon the applied magnetic field, as the corresponding Zeeman shifts are small (see Fig. 4.6(b) below) compared to the light detuning from resonance.

The OSG separation sequence starts by switching off the optical dipole trap and simultaneously switching on the OSG beam, after adiabatically ramping the magnetic field to the desired value. The cloud needs approximately 3 ms to fall out of the OSG beam waist; the OSG light is on for a duration of typically 4 ms, and longer pulses do not increase the state separation. Atoms are then falling under the influence of gravity alone for a time of flight of 10 ms to 14 ms, which is appropriate in order for the states to be well distinguishable. Absorption images are taken using linearly polarised light resonant with the $^1S_0 \rightarrow {}^1P_1$ transition with a weak external magnetic field of 2 G applied. Experimental images of mixtures of all six spin states are shown in Fig. 4.5. The atoms in different m_F states are counted trough six integration regions, each suitably defined to include only atoms of an individual spin state, as depicted in Fig. 4.5(b).

As the waist size of the OSG beam in the horizontal direction is larger than but comparable to the horizontal atomic cloud size, the dipole force generated by the intensity gradient is not exactly vertical across the entire sample. This explains the evident curvature in some of the m_F states imaged after time of flight, as shown in Fig. 4.5. The curvature is more visible on the states which experience the largest downward force.
The choice of blue detuned OSG beam has another consequence, which is an advantage compared to a red detuned beam. While the atoms are pushed down by the light force, the vertical extension of the each cloud corresponding to the various spin states is reduced, compared to a free time of flight, and this of course improves the state separation. As atoms are accelerated away from the region of highest light intensity, they get "jammed" together, resulting in more compact distributions in the direction of the force. In order to obtain a sufficient separation of the spin states, the beam vertical alignment and the timing of the OSG sequence need to be carefully adjusted. Depending on the vertical alignment and the power of the OSG beam, either the separation or the distortion of the different

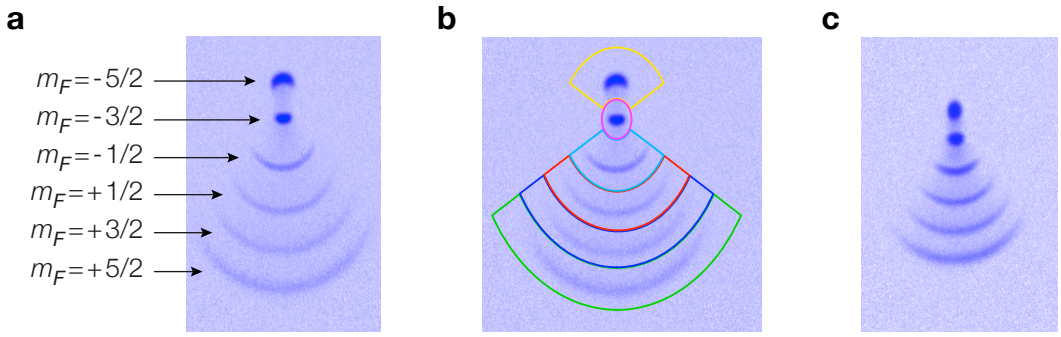

Figure 4.5 – Optical Stern-Gerlach separation of the nuclear spin states. A 3.5 ms OSG light pulse is applied at the release of the gas from the dipole trap and absorption imaging is performed after a time-of-flight expansion of 12 ms. (a) A close alignment of the OSG laser beam to the atomic cloud position in the trap produces a superior spin-state separation but a large deformation of the density distribution as well (b) Suitable integration regions are defined to determine the absolute population of each spin state. As the spatial separation is large enough to have a negligible overlap between different spin-state distributions, no further analysis is necessary. (c) With the OSG beam aligned further away from the atomic cloud centre, both the state separation and the deformation are reduced.

density distributions can be optimised, as visible in the comparison between Fig. 4.5(a) and (c). The OSG method provides a good state distinguishability only for very cold ensembles: when the temperature is too high, atoms expand too fast and the different state distributions start overlapping. All the images displayed in this and the next Section are taken for a ^{173}Yb gas at a temperature well below Fermi degeneracy.

One great disadvantage of the OSG technique compared to a standard Stern-Gerlach method is the nearly complete loss of information about the momentum distribution of the various spin states. All the spin states are in thermal equilibrium before releasing the gas from the trap, so that simultaneous time of flight expansion followed by absorption imaging is sufficient to estimate the global temperature of the Fermi gas. Nevertheless, the spin state number distribution cannot be measured at the same time as the temperature, since the spin state momentum distributions are largely deformed by the OSG force during the initial part of the expansion. The decision of exploiting the $^1S_0 \rightarrow {}^3P_1$ transition for OSG as opposed to the $^1S_0 \rightarrow {}^1P_1$ transition is motivated by its narrow linewidth: only a relatively small detuning is required to prevent excessive heating of the atomic cloud by photon scattering. The OSG light can thus be supplied by the same laser source that is tuned into resonance with the green MOT transition. The required detuning is produced through an acousto-optic modulator in a double-pass configuration (see Section 3.3.2).

State-dependent detection efficiency

In order to correctly determine the integrated atom number in each nuclear spin state, or at least to correctly estimate the relative population of each state, the influence of the imaging light polarisation has to be considered. When an internal magnetic substructure is present in the electronic states connected by the transition used for absorption

imaging, the choice of polarisation of the imaging beam becomes indeed very important. The conventional approach is to maximise the absorption cross section by using circularly polarised light, driving a strong $\Delta m_F = \pm 1$ stretched transition [86]. In the case of ^{173}Yb, this would correspond to using a $\sigma^{\pm}$-polarised imaging beam resonant with the $^1\mathrm{S}_0\,(F = 5/2, m_F = \pm 5/2) \rightarrow {}^1\mathrm{P}_1\,(F' = 7/2, m'_F = \pm 7/2)$ transition. However, in some circumstances this is not the most appropriate option, in particular when an equal detection efficiency for all m_F states is desirable. In our system, approximately 100 photons are scattered within the typical imaging pulse duration of 80 μs, and optical pumping processes, namely cycles of absorption and emission that drive the atomic population towards the stretched states, have a non-negligible effect. The total absolute number of scattered photons has a dependence on the initial population distribution over the different nuclear spin states, essentially owing to the m_F-state dependent line strengths of the imaging transition (see Fig. A.1), which cause states with weaker line strengths to scatter comparatively fewer photons before being finally pumped to a stretched state. In order to minimise the effect of the initial spin state on the detection efficiency, we opted for employing linearly polarised light propagating along the quantisation axis defined by the weak external magnetic field. In this way, the imaging light couples equally to both $\sigma^{\pm}$ transitions, and the spin-state dependence is almost completely suppressed[2]. As a drawback, the atoms spend more cycles populating the spin states with the weaker line strengths, and therefore the overall detection efficiency is slightly lower than the one obtained with circularly polarised imaging light. A calibration of this reduction gives a correction factor on the measured atom number N_{lin} in a six-component ^{173}Yb gas[3]: $N_{\mathrm{circ}} \simeq 1.4\,N_{\mathrm{lin}}$.

4.2 Nuclear spin state preparation

In this Section we will present the experimental technique for the preparation of arbitrary spin mixtures with ^{173}Yb. Our implementation is based on multiple-pulse optical pumping on the green intercombination transition. The protocol exploits the individual nuclear spin-state addressability obtained by tuning the frequency and the polarisation of the pumping laser light, when a sufficiently strong external magnetic field is applied. Thanks to the collisional stability of any spin mixture stemming from the SU(N) symmetry of the interactions, the number of participating spin states in the system can be tuned to explore SU(N)-symmetric models with dimension N varying from 1 to 6. We will first summarise the operating scheme of the spin mixture preparation to then discuss the experimental details of our implementation.

4.2.1 Spin state-resolved addressing of the intercombination transition

There exists a variety of optical pumping scheme implementations devoted to the preparation of specific or arbitrary mixtures of the nuclear spin states of ^{173}Yb or of other

[2] In particular, the bias is completely absent for spin-mixture preparations including only two opposite-m_F spin states.

[3] The correction factor is different for mixtures with a smaller subset of populated spin states, e.g. it is close to 1 for a symmetric mixture of the stretched states only.

fermionic AEL atoms [71–73, 311]. The most simple implementations are based on optical pumping to stretched (possibly dark) states through the application of light pulses resonant with the $^1S_0 \rightarrow {}^1P_1$ or $^1S_0 \rightarrow {}^3P_1$ transitions and circularly/linearly polarised along a weak magnetic field, which serves exclusively to set the angular momentum quantisation direction. Although the simplicity of such schemes is a clear advantage, a very limited variety of balanced spin state combinations is attainable in this way. Only spin-polarised samples of one stretched state ($m_F = +5/2$ or $m_F = -5/2$) and few balanced two-component mixtures of the stretched states were thus implemented [71, 72]. By applying a stronger magnetic field, all m_F states of the of the $^3P_1$ state can readily be split with a shift between neighbouring spin states that is larger than the linewidth of the $^1S_0 \rightarrow {}^3P_1$ transition and of the green laser source (see Fig. 2.5). All transitions connecting different m_F states can therefore be separately addressed simply by tuning the

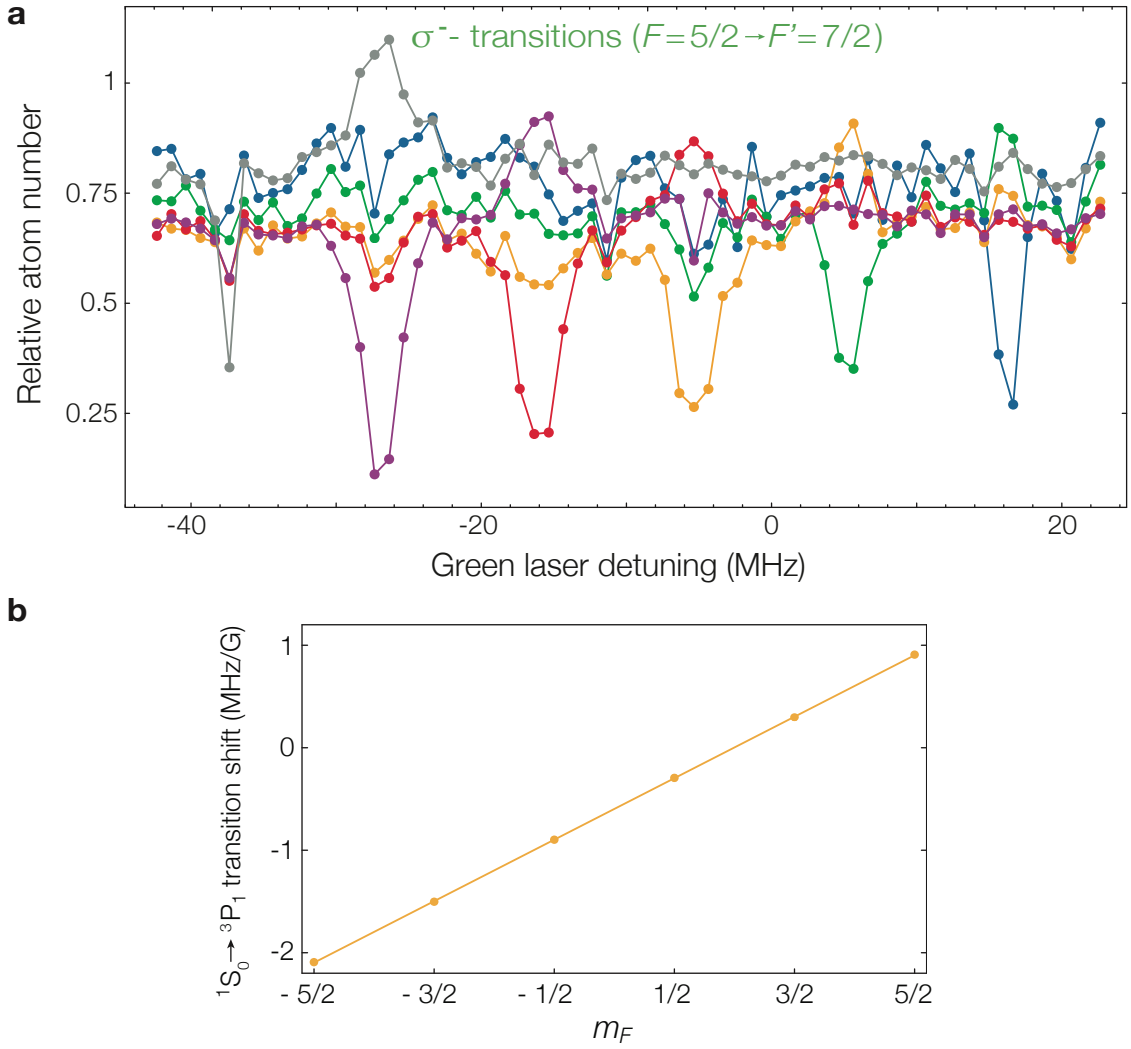

Figure 4.6 – (a) Spectroscopy of the $^1S_0(F = 5/2) \rightarrow {}^3P_1(F' = 7/2)$ transition with σ^--polarised light in a magnetic field $B \simeq 18$ G. (b) The measurement is used for the calibration of the magnetic coils and for the adjustment of optical pumping pulse frequencies.

frequency and the polarisation of the excitation laser. In Fig. 4.6 the spectroscopy of the $^1S_0\,(F = 5/2, m_F) \rightarrow {}^3P_1\,(F' = 7/2, m'_F = m_F - 1)$ transitions in a magnetic field of 18 G is shown. By means of subsequent multiple $\sigma^{\pm}$-polarised light pulses, individually resonant with the various $^1S_0\,(F = 5/2, m_F) \rightarrow {}^3P_1\,(F' = 7/2, m'_F = m_F \pm 1)$ lines, any combination of spin states can be prepared, as exemplified in Fig. 4.7 for different target spin combinations.

4.2.2 Optical pumping on the intercombination transition

The same light beams used for cooling in the green MOT are used for the implementation of the optical pumping sequence. A uniform magnetic field of 18 G is produced by the MOT coil pair, which is rapidly switched from an anti-Helmholtz to a Helmholtz configuration after the atoms have been loaded from the MOT to the optical dipole trap. The pumping light is applied shortly after the atoms have been transferred to the dipole trap, in the very initial stage of the evaporation. The two vertical MOT beams, which are circularly polarised and couple only to the required $\sigma^{\pm}$ transitions, are sequentially pulsed according to the desired preparation protocol.

The near-abrupt switching of the magnetic field substantially contributes in depolarising the atomic sample after cooling in the MOT. In the last stage of the cooling at low light intensity, the atoms preferentially absorb photons from the MOT beam propagating against gravity; this uneven absorption effectively results in some degree of spin polarisation, i.e. imbalance between different m_F states. For the preparation of balanced few-component mixtures, it is highly desirable to start from a balanced six-component ensemble, as an initial spin imbalance may propagate to the final distribution. The diabatic field switching projects the ensuing spin mixture at the end of the optical cooling into position-dependent coherent superpositions of spin states, which then dephase during the evaporation due to magnetic field inhomogeneities or optical pumping photon scattering. The measured relative spin distribution at the end of the evaporation (without any optical pumping sequence applied) is found to be $p_{m_F} = \big(0.18(1),\, 0.14(1),\, 0.15(1),\, 0.15(1),\, 0.18(1),\, 0.20(1)\big)$ for $m_F = -5/2, \ldots, +5/2$. Part of the residual imbalance could be due to the linear polarisation of the imaging light beam (see previous Section). It is important to point out that only statistical mixtures of different spin states can be engineered by optical pumping schemes based on cycles of photon absorption and spontaneous emission, as the emission obviously destroys any coherent superposition between spin states. One way to engineer coherent spin-state superpositions exploits schemes based on off-resonant two-photon Raman processes, by which two ground state spin states at a time are coherently coupled by two laser fields, equivalently to optical Raman coherent coupling of internal states of alkali atoms [101, 312]. Nevertheless, the preparation of arbitrary nuclear spin superpositions is more desirably achieved through the coherent coupling to the different magnetic sub-levels of the metastable $^3P_0$ state [59], which completely eliminates the problem of spontaneous photon emission. Such couplings can be implemented by using σ-polarised clock excitation light and magnetic fields of just a few Gauss, as it will become clear in the next Chapter.

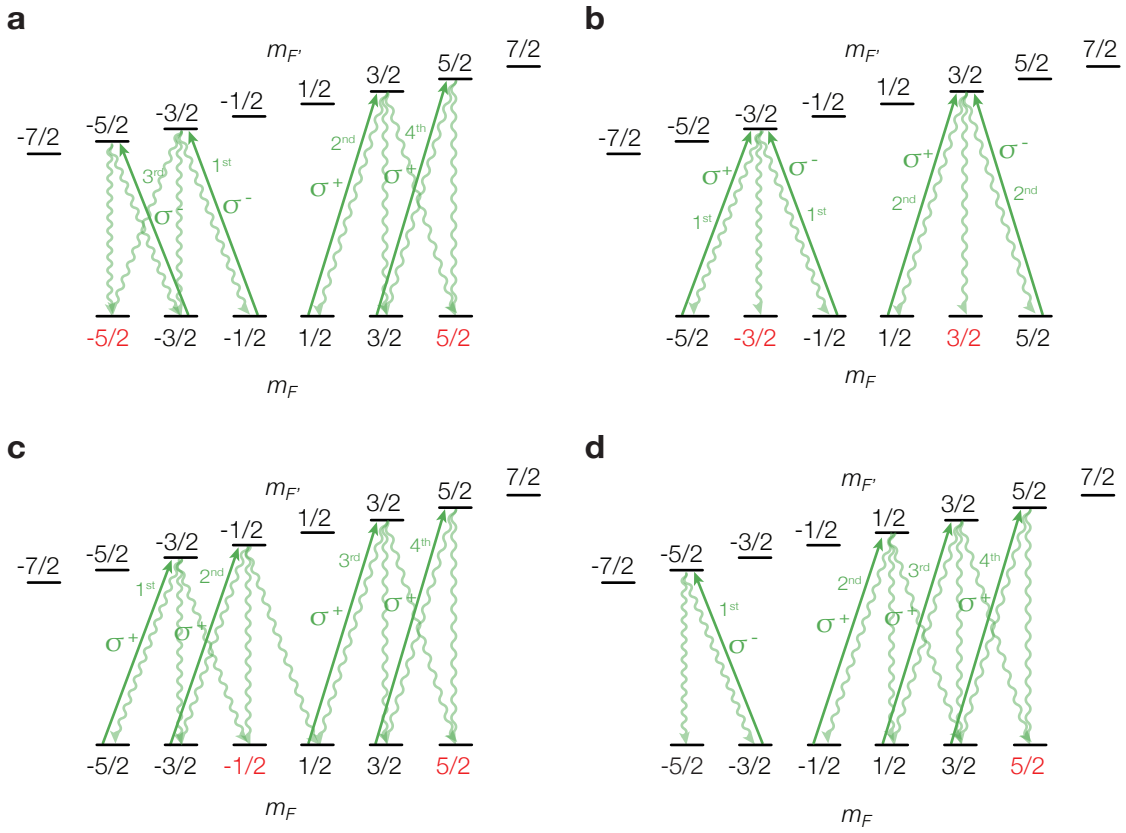

Figure 4.7 – Optical pumping on the ${}^1S_0(F = 5/2) \rightarrow {}^3P_1(F' = 7/2)$ lines. The sequences for achieving balanced two-component nuclear spin mixtures (a)-(c) or spin-polarised samples (d) are illustrated. Target spin states are depicted in red. The respective polarisation and sequential order of each light pulse are also indicated. In case (d), an auxiliary stretched spin state is populated in order to provide a coolant for the evaporation of the target spin state to degeneracy.

Spin mixtures experimental preparation

For the experiments presented in the following part of this thesis, mixtures of two spin states are predominantly employed. Typical images resulting from OSG separation of two-component samples after evaporation are displayed in Fig. 4.8. The samples are prepared according to the pulse sequences illustrated in Fig. 4.7, using 100 ms light pulses with a weak intensity $I \simeq 0.05 I_{\mathrm{sat}}$ in an external magnetic field $B \simeq 18\,G$. However, spin mixtures with any other number of occupied spin states have also been realised. For instance, three, four and five-component gases were generated by leaving the appropriate pulses out of the sequences in Fig. 4.7(a)-(c), where the number imbalance between spin states tends to be neutralised through the evaporation.

Owing to the reduction of the number of spin states which are populated, the total collision rate per spin state during the evaporation is reduced, as collisions in the s-wave regime are only possible between atoms with different nuclear spin. On the other hand, when only two spin states are present, each of them has a population that is three times larger compared to the six-spin scenario. By using the same evaporation sequence, we

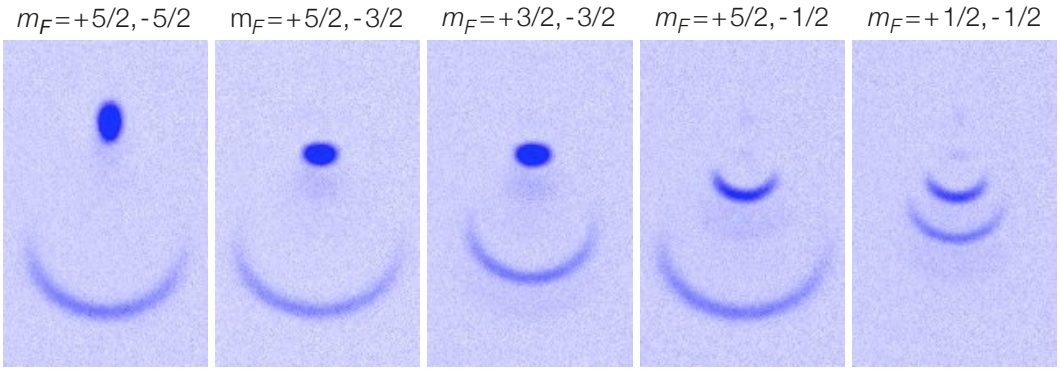

Figure 4.8 – Absorption images of different two-component spin mixtures obtained by employing the optical pumping schemes illustrated in Fig. 4.7(a)-(c). Unwanted spin states are typically kept below 3% of the total atom number and the balancing between the two target spin states is usually better than 5%. These specific spin-state combinations are used for the experimental demonstration of the SU(N) symmetry of two-orbital interactions presented in Section 6.1.2.

achieve a final T/T_F which is up to approximately 20% larger than the one of a six-component gas with a similar final total atom number N, so that typically $0.2 \leq T/T_F \leq 0.25$. It is essential to apply the resonant optical pumping light at the very early stage of the evaporation, when the temperature of the cloud of few μK is still above the recoil temperature. The heating caused by photon scattering is otherwise too severe and results in significantly increased final temperatures after evaporation. In order to characterise the excitation to the metastable state and to perform reference measurements, it is very convenient to employ a clean and non-interacting system represented by a spin-polarised gas. Degenerate spin-polarised samples with atom number $N < 10^5$ can be prepared by evaporating an imbalanced two-component spin-mixture. The minority component is completely removed during the evaporation, allowing the remaining spin state to reach degeneracy with a final $T/T_F \simeq 0.35$ (see e.g. Fig. 5.7). We typically initialise the gas for the evaporation into a spin-polarised sample by pumping three spin states to the target stretched state ($m_F = \pm 5/2$) and only one spin state to the auxiliary stretched state ($m_{F'} = \mp 5/2$), achieving a ratio of approximately 2:1 (see Fig. 4.7(d)).

4.3 SU(N)-symmetric ground state interactions

As discussed in Chapter 1, the decoupling between nuclear and electronic angular momentum is expected to make the s-wave scattering length a_{gg} between atoms in the ground state largely independent of the nuclear spin. We have seen also how this spin invariance gives rise to an underlying SU(N) symmetry of the interactions [53, 55, 63]. In this Section, we report on the verification of the SU(N)-symmetric nature of the interactions in the ground state of ^{173}Yb.

One clear manifestation of the extended symmetry is the conservation of the population of each nuclear spin state separately, i.e. the absence of spin-changing collisions. The residual nuclear spin-dependent variation of a_{gg} can be expressed by $\delta a_{gg}/a_{gg}$, i.e. the

relative deviation of the scattering lengths corresponding to different spin configurations. The order of magnitude of such deviation can be estimated by considering the change in the scattering phase shift associated with different nuclear spin states [55]. The scattering length is in fact a measure of the phase ϕ accumulated by the colliding atoms relative wave function when moving through the inter-atomic potential from the turning point to infinity (computed at zero energy). The spin-dependent variation of the phase is proportional to the relative variation of the scattering length: $\delta a_{gg}/a_{gg} \propto \delta\phi = \Delta t_{\mathrm{coll}}\,\delta V/\hbar$, where Δt_{coll} is the typical time spent by the atoms in the short-range part of the inter-atomic potential and δV is the typical inter-atomic potential energy difference between different spin configurations at short range [55]. $\delta\phi$ can be estimated through the hyperfine interaction strength [55], resulting for ytterbium in $\delta a_{gg}/a_{gg} \approx 10^{-8}$. Such a small deviation requires incredibly long time scales to play a role in the spin dynamics of a cold gas, and in practice the SU(N) symmetry of interactions is satisfied for every measurement time scale typically used in our experiment.

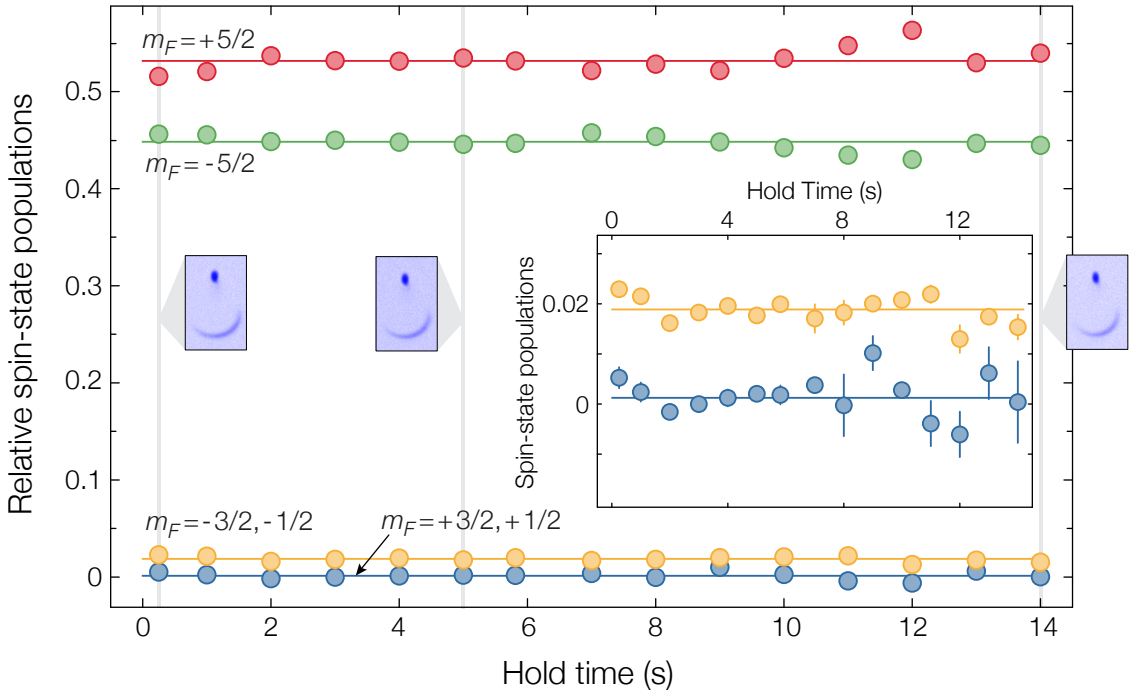

Figure 4.9 – Absence of spin relaxation in a two-component Fermi gas held in a harmonic trap. An almost pure two-spin mixture of the $m_{F,F'} = \pm 5/2$ states of ^{173}Yb is prepared by optical pumping, evaporated to degeneracy and held in the dipole trap. The time evolution of the relative spin-state populations is monitored by spin-resolved imaging. Populations are normalised to the total number of atoms, in order to compensate a global atom number decay caused by imperfect vacuum losses. Solid lines indicate the mean value of different spin-state populations. Experimental images corresponding to different hold times are also displayed. No detectable population of additional spin states is appearing during the hold time, demonstrating the absence of spin-relaxation processes and verifying the SU(N) symmetric nature of atomic interactions. In the inset, a zoom on the population evolution of the $m_F = \pm 3/2,\ \pm 1/2$ is shown.

4.3.1 Absence of spin relaxation

The absence of spin relaxation in the ground state can be directly experimentally verified with a simple measurement. By preparing a degenerate gas having only two populated spin states, and by monitoring the population of the empty spin states over time, we can determine an upper limit for the spin-changing collision rate [311]. We initialise the system in a mixture of the $m_{F,F'} = \pm 5/2$ states, as described in the previous Section. After degeneracy is reached, we increase the height of the optical potential again to prevent further evaporation and hold the gas in the trap for a variable amount of time. During 15 s of hold time, no detectable population of additional spin states is revealed, indicating an extremely low spin-relaxation rate (see Fig. 4.9).

Due to the conservation of coupled angular momentum throughout atomic collisions (see Section 1.2), associated with the SU(2) symmetry of contact interactions, the sum of the nuclear spin projections of two atoms is conserved after a collision even in the presence of spin-changing collisions. Therefore, only pairs of atoms with opposite m_F-states can appear during the hold time. The linear Zeeman effect does not lift the degeneracy between all pair states with the same total nuclear spin projection, associated with the conservation of coupled angular momentum. A weak external magnetic field $B \simeq 3\,\mathrm{G}$, which is used to keep a stable quantisation axis during the evaporation and the final hold, does consequently not inhibit spin-changing collisions. A quadratic Zeeman effect could actually lift the degeneracy and suppress spin-changing collisions as long as the Zeeman shift is larger than the coupling of states with different spin orientations (see Section 1.2). However, the quadratic Zeeman shift of the ground state can be estimated to be smaller than $1\,\mathrm{mHz/G^2} \times m_F B^2$, and it is then negligible with respect to couplings Ω_{sc} which could generate any spin dynamics during the 15 s long hold ($\Omega_{\mathrm{sc}} \geq 2\pi \cdot 65\,\mathrm{mHz}$).

The initial spin state $|m_1 = -5/2;\, m_2 = +5/2\rangle$ can only be coupled by the interaction to the states[4] $\left|m_3 = -3/2, -1/2;\, m_4 = +3/2, +1/2\right\rangle$. The variation of total population N_{sc} of these four nuclear spin states can be expressed as:

$$\dot{N}_{\mathrm{sc}} = N_i\, \bar{n} \cdot 2\gamma_{\mathrm{sc}} \tag{4.3}$$

where N_i is the initial atom number in each of the $m_F = \pm 5/2$ states, $\bar{n}$ is the mean density of the gas and γ_{sc} is the spin-changing collision rate coefficient. The factor of 2 here accounts for the fact that two atoms are changing their spin throughout each collision. Given that the increase in N_{sc} is below our detection limit of approximately 10^3 atoms along 15 s of hold time, as visible in Fig. 4.9, and the density in the optical trap during the hold is $\bar{n} \simeq 4 \times 10^{12}\,\mathrm{atoms/cm^3}$, an upper limit $\gamma_{\mathrm{sc}} < 8 \times 10^{-16}\,\mathrm{cm^3/s}$ can be established. This rate coefficient is about 10^4 times smaller than the total elastic collision rate coefficient γ_{el}, estimated by setting $a = a_{gg}$ in Eq. (1.22).

As written in Eq. (1.26), the elementary spin-changing collision process amplitude depends on the spatial overlap between the interacting pair wave functions. Assuming the spin-changing process is mode-conserving, due to the associated small energy scales compared to any other relevant energy scale of the system in the harmonic trap, the spin-

[4] An expression of the couplings can be obtained by using Eq. 1.26 with $|m_1 = -5/2;\, m_2 = +5/2\rangle$ as the initial state.

changing collision rate can then be seen in a single-mode approximation as an ensemble average of the microscopic couplings plus additional incoherent spin-relaxation processes [313, 314]. It is difficult to directly provide a relation between $\gamma_{\mathrm{sc}}/\gamma_{\mathrm{el}}$ and $\delta a_{gg}/a_{gg}$. Due to the absence of any spin dynamics, it is unclear if an incoherent spin-relaxation[5] is the dominant contribution at the measurement timescale. Only coherent spin dynamics could be directly related to δa_{gg}, and we may estimate an order-of-magnitude experimental upper bound of $\delta a_{gg}/a_{gg} \approx \gamma_{\mathrm{sc}}/\gamma_{\mathrm{el}} < 10^{-4}$.

The measurement itself provides nonetheless the experimental evidence of the complete spin-state collisional stability, during a time scale that is long compared to typical experimental time scales, verifying indirectly the SU(N) symmetry of interactions in the ground state of ^{173}Yb. In Section 6.1.2, the direct spectroscopic demonstration of the SU(N) symmetry of interactions in the two orbital system formed by the $^1\mathrm{S}_0$ and $^3\mathrm{P}_0$ states of ^{173}Yb is presented. For a discussion on the significance and the implications for quantum simulation of the measurement uncertainty in the experimental demonstration of SU(N) symmetry of interactions, the reader can refer to Section 5.2.2.

[5] An incoherent spin relaxation dynamics could be caused by a slight breaking of the smaller SU(2) symmetry of collisions or by dipolar relaxation in the applied magnetic field.

CHAPTER 5

The second orbital: optical coherent control of the electronic state

One of the remarkable features of ytterbium and other alkaline-earth-like atoms is the existence of metastable excited states in the triplet manifold ($S = 1$) of the electronic level structure (see Section 2.1.2). The $^3P_0$ state is especially interesting with a zero electronic angular momentum $J = 0$, like the ground state $^1S_0$: a strong independence of scattering properties from the nuclear spin orientation has been theoretically predicted within the entire set of collision processes involving atoms in either state. We have already seen in Chapter 1 how a two-orbital SU(N)-symmetric description of interactions is thus suitable, where the two orbitals are represented by the two (meta-) stable electronic states. ^{173}Yb is one of the most attractive candidates for the investigation of SU(N)-symmetric models, owing to the possibility of tuning N from 1 to 6. At the same time, gaining control over its orbital degree of freedom through the coherent coupling to the $^3P_0$ state, via the associated ultranarrow optical clock transition, provides exciting possibilities for quantum simulations of orbital magnetism and spin-orbital interactions in solid materials.

In this Chapter, we will illustrate the essential experimental aspects of optical precision spectroscopy in a state-independent optical lattice, which represents a powerful and versatile tool for probing the energy spectrum of lattice gases. We will moreover describe how coherent control of the metastable state population is experimentally achieved in a spin-state-resolved fashion, by means of the optical excitation of ground state atoms in the presence of an external magnetic field. In the second part of the Chapter, we will introduce a simple model of two-orbital Hubbard interactions between fermionic atoms and we will specifically explain how they can be directly probed by precision spectroscopy, in preparation of the experimental results reported in Chapter 6. We will conclude by briefly addressing the relevance of a small SU(N) symmetry breaking for experimental many-body physics observations.

5.1 Excitation to the metastable state

This Section is devoted to the description of the experimental techniques for the coherent excitation of ground state atoms to the $^3P_0$ state and the spectroscopic probing of lattice states. We will start by providing some details about state-dependent optical potentials for ytterbium atoms, including an experimental characterisation of the wavelength dependent

differential AC-Stark shift in our setup. We will then proceed by illustrating how the clock transition is addressed in a three-dimensional magic optical lattice, by either incoherent spectroscopy or Rabi driving. We will focus especially on the excitation of spin-polarised samples in the presence of a magnetic field. The accurate evaluation of the clock transition Zeeman shifts provides a useful reference for the cancellation of otherwise uncontrolled frequency shifts, greatly enhancing our relative frequency precision. The achieved level of spectral precision and the high degree of control presented here are crucial for the successful investigation of two-orbital spin-exchange interactions reported in the following Chapter.

5.1.1 State-dependent optical potentials for ytterbium

In Section 1.1.3 we have recalled how light potentials are intrinsically state-dependent, as they arise from the distinct AC-Stark shifts of each electronic level, which depend on the available transitions energy and strength [97]. The wavelength dependence of the AC-Stark shift for the two lowest (meta-) stable states of ytterbium, which we always denote as $^1S_0 = |g\rangle$ and $^3P_0 = |e\rangle$, can be theoretically calculated by including contributions from all available transitions starting from the two states respectively (see Eq. (A.1)). In order to obtain accurate results, dipole matrix elements and state energies need to be evaluated using relativistic many-body calculations [263, 315]. The calculation by Dzuba *et al* [263] includes also an empirical correction, in order to incorporate the result of an accurate experimental determination of the magic wavelength for ^{174}Yb [121].

In Fig. 5.1 the calculated AC-Stark shifts for the $|g\rangle$ and $|e\rangle$ states are plotted as a function of frequency[1]: spectral intervals where the two Stark shifts are either very similar or very dissimilar (in magnitude or sign) can be recognised, so that a variety of possible relative potential depths may be implemented by an appropriate choice of the wavelength. The Stark shift of the ground state is dominated by the contribution of the broad $^1S_0 \rightarrow {}^1P_1$ transition at 399 nm, and the $^1S_0 \rightarrow {}^3P_1$ resonance at 556 nm appears as a narrow pole-like feature but has a very limited contribution to the Stark shift at large detunings. On the other hand, the contributions of the $^3P_0 \rightarrow {}^3S_1$ transition at 649 nm and of the $^3P_0 \rightarrow {}^3D_1$ transition at 1389 nm are dominant in the visible to near-infrared range Stark shift of the metastable state.

For the spectral region shown in Fig. 5.1, two magic wavelengths, i.e. wavelengths where the two Stark shifts are identical, can be found: $\lambda_m \simeq 759.4$ nm and $\lambda'_m \simeq 551.5$ nm. Moreover, three anti-magic wavelengths are present, for which the Stark shifts are equal in magnitude but opposite in sign: $\lambda_{am} \simeq 1115$ nm, $\lambda'_{am} \simeq 635$ nm and $\lambda''_{am} \simeq 553$ nm (not marked in Fig. 5.1). Other peculiar wavelengths are the state-selective ones, for which the polarisability of one state vanishes: $\lambda_{zc} \simeq 552$ nm ($|g\rangle$ state zero-crossing), $\lambda'_{zc} \simeq 590$ nm and $\lambda''_{zc} \simeq 980$ nm ($|e\rangle$ state zero-crossings).
As a general consideration, only wavelengths which are sufficiently far from an atomic resonance can be safely employed for optical trapping without resulting in excessive photon scattering of atoms in either state. Consequently, the preferable choices of a magic and

[1] For values of the polarisabilities across a broader spectral region, see the original reference [263].

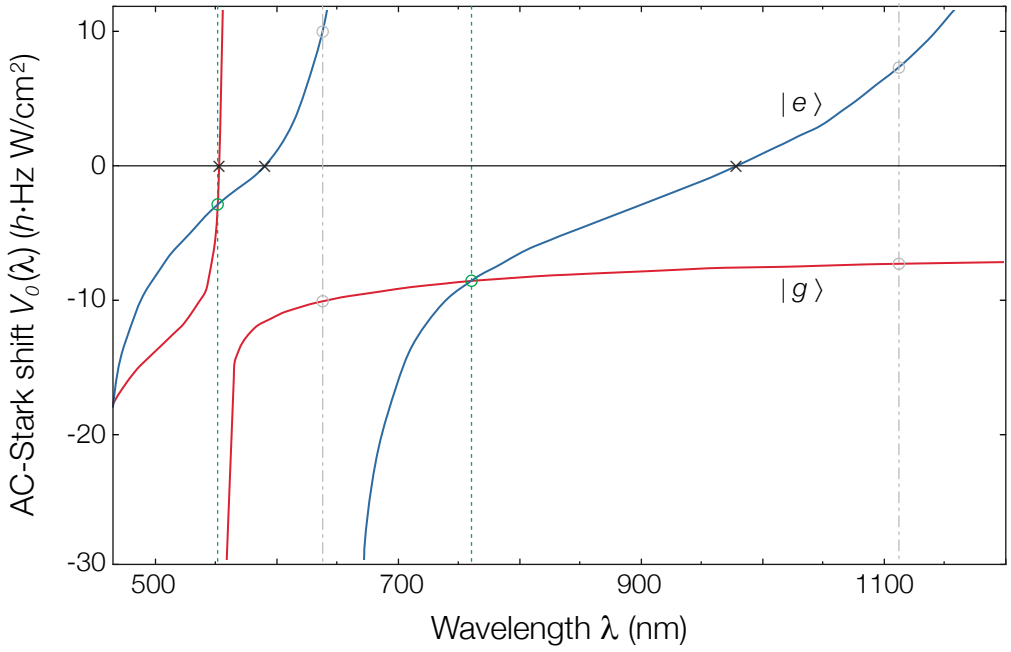

Figure 5.1 – AC-Stark shift of the ground (red) and clock (blue) states of ytterbium as a function of wavelength in the visible/near-infrared region. Values of the state polarisabilities are taken from Ref. [263]. The Stark shifts have poles at the wavelengths associated with the electronic transitions for the two states, respectively the $^1S_0 \rightarrow ^3P_1$ transition at 556 nm for the $|g\rangle$ state and the $^3P_0 \rightarrow ^3S_1$ at 649 nm for the $|e\rangle$ state. Magic (anti-magic) wavelengths are indicated by green (grey) circles and vertical dotted (dash-dotted) lines, whereas Stark shift zero-crossing points are marked with a cross.

an anti-magic wavelength are $\lambda_m \simeq 759.4$ nm and $\lambda_{am} \simeq 1115$ nm, and such wavelengths are currently used respectively in optical lattice clocks [51, 122] and artificial gauge field generation schemes [64]. Moreover, narrow-line high-power laser sources are commonly available at such wavelengths, namely Ti:Sapph and Yb-doped fiber lasers.

Magic wavelength optical lattices are the ideal choice for AEL-based optical lattice clocks [49, 90] and in general for cold atom precision spectroscopy. On the one hand, deep lattice potentials bring many advantages to optical precision spectroscopy as they enable Doppler-free, recoil-free interrogation of the clock transition. On the other hand, optical potentials normally induce differential light shifts on atom internal states that need to be cancelled, compromising otherwise the attainable spectral precision and accuracy. Lattices tuned at the magic wavelength represent a neat solution to this issue, providing an electronic state-independent trapping potential, where the differential AC-Stark shift is cancelled to leading order. Other systematic shifts are introduced by the lattice light, namely due to higher-order AC-Stark shift, usually termed hyperpolarisability [121, 316], and for odd isotopes due to vector and tensor Stark shifts [90, 96, 122]. Stabilising these shifts is a primary concern in state-of-the-art lattice clocks [90]. However, provided that linearly polarised light is used to implement the magic lattice, light-induced effects just give rise to sub-Hz frequency shifts. As we will see in the following Section and in Chapter 6, a resolution of 10 Hz is widely sufficient for detecting the typical magnetic and

interaction frequency shifts in ultracold gases. In this context, every lattice light-induced shift is therefore negligible as long as the lattice laser operates at the magic wavelength.

The magic wavelength shows a weak isotope dependence, and experimental values with a relative precision of more than 10^{-7} obtained in lattice clock setups have been reported for ^{174}Yb [121] and ^{171}Yb [122], yielding respectively $\lambda_m \simeq 759.353740(67)$ nm and $\lambda_m \simeq 759.355944(19)$ nm. The frequency dependence of the differential Stark shift $V_d(\omega)$ in the vicinity of the magic wavelength was also measured, resulting in a shift slope $\Delta V_d(\omega) = -22(2)\,\mathrm{mHz}/(\mathrm{GHz}\ E_r)$ for both isotopes. This value indicates a considerable robustness, as a detuning of 1 GHz of the lattice light from the magic wavelength leads only to a differential shift of approximately 1 Hz for a depth of $50\,E_r$. For this reason, the standard scheme for the creation of separable three-dimensional optical lattice potentials by employing three linearly polarised retro-reflected laser beams detuned from each other by ~ 100 MHz (see Section 3.3.3) does not pose any problem for precision spectroscopy above Hz level. A relative stability of the lattice laser source wavelength of $\sim 10^{-5}$ is sufficient (corresponding to an absolute stability of ~ 5 GHz).

For all experiments presented in the following part of this work, we adopted a lattice tuned to the magic wavelength. In the following Section, we introduce precision spectroscopy in such a lattice and show measurements that were performed to ascertain the "magicness" of the optical lattice for ^{173}Yb. Before then, we briefly consider here a state-dependent optical lattice tuned away from the magic wavelength, in connection to the planned experimental implementation of the Kondo lattice model.

A state-dependent lattice for the Kondo lattice model

We have seen in Chapter 1 how the exchange coupling V_{ex} emerges as an intrinsic consequence of the on-site interaction energy difference between the singlet and triplet state of two atoms in the $|g\rangle$ and $|e\rangle$ states, and we will see in Chapter 6 how the exchange interaction was directly observed and characterised in ^{173}Yb. This provides one of the essential ingredients for the implementation of the Kondo lattice model (KLM), which we have presented in Section 1.3. The other essential ingredient is a mobile band of ground state atoms, which mimics the conduction band of electrons in a solid material. Simultaneously, atoms in the $|e\rangle$ state must be localised, in order to play the part of the magnetic impurities in the KLM. It is therefore necessary to create independent lattice potentials for the two electronic states, in order to be able to appropriately tune the tunnelling of each state. For this purpose, a state-dependent optical lattice needs to be employed, similar to the one depicted in Fig. 1.3(a).

A suitable wavelength for the lattice has to be found, which generates a potential depth as low as possible for the ground state atoms while still keeping excited atoms completely isolated from each other. By looking at the states Stark shift plotted as function of wavelength in Fig. 5.1, we can select two ranges of wavelengths which could in principle be appropriate for the purpose. One broad range can be found in the vicinity of the $^3P_0 \rightarrow {}^3S_1$ transition wavelength: a factor-of-3 difference in the Stark shifts is achieved at approximately 670 nm, and the factor increases towards the resonance to arbitrarily high values. Another very small usable range can be found in the vicinity of the $^1S_0 \rightarrow {}^3P_1$ transition:

around 552 nm the polarisability of the ground state vanishes. The former alternative presents two advantages in comparison to the latter: (i) the $|e\rangle$ state polarisability is considerably larger, so that a lower laser power is required to generate a given lattice potential depth, and (ii) the wavelength sensitivity of the Stark shift is much smaller, implying a coarser frequency stabilisation of the lattice wavelength is required. The detuning to the respective transitions, which is relevant concerning the heating caused by lattice photon scattering, is comparable between the two options, with $\Gamma/\Delta \approx 1 \times 10^{-7}$. For these reasons, we are currently implementing a state-dependent lattice potential at approximately 670 nm, which will be described in Ref. [279], along with a spectroscopic characterisation of the associated state-dependent Stark shifts.

In order to implement the KLM in two or one dimensions, deep magic lattices on one or two axes can be used to isolate different copies of the lower-dimensional system and provide a state-independent harmonic confinement. This is particularly convenient as it permits to perform clock spectroscopy and coherent excitation in the Lamb-Dicke regime (see below). However, the light shifts produced by the non-magic lattice potential in orthogonal directions broaden the resonances and give rise to an inhomogeneous Rabi coupling, and might therefore have to be compensated by additional laser beams in order to attain a sufficient degree of spectral precision.

5.1.2 Addressing the clock transition in a magic optical lattice

First spectroscopy of the clock transition

In order to initially locate the $^1S_0 \rightarrow {}^3P_0$ clock transition of ^{173}Yb, we calibrated our wavelength meter[2] by using the measured frequency of the green MOT transition, reaching an absolute precision close to 60 MHz, limited by the resolution of the wavelength meter itself. We then proceeded by shining 5 mW of clock excitation light on a cold sample of ^{173}Yb in the dipole trap and varying the laser frequency[3] over a range of 40 MHz around the location where the resonance was reported [274]. By monitoring the number of ground state atoms after the clock light had been applied, we could observe a deep absorption feature in the vicinity of the expected resonance frequency. After the clock line was thus found, we performed higher-resolution spectroscopy on free-falling atoms, in order to exclude the light-induced clock shift on the resonance position. Although the free-space resonance does not suffer any light-shift, it is still Doppler-broadened to approximately 2 kHz and is shifted by the clock photon recoil energy.

Spectroscopy in the optical lattice

In order to achieve sideband-resolved excitation, we adiabatically load a ^{173}Yb Fermi gas into a deep three-dimensional lattice tuned to the magic wavelength reported in Ref. [121] for ^{174}Yb (see Section 2.2.4 for details on the lattice implementation and the loading procedure). The clock excitation laser beam is π-polarised and aligned along one of the

[2] HighFinesse/Ångstrom WS7

[3] In order to speed up the line search, a chirped clock light pulse with a duration of 20 s was applied during each experimental cycle, for a resulting frequency sweep of 1 MHz/cycle.

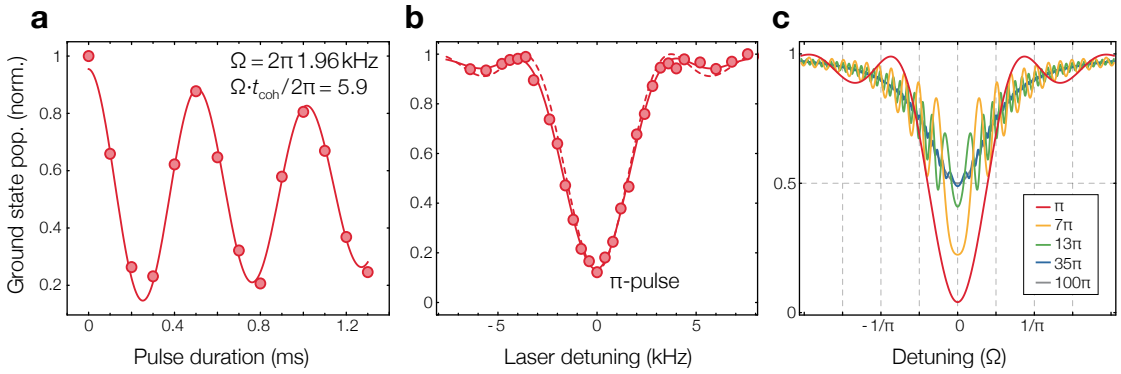

Figure 5.2 – Rabi π-pulse clock spectroscopy of a two-component Fermi gas ($m_{F,F'} = \pm 5/2$) in a three-dimensional magic optical lattice. The lattice depth in the direction of the clock excitation beam is 45 E_r. (a) A Rabi oscillation with $\Omega = 2\pi \cdot 1.96$ kHz is observed by driving the transition with an intensity of 2.7 W/cm^2. The resulting π-pulse duration is $\tau_\pi = \pi/\Omega = 0.255$ ms. The expected Rabi frequency obtained for the estimated intensity of the clock laser at the atom position equals $\Omega = 2\pi \cdot 1.82(15)$ kHz. The fitted coherence time is $t_{\text{coh}} = 2.98$ ms (see also Fig. 5.12). (b) A Fourier-limited spectrum is obtained by applying a clock π-pulse and varying the clock laser detuning while the gas is held in a deep lattice. The solid line is a fit of a sinc^2 function to the data points. The dashed line is the expected spectrum calculated through the Rabi frequency Ω and the amplitude obtained by the sinusoidal fit in the (a) panel. (c) Line-shapes for different pulse durations. The ratio between the coherence time t_{coh} and the π-pulse duration π/Ω is taken equal to 11.8, resulting from fitting the data in panel (a). For pulse durations $t_{\text{pulse}} \gg t_{\text{coh}}$, an excitation fraction of 0.5 is observed and the line-shape is a Lorentzian with Fourier-limited width.

lattice axes by overlapping it with the corresponding lattice beam (see Fig. 5.4), in order to satisfy the Lamb-Dicke condition for quasimomentum-independent coupling [49, 317] (see below for more details on sideband-resolved spectroscopy). Incoherent spectroscopy is implemented by illuminating the trapped atoms with a 100 ms clock excitation pulse, having a light intensity typically between 0.2 mW/cm^2 and 20 mW/cm^2. Provided the pulse duration is longer than the typical system's coherence time and its area covers several π, an excitation fraction of 0.5 should result, independently of the Rabi coupling, as displayed in Fig. 5.2(c). The Rabi coupling for a given light intensity is given in the usual way as [97]:

$$\hbar\Omega = -d_{eg} E_0 = -d_{eg}\sqrt{\frac{2I_0}{c\epsilon_0}} \tag{5.1}$$

where d_{eg} is the dipole matrix element of the transition, E_0 and I_0 are respectively the amplitude and the intensity of the light field. For fermionic isotopes, the finite coupling is a consequence of the hyperfine interaction (HFI) (see Section 2.1.2 for details) and is proportional to the nuclear spin state-dependent dipole matrix element, which can be determined through the Clebsch-Gordan coefficients inherited from the $^1S_0(F = 5/2) \rightarrow {}^3P_1(F' = 5/2)$ transition (see Appendix A). The expected Rabi coupling for a given m_F state can be thus calculated by inferring the reduced dipole matrix element from the natural linewidth of the clock transition, which was theoretically calculated to equal 7 mHz in ^{173}Yb [260]. We find excellent agreement between the measured Rabi frequencies Ω and the expected values computed using Eq. (5.1). The typical clock light

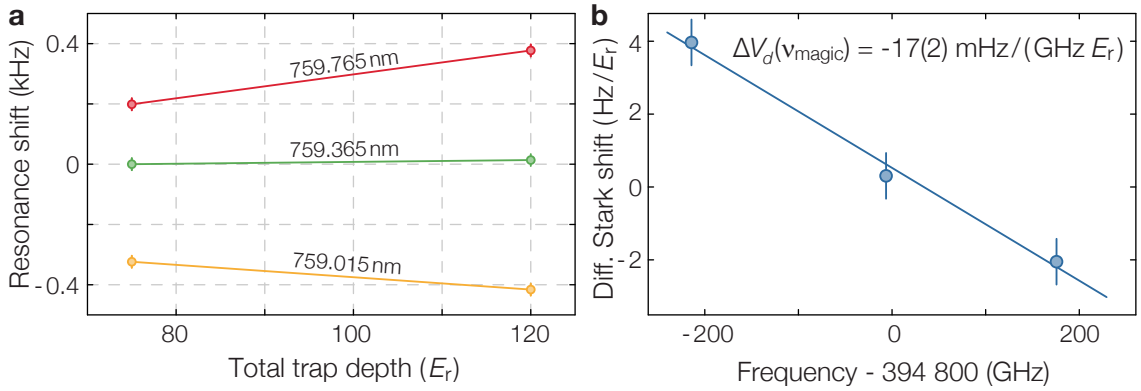

Figure 5.3 – Differential AC-Stark shift for ^{173}Yb in an optical lattice as a function of lattice wavelength. (a) The differential AC-Stark shift V_d for three values of the lattice wavelength close to the magic one is measured by incoherent spectroscopy. (b) By the slope of the shift relative to power and to lattice frequency, a sensitivity $\Delta V_d(\nu_m) = -17(2)$ mHz/(GHz E_r) of the light-shift cancellation around the magic wavelength is estimated.

intensities used for incoherent spectroscopy[4] yield Rabi frequencies Ω comprised between $2\pi \cdot 15$ Hz and $2\pi \cdot 150$ Hz for the $m_F = \pm 5/2$ states. Clock transition spectra are obtained by detecting the ground state population as the clock pulse detuning is varied. Incoherent precision spectroscopy measurements for different spin and magnetic field configurations will be displayed later in this Section.

Another possibility is Rabi spectroscopy, where a single Rabi π-pulse is applied to the atoms and therefore an excitation fraction close to 1 is expected (see Fig. 5.2). However, incoherent spectroscopy is the preferable option when spectra including various transitions with different Rabi couplings need to be measured using the same light intensity, and especially when the desired information resides mainly in the position of the different resonances. As we will see later, the width of resonances measured with either methods in the magic lattice is Fourier-limited to values as low as approximately 40 Hz; our clock laser absolute short-term frequency stability prevents the possibility of observing narrower resonances.

Validation of lattice "magicness"

Although our wavelength meter is re-calibrated by the position of the free-space clock resonance and our lattice wavelength assessment should therefore be rather accurate, we further experimentally ascertain the magic wavelength value[5] and its robustness for ^{173}Yb, by proceeding as follows: we measure the differential light-shift of the clock transition for three different wavelengths of the lattice laser near 759.35 nm, as displayed in

[4] A beam waist of approximately $w_0 \simeq 150\,\mu$m and a power between $P \simeq 0.1\,\mu$W and $P \simeq 10\,\mu$W are typically employed.

[5] From to the small isotope shift of the clock transition between ^{173}Yb and ^{174}Yb (see Table 2.3), it is reasonable to assume that the magic wavelength of ^{173}Yb is located close to the one already measured for ^{174}Yb [121]. However, due the presence of HFI interactions in the fermionic isotopes, different transition coupling strengths could lead in principle to a non-negligible shift of the magic wavelength.

Fig. 5.3(a), by performing clock spectroscopy at different lattice depths. By determining the lattice frequency-dependent slope of the differential light-shift relative to the lattice depth, we can estimate the sensitivity $\Delta V_d(\nu) = \partial V_d/\partial \nu$ of the differential-shift cancellation around the magic wavelength (see Fig. 5.3(b)), and we found good agreement with Refs. [121, 122]. By the zero-crossing of the differential shift, we also obtain a working value of the magic wavelength for our setup $\lambda_{\mathrm{m}} \simeq 759.30(4)$ nm. This should not be taken as an accurate measurement of the magic wavelength in ^{173}Yb, as the determination of the resonance centres is affected by severe line-shape deformations away from the magic wavelength, owing to the inhomogeneity of the light-shift caused by the Gaussian lattice beam profiles.

Experimental configuration

As already mentioned earlier, the clock excitation light is linearly polarised along the direction of an external uniform magnetic field in order to couple only to the π-transitions ($\Delta m_F = 0$), as sketched in Fig. 5.4(a). The magnetic field can be used to split transitions corresponding to different nuclear spin states (see Section 5.1.3) or can be tuned to sufficiently low strength to only provide a stable quantisation axis, when the associated Zeeman splitting is lower than the Fourier-limited linewidth.

The clock laser is frequency stabilised to an ultralow-expansion (ULE) glass cavity reference (see Section 3.4 and Appendix C) with a finesse $\mathcal{F} \simeq 10^5$. A drift of the cavity reference, due to the age-related mechanical flow of the glass spacer, needs to be compensated (see Appendix C). For this reason, a linearly time-varying frequency offset of

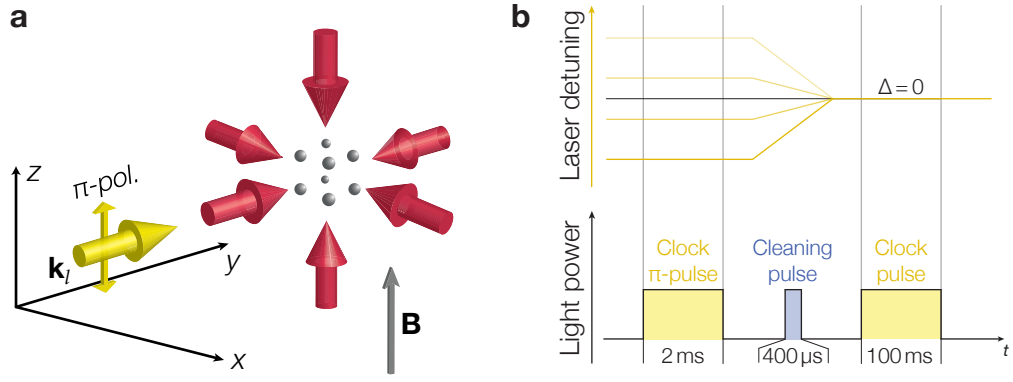

Figure 5.4 – (a) Experimental configuration for the addressing of the clock transition in a three-dimensional optical lattice. The yellow excitation light is directed along one of the lattice axes, in this case the y-axis. The quantisation axis of the nuclear spin is provided by an external magnetic field with a minimum value of 0.3 G. The excitation light is linearly polarised along the magnetic field direction, so that it couples only to the π-transitions. (b) Experimental sequence used for the measurement displayed in Fig. 5.5. After a clock π-pulse at variable detuning Δ from the clock resonance (located at $\Delta = 0$) is applied, the relative $|e\rangle$ state population is mapped to the $|g\rangle$ state population. First, a cleaning pulse resonant to blue transition is used to remove residual $|g\rangle$ state atoms, and secondly, a long clock pulse is used to bring half of the $|e\rangle$ state population back to $|g\rangle$.

approximately 80 mHz/s is applied in a feed-forward scheme to the clock laser frequency set value. Reference spectroscopic measurements are performed to calibrate the absolute frequency of the clock laser, using spin-polarised gases with low-atom number $N \simeq 3 \times 10^4$ in order to exclude any interaction-induced frequency shifts. Typical conditions of spin-polarised and two-component Fermi gases of ^{173}Yb used for precision spectroscopy are described later in this Section and summarised in Figs. 5.7-5.8.

Lattice sideband spectroscopy

When the Lamb-Dicke condition is satisfied in a deep lattice [317], i.e. when each atom is confined to a space smaller than the clock wavelength, transitions between Bloch bands with indices differing by more than 1 are suppressed. In a lattice potential, the Lamb-Dicke regime coincides to the regime of quasimomentum-independent Rabi couplings: when the lattice depth is increased, the quasimomentum dispersion relation of the Bloch bands gradually flattens; in the large depth limit each lattice site can be approximately treated as an individual isolated harmonic trap with a large oscillator level spacing $\hbar\omega_{\mathrm{ho}} \gg E_r$. The clock light field can couple Bloch bands with different band indices only along the direction of $\mathbf{k}_l$, the clock laser wave vector, and couples quasimomenta differing by k_l inside the first Brillouin zone. The quasimomentum-dependent coupling between the $|g\rangle$ state in the n-th Bloch band and the $|e\rangle$ state in the m-th Bloch band can be written as:

$$\Omega_{n,m}(q_1, q_2) = \Omega \int dy\, \psi^{(m)*}_{q_2}(y)\, \psi^{(n)}_{q_1}(y)\, \exp(ik_l y) \tag{5.2}$$

where the clock laser propagates along the y-axis and $\psi^{(n)}_q(y)$ is the Bloch wave function in the n-th band at quasimomentum $q = \mathbf{q} \cdot \hat{\mathbf{y}}$. For a sufficiently deep lattice the $\Omega_{n,m}$ coefficients become substantially independent of quasimomentum, as the Bloch band widths become smaller than the clock laser linewidth, so that all quasimomenta are equally coupled. This is equivalent to saying that the associated resonances do not suffer any Doppler broadening and become Fourier limited. As the Bloch bandwidths are very different for different band indices, quasimomentum-independent excitation is achieved at different lattice depths for the different bands (see Fig. A.3). For a typical value of the bare Rabi coupling $\Omega = 2\pi \cdot 100$ Hz used in our spectroscopy measurements, such a regime is reached for lattice depths above $11\, E_r$ for the lowest band carrier resonance ($n = 1 \rightarrow m = 1$), above $32\, E_r$ for the first excited band carrier resonance ($n = 2 \rightarrow m = 2$) and above $28\, E_r$ for the lowest blue sideband ($n = 1 \rightarrow m = 2$), which are the only relevant resonances when an ultracold gas is loaded into the lattice. For the lattice depths between 25 and $50\, E_r$ which are normally used in our precision spectroscopy experiments, the ratio $\Omega_{1,2}/\Omega_{1,1}$ is constant and approximately equal to 0.37 (see Fig. 5.5). For more details on clock spectroscopy in the presence of confining potentials, Refs. [318, 319] are suggested.

In order to experimentally characterise the clock excitation within the band structure of the lattice potential, we perform incoherent spectroscopy with a two-spin Fermi gas and reveal the relevant resonances, as displayed in Fig. 5.5. A pulse duration corresponding to a π-pulse area on the lowest band carrier is chosen and a second long pulse is applied to map the $|e\rangle$ state population to the $|g\rangle$ state one (see Fig. 5.4(b)). This technique is well

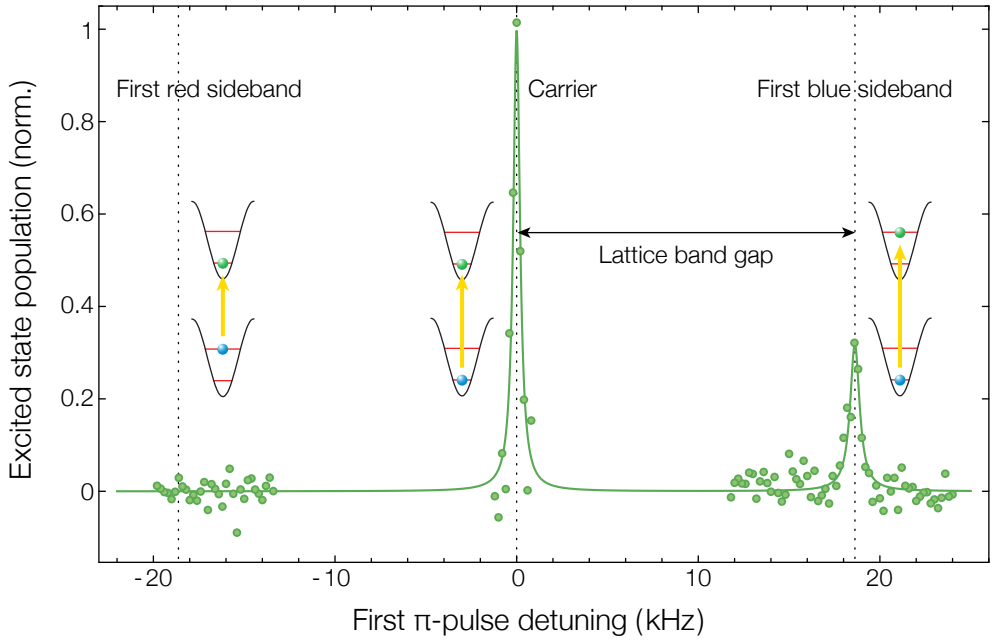

Figure 5.5 – Spectroscopy of the lattice structure using a two-component ($m_{F,F'} = \pm 5/2$) Fermi gas of ^{173}Yb with $T/T_F \simeq 0.25$ and $N \simeq 5 \times 10^4$ atoms. Distinct resonances reveal the motional structure of the lattice potential: as the population of the first excited band in the clock-laser propagation direction is small, the first red sideband lies below the detection limit. In agreement with a lattice depth of $29E_r$, a lattice first band-gap of 18.7 kHz is observed. Only a weak external magnetic field of 0.3 G is used for this measurement, which is not sufficient to resolve the two m_F state transitions with a Rabi frequency $\Omega \simeq 2\pi \cdot 350$ Hz. The sequence represented in Fig. 5.4(b) is adopted to map the relative $|e\rangle$ state population to the $|g\rangle$ state population, subsequently detected by absorption imaging. The ratio between the amplitude of the first blue sideband and of the carrier resonance matches the theory ratio $\Omega_{1,2}/\Omega_{1,1} \simeq 0.35$ of the corresponding Rabi couplings.

suited to the detection of resonant features with small amplitudes, as a positive signal over the zero-atom noise level maximises the signal-to-noise ratio, and is also used for $|e\rangle$ state loss measurements that will be reported in the last part of Chapter 6. In the remainder of this thesis, we will refer to the lattice carrier transition simply as the clock transition, as other lattice inter-band transitions are avoided.

The spectroscopic measurements presented so far are realised through two-component spin mixtures formed by opposite m_F states. This is motivated by the spin-dependent dipole matrix element of the clock transition, whose magnitude is symmetric with respect to m_F. We were able to experimentally detect the relative strength of the Rabi couplings for different clock π-transitions by coherently driving the carrier transition of a six-spin Fermi gas loaded into the optical lattice in a 0.3 G B-field. The observed coherent dynamics is displayed in Fig. 5.6: an oscillation with three distinct Rabi frequency components is clearly visible and the fitted ratios between them match remarkably well the ratios 5:3:1 between the dipole matrix elements of the associated π-transitions, i.e. $m_F = \pm 5/2, \pm 3/2, \pm 1/2 \rightarrow m'_F = \pm 5/2, \pm 3/2, \pm 1/2$ (see Appendix A). In the remainder of this Section, we will describe experiments making use of spin-polarised or two-spin gases within the two states $m_{F,F'} = \pm 5/2$, which were chosen since they posses the largest Rabi coupling on the π-transition, and will be often labeled for brevity as $|\uparrow\rangle$ and $|\downarrow\rangle$.

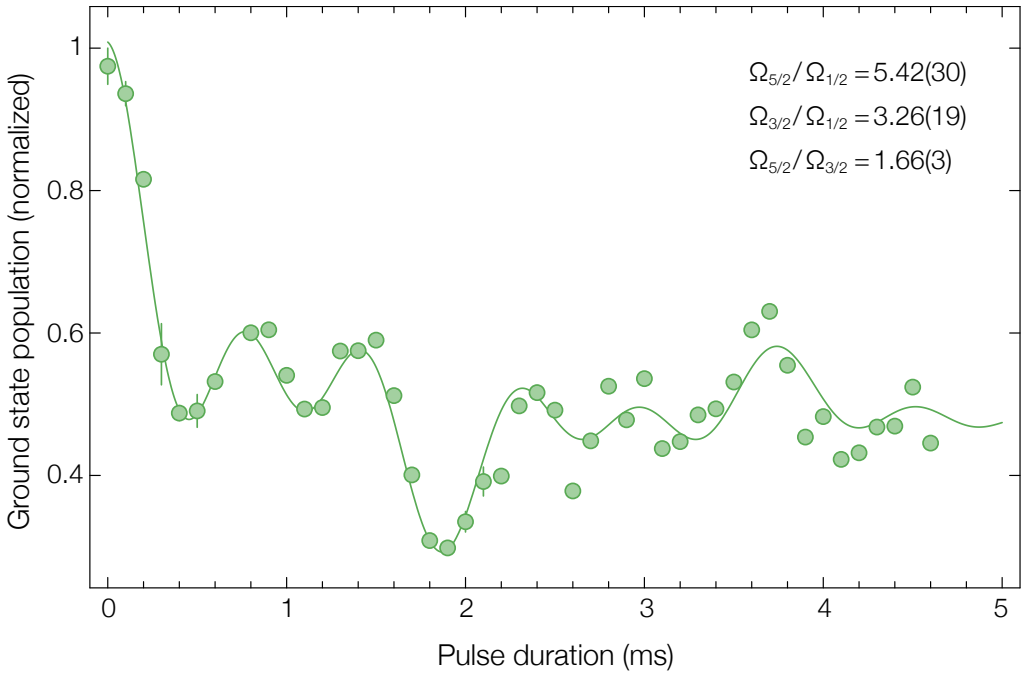

Figure 5.6 – Coherent Rabi driving of the clock transition in a six-spin state mixture. States with different $|m_F|$ are coupled with different Rabi strengths on the π-transitions. The solid line is a fit of three combined cosine functions with identical amplitude and zero-phase to the data. The relative ratio of the couplings from Eq. (A.5) is 5:3:1 and is well matched by the fitted Rabi frequencies.

Fermi gas preparation for precision spectroscopy

The typical conditions of ultracold gases of ^{173}Yb that are used for spectroscopy experiments are summarised here and displayed in Figs. 5.7-5.8. Spin-polarised gases are mostly used for calibration measurements, e.g. for the evaluation of the magnetic field sensitivity of the clock transition or of the ULE frequency reference linear drift, and further as an absolute reference of the clock laser frequency.

Ultracold spin-polarised samples do not suffer any interaction-induced clock shift in a three-dimensional lattice. First of all, multiple site occupancies are prohibited by Pauli blocking as long as higher Bloch bands are unoccupied. Even in the presence of a significant excited-band population, the spatial pair wave function of identical fermions on the same lattice site must be antisymmetric; contact interactions in the s-wave regime are therefore completely suppressed and only p-wave interactions could lead to measurable effects [280, 281]. Nevertheless, a small difference between the Rabi couplings of the different intra-band transitions, due to the finite lattice depth, can cause two fermions to become distinguishable while the clock transition is coherently driven [281, 320–322]. This mechanism may enable on-site s-wave interactions, possibly leading to inelastic collisions as well. Unwanted interactions might also be caused by spatial inhomogeneity of the Rabi couplings, with the higher-band population tunnelling over lattice sites in a time scale comparable to the measurement duration and possibly experiencing inelastic collisions with other distinguishable atoms. As long as relatively small atom numbers

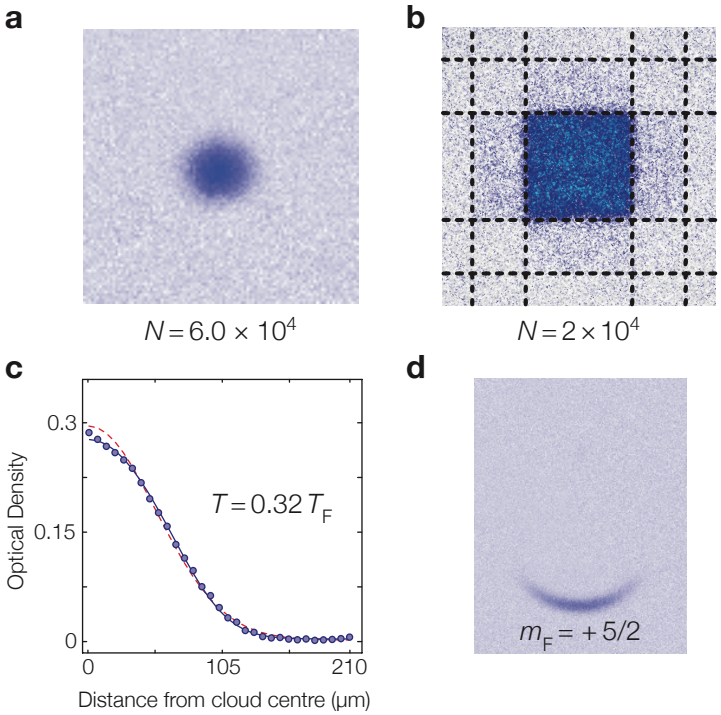

Figure 5.7 – A spin-polarised gas in the $|\uparrow\rangle$ state ($m_F = +5/2$) with $T/T_F = 0.32$. (a) TOF image of a Fermi gas with $N = 6 \times 10^4$ released from the dipole trap. (b) Band-mapping in the $x - y$ plane: the gas is released from a 3D-lattice with a depth of $V_x = V_y = 35E_r$. With $N = 2 \times 10^4$, a fraction of approximately 10% of the entire population is distributed over the second and third Brillouin zones, indicating a 5% population of the first excited band in the x and in the y direction. (c) Azimuthally integrated column density after TOF. A Thomas-Fermi fit (solid blue line) yielding $T/T_F = 0.32$ and a gaussian fit (red dashed line) to the data are displayed. (d) An OSG absorption image is used to inspect the purity of the spin mixture. Only the $m_F = +5/2$ state is populated above our detection limit.

$N \lesssim 3 \times 10^4$ are adopted, only a small first excited-band population is present and such effects are modest. Spectra acquired with spin-polarised samples like the one from Fig. 5.7 indeed display the narrowest and most symmetric resonant line-shapes and the longest Rabi coherence time (see Fig. 5.11 and Fig. 5.12).

On the other hand, a two-component Fermi gas with two coherently coupled electronic orbitals $|g\rangle$ and $|e\rangle$ represents the prototypical system to investigate two-orbital interactions between fermions. For the experimental validation of SU(N) symmetry of two-orbital interactions, it is sufficient to prove that interactions are identical in few binary combinations of spin states, without the necessity of employing multi-spin mixtures (see also next Section). Fig. 5.8 shows the characteristic state of a Fermi gas used for precision interaction spectroscopy experiments described in Chapter 6. For atom numbers up to $N \simeq 6 \times 10^5$ no significant higher-band population is present. However, a larger atom number is desirable to increase the number of doubly occupied lattice sites, which are necessary for revealing on-site interactions, and we thus typically work with $N \simeq 1 \times 10^5$ atoms. A degeneracy T/T_F between 0.2 and 0.25 can still consistently be achieved at such high atom numbers, owing to our relatively large volume dipole trap (see Section 2.2.3).

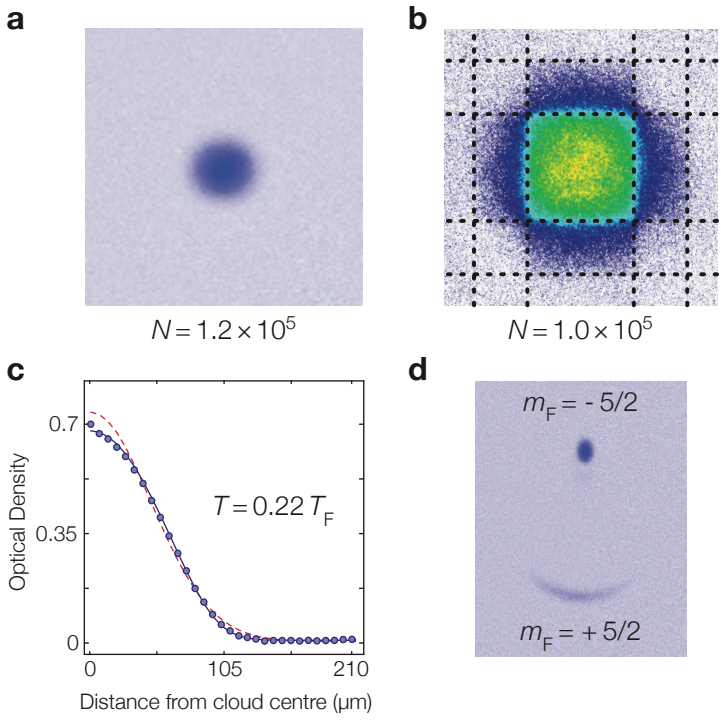

Figure 5.8 – A two-component Fermi gas in the $|\uparrow\rangle$ and $|\downarrow\rangle$ states ($m_{F,F'} = \pm 5/2$) with $T/T_F = 0.22$. (a) TOF image of a Fermi gas with total atom number $N = 1.2 \times 10^5$ released from the dipole trap. (b) Band-mapping in the $x - y$ plane: the gas is released from a 3D-lattice with a depth of $V_x = V_y = 35E_r$. With $N = 1 \times 10^5$, a fraction of approximately 10% of the entire population is distributed over the second and third Brillouin zones, indicating a 5% population of the first excited band along each of the horizontal directions. (c) Azimuthally integrated column density after TOF. A Thomas-Fermi fit (solid blue line) yielding $T/T_F = 0.22$ and a gaussian fit (red dashed line) to the data are displayed. (d) An OSG absorption image is used to inspect the purity of the spin mixture. No state except the $m_{F,F'} = \pm 5/2$ is populated with more than 3%.

5.1.3 Addressing the clock transition in a magnetic field

Differential Zeeman shift

An external magnetic field generates a nuclear Zeeman shift of both the $|g\rangle$ and $|e\rangle$ states, owing to the finite nuclear Landé g-factor g_I (see Table 2.1). On the other hand, clock π-transitions are only sensitive to the difference δg between the two g-factors, and not to the individual g_I factors which generate a shift $\Delta_{\mathrm{NZ}} = g_I\, m_F\, \mu_B B$ on both states (see Fig. 5.9 for ^{173}Yb). Owing to the non-zero differential Landé g-factor between the $|g\rangle$ and $|e\rangle$ states [96], the clock π-transition frequency associated with each nuclear spin sublevel shifts as:

$$\Delta_B = \delta g\, m_F\, \mu_B B \tag{5.3}$$

The nuclear g-factor of the $|g\rangle$ state can be determined from Eq. (2.3). Without the nuclear spin-induced HFI generating a mixing with the $^3\mathrm{P}_1$ state, the $|e\rangle$ state would share the same g-factor. Since the $|e\rangle$ state electronic wave function is distorted by the mixing, $\delta g \neq 0$. The consequent differential Zeeman shift in ^{173}Yb was theoretically estimated by HFI theory [265] to equal $\Delta_B = h\, m_F\, B \cdot 113\,\mathrm{Hz/G}$ and our measurements yield a highly

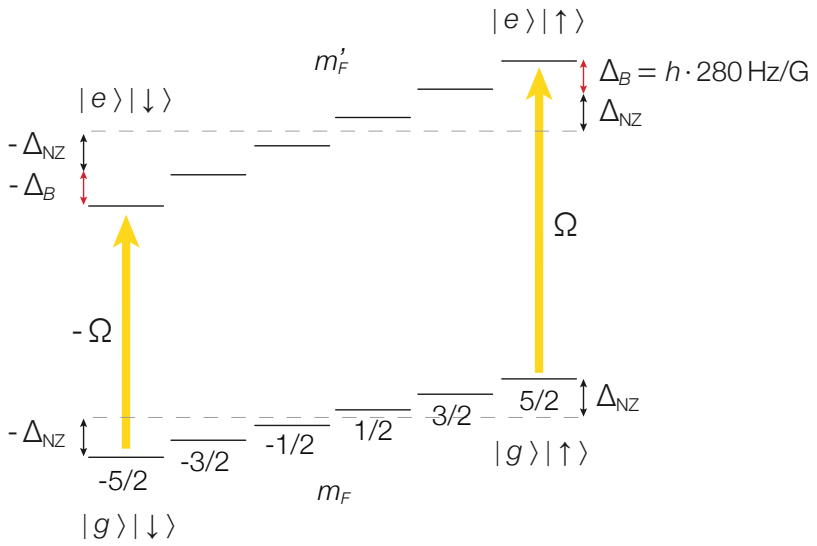

Figure 5.9 – Differential Zeeman shift between the $|g\rangle$ and the $|e\rangle$ state. A non-zero differential g-factor δg between the two electronic states gives rise to a positive linear Zeeman shift Δ_B of the clock π-transitions, which are not sensitive to Δ_{NZ}, the individual state nuclear Zeeman shift. We experimentally measure this shift with high precision for ^{173}Yb, as shown in Fig. 5.10. Due to the Clebsch-Gordan coefficients having opposite signs for opposite m_F-states π-transitions, the Rabi couplings are equal in magnitude but opposite in sign (see Section 6.1).

consistent value of $\Delta_B = h\, m_F\, B \cdot 112(1)\,\mathrm{Hz/G}$, as displayed in Fig. 5.10.

The nuclear spin-independent quadratic Zeeman shift of the $|e\rangle$ state [96] was experimentally quantified as $\Delta_B^{(2)} \simeq -h \cdot 6.2 \times 10^{-2}\, B^2\,\mathrm{Hz/G^2}$ [122, 273], and it starts to become relevant with our resolution only at fields $B \gtrsim 30\,\mathrm{G}$, where $\Delta_B^{(2)} \gtrsim h \cdot 50\,\mathrm{Hz}$. A precision measurement of this shift could also be recently achieved in our setup, owing to newly upgraded magnetic field coils (see Section 3.2), and specifically in connection with magnetically induced spectroscopy of bosonic ^{174}Yb [279].

Magnetic field spectroscopy

A measurement scheme which takes advantage of the linear Zeeman shift of fermionic isotopes consists of measuring the average frequency between the π-transitions associated with opposite m_F states, in the presence of an adequate bias field. Each spin state can be spectroscopically resolved and, for weak fields ($\Delta_B^{(2)} \ll \Delta_B$) the zero-field position of the clock resonance is located at the centre between the two resonances. This scheme is used to reference the absolute frequency of the clock transition, and particularly to characterise the linear frequency drift of the ULE cavity reference and other possible slow drifts. Spectroscopy runs at varying B-field in a spin-polarised sample are displayed in Fig. 5.10. In addition to characterisation of systematic frequency shifts, such spectra are used to reference in real time each interaction shift measurement, as presented in the following Chapter.

The Zeeman separation of clock transitions associated with each spin state permits

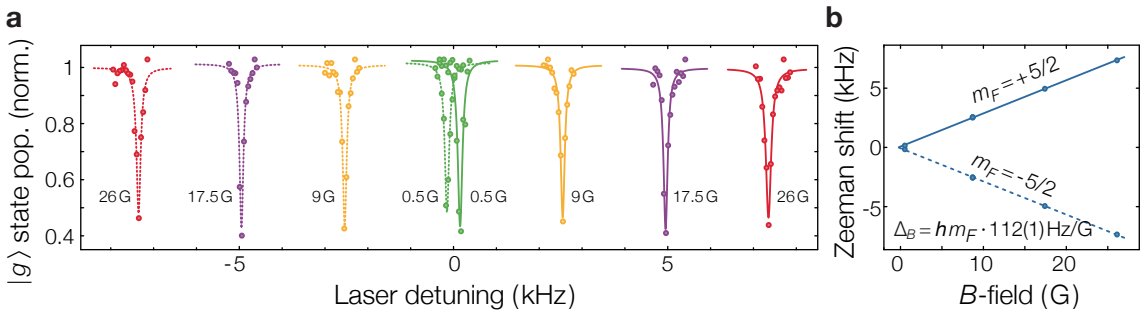

Figure 5.10 – Magnetic field spectroscopy with spin-polarised gases of ^{173}Yb. (a) Fermi gases of $|\uparrow\rangle$ (solid curves) or $|\downarrow\rangle$ (dashed curves) are spectroscopically probed in a varying B-field with a 100 ms pulse and a Rabi frequency $\Omega \simeq 2\pi \cdot 50$ Hz. (b) The differential linear Zeeman shift is separately fitted on both $|\uparrow\rangle$ and $|\downarrow\rangle$ states, yielding $\Delta_B = h\, m_F \cdot 112(1)$ Hz/G.

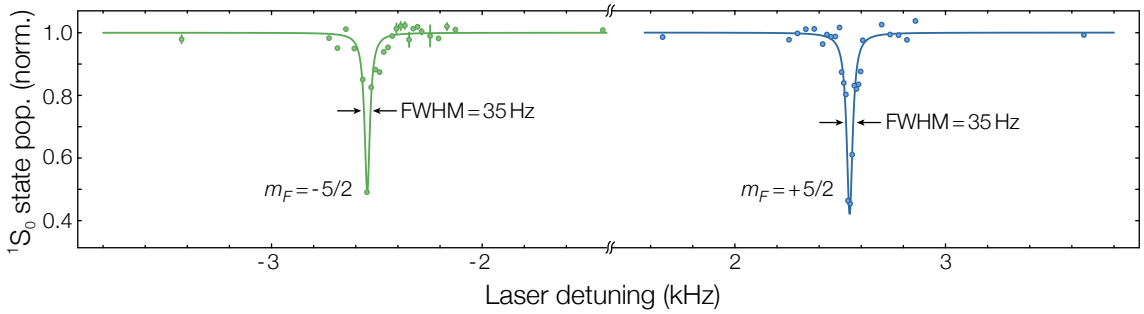

Figure 5.11 – Ultranarrow clock resonances in spin-polarised gases. A 100 ms pulse with an intensity of 0.2 μW/cm^2, corresponding to $\Omega \simeq 2\pi \cdot 20$ Hz, is used. A minimum Lorentzian absorption linewidth of 35 Hz is observed, corresponding to a short-term fractional frequency stability of 7×10^{-14}. A B-field of 9 G is employed for these measurements.

to remove residual-field broadening of resonant line-shapes, when multiple-spin mixtures are employed or unwanted residual spin states are present due to imperfect optical pumping. The best suited spectroscopy scheme for observing absorption spectra with linewidths limited only by laser stability is to probe a spin-polarised gas with a low atom number in a three-dimensional lattice. A spectrum is displayed in Fig. 5.11, obtained by exciting either the $|\uparrow\rangle$ or $|\downarrow\rangle$ state with a Rabi frequency $\Omega \simeq 2\pi \cdot 20$ Hz. Using lower Rabi frequencies reduces the resonance relative amplitudes below 0.5, indicating that the measured linewidth is ultimately limited by the laser stability over the measurement time scale.

Rabi oscillations in spin-polarised gases

The degree of coherence of the $|e\rangle$-state coupling can be further investigated by Rabi oscillation measurements. In order to limit interaction effects and excited band occupations, Rabi oscillations are performed using spin-polarised samples in the same conditions as for B-field precision spectroscopy. Rabi oscillations with three different frequencies are shown in Fig. 5.12. The transfer efficiency of a single π-pulse is typically above 90%, but

a clear damping of the oscillation is visible and after some time the excited population stabilises at approximately 50%. The visibility decay depends on the Rabi frequency, yet the product of the fitted coherence time t_{coh} and Rabi frequency is approximately constant, with ~ 6 full oscillations within $t = t_{\mathrm{coh}}$. This is an indication that the coherence is limited by dephasing between atoms in singly occupied sites. Spatial inhomogeneities in the Rabi coupling would explain this effect, and could be caused for instance by clock light intensity modulation due to etaloning inside the silica viewports or dichroic beam splitters, as well as by a slight interference of the excitation beam with its reflection off the internal surface of the viewport. The size of the excitation beam at the atoms position and its alignment were varied and revealed to have little influence on the coherence

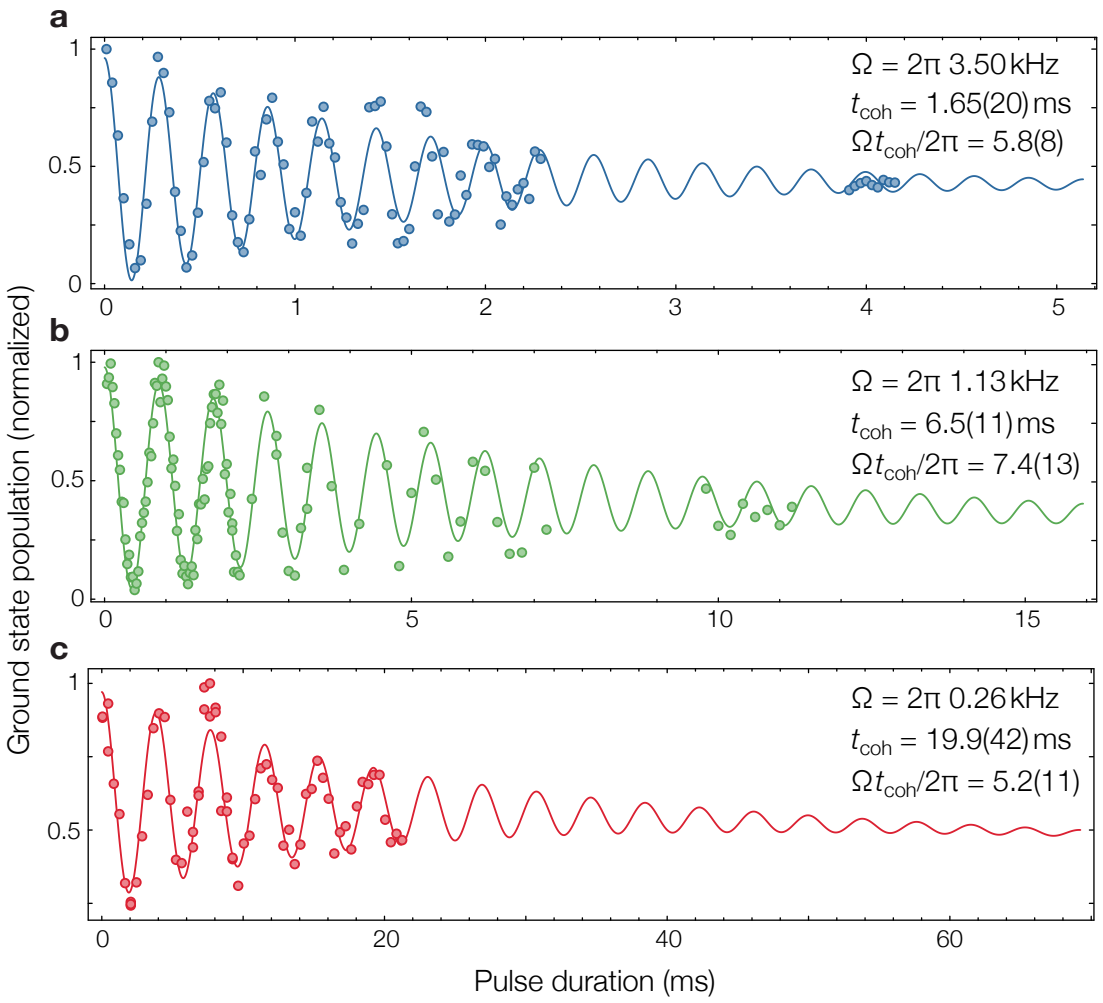

Figure 5.12 – Rabi oscillations in a spin-$|\uparrow\rangle$ polarised Fermi gas of ^{173}Yb with varying clock light intensities. A lattice depth of 30 E_r in the horizontal plane and a B-field of 10 G were adopted. A light-intensity-dependent damping of the oscillations is clearly visible. The $1/e$ time of the decay is roughly constant at $t_{\mathrm{coh}} \simeq 6 \cdot 2\pi\Omega^{-1}$, i.e. $\sim$ 6 oscillation periods are completed before the contrast is reduced by a factor e. The single π-pulse efficiency is typically close to 100%, with the exception of measurement (c) where a small detuning from resonance causes a reduced contrast. A weak overall atom number decay is visible, most likely due to inelastic collisions involving highly mobile atoms in excited Bloch bands.

time of the oscillation, supporting the hypothesis that residual spatial inhomogeneities are mainly responsible for the dephasing. On the other hand, the atom dephasing mechanism dominates the coherence time of the system only until the laser-limited coherence time $t_{\mathrm{coh,las}} \simeq 28\,\mathrm{ms}$ is reached, estimated by the measurement in Fig. 5.11. The damping time due to atom dephasing approaches $t_{\mathrm{coh,las}}$ for $\Omega \simeq 2\pi \cdot 210\,\mathrm{Hz}$.
A weak decay of the offset level of the oscillation is also visible, which indicates atom losses caused by the driving. The $1/e$ time of this loss process is approximately 100 ms and is compatible with the tunnelling time scale of atoms in the first excited band for the $30\,E_r$ deep lattice that was used. Losses may therefore be caused by p-wave inelastic collisions between $|e\rangle$ state atoms [280] or s-wave inelastic collisions between distinguishable atoms [124, 280, 282].

5.2 SU(N)-symmetric inter-orbital interactions

In this Section, starting from two-orbital interactions introduced in Section 1.2, we will develop a simple model of SU(N)-symmetric interactions between two fermionic atoms in the $|g\rangle$ and $|e\rangle$ states trapped in a site of the optical lattice. As we will see, the external magnetic field plays an important role as well, generating a mixing between the two-orbital interaction eigenstates, which allows to spectroscopically characterise the inter-orbital scattering channels at once and to directly observe inter-orbital spin-exchanging collisions. Concluding the Chapter, we will argue that a small experimental uncertainty on the demonstration of the collisional spin independence does not raise concerns regarding quantum simulations of SU(N)-symmetric models.

5.2.1 Inter-orbital interactions in a magic lattice

Two-orbital Hubbard interactions

In Section 1.2 we have already described interactions between fermionic ultracold AEL atoms including the orbital degree of freedom, represented by the electronic states $|g\rangle$ and $|e\rangle$. We have shown how two parameters V and V_{ex} are characterising the Hubbard on-site interactions for atoms trapped in an optical lattice potential with a single occupied Bloch band. Let us now consider more specifically the case of experimental interest for interaction spectroscopy, namely a pair of atoms confined to a single site of a deep three-dimensional magic lattice. The interaction energy of a single atomic pair depends upon the on-site wave function overlap (see Eq (1.46)). When both atoms occupy the lowest Bloch band of a state-independent lattice, the Hubbard interaction strengths can be written as:

$$U_X = \frac{4\pi\hbar^2}{M}\, a_X \int d^3r\, |w(\mathbf{r})|^4\,, \tag{5.4}$$

where $X = gg, ee, eg^+, eg^-$ and $w(\mathbf{r})$ is the Wannier function shared by both atoms in the lattice[6]. We remind here that the scattering lengths $a_{eg}^{\pm}$ are respectively associated with

[6] We assume here negligible contributions of inelastic collision channels to the interaction strength, so a_X is taken as real-valued.

the symmetric and antisymmetric two-particle electronic states $(|eg\rangle \pm |ge\rangle)/\sqrt{2}$, whereas a_{gg} and a_{ee} correspond to two atoms colliding in the same electronic state.
The above expression is valid in the regime of sufficiently weak interactions, i.e. $a_X \ll a_{\mathrm{ho}}$, with $a_{\mathrm{ho}} = \sqrt{\hbar/(M\omega_{\mathrm{lat}})}$ being the on-site harmonic oscillator length. In such regime, the on-site interaction does not couple different Bloch bands and the two-particle wave function is factorised into single-particle Wannier functions: in other words the interaction Hamiltonian is assumed diagonal in the on-site Wannier basis. We will separately discuss the case of strong on-site interactions in the following Chapter, in the context of the evaluation of inter-orbital scattering lengths from clock spectroscopy measurements. When a non-negligible excited band population is present, we can immediately generalise Eq. (5.4) for atoms occupying arbitrary bands a and b:

$$U_X^{ab} = \frac{4\pi\hbar^2}{M} a_X \int d^3r\, |w_a(\mathbf{r})|^2 |w_b(\mathbf{r})|^2 \,, \tag{5.5}$$

where $w_{a,b}(\mathbf{r})$ are the on-site Wannier functions of the two atoms.

The four different Hubbard interaction strengths are obviously a direct manifestation of the four scattering channels included in the Hamiltonian (1.44), which only depend on the electronic state. However, we have already argued that in order for atoms to experience s-wave contact interactions the spatial part of the two-particle relative wave function must be symmetric[7] (see Section 1.2.3). Owing to this, a direct correspondence between the spin state of the atomic pair and the applicable scattering channel also exist. As a result, inter-orbital scattering is described by the symmetric channel a_{eg}^{+} in the spin singlet state and by the anti-symmetric channel a_{eg}^{-} in the spin triplet states. All two-particle states relevant for interaction spectroscopy and the associated interaction energies are illustrated in Fig. 5.13(b). We will explain in the following the idea behind direct spectroscopical probing of all Hubbard interaction strengths represented in Fig. 5.13(b).

Onsite Hamiltonian in a magnetic field

We have just seen how Hubbard interactions are diagonal in the spin singlet-triplet basis, owing to the anti-symmetrisation of the two-particle states. We will now include an additional energy contribution resulting from the application of an external magnetic field $\mathbf{B}$, which also sets the nuclear spin quantisation axis. As described in the previous Section (see Fig. 5.9), the single-particle $|g, m_F\rangle$ and $|e, m_F\rangle$ states experience an individual linear nuclear Zeeman shift Δ_{NZ} and a linear differential Zeeman shift Δ_B, given by Eq. (5.3). We now want to specify the influence of a magnetic field on the on-site singlet-triplet two-particle states, which form a basis of the Hilbert space spanned by the electronic and the spin degree of freedom of two-fermions. Let us assume for simplicity that the spin states $|\uparrow\rangle$ and $|\downarrow\rangle$ represent nuclear spin states with opposite m_F. In this case, only the differential Zeeman shift becomes relevant for two-particle states with one atom in $|g\rangle$ and one in $|e\rangle$, as the individual state nuclear Zeeman shifts Δ_{NZ} cancel each other. In addition, when the two atoms are in the same electronic state, the total Zeeman shift is canceled as

[7] Note that this is necessary but not sufficient: symmetric wave functions with a zero at zero inter-atomic distance also lead to vanishing interactions; such wave functions are usually termed "fermionised".

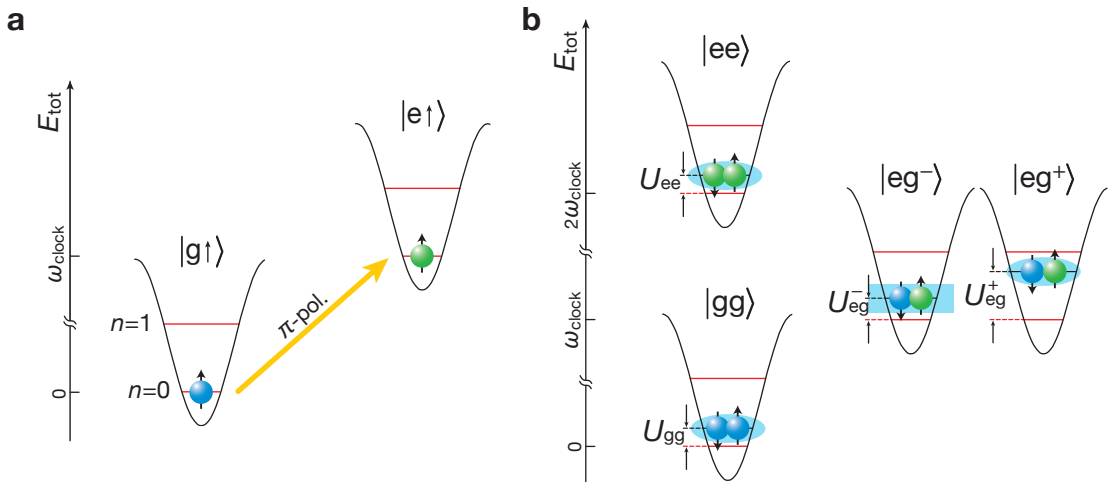

Figure 5.13 – Relevant single-band states and their energies for two fermions interacting on a lattice site with orbital and spin degrees of freedom. (a) Single-particle states: $|g\rangle$ state (blue) and $|e\rangle$ state (green). In a zero B-field, the energy difference between the two states equals the clock transition energy $E_0 = \hbar\omega_{\text{clock}}$. The optical excitation on the π-transition preserves the nuclear spin state. (b) Two-particle eigenstates in a zero B-field: two $|g\rangle$ or $|e\rangle$ state atoms can only occupy a spin singlet (ellipse), whereas atoms in different orbitals can also occupy a spin triplet (rectangle). The total energies and the different interaction energies associated with each pair state are also illustrated. The optical couplings between the various two-particle states will be clarified in Section 6.1. The figure is adapted from [124].

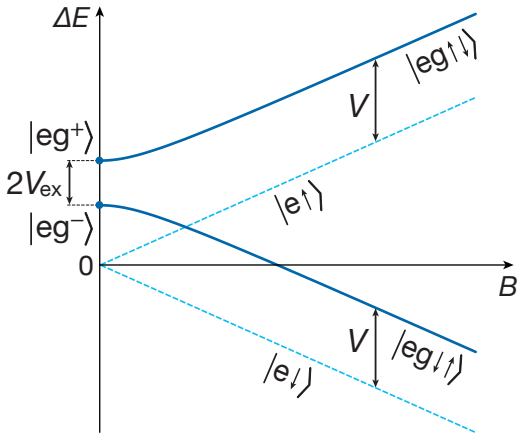

Figure 5.14 – Illustrative plot of the eigenenergies for single-particle (dashed light blue) and inter-orbital two-particle (solid blue) states in a magnetic field. The vertical axis represents the clock transition energy and the zero is set to the transition energy $E_0 = \hbar\omega_{\text{clock}}$ exciting one isolated atom at zero B-field. The transition energy of atoms on singly occupied lattice sites is linearly shifted by the differential Zeeman shift Δ_B. Two-particle eigenstates $|eg^+\rangle$ and $|eg^-\rangle$ experience different interactions at zero field, where their energies are separated by $2V_{\text{ex}} = U_{eg}^+ - U_{eg}^-$. With increasing magnetic field strength, the two zero-field eigenstates mix and the eigenenergies approach the energy $E = V + \Delta_B$ of the polarised states $|eg\uparrow\downarrow\rangle$ and $|eg\downarrow\uparrow\rangle$ (see Eqs. (5.6) and (5.8)). The figure is adapted from [124].

well. Only the two-particle "polarised" states $|eg\uparrow\downarrow\rangle$ and $|eg\downarrow\uparrow\rangle$ experience a differential Zeeman shift, and they form the symmetric and antisymmetric superpositions of the $|eg^+\rangle$ and $|eg^-\rangle$ states. We can directly write the Zeeman Hamiltonian as:

$$\hat{H}_B^{(2)} = \Delta_B\big(|eg\uparrow\downarrow\rangle\langle eg\uparrow\downarrow| - |eg\downarrow\uparrow\rangle\langle eg\downarrow\uparrow|\big) \tag{5.6}$$

where $|eg\uparrow\downarrow\rangle = (|e,\uparrow\rangle|g,\downarrow\rangle - |g,\downarrow\rangle|e,\uparrow\rangle)/\sqrt{2}$ and $|eg\downarrow\uparrow\rangle = (|e,\downarrow\rangle|g,\uparrow\rangle - |g,\uparrow\rangle|e,\downarrow\rangle)/\sqrt{2}$. We can now write the total two-particle Hamiltonian in the singlet-triplet basis[8] $\{|gg\rangle\otimes|s\rangle, |eg^+\rangle, |eg^-\rangle, |ee\rangle\otimes|s\rangle\}$ in a matrix representation:

$$\hat{H}_{eg} = \begin{pmatrix} U_{gg} & 0 & 0 & 0 \\ 0 & U_{eg}^+ & \Delta_B & 0 \\ 0 & \Delta_B & U_{eg}^- & 0 \\ 0 & 0 & 0 & U_{ee} \end{pmatrix} \tag{5.7}$$

This Hamiltonian is nothing else than the projection of the two-orbital on-site interaction in Eqs. (1.41)-(1.46) and of the differential Zeeman effect on the subspace spanned by the two-particle states which were defined in Section 1.2.3 (see Eq. (1.43)). The central block can be readily diagonalised, resulting into two eigenenergy branches:

$$E_{u,d} = V \pm \sqrt{V_{\mathrm{ex}}^2 + \Delta_B^2}\,, \tag{5.8}$$

where $V = \frac{1}{2}\left(U_{eg}^+ + U_{eg}^-\right)$ and $V_{\mathrm{ex}} = \frac{1}{2}\left(U_{eg}^+ - U_{eg}^-\right)$. The eigenenergy dependence on the B-field amplitude for the two-orbital states is illustrated in Fig. 5.14, along with the energy dependence of single-particle excited states given as a reference. The parameters V and V_{ex} defined here are precisely the magic-lattice version of the parameters defined in Eq. (1.46) for an arbitrary lattice potential. The important fact needs to be emphasised: the magnetic field generates a coupling between the inter-orbital interaction eigenstates, $|eg^+\rangle$ and $|eg^-\rangle$. Owing to this coupling, the energy of a single eigenstate of Eq. (5.7) depends on both U_{eg}^+ and U_{eg}^- at once. By analysing the frequency shift of the clock transition which connects the $|gg\rangle$ state to the lowest-energy eigenstate of Eq. (5.7) through precision spectroscopy at varying B-field, the interaction strength in both the symmetric and the antisymmetric channel can be determined [124]. The spectroscopic measurements of such interaction shifts in ^{173}Yb and the consequent determination of the so far unknown scattering lengths a_{eg}^+, a_{eg}^- and a_{ee} is reported in Section 6.1. The influence of atomic collisions on to the clock transition energy, which in optical lattice clocks represent a source of unwanted systematic shifts and needs to be canceled [280–282, 320, 323], turns in this context into a resource for the precise characterisation of inter-orbital interactions.

Furthermore, we note that at zero-field the polarised states $|eg\uparrow\downarrow\rangle$ and $|eg\downarrow\uparrow\rangle$ are coupled by the on-site interactions, through the exchange coupling V_{ex}. When only two spin states are populated, the exchange term in Hamiltonian (1.44) has indeed the form $\hat{\mathcal{V}}_{\mathrm{ex}} \propto \hat{S}_g^+\hat{S}_e^- + \hat{S}_g^-\hat{S}_e^+$. The difference between the energies of the singlet and triplet states

[8] The aligned triplet states $(|eg\rangle - |ge\rangle)/\sqrt{2}\otimes|\uparrow\uparrow\rangle$ and $(|eg\rangle - |ge\rangle)/\sqrt{2}\otimes|\downarrow\downarrow\rangle$ were left out of the discussion for simplicity, since they anyway cannot be coupled through π-polarised clock light to our experimental initial state, i.e. $|gg\rangle\otimes|s\rangle$.

leads therefore to spin exchange between the two orbitals at zero-field, as was shown in Section 1.2.3. The spin dynamics generated by this mechanism can be directly observed experimentally [124, 176]: such observations will be presented in Section 6.2.

5.2.2 Two-orbital SU(N) symmetry

So far we have assumed completely nuclear spin-independent interactions involving the $|e\rangle$ state. We will now shortly elaborate on the extension of the SU(N) symmetry to the second electronic orbital. We explained in Chapter 1 how the decoupling between nuclear and total electronic angular momentum for all states with $J = 0$ guarantees the independence of short-range molecular potentials from the nuclear spin orientation. However, the small admixture of the $|e\rangle$ state with higher-lying ^3P states caused by hyperfine interaction (HFI) slightly breaks the decoupling [96]. The relative deviation of the scattering lengths associated with different nuclear spin combinations can be estimated in a similar way as described for the ground state in Section 4.3, yet accounting for the HFI strength in the ^3P manifold of the electronic level structure [55]. For ytterbium, this yields a conservative estimate of $\delta a_{ee}/a_{ee} \sim \delta a_{eg}^{\pm}/a_{eg}^{\pm} < 10^{-2}$, somewhat larger than for strontium. We were able to experimentally verify the SU(N) symmetry in all collision channels of the two-orbital system by direct spectroscopic investigation of interactions in different spin mixtures, and found no violation down to our experimental uncertainty of a few percent (see the measurements in Section 6.1.2). It is clear from Eq. (1.26) that, if the SU(N) symmetry were broken, any colliding pair of spin states within the six-spin manifold of ^{173}Yb would correlate to various coupled spin collision channels[9]. In order to experimentally demonstrate the two-orbital SU(N) symmetry, it is therefore sufficient to verify the equivalence of two-orbital interactions amongst distinct two-spin mixtures, without the necessity of adopting a six-spin mixture.

Wether the measured degree of fulfilment of SU(N) symmetry is sufficient or not to observe SU(N)-symmetric many-body phenomena clearly depends on the particular physical system of interest. As a general conservative condition, the system will behave symmetrically as long as all relevant energy scales are much larger than the energy deviations associated with different spin configurations. Let us briefly elucidate this criterion with regard to the lattice models which we plan to implement (see Section 1.3).

For the KLM the relevant energy scales are $|V_{\mathrm{ex}}|$ and V_{ex}^2/J_g, in the strong and weak exchange coupling regime, respectively [55] (see Section 1.3.1). The SU(N) symmetry breaking is at most ΔV_{ex}, which we can estimate as: $\Delta V_{\mathrm{ex}}/|V_{\mathrm{ex}}| \sim \Delta U_{eg}^{\pm}/|V_{\mathrm{ex}}| = \delta a_{eg}^{\pm}/|a_{eg}^{+} - a_{eg}^{-}| \lesssim 10^{-2}$. The condition in the two regimes is given as $\Delta V_{\mathrm{ex}} \ll |V_{\mathrm{ex}}|$ or $\Delta(V_{\mathrm{ex}}^2/J_g) = 2\Delta V_{\mathrm{ex}} V_{\mathrm{ex}}/J_g \ll V_{\mathrm{ex}}^2/J_g$, and they are both satisfied as long as $\Delta V_{\mathrm{ex}} \ll |V_{\mathrm{ex}}|$, which is directly checked experimentally.

On the other hand, the relevant energy scale for SU(N)-symmetric Heisenberg spin models is the super-exchange coupling J^2/U. In a similar way, the SU(N) symmetry breaking ΔU yields a deviation $\Delta\left(J^2/U\right) = (J/U)^2\,\Delta U$. The condition $\Delta\left(J^2/U\right) \ll J^2/U$ is then satisfied for $\Delta U \ll U$, and again this is experimentally confirmed to a few percent level. Conse-

[9] The only exception is a mixture of two marginal states e.g. $m_F = 5/2$ and $m_F' = 3/2$, which is collisionally stable in SU(2) symmetric systems as well.

quently, our precision in the determination of the two-orbital SU(N) symmetry in ^{173}Yb can be considered sufficient in relation to quantum simulation of these SU(N)-symmetric models.

CHAPTER 6

Two-orbital SU(N)-symmetric spin-exchange interactions

Spin-exchange interactions between ultracold alkaline-earth-like atoms in the two lowest electronic states are well suited to realise the elementary building block of orbital quantum magnetism, as discussed in Chapter 1. This type of interaction gives rise to many strongly-correlated quantum phenomena in condensed matter, from heavy-Fermi behaviour [75–77] and Kondo effect [127, 177, 185] to magnetic ordering [198–200, 205] and non-Fermi liquid behaviour [191, 192, 201]. Ultracold gases of ytterbium and other alkaline-earth-like atoms in optical lattices could shed light on the long-standing open issues related to the modelling of such phenomena, implementing defect-free and controlled realisations of models such as the Kondo lattice model [127, 177] or the Kugel-Khomskii model [128, 183], which were formulated to explain the role of orbital spin-spin interactions between electrons in solid materials.

In this Chapter we present how spin-exchange interactions between the two (meta-) stable states of ^{173}Yb are experimentally revealed and quantitatively characterised, representing an important step towards the realisation of orbital magnetism in atomic systems. Using a Fermi gas of ^{173}Yb loaded into a state-independent optical lattice, the contact interactions in the two-orbital system are spectroscopically probed exploiting the high measurement precision obtained by addressing the clock transition. The resonance frequency shifts caused by the different collision channels between atoms in different electronic states are detected and related to the associated scattering lengths. The SU(N) symmetry of the two-orbital collisions, arising from the strong decoupling between nuclear and electronic spin, is experimentally demonstrated by analysing different spin ensembles. Furthermore, we directly observe the real-time evolution of the spin distribution of an initially out-of-equilibrium sample, induced by the spin-exchanging magnetic interactions between the two atomic orbitals. Finally, we address the role of inelastic collisions in two-orbital ensembles in order to support the feasibility of quantum simulation with the two lowest electronic states of ^{173}Yb atoms in optical lattices.

6.1 Interaction spectroscopy in the magic optical lattice

A fundamental quantity, in order to determine whether ^{173}Yb is a well-suited candidate for the quantum simulation of orbital magnetism, is the strength of the spin-exchange

coupling between the electronic ground state $^1S_0$ and the metastable excited state $^3P_0$. Interactions between ultracold ytterbium atoms in the ground state have already been characterised for all isotopes by two-colour photoassociation spectroscopy [226]. Those (p-wave) scattering parameters which are relevant for interaction processes occurring in optical lattice atomic clocks with ^{171}Yb have also recently been estimated [280, 281]. Yet the strength of the interactions between the $^1S_0$ and the $^3P_0$ state in ^{173}Yb, and especially of the spin-exchange coupling and of the different inelastic collision channels, has previously been unknown. In this Section, we will present a complete spectroscopic characterisation of the elastic scattering channels in the two-orbital system. The minimal system suitable to investigate contact interactions is represented by an isolated atom pair, which is also the cleanest system in the case of pairwise interactions. A large number of copies of such an elementary system are prepared by loading a two-spin Fermi gas into a three-dimensional magic optical lattice, using samples with an atom number approximately suited to reach the band-insulating regime. By successively probing the lattice gas with clock excitation light, we directly detect the transition energy shifts caused by the atomic interactions in the two-particle final states. By this method we provide moreover an experimental demonstration of occupation number-selective clock excitation in a three-dimensional lattice, which represent in itself a powerful resource for probing the density of many-body states in the lattice. We will conclude this Section by showing how the SU($N = 6$)-symmetric nature of the interactions was directly revealed by performing spectroscopy on different preparations of the nuclear spin degree of freedom.

6.1.1 Spectroscopic determination of the scattering parameters

Two-particle state Rabi couplings

We start by analysing the coupling induced by π-polarised clock light between the two-particle interacting states that we have discussed in Section 5.2.1. This will allow us to understand in detail in which way their interaction energies can be measured through clock excitation spectroscopy. Again let us consider atoms occupying two nuclear spin states with opposite m_F: $\uparrow = m_F$ and $\downarrow = -m_F$. The single-particle Hamiltonian describing the coherent atom-light interaction for π-polarised light is given by:

$$\begin{aligned}\hat{H}_\pi^{(1)} &= \frac{\hbar\Omega}{2}(|e\uparrow\rangle\langle g\uparrow| - |e\downarrow\rangle\langle g\downarrow|) + \text{h.c.} \\ &= \frac{\hbar\Omega}{2}\sigma_{eg}^x \otimes \sigma_{\uparrow\downarrow}^z\end{aligned} \tag{6.1}$$

where σ_{eg}^μ and $\sigma_{\uparrow\downarrow}^\mu$ are the Pauli matrices respectively in the $\{|e\rangle, |g\rangle\}$ and $\{|\uparrow\rangle, |\downarrow\rangle\}$ basis. The minus sign between the two Rabi frequencies for spin-up and spin-down arises from the sign difference of the Clebsch-Gordan coefficient between the two π-transitions $|\pm m_F\rangle \rightarrow |\pm m_F\rangle$ (see Appendix A). We can now write the two-particle atom-light Hamiltonian:

$$\hat{H}_\pi^{(2)} = \frac{\hbar\Omega}{2}\left(\sigma_{eg}^x \otimes \sigma_{\uparrow\downarrow}^z\right)_1 \otimes \left(1_{eg} \otimes 1_{\uparrow\downarrow}\right)_2 + \frac{\hbar\Omega}{2}\left(1_{eg} \otimes 1_{\uparrow\downarrow}\right)_1 \otimes \left(\sigma_{eg}^x \otimes \sigma_{\uparrow\downarrow}^z\right)_2 \tag{6.2}$$

Considering the two-particle set of states $\{|gg\rangle \otimes |s\rangle, |eg^+\rangle, |eg^-\rangle, |ee\rangle \otimes |s\rangle\}$, we find only two non-vanishing couplings:

$$\frac{\hbar}{2}\Omega_D^- = \langle eg^-|H_\pi^{(2)}|gg\rangle \otimes |s\rangle = \sqrt{2}\frac{\hbar\Omega}{2} \tag{6.3a}$$

$$\frac{\hbar}{2}\Omega_D^{ee} = \langle eg^-|H_\pi^{(2)}|ee\rangle \otimes |s\rangle = -\sqrt{2}\frac{\hbar\Omega}{2} \tag{6.3b}$$

We note here that for two nuclear spin states with non-opposite m_F, both couplings between the $|gg\rangle$ state and the $|eg^\pm\rangle$ states are finite[1], since the associated single-particle Rabi couplings are not opposite as we have assumed in Eq. (6.1).

The Rabi couplings of the $|gg\rangle$ state can be generalised to the case of an applied external magnetic field where the interaction eigenstates $|eg^\pm\rangle$ are mixed, yielding the two eigenstates $|eg^u\rangle$ and $|eg^d\rangle$, respectively associated with the two eigenenergies E_u and E_d given in Eq. (5.8). The explicit form of $|eg^u\rangle$ and $|eg^d\rangle$ results from diagonalisation of Eq. (5.7):

$$|eg^u\rangle = c_1(\Delta_B)|eg^+\rangle + c_2(\Delta_B)|eg^-\rangle \tag{6.4a}$$

$$|eg^d\rangle = c_1(\Delta_B)|eg^-\rangle - c_2(\Delta_B)|eg^+\rangle \tag{6.4b}$$

with

$$c_1(\Delta_B) = \frac{V_{\mathrm{ex}} + \sqrt{V_{\mathrm{ex}}^2 + \Delta_B^2}}{\sqrt{2V_{\mathrm{ex}}^2 + 2\Delta_B^2 + 2V_{\mathrm{ex}}\sqrt{V_{\mathrm{ex}}^2 + \Delta_B^2}}} \tag{6.5a}$$

$$c_2(\Delta_B) = \frac{\Delta_B}{\sqrt{2V_{\mathrm{ex}}^2 + 2\Delta_B^2 + 2V_{\mathrm{ex}}\sqrt{V_{\mathrm{ex}}^2 + \Delta_B^2}}} \tag{6.5b}$$

The limiting cases are retrieved for $\Delta_B \ll V_{\mathrm{ex}}$, with $c_1 \simeq 1$ and $c_2 \simeq 0$, and for $\Delta_B \gg V_{\mathrm{ex}}$, with $c_{1,2} \simeq 1/\sqrt{2}$ (see also Fig. 5.14). The Rabi couplings can then be written as:

$$\begin{aligned}\frac{\hbar}{2}\Omega_D^u(\Delta_B) &= \langle eg^u|H_\pi^{(2)}|gg\rangle \otimes |s\rangle = \sqrt{2}\frac{\hbar\Omega}{2}c_2(\Delta_B)\\ \frac{\hbar}{2}\Omega_D^d(\Delta_B) &= \langle eg^d|H_\pi^{(2)}|gg\rangle \otimes |s\rangle = \sqrt{2}\frac{\hbar\Omega}{2}c_1(\Delta_B)\end{aligned} \tag{6.6}$$

Interaction clock shifts in a magnetic field

Having clarified the Rabi couplings between the relevant two-particle states in our system, we present here the spectra obtained by incoherent clock spectroscopy in the magic lattice. The experimental sequence for precision spectroscopy was described in Section 5.1.2, and consists of loading a two-spin Fermi gas of ^{173}Yb into a deep three-dimensional lattice in 200 ms and applying a 100 ms π-polarised clock pulse[2], with a single-particle Rabi

[1] The two-particle Rabi frequencies associated with the $|eg^\pm\rangle$ states are in general $\Omega_D^\pm = (\Omega_{m_F} \mp \Omega_{m_F'})/\sqrt{2}$, where Ω_{m_F} is the Rabi frequency of a particular m_F state on the π-transition.

[2] As the adopted lattice depths are always above $30\,E_r$ and the measurement time scale is around 100 ms, tunnelling processes in the lattice having a rate $J/h \lesssim 1$ Hz can be neglected.

frequency $\Omega \simeq 2\pi \cdot 200\,\mathrm{Hz}$. The detuning of the clock laser is varied from one experimental cycle to the next and the ground state atom number after the application of the spectroscopy pulse is detected by means of TOF absorption imaging, releasing the cloud directly out of the lattice.

Instead of simply varying the clock laser detuning monotonically, the spectra are collected using an alternating frequency sampling: resonances related to singly occupied lattice sites, equivalent to the ones observed using spin-polarised samples, are probed simultaneously with other spectral features stemming from interactions. In this way, the influence of uncontrolled frequency drifts of the clock laser occurring in the course of a single spectroscopy run can be minimised. Moreover, the known linear Zeeman shift of the single-particle states can be used as an absolute frequency reference among measurements at different B-field amplitudes. When employing symmetric spin mixtures, the clock frequency offset is calibrated to 0 at the centre between the two observed single-particle resonances, separately for each spectroscopy run. The atom number after the application of the spectroscopy pulse is detected by means of time-of-flight absorption imaging, releasing the cloud directly out of the optical lattice.

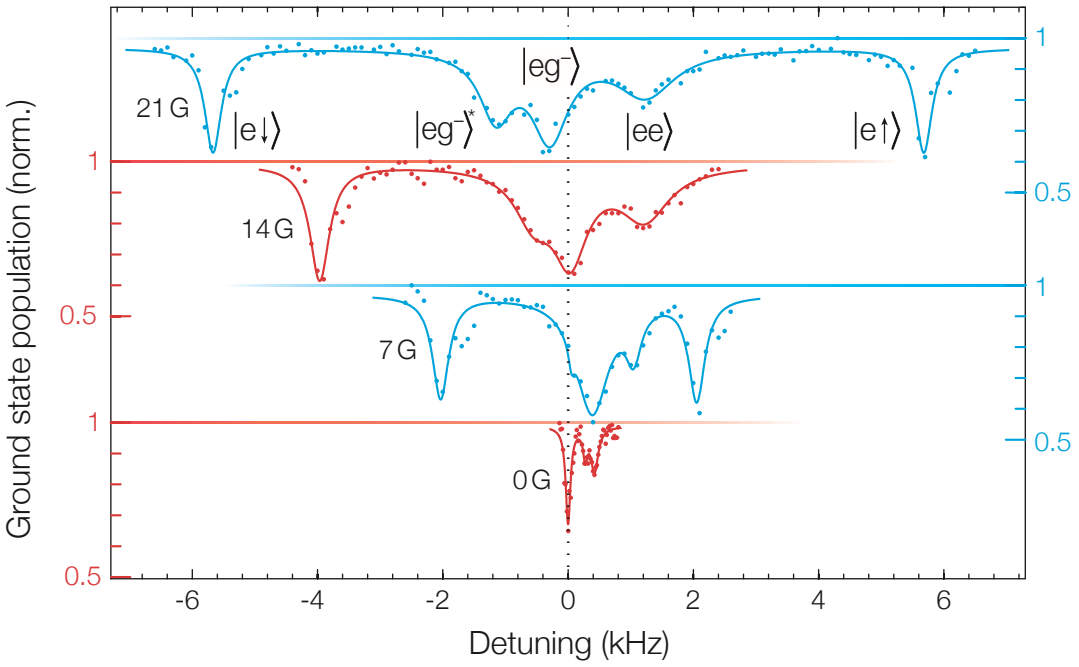

Figure 6.1 – Clock transition spectra for a two-spin Fermi gas ($m_{F,F'} = \pm 5/2$) with a total atom number $N \simeq 1 \times 10^5$ in a 3D magic optical lattice. Spectroscopy runs at different magnetic field strengths are shown. Solid lines are multiple-Lorentzian fits to determine the resonance positions. The figure is adapted from [124].

Without any magnetic field and using a symmetric spin mixture, with two states m_F and $m_{F'} = -m_F$, the clock light only couples to the $|eg^-\rangle$ state and the coupling is given in Eq. (6.3a). At zero-field, the frequency shift between the clock resonance associated with singly occupied lattice sites and the one associated with doubly occupied lattice sites is therefore a direct measurement of the energy difference $U_{eg}^- - U_{gg}$, as illustrated in

Fig. 5.13(b). At increasing magnetic field, the $|eg^d\rangle$ state, which coincides with $|eg^-\rangle$ at zero-field, decreases its energy due to the differential Zeeman shift and the associated clock shift changes accordingly, as sketched in Fig. 5.14. A measurement of the B-field dependence of the eigenenergy E_d allows for the experimental determination of the two Hubbard parameters V and V_{ex} through Eq. (5.8). Typical spectra in a $m_{F,F'} = \pm 5/2$ mixture are displayed in Fig. 6.1, where runs performed at various magnetic field amplitudes are plotted together with multiple-Lorentz fits to the observed resonant features. The spectra are found to exhibit multiple absorption features, which will be individually elucidated in the following.

First of all, the resonances associated with singly occupied sites can be clearly identified as the two lines shifting linearly outwards for increasing B-field, with a slope of $\Delta_B/h = m_F \cdot 112(1)\,\mathrm{Hz/G}$ (see Section 5.1.3).

Three additional absorption lines are clearly visible, with increasing relative shifts from one another at larger magnetic fields. The fitted centre positions of the observed resonances in a $m_{F,F'} = \pm 5/2$ mixture are plotted in Fig. 6.2(a). Two resonances shift quadratically with the magnetic field and we identify them with the transition from the $|gg\rangle$ to the $|eg^d\rangle$ state and from the $|gg\rangle^*$ to the $|eg^d\rangle^*$ state, respectively. The states $|gg\rangle^*$ and $|eg^d\rangle^*$ are simply the analogue of the $|gg\rangle$ and $|eg^d\rangle$ states with one of the two atoms occupying the first excited Bloch band. We denote the associated Hubbard interaction strengths by U^*_{gg} and U^{-*}_{eg}, which are given by Eq. (5.5) with $a = 1, b = 2$. By fitting the field-dependent shift of the $|eg^d\rangle$ resonance with the lower eigenenergy E_d in Eq. (5.8), we can obtain $V - U_{gg}$ and V_{ex}, or equivalently $U^-_{eg} - U_{gg}$ and $U^+_{eg} - U_{gg}$. Likewise, we can obtain the values for the states with one band excitation. Fits to the measured $|eg^d\rangle$ state resonance shifts are shown Fig. 6.2(b) for different mean lattice depths $\tilde{V} = (V_x V_y V_z)^{1/3}$, and the fit results are summarised in Table 6.1. Spectroscopy was performed on a total of five different two-spin mixtures, namely $m_{F,F'} = \pm 5/2, \pm 3/2, \pm 1/2$, $m_{F,F'} = +5/2, -3/2$ and $m_{F,F'} = +5/2, -1/2$ (see Section 4.2 for details on the spin state preparation). Spectra acquired with the various spin mixtures are displayed in Fig. 6.4.

The zero-field shifts are the interaction shifts of the $|eg^-\rangle$ and $|eg^-\rangle^*$ states, and represent directly $U^-_{eg} - U_{gg}$ and $U^{-*}_{eg} - U^*_{gg}$. The scattering length a^-_{eg} can then be deduced through Eq. (5.4), using the computed lowest-band Wannier functions for each adopted lattice depth. Zero-field spectroscopy was additionally carried out in a balanced six-spin mixture, where doubly occupied sites with every allowed spin combination are

Lattice depth $\tilde{V}$	V_{ex} ($h\cdot$ kHz)	$U^-_{eg} - U_{gg}$ ($h\cdot$ kHz)	$U^+_{eg} - U_{gg}$ ($h\cdot$ kHz)
$30\,E_r$	14.73 ± 2.40	0.28 ± 0.14	29.75 ± 4.80
$33\,E_r$	16.16 ± 0.83	0.33 ± 0.05	32.65 ± 1.65
$43\,E_r$	22.25 ± 0.95	0.37 ± 0.05	44.87 ± 1.89

Table 6.1 – Inter-orbital Hubbard interaction strengths for different lattice depths. The parameter values are obtained through fitting the clock spectra from a $m_{F,F'} = \pm 5/2$ spin mixture with the lower eigenenergy of the single-band Hamiltonian in Eq. (5.8).

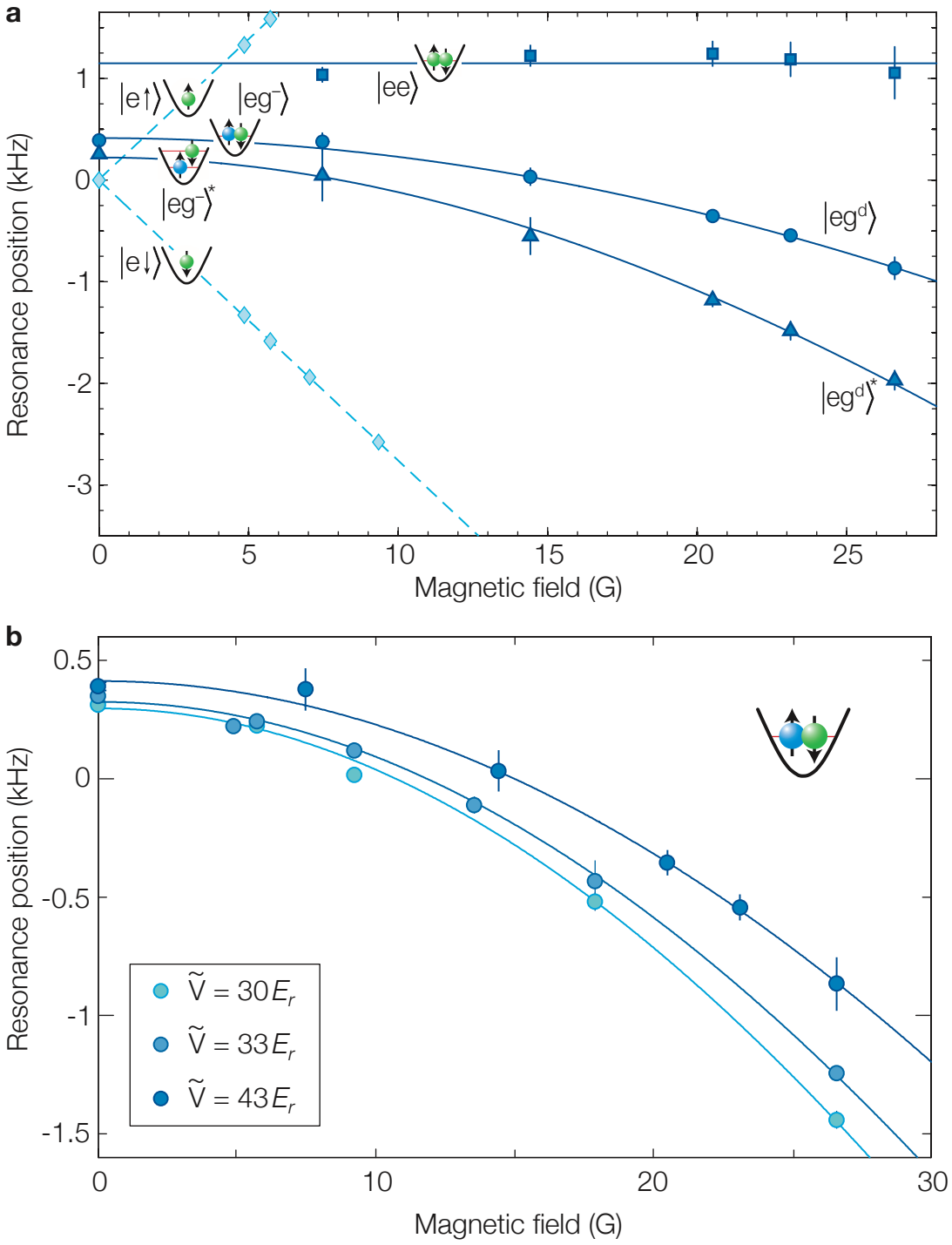

Figure 6.2 – Magnetic-field dependence of clock transition frequencies with two-orbital on-site interactions. (a) Resonance positions in an $m_{F,F'} = \pm 5/2$ spin mixture are shown for a lattice depth $\tilde{V} = 43\,E_r$. Squares indicate transitions to the $|ee\rangle$, circles to $|eg^{\,d}\rangle$, triangles to $|eg^{\,d}\rangle^*$ and diamonds to $|e\uparrow\rangle$ and $|e\downarrow\rangle$ states. The solid blue lines are fits to the $|eg^{\,d}\rangle$ and $|eg^{\,d}\rangle^*$ data with Eq. (5.8). Error bars represent the 95% confidence interval of resonance position Lorentzian fits. (b) The $|eg^{\,d}\rangle$ resonance shifts are plotted at varying magnetic field for different lattice depths. The figure is adapted from [124].

present (see the last panel in Fig. 6.4). By averaging more than 20 spectroscopy measurements with different lattice depths and spin combinations, we obtain $\Delta a_{eg}^{-} = a_{eg}^{-} - a_{gg} = 20.1(20)\,a_0$, and consequently an estimate of the scattering length $a_{eg}^{-} = 219.5(29)\,a_0$, where we included the experimental uncertainty of the measurement of a_{gg} from Ref. [226].

Furthermore, fitting the shift of the $|eg^{-}\rangle^{*}$ resonances and using Eq. (5.4) with different Wannier functions for the two atoms yields $\Delta a_{eg}^{-} = 22.7(73)\,a_0$, which is consistent with the more precise value obtained from the measurement of the $|eg^{-}\rangle$ resonance shifts. We find the $|eg^{d}\rangle^{*}$ state absorption line to be more pronounced for large samples with $N \gtrsim 10^5$, indicating a significant population of the excited band, as expected by band mapping measurements (see Section 2.2.4).

On the other hand, the fits with Eq. (5.8) yield extremely large estimates of U_{eg}^{+}, exceeding the energy of the first excited band in the lattice. Such values are unphysical: the Hubbard interaction strength can only grow until it saturates the first lattice band gap. For increasing interaction strength, the wave function overlap between the two atoms decreases compared to the lowest-band Wannier absolute square overlap, and the two-particle wave function cannot any longer be expressed in terms of lowest-band Wannier functions [165, 324]. The two atoms gradually separate, and for infinite s-wave scattering length the two atoms cannot be found at same position at all. The complete vanishing of the pair spatial overlap is usually denoted as "fermionisation" and leads to the total suppression of contact interaction [24, 325]. It has been shown that for two atoms confined to a harmonic potential well, in the limit of strong repulsive interactions $a \gg a_{\mathrm{ho}}$, the ground state energy saturates at the energy of the first excited motional state [133, 325]. In other words the interaction is completely suppressed at the cost of a motional excitation with energy $\hbar\omega_{\mathrm{ho}}$. The situation is analogous with on-site interactions in a deep lattice potential: for strong interactions the absolute square of the two-particle relative wave function approximately approaches the absolute square of the first-excited Wannier function, which has a zero at $\mathbf{r} = \mathbf{r}_1 - \mathbf{r}_2 = 0$ (see Fig. A.4). Therefore, the Hubbard interaction strength saturates approximately at the energy gap $\hbar\omega_{\mathrm{lat}}$ between the lowest and the first excited band [176, 326, 327]. Nevertheless, an important difference is the anharmonicity of the lattice potential, which couples the centre-of-mass and the relative motion and has to be taken into account to compute the correct dependence of the interaction energy upon the scattering length even for very deep lattices [176, 327, 328]. In the regime of strong interactions, it is therefore clear how the single-band Hubbard formula in Eq. (5.4) is completely inaccurate for quantifying the interaction strength and relating it to the associated scattering length. However, we can already safely state that the U_{eg}^{+} interaction strength is on the order of the first lattice band gap, which reaches up to approximately $\hbar\omega_{\mathrm{lat}} \simeq h \cdot 25\,\mathrm{kHz}$ for the employed lattice depths. This implies a surprisingly strong exchange interaction $V_{\mathrm{ex}} \approx h \cdot 10\,\mathrm{kHz}$ for lattice depths close to $40\,E_r$. Later we will discuss the implications of such a large exchange coupling and how more accurate estimates of the scattering length a_{eg}^{+} could be obtained by taking into account the lattice band structure and the regularisation of the interaction pseudo-potential.

A last distinct absorption line is found in the clock spectra, located nearby the $|eg^{-}\rangle$ state resonance at zero B-field. Yet its position is independent of the field strength and we

identify this resonance with the detuned two-photon transition to the $|ee\rangle \otimes |s\rangle$ state, which experiences no field shift for symmetric spin mixtures as the differential Zeeman shifts of the two atoms cancel each other. The resonance shift is thus given by $E_{ee} = \frac{1}{2}(U_{ee} - U_{gg})$, where the factor 1/2 accounts for the two-photon character of the excitation. This two-photon excitation relies upon $|eg^d\rangle$ as an intermediate detuned state and the detuning varies with the B-field owing to the Zeeman shift of the $|eg^d\rangle$ state. The two-photon coupling is given by:

$$\Omega_2^{ee}(\Delta_B) \simeq \frac{\Omega_D^- \Omega_D^{ee}}{2\Delta_{eg}} \tag{6.7}$$

where $\hbar\Delta_{eg} = \frac{1}{2}(U_{ee} - U_{gg}) - E_d(\Delta_B)$. The strength of this line decreases therefore with the B-field amplitude[3] and the resonance should completely disappear for high fields. The line shape is moreover affected by the strong $|e\rangle$ state two-body inelastic collisions (see Section 6.3). By fitting for its centre position in all spectroscopy runs and using Eq. (5.4) to compute a_{ee}, we obtain $\Delta a_{ee} = a_{ee} - a_{gg} = 106.8(104)\, a_0$, which in turn yields $a_{ee} = 306.2(106)\, a_0$. This value is computed including all adopted spin combinations as well.

A clear resonance corresponding to the excitation to the $|eg^u\rangle$ state has not been observed to date. When using symmetric spin mixtures the Rabi coupling to the $|eg^u\rangle$ state is very small for the magnetic fields within reach of our experimental setup, with $\Delta_B \ll V_{\mathrm{ex}}$ (see Eq. (6.6)). The coupling is moreover affected by the reduced spatial wave function overlap due to the strong interaction that was found. Thanks to the larger magnetic-field capability achieved through recent upgrades of the experimental setup, this transition could be directly probed in the near future.

Two-particle Rabi oscillations

The indistinguishable two-particle nature of the $|eg^-\rangle$ state can be confirmed by driving Rabi oscillations with the excitation light tuned at the resonant frequency of the $|gg\rangle \otimes |s\rangle \rightarrow |eg^-\rangle$ transition. Since the final state is a two-particle spin superposition, one expects a Rabi frequency which is a factor of $\sqrt{2}$ larger than the Rabi frequency obtained by driving the single-atom transition with an equal light intensity (see Eq. (6.3a)). This factor is experimentally detected by comparing separate Rabi oscillation measurements where the clock laser is respectively tuned into resonance with the single-atom or the two-atom transition at a low magnetic field. A non-zero field is used to increase the spectral separation of the two resonances, in order to allow a Rabi driving with a frequency larger than the zero-field interaction shift between the two states. As the two-particle state coupled at such weak B-fields is nearly equal to $|eg^-\rangle$, no detectable deviation from $\Omega_D^-/\Omega = \sqrt{2}$ is expected[4]. Such measurements are displayed in Fig. 6.3, along with fits of the Rabi frequencies, showing excellent agreement with the expected ratio. Additionally, an atom loss is clearly visible, next to the Rabi flopping of the $|eg^-\rangle$ state. Inelastic e-g

[3] We are neglecting the effect of the admixture of the $|eg^+\rangle$ state into the $|eg^d\rangle$ state, as it is very small at the B-field strengths employed for the reported measurements.

[4] The two-particle coupling is only affected at a 2% level by the reduced spatial wave function overlap due to the interactions with $a_{eg}^- = 219.5\, a_0$ [176].

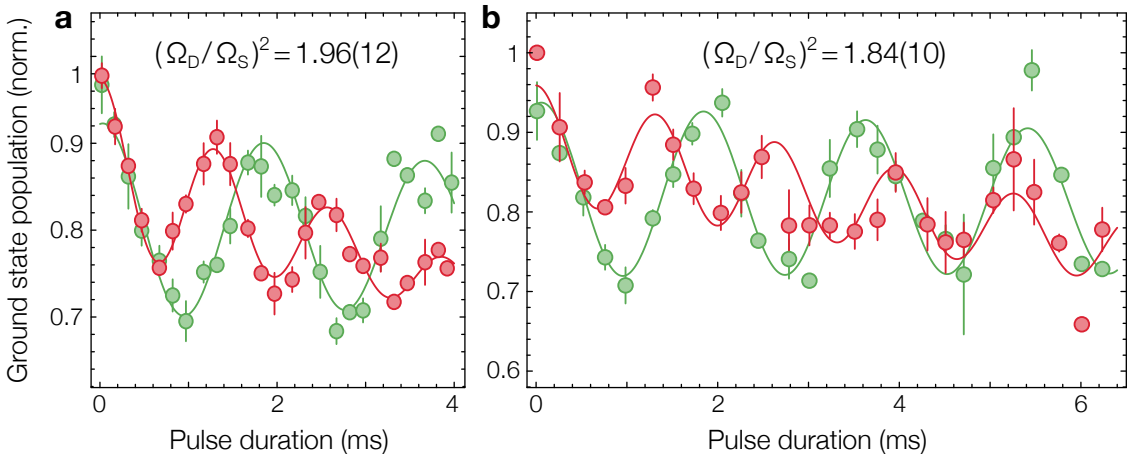

Figure 6.3 – Two-particle state Rabi oscillations. Rabi oscillations on the single-atom $|e\uparrow\rangle$ state resonance (green) and on the two-particle $|eg^-\rangle$ state (red) resonance are measured in a 7 G B-field (a) and in a 10 G B-field. Error bars represent the standard error around the mean of 2-3 measurement points. The two observed Rabi frequencies are directly compared, yielding a ratio in good agreement with the expected factor $\Omega_D^-/\Omega \simeq \sqrt{2}$.

losses caused by the simultaneous excitation of the mobile $|eg^-\rangle^*$ state could be partially responsible for the observed underlying atom number decay. A detailed investigation of inelastic losses will be presented in Section 6.3.

This measurements clearly illustrate how the selective coherent driving of the clock transition on singly and doubly occupied lattice sites constitutes a quantitative probe of particle pairs: the high-efficiency transfer of doubly occupied sites to the $|eg^-\rangle$ state by a clock π-pulse allows to determine the total number of on-site pairs in the 3D lattice. Such probe is moreover non-destructive, and the initial $|g\rangle$ pair state can be approximately restored by applying a second π-pulse. An appealing application of this probing method is the spatially-resolved detection of single and double site occupations in the lattice. By combining the coherent driving of the clock transition with very high B-field gradients $\sim 10^3$ G/cm, a spatial resolution of few micrometers in the detection of doubly occupied sites could be achieved, in a similar way as done in Refs. [40, 277]. Alternatively, atoms in singly or doubly occupied sites could be selectively darkened (also depending on their spin state) and high-resolution absorption imaging could provide an accurate reconstruction of the density distribution in the lattice.

6.1.2 Demonstration of two-orbital SU(N) symmetry

We have already explained how the scattering lengths $a_{eg}^- = 219.5(29)\,a_0$ and $a_{ee} = 306.2(106)\,a_0$ are obtained by including data from various spin state preparations. In Fig. 6.4 the B-field resonance shifts of the $|eg^d\rangle$ and $|ee\rangle$ states for different preparations are plotted, together with the linear Zeeman shifts of the single-particle states as a reference. The B-field dependence of the E_d eigenenergy needs to be modified for two-particle

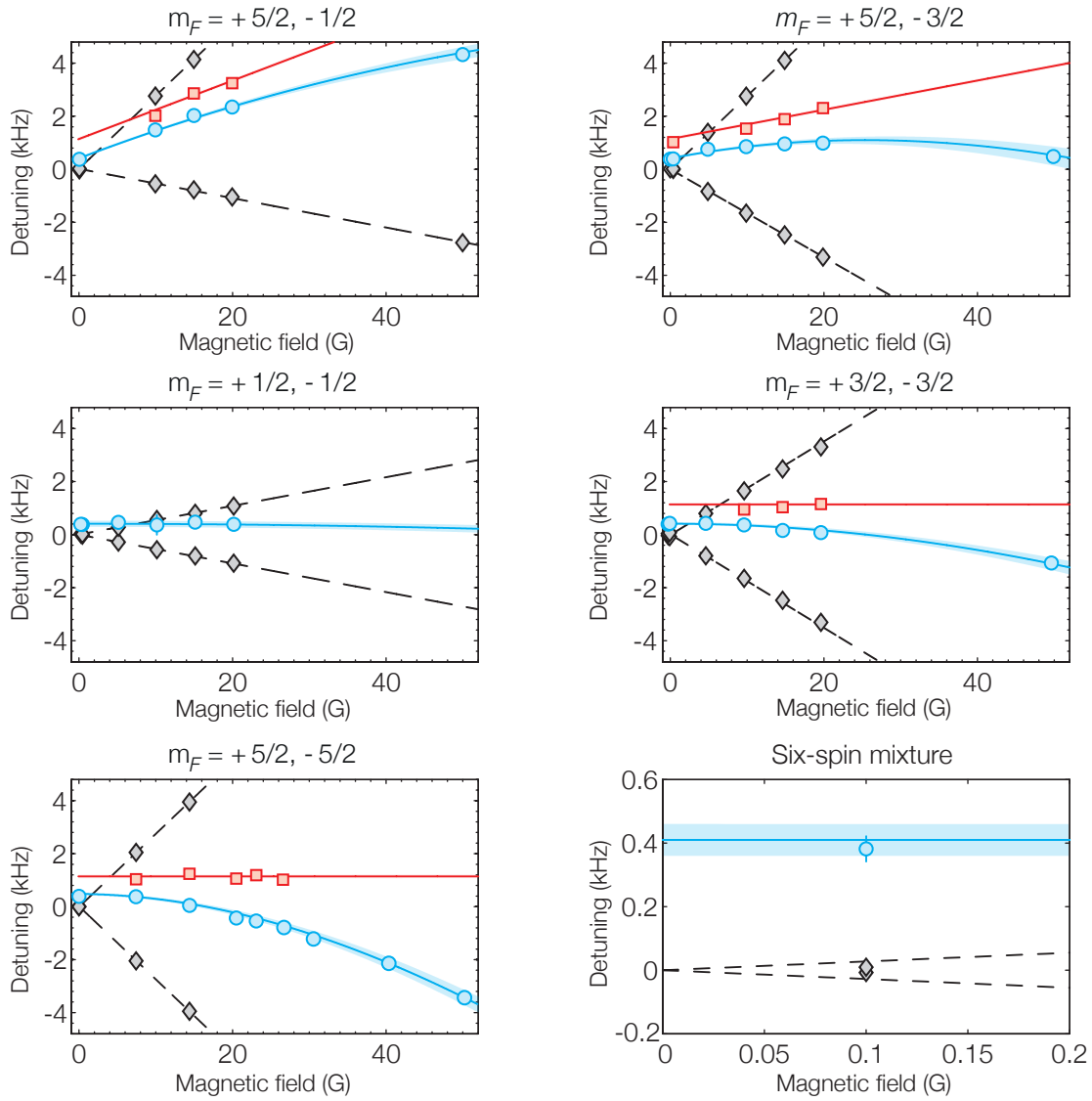

Figure 6.4 – Resonance position shifts at varying B-field strength in different spin mixtures. Diamonds denote singly occupied site resonances, circles denote the $|eg^d\rangle$ state resonances, and squares mark $|ee\rangle$ state resonances. A lattice depth $\tilde{V} = 43.0(5)\, E_r$ is adopted. The blue solid lines reproduce Eq. (6.8) with values of V and V_{ex} obtained from fitting only the $m_{F,F'} = \pm 5/2$ mixture spectroscopy data (see text). The red solid lines reproduce Eq. (6.9) evaluated with our estimation of a_{ee} reported in the text. Shaded regions correspond to 95% confidence intervals of the fits. Data point error bars represent the confidence intervals of the resonance position fits. The figure is taken from [124].

states formed by non-opposite nuclear spin states m_F, m_F':

$$E_d(B, m_F, m_F') = \frac{1}{2}(m_F + m_F')\,\delta g\,\mu_B B + \left(V - U_{gg}\right) - \sqrt{V_{\mathrm{ex}}^2 + \left(\frac{1}{2}\left(m_F - m_F'\right)\delta g\,\mu_B B\right)^2} \tag{6.8}$$

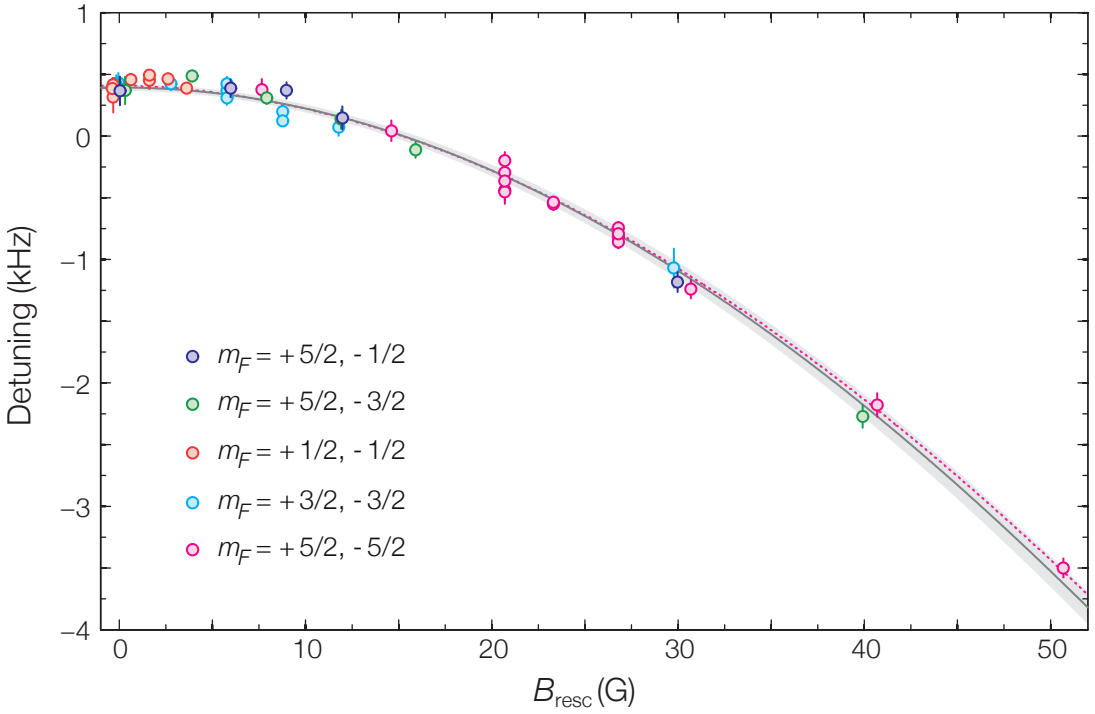

Figure 6.5 – Interaction spectroscopy for various spin mixtures with rescaled magnetic field strength $B_{\mathrm{resc}} = \frac{1}{5}(m_F - m'_F)\,B$. The linear Zeeman term in Eq. (6.8) is also subtracted. A lattice depth of $\tilde{V} = 42(1)\,E_r$ is adopted. The solid line is obtained through a common fit of all shown data points with Eq. (6.8). The shaded area corresponds to the fit 95% confidence interval and data points error bars denote the confidence interval of the resonance position fits. The dotted line is a fit to only the $m_{F,F'} = \pm 5/2$ mixture data points. The figure is adapted from [124].

In addition, the $|ee\rangle$ resonance retains in general a magnetic-field dependence:

$$E_{ee}(B, m_F, m'_F) = \frac{1}{2}(m_F + m'_F)\,\delta g\,\mu_B B + \frac{1}{2}(U_{ee} - U_{gg}) \tag{6.9}$$

Independently of the accuracy of the model for estimating the precise values of U_{eg}^{+} and V_{ex}, which are known to be respectively close to $\hbar\omega_{\mathrm{lat}}$ and $\frac{1}{2}(\hbar\omega_{\mathrm{lat}} - U_{eg}^{-})$, we can directly check if the values of U_{eg}^{-}, U_{eg}^{+} and U_{ee} for different spin mixtures are consistent with one another. As the B-field linear term in Eqs. (6.8)-(6.9) can be subtracted using our precise knowledge of the differential Zeeman shift (see Section 5.1.3), data for each mixture can be separately fitted with U_{eg}^{-}, U_{eg}^{+} and U_{ee} as the only free parameters. In the case of U_{eg}^{-} and U_{ee}, all fits yield consistent estimates with comparable precision, and the deduced reported values of a_{eg}^{-} and a_{ee} result from the mean of all fitted values (including a six-spin measurement at zero-field for U_{eg}^{-}). On the other hand, owing to the decreasing magnetic sensitivity associated with lower m_F states, the fit with the smallest uncertainty on the value of U_{eg}^{+} (and therefore of V_{ex}) is the fit to the $m_{F,F'} = \pm 5/2$ mixture data, with an uncertainty below 5% for $\tilde{V} = 43\,E_r$ (see Table 6.1). Nonetheless, the estimates of U_{eg}^{+} are highly consistent, with a spread below 10% between the fitted values (excluding the mixtures containing the most magnetically insensitive $m_F = \pm 1/2$ states). As larger magnetic

field amplitudes have recently become attainable in our upgraded setup, the precision of the U_{eg}^{+} fits could likely be increased by an order of magnitude. Different mixture data can also be compared more directly by rescaling the magnetic field strength in each dataset as $B_{\mathrm{resc}} = \frac{1}{5}(m_F - m_F')B$ and subtracting the linear Zeeman term in Eqs. (6.8)-(6.9). Such rescaled data sets are shown in Fig. 6.5 together with a common fit, with V and V_{ex} as free parameters. The obtained values are consistent with the $m_{F,F'} = \pm 5/2$ result within the respective uncertainties.

In conclusion, we are able to directly demonstrate the SU(N) symmetry of a_{eg}^{-} and a_{ee}, respectively with 1% and 3% uncertainty. The SU(N) symmetry of a_{eg}^{+} is probed only at a 10% level, due to the low available B-field strength which substantially limits the precision of our interaction shift estimation. A direct excitation of the $|eg^{u}\rangle$ state transition in a strong field would also provide a robust alternative for refining the evidence of SU(N) symmetry of a_{eg}^{+}. On the other hand, the SU(N) symmetry of a_{eg}^{-} and a_{ee} is strongly supporting the overall symmetric nature of two-orbital interaction channels. In addition, we will see in Section 6.2 how the absence of spin-changing collisions in a two-orbital bulk ensemble was observed, over a much larger time scale than the one associated with elastic scattering processes.

6.1.3 Estimation of the inter-orbital singlet scattering length

In order to correctly express the large U_{eg}^{+} interaction strength in terms of the a_{eg}^{+} scattering length, it is necessary to take higher lattice bands into consideration. As both the real value of interaction strength and of the scattering length are unknown, we must include higher bands in the initial two-particle Hamiltonian describing the the on-site interactions, which is then numerically diagonalised. The total Hamiltonian can be written as[5]:

$$\hat{H} = \hat{H}_{\mathrm{at}}^{(2)} \otimes 1_{\mathrm{lat}} + 1_{\mathrm{at}} \otimes \hat{H}_{\mathrm{lat}}^{(2)} + \hat{\mathcal{U}} \tag{6.10}$$

where the first Hilbert subspace refers to the internal degrees of freedom of the atoms, whereas the second Hilbert subspace refers to their motional degree of freedom in the lattice potential. Without a magnetic field, the interaction term $\mathcal{U}$ would only couple different motional states in the lattice but different internal states would be uncoupled, i.e. $\mathcal{U}$ would be block-diagonal in the singlet-triplet basis. Including only states with one $|g\rangle$ and one $|e\rangle$ atom, and in the presence of a magnetic field we have $\hat{H}_{\mathrm{at}}^{(2)} = \hat{H}_{B}^{(2)}$ (see Eq. (5.6)). In addition, using the on-site Wannier state basis we define:

$$\begin{aligned} \hat{H}_{\mathrm{lat}}^{(2)} &= \hat{H}_{\mathrm{lat}}^{(1)} \otimes 1 + 1 \otimes \hat{H}_{\mathrm{lat}}^{(1)} \\ \hat{H}_{\mathrm{lat}}^{(1)} &= \sum_{n_x,n_y,n_z} (\mathcal{E}_{n_x} + \mathcal{E}_{n_y} + \mathcal{E}_{n_z}) \mathcal{P}(n_x, n_y, n_z) \end{aligned} \tag{6.11}$$

where $\mathcal{E}_{n_\mu}$ are the band mean energies, with n_μ being the band indices in the three directions, and $\mathcal{P}(n_x, n_y, n_z)$ is the projector on the three-dimensional Wannier state w_{n_x,n_y,n_z}.

[5] We omit the atom-light Hamiltonian as we are only interested in the two-particle eigenenergies. The dominant spin-triplet Rabi coupling is anyway substantially unaltered by strong interactions in the spin-singlet channel.

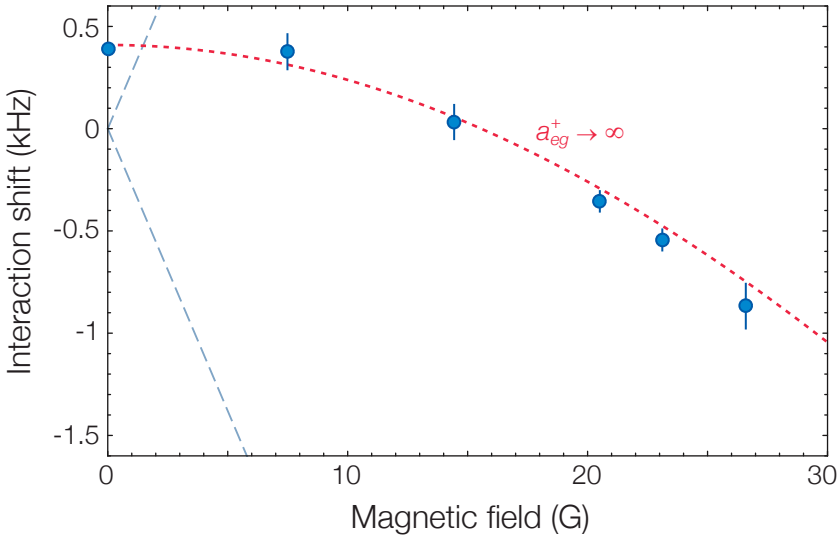

Figure 6.6 – Result of a numerical diagonalisation of the Hamiltonian in Eq. (6.10) with $a^-_{eg} = 219.5\,a_0$ and $a^+_{eg} = 1 \times 10^6$ (corresponding to a spatial wave function overlap $\simeq 0.79$ between the singlet and triplet interacting states). The computed eigenenergy (dashed line) dependence on the B-field strength does not strongly deviate from the data ($m_{F,F'} = \pm 5/2$ mixture, $\tilde{V} = 43\,E_r$).

For a Fermi contact pseudo-potential, all matrix elements of $\hat{u}$ can be computed through the Wannier function overlaps

$$\tilde{U}^{pq\,\pm}_{nm} = \frac{4\pi\hbar^2}{M} a^{\pm}_{eg} \int d^3r\, w^*_n(\mathbf{r})\, w^*_m(\mathbf{r})\, w_p(\mathbf{r})\, w_q(\mathbf{r}) \tag{6.12}$$

For our numerical computation, only higher bands in the shallowest lattice direction were included. In this case the indices n, m, p and q, which are in principle three-component vectors, can be interpreted as the band indices along the shallowest lattice axis. In order to ensure the complete state anti-symmetrisation, the motional and interaction terms in the Hamiltonian need to be transformed to the symmetrised/anti-symmetrised Wannier state basis, which is achieved through a matrix transformation. Additionally, in order to remove the influence of the bosonic states on the numerically computed lowest eigenenergy, an artificial large energy offset is added to all completely symmetric states. In order to perform the diagonalisation, we fix the value of a^-_{eg} to the value reported above and we adjust a^+_{eg} to best reproduce the data in the $m_{F,F'} = \pm 5/2$ mixture. Unfortunately, the resulting eigenenergy is quite insensitive to the exact value of the scattering length, especially at our relatively low B-field amplitudes. Including four excited bands in the numerical diagonalisation, we find $a^+_{eg} \approx 4000\,a_0$ to give the B-field dependence closest to the data. However, even assuming an exceedingly large scattering length, the computed magnetic-field dependence of the lower eigenenergy remains fairly close to the data (see Fig. 6.6). Moreover, a non-regularised contact pseudo-potential was assumed to compute the interaction matrix elements, which is expected to significantly underestimate the eigenenergies for large interactions in three dimensions [324].

Our simple numerical method is therefore not sufficiently accurate to give a reliable

estimate in such a regime of large interactions. However, recently another experimental research group could directly measure V_{ex} in ^{173}Yb, without resorting to any model-dependent estimation, and report an estimated scattering length $a_{eg}^{+} = 3300(300)\,a_0$ [176]. This estimate is based on a perturbative approach to include anharmonic corrections in the so-called Busch model of two interacting atoms in a harmonic trap [133, 176, 327, 328]. A remarkably large singlet-triplet scattering length difference $\Delta a_{eg} = a_{eg}^{+} - a_{eg}^{-}$ is therefore uncovered (confirmed by two completely independent experimental studies), making ^{173}Yb in optical lattices an exemplary system for the simulation of exchange-based many-body models. In addition, such a large value of the a_{eg}^{+} scattering length suggests that the associated scattering potential possesses a molecular bound state in proximity of the dissociation energy threshold [20]. For this reason, a photoassociation resonance at close red-detuning from the frequency of the single-atom clock resonance is expected. Such a transition could represent a valuable tool to selectively associate atoms on doubly occupied sites in a lattice, improving existing schemes based on photoassociation on the $^1\mathrm{S}_0 \rightarrow {}^3\mathrm{P}_1$ transition [72]. Moreover, it would have interesting applications with regard to optical Feshbach resonances with low associated heating rates[6] [140]. It was unfortunately not yet possible to locate the molecular photoassociation resonance in our experiment. Additional efforts are ongoing, taking advantage of the increased Rabi coupling of the $|eg^{u}\rangle$ state to non-opposite spin state singlets $m_{F'} \neq -m_F$ (see Section 6.1.1).

6.2 Direct observation of spin-exchange interactions

The interaction energy difference between the singlet and the triplet states, $|eg^{+}\rangle$ and $|eg^{-}\rangle$, drives spin-exchange processes when an atomic pair is found in a superposition between the two states (see also Section 1.2.3). For an isolated pair at zero magnetic field, the state oscillates between the two polarised states $|eg\uparrow\downarrow\rangle$ and $|eg\downarrow\uparrow\rangle$ at a frequency $\omega_{\mathrm{ex}} = |V_{\mathrm{ex}}|/\hbar$, similarly to what was already observed using different Bloch bands [116]. For non-zero magnetic fields, the oscillation frequency increases due to the larger energy separation between the eigenstates $|eg^{d}\rangle$ and $|eg^{u}\rangle$. On the other hand, the spin-exchange amplitude is gradually suppressed by tuning the magnetic field to the regime where $V_{\mathrm{ex}} \ll \Delta_B$ [176]. In order to directly observe the spin-exchanging dynamics at a single atomic pair level, one needs to generate a superposition of $|eg^{+}\rangle$ and $|eg^{-}\rangle$ at a low magnetic field, which can be achieved either by a Rabi coupling comparable to the states energy difference ($\Omega \sim |V_{\mathrm{ex}}|$), or by preparing the $|eg^{d}\rangle$ eigenstate in a high B-field and subsequently quenching the field to zero. Unfortunately, neither of the two possibilities can be realised with our experimental setup[7], due to the very large measured V_{ex}. The coherent spin-exchange oscillation of single atomic pairs could recently be observed

[6] We note that the optical coupling of a colliding pair to a weakly bound molecule formed by $J = 0$ states breaks the nuclear spin decoupling only as a consequence of the photoassociation transition Clebsch-Gordan coefficients. An OFR working on this photoassociation transition could be made approximately SU(N) symmetry-conserving by engineering the intensity distribution of the coupling light among different polarisations and the magnetic field.

[7] A magnetic field-switching time scale well below 100 μs ($\sim h/V_{\mathrm{ex}}$) is technically infeasible, due to eddy currents developing in the vacuum copper gaskets of our main chamber viewports.

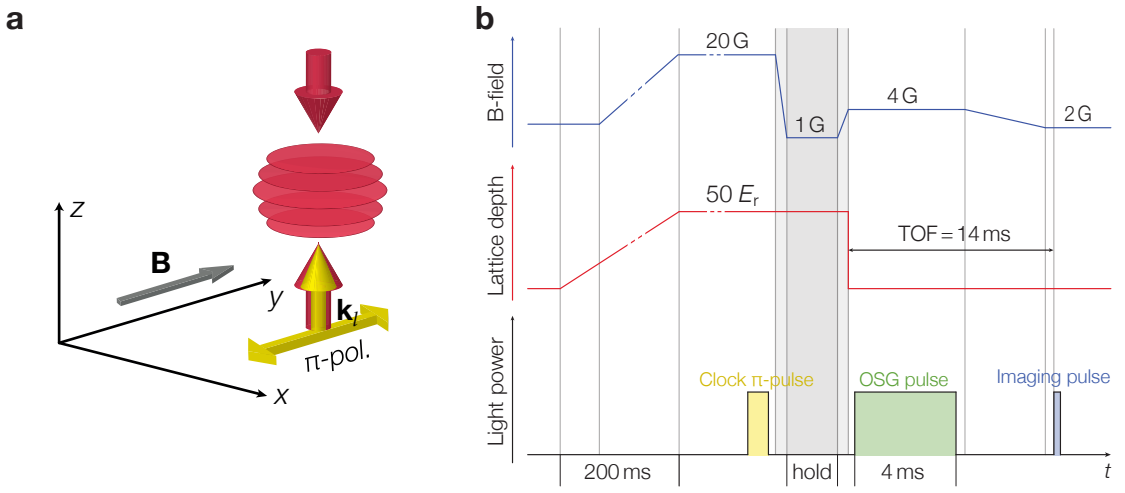

Figure 6.7 – (a) Experimental configuration for the observation of spin-exchange dynamics in two-dimensional gases. A two-component Fermi gas ($m_{F,F'} = \pm 5/2$) is loaded into a 1D vertical optical lattice; π-polarised clock excitation light is vertically directed as well. (b) Experimental sequence: after loading into the 50 E_r deep lattice, an approximately equal mixture of $|g\uparrow\rangle$ and $|e\downarrow\rangle$ atoms is created by means of a clock π-pulse. The spin-imbalanced ensemble is let free to evolve in a 1 G magnetic field and the spin populations are detected after a variable hold time by means of OSG imaging. The figure is adapted from [124].

with ^{173}Yb atoms by another experimental group, thanks to a very short attainable field-switching time [176], confirming our estimation of V_{ex} and increasing the precision on the determination of the a_{eg}^{+} scattering length (see above).

6.2.1 Spin-exchange dynamics in imbalanced bulk ensembles

Experimental sequence and spin imbalance preparation

In order to observe the spin dynamics induced by the exchange interactions, we employ a different experimental configuration than the one used for interaction spectroscopy (see Fig. 6.7(a)). A two-spin Fermi gas ($m_{F,F'} = \pm 5/2$) is loaded into a vertical one-dimensional deep lattice potential at the magic wavelength. The initial gas is therefore distributed into several quasi two-dimensional ensembles localised within separate sites of the vertical lattice. In this way, the pair density and thus the effective ensemble exchange coupling can be considerably reduced compared to a three-dimensional lattice configuration. A strongly spin-imbalanced state is prepared by exciting all spin-down atoms, so that an almost completely polarised mixture of the $|g\uparrow\rangle$ and $|e\downarrow\rangle$ states is created, with a small residual number of $|g\downarrow\rangle$ atoms. In order to perform the excitation, a π-pulse solely resonant with the $|g\downarrow\rangle \rightarrow |e\downarrow\rangle$ transition is applied in a 20 G magnetic field. Such a resonance is blue-shifted owing to interactions in the bulk ensemble by approximately 0.5 kHz for $N_0 \simeq 10^5$ atoms, compared to the same resonance in a spin-polarised two-dimensional ensemble. In order to achieve a high π-pulse efficiency, a large $\Omega = 2\pi \cdot 3.56$ kHz is used, corresponding to a π-pulse duration $\pi/\Omega = 140\,\mu$s. In order to initiate the spin-exchange

dynamics, the magnetic field is ramped to a value of 1 G in 200 μs, for which the Zeeman energy becomes smaller than the exchange coupling. Atoms are then held in the lattice for a variable time and the spin population evolution is monitored; the spin state populations are detected by releasing the atoms from the lattice and performing optical Stern-Gerlach separation along with absorption imaging. The experimental sequence is illustrated in Fig. 6.7(b).

Evolution of the spin imbalance

As soon as the B-field strength is lowered, a fast equilibration of the $|g\rangle$ state spin populations is observed, as expected due to the large exchange coupling. We do not detect any emerging population of initially unoccupied spin states during the spin redistribution, confirming the SU(N)-symmetric character of the spin-exchanging process by the absence of spin-changing collisions. The $|g\rangle$ state spin distribution approaches, for long holding times, a stationary ratio, in agreement with the spin distribution that is detected beforehand the clock excitation pulse. The time scale over which the spin distribution reaches the equilibrium value is found to clearly depend on the initial density of the atomic samples. In Fig. 6.8, the evolution of the relative $|g\rangle$ state spin populations is displayed for three different initial densities, varied by tuning the atom number N_0 of the Fermi gas loaded into the lattice.

Collective coherent dynamics is expected to be completely inhibited in such a bulk system, owing to the presence of strong $|e\rangle$ state pair losses that completely suppress the build-up of coherence between the $|eg\uparrow\downarrow\rangle$ and $|eg\downarrow\uparrow\rangle$ states. However, even in the absence of losses, collective coherent spin dynamics in a Fermi sea is observed only under particular initial conditions [313, 314]: in order to initiate the spin dynamics, small but non-zero single-particle coherences between the internal states coupled by the exchange process are required, as observed in spinor Bose gases [147, 329]. Moreover, in a Fermi system, the time scale of the atomic motion in the trap needs to be short compared to the spin-dynamics time scale. Under these conditions, the spatial dependence of the interactions due to the trapped state wave functions gives rise to an effective long-range spin coupling, inducing a single-mode-like spin dynamics which disregards the spatial structure of single-particle states [330]. On one hand, it is difficult to engineer state coherences between the $|g\uparrow\rangle$ and $|g\downarrow\rangle$ states in a bulk ensemble, which could only be realised by creating spin coherences before the excitation[8]. On the other hand, due to the large exchange coupling, the fast spin-exchanging dynamics takes place on a time scale much smaller than the in-trap motion, with an observed spin-exchange rate $\Omega_{\mathrm{ex}} \gtrsim 2\pi \cdot 500\,\mathrm{Hz}$ much larger than the in-plane trap frequencies $\omega_{x,y} \simeq 2\pi \cdot 37\,\mathrm{Hz}$ (see below for the determination of the spin-exchange rate). In such conditions, collective coherent dynamics in the Fermi sea is therefore excluded already without considering atom pair losses, and we may use a simple approximate model to describe the uncorrelated spin-exchanging dynamics, which will be illustrated in the following part of this Section.

[8] Quenching the orientation of the magnetic field generates spin superpositions, however it populates unwanted spin states. Two-photon coherent spin transfer represents the only viable alternative to create controlled spin superposition states.

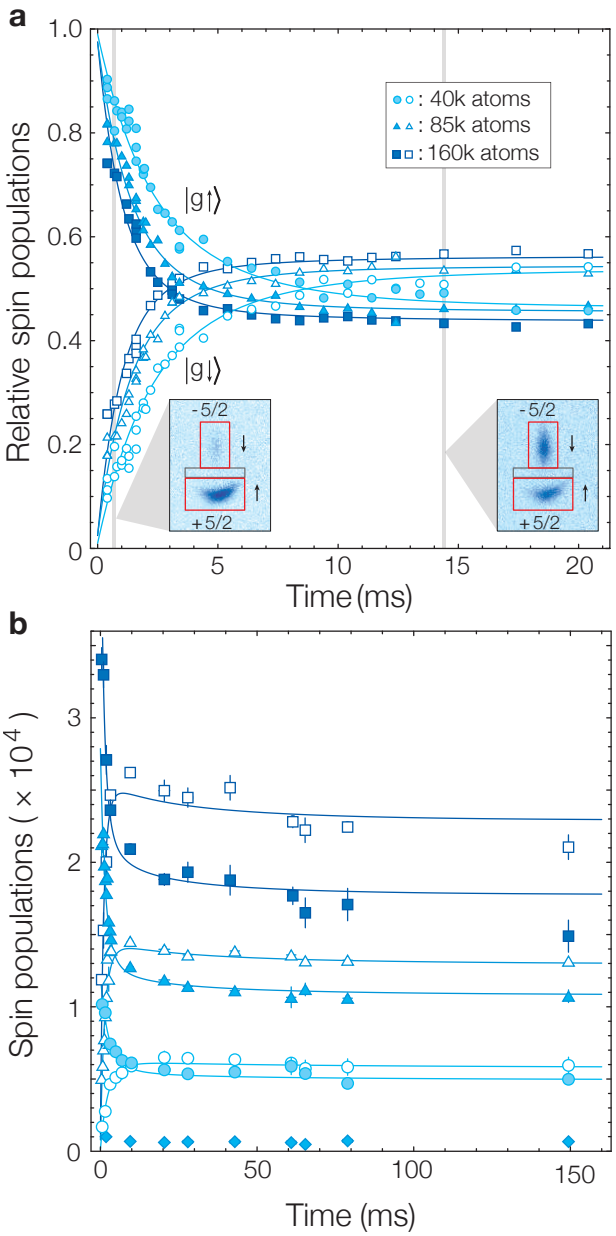

Figure 6.8 – Inter-orbital spin-exchange dynamics in two-dimensional ensembles. (a) Evolution of the relative populations of the $|g\uparrow\rangle$ and $|g\downarrow\rangle$ states in a 1 G magnetic field. The fitted curves are obtained using the two-body rate equation model in Eqs. (6.13), which includes *e*-*g* and *e*-*e* state inelastic losses. The OSG absorption images displayed below the curves correspond respectively to a hold time of 0.4 ms and 14 ms with $N = 0.85 \times 10^5$ atoms. The integration regions associated with different spin states are also shown: the red rectangles delimit atoms in the $m_{F,F'} = \pm 5/2$ states, whereas the grey rectangle delimits atoms occupying other intermediate spin states. (b) Long-time evolution of the ground state spin populations. A slow atom loss process is visible, caused by inelastic collisions between $|g\rangle$ and $|e\rangle$ atoms. The population of intermediate spin states is also plotted for $N = 0.85 \times 10^5$ atoms, marked by filled diamonds; the initially unoccupied spin state populations remain below our detection limit $N \sim 10^3$ during the entire hold time, verifying the absence of spin-changing collisions. Error bars mark the standard deviation of the mean of 2-3 measured points. The figure is adapted from [124].

6.2.2 Rate equation dynamics description

The spin distribution evolution is fitted using a two-body collisional rate equation model. Three different collision channels are described by just as many two-body collision rate coefficients: the elastic spin-exchange rate coefficient γ_{ex}, the inelastic e-g collision rate coefficient β_{eg} and the inelastic e-e collision rate coefficient β_{ee}. Inelastic collisions involving the $|e\rangle$ state lead with very high probability to pair losses from the trap, and atom number losses can therefore be directly described in terms of the inelastic collision rate coefficients (see Section 1.2.1).

The spin-exchange process depletes the initially balanced states $|g\uparrow\rangle$ and $|e\downarrow\rangle$, and transfers atoms to the initially unpopulated $|g\downarrow\rangle$ and $|e\uparrow\rangle$ states until equilibrium is reached. The strong e-e pair-lossy collisions are initially suppressed by Pauli blocking, as only the $|e\downarrow\rangle$ state is prepared through the applied clock π-pulse. However, the $|e\uparrow\rangle$ state becomes populated as soon as the spin-exchange process flips atoms from the $|e\downarrow\rangle$ state via collisions with the $|g\uparrow\rangle$ state, and inelastic collisions can then occur. As a consequence of strong e-e inelastic collisions, the $|e\uparrow\rangle$ state remains scarcely occupied throughout the entire evolution. The build-up of coherence between inter-orbital pair states is strongly suppressed by this loss mechanism, justifying further the use of a classical rate equation description of the spin-exchanging binary collisions, which can be expressed in analogy to the description of inelastic binary collisions in terms of rate coefficients [135, 136] (see also Section 1.2.1). Only the evolution of the state mean densities is considered by such a description, and quantum many-body effects in the Fermi seas are entirely disregarded [9]. The spin-exchange is moreover off-resonant, due to a differential Zeeman shift between the $|eg\uparrow\downarrow\rangle$ and $|eg\downarrow\uparrow\rangle$ states of $2\Delta_B \simeq +h\cdot 500\,\mathrm{Hz}$ in the 1 G B-field. This causes a slight reduction of the exchange rate in conjunction with the initial $|g\uparrow\rangle$-$|e\downarrow\rangle$ mixture, as the exchange process is energetically costly, and larger fields can indeed be used to completely inhibit the dynamics[10]. Conversely, by preparing an initial $|g\downarrow\rangle$ -$|e\uparrow\rangle$ mixture, an enhancement of the exchange rate with increasing magnetic field is observed.

Four coupled two-body rate equations are used to describe the evolution of the density in the states $|g\uparrow\rangle$, $|e\downarrow\rangle$, and in the initially unoccupied $|g\downarrow\rangle$ and $|e\uparrow\rangle$ states. Denoting the relative state populations as $P_{\alpha m}(t) = n_{\alpha m}(t)/n_0$, where n_0 is the density of the initial Fermi gas, their evolution is described by:

$$
\begin{aligned}
\dot{P}_{g\uparrow}(t) &= n_0\gamma_{\mathrm{ex}}\big(P_{e\uparrow}(t)P_{g\downarrow}(t) - P_{e\downarrow}(t)P_{g\uparrow}(t)\big) - n_0\beta_{eg}P_{g\uparrow}(t)\big(P_{e\uparrow}(t)+P_{e\downarrow}(t)\big)\\
\dot{P}_{g\downarrow}(t) &= n_0\gamma_{\mathrm{ex}}\big(P_{e\downarrow}(t)P_{g\uparrow}(t) - P_{e\uparrow}(t)P_{g\downarrow}(t)\big) - n_0\beta_{eg}P_{g\downarrow}(t)\big(P_{e\uparrow}(t)+P_{e\downarrow}(t)\big)\\
\dot{P}_{e\uparrow}(t) &= n_0\gamma_{\mathrm{ex}}\big(P_{e\downarrow}(t)P_{g\uparrow}(t) - P_{e\uparrow}(t)P_{g\downarrow}(t)\big) - n_0\beta_{eg}P_{e\uparrow}(t)\big(P_{g\uparrow}(t)+P_{g\downarrow}(t)\big) - n_0\beta_{ee}P_{e\uparrow}(t)P_{e\downarrow}(t)\\
\dot{P}_{e\downarrow}(t) &= n_0\gamma_{\mathrm{ex}}\big(P_{e\uparrow}(t)P_{g\downarrow}(t) - P_{e\downarrow}(t)P_{g\uparrow}(t)\big) - n_0\beta_{eg}P_{e\downarrow}(t)\big(P_{g\uparrow}(t)+P_{g\downarrow}(t)\big) - n_0\beta_{ee}P_{e\uparrow}(t)P_{e\downarrow}(t)
\end{aligned}
\tag{6.13}
$$

[9] We neglect for instance the hole-heating effect in the $|g\uparrow\rangle$ and $|e\downarrow\rangle$ Fermi seas due to atom losses, which causes a decrease of the sample density beyond the simple linear decrease due to the atom number loss.

[10] Measurements with $B = 0.3\,G$ have also been performed, but an imperfect compensation of the earth magnetic field results in OSG detection artefacts due to field switching; such low fields are therefore avoided. The observed short-time spin evolution is anyhow barely distinguishable from the one observed with $B = 1\,G$.

The three rate coefficients are independent of the considered spin states, due to the collisional SU(N) symmetry. In order to estimate the initial mean density n_0, a finite-temperature model for the adiabatic transfer from the dipole trap to the one-dimensional lattice is used (see Appendix B), where n_0 is taken as a number-weighted mean of the computed in-plane densities in each vertical lattice site. We fit this model to the measured spin populations with γ_{ex}, β_{eg} and $P_{g\downarrow}(0)$ as free parameters. The sum $P_{e\downarrow}(0)+P_{g\downarrow}(0)$ is fixed to the fraction of $|g\downarrow\rangle$ atoms detected before the application of the excitation pulse, and is monitored to be constant during the experimental run. $P_{g\downarrow}(0)$ takes into account the non-unity efficiency of the clock π-pulse, with $\sim 5-10\%$ of the $|\downarrow\rangle$ atoms left in the $|g\downarrow\rangle$ state. Similarly, $P_{g\uparrow}(0)$ is constrained to the relative population of $|g\uparrow\rangle$ atoms in the gas before the application of the excitation pulse. A two-dimensional fitting procedure is adopted: the measured relative spin state population is fitted with $P_{g\uparrow}(t)/(P_{g\uparrow}(t)+P_{g\downarrow}(t))$, and the total detected $|g\rangle$ state atom number is fitted with $N_{0g}\left(P_{g\uparrow}(t)+P_{g\downarrow}(t)\right)$, where N_{0g} is the number of $|g\rangle$ state state atoms detected before the dynamics is initiated.

The fits to a set of three different initial gas densities yield a spin-exchange rate coefficient $\gamma_{\mathrm{ex}} = 1.2(2)\times 10^{-11}\,\mathrm{cm}^3/\mathrm{s}$, showing good agreement between the three independent fits. The e-g inelastic rate is estimated as $\beta_{eg} = 3.9(16)\times 10^{-13}\,\mathrm{cm}^3/\mathrm{s}$, including both results from fitting the spin-exchange evolution measurements displayed in this Section with Eqs. (6.13) and from separate e-g inelastic loss measurements (see next Section). This value of the rate coefficient includes symmetric ($|eg^+\rangle$ pair) and antisymmetric ($|eg^-\rangle$ pair) inelastic collisions, which both contribute to atom losses in the quasi-2D bulk ensembles. The strong e-e losses lead to a large inelastic rate coefficient $\beta_{ee} = 2.2(6)\times 10^{-11}\,\mathrm{cm}^3/\mathrm{s}$, which is determined by separate measurements devoted to the independent characterisation of this inelastic channel (see next Section), and is taken as a fixed parameter in Eqs. (6.13). The uncertainties on the rate coefficients reported here are obtained by combining the uncertainties on the determination of the in-plane density n_0 and the errors on the fit results themselves. The evolution of the spin populations resulting from Eqs. (6.13) is displayed in Fig. 6.8 for three different total atom numbers N_0, where the same rate coefficient values are used for all curves. The associated in-plane mean densities vary between[11] $4\cdot 10^{13}$ and $8\cdot 10^{13}\,\mathrm{atoms/cm}^3$. The fitted evolution shows very good agreement with the measured data and exhibits the expected dependence for two-body processes on the in-plane density, both for the exchange-dominated short-time dynamics and for the long-time dynamics, where the e-g losses become important as well.

An accurate modelling of the in-trap dynamics, including many-body correlations of the motional and internal degrees of freedom, would be required to quantitatively relate the measured exchange rate to the microscopic interaction processes and ultimately to the scattering length difference $\Delta a_{eg} = a_{eg}^+ - a_{eg}^-$. Such a modelling is quite complicated, and two-orbital interacting quasi-2D ensembles have to date only been treated at a mean-field level by means of the truncated Wigner approximation (see Ref. [214] and attached supplementary materials). Such a treatment is valid however only in the case of mode-conserving interactions, i.e. with an associated energy much smaller than the trap-level

[11] As a reference, these correspond in turn to mean in-plane Fermi energies between $E_F = h\cdot 2.1\,\mathrm{kHz}$ and $E_F = h\cdot 3.7\,\mathrm{kHz}$.

spacing[12] $\Omega_{\rm ex} \sim n_0\gamma_{\rm ex} \ll \omega_{x,y}$. Nevertheless, from the evolution shown in Fig. 6.8(b), it is evident how the spin-exchange is found to be the strongest process in the two-orbital system, provided that pair $|e\rangle$ losses are avoided, e.g. by isolating the $|e\rangle$ atoms from one another in a state-dependent three-dimensional lattice. A quantitative comparison between the various elastic and inelastic collision rates, with regard to the stability of the two-orbital system for quantum simulation of orbital magnetism, will follow in the next Section.

6.3 Two-orbital inelastic collisions

A careful evaluation of the inelastic collision channel strengths is very important for supporting the feasibility and understanding the restrictions on quantum simulation with the two electronic states of ^{173}Yb. We already emphasised how strong $|e\rangle$ state pair losses are detrimental for the stability of bulk atomic ensembles where $|e\rangle$ atoms are free to inelastically collide with each other. On the other hand, a rather weak $|g\rangle$ state loss process was observed, caused by inelastic collisions between $|g\rangle$ and $|e\rangle$ atoms. Throughout $|g\rangle$-$|e\rangle$ and $|e\rangle$-$|e\rangle$ state atomic collisions, several orbital molecular states connect to the single-particle states of the approaching atoms. The couplings between the various molecular orbitals lead to inelastic collisions which can change the internal state of the colliding atoms. Atoms in the $|e\rangle$ state may therefore decay to the $|g\rangle$ state, in which case the atomic pair gains a large kinetic energy equal to the optical excitation energy causing both atoms to leave the trap [283]. Inelastic collisions involving ytterbium metastable $|e\rangle$ atoms have so far only been studied at very low densities in two-dimensional ensembles of ^{171}Yb [280], and rather large two-body loss rate coefficients have been reported: $\beta_{ee} = 5(3)\times10^{-11}\,\mathrm{cm}^3/\mathrm{s}$ and $\beta_{eg} = 3(2)\times10^{-11}\,\mathrm{cm}^3/\mathrm{s}$. However, no measurements have been published for ^{173}Yb. We will present in the following our characterisation of metastable state inelastic losses both in two-dimensional ensembles and isolated pairs of ^{173}Yb atoms.

6.3.1 Inelastic collisions in two-dimensional ensembles

In order to better isolate the role of inelastic *e*-*e* and *e*-*g* collisions in the atom number evolution shown in Fig. 6.8, we employed different experimental procedures.

Inelastic collisions between excited atoms

Inelastic *e*-*e* losses are measured by creating a balanced $|e\uparrow\rangle$-$|e\downarrow\rangle$mixture and successively monitoring the atom number evolution. The $|e\rangle$ atom ensemble is prepared by applying a resonant clock π-pulse in a nearly zero magnetic field to a two-spin Fermi gas loaded into a $50\,E_r$ deep vertical lattice. An equal portion of the two spin states is excited to the $|e\rangle$ state and a blast pulse resonant with the strong $^1\mathrm{S}_0 \rightarrow {}^1\mathrm{P}_1$ transition is used to remove the

[12] This is the applicable regime in optical lattice atomic clocks, as extremely low in-plane densities are employed, yielding correspondingly low interaction strengths on the order of 1 Hz.

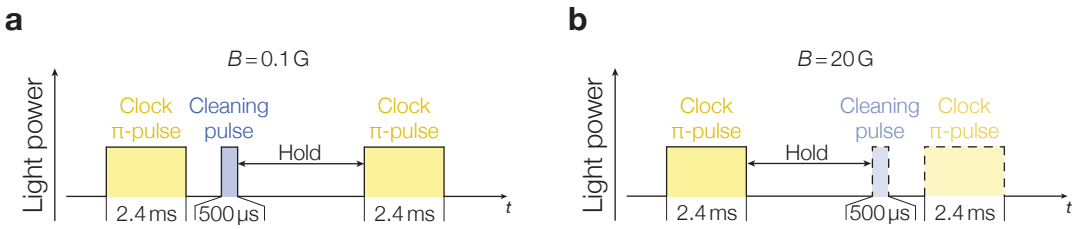

Figure 6.9 – Experimental sequences for the characterisation of $|e\rangle$ state inelastic losses in two-dimensional ensembles. (a) Pulse sequence for the measurement of *e*-*e* atom losses. The residual $|g\rangle$ atoms after a first clock pulse are removed by a blue cleaning pulse. The $|e\rangle$ state population is mapped back to the $|g\rangle$ state using a second clock pulse. (b) Pulse sequence for the measurement of *e*-*g* atom losses. Applying a single clock pulse, the $|g\rangle$ state population is detected as a function of hold time. Alternatively, by applying a cleaning pulse and a second clock pulse the $|e\rangle$ state population can be measured.

residual $|g\rangle$ atoms. The $|e\rangle$ atom ensemble is held inside the optical lattice for a variable time, at the end of which the population is mapped back to the $|g\rangle$ state by the application of a second π-pulse. The experimental sequence is illustrated in Fig. 6.9(a).

A fast decay of the $|e\rangle$ state population on a few milliseconds scale is detected, and a two-body loss rate coefficient $\beta_{ee} = 2.2(6) \times 10^{-11}\,\mathrm{cm}^3/s$ is obtained. The loss rate coefficient is determined by fitting the data with $N_{0e}\left(P_{e\uparrow}(t) + P_{e\downarrow}(t)\right)$, obtained by solving Eqs. (6.13) with the $P_{g\uparrow}$ and $P_{g\downarrow}$ set to zero. N_{0e} is the number of atoms present at hold time $t = 0$ after the double pulse sequence, which takes into account the efficiency of the double π-pulse and is fitted as a free parameter, as a minimum experimental hold time $t > 0.5\,ms$ is necessary for the cleaning pulse to be applied. The initial density n_0 was computed through the number of $|e\rangle$ atoms after a single π-pulse, estimated through the π-pulse efficiency. The result of such a measurement and the corresponding fit are shown in Fig. 6.10(a).

Inter-orbital inelastic collisions

In order to address *e*-*g* atom losses, a nearly balanced mixture of $|g\uparrow\rangle$ and $|e\downarrow\rangle$ atoms is prepared by applying a π-pulse in a 20 G magnetic field. Without lowering the magnetic field, unlike the spin-exchange dynamics measurements presented in the previous Section, the population evolution is dominated by two-body losses caused by inelastic inter-orbital collisions. The spin-exchange is strongly suppressed due to the large associated Zeeman energy cost of $2\Delta_B \simeq h \cdot 10\,\mathrm{kHz}$. The population of both the $|g\rangle$ and $|e\rangle$ states are monitored in separate experimental runs as a function of the hold time after the excitation clock pulse. The $|e\rangle$ state population can be mapped back to the $|g\rangle$ state in the same way as described above (see Fig. 6.9(b)). The same decay on a 100 ms typical time scale is observed in both the $|g\rangle$ and the $|e\rangle$ state populations, indicating the presence of *e*-*g* pair losses. The two-body loss rate coefficient β_{eg} is determined by fitting in combination $N_{0g}\left(P_{e\uparrow}(t) + P_{e\downarrow}(t)\right)$ and $N_{0e}\left(P_{e\uparrow}(t) + P_{e\downarrow}(t)\right)$ to the measured $|e\rangle$ and the $|g\rangle$ state populations respectively, again using the numerical solution of Eqs. (6.13). The fitted value of β_{eg} is found in good agreement with the fit results from the measurements in Fig. 6.8(b)

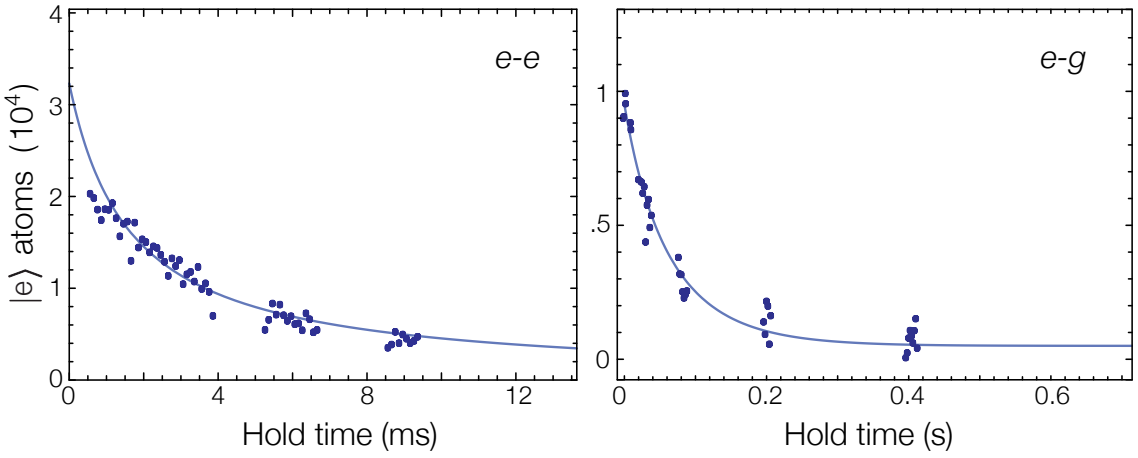

Figure 6.10 – Metastable state inelastic loss measurements in two-dimensional ensembles. The decay of the $|e\rangle$ state population associated with e-e (a) and e-g (b) inelastic collisions. The solid line in (a) is a fit to the data with the $|e\rangle$ state population evolution resulting from Eqs. (6.13) (rescaled by the second clock pulse efficiency). The solid line in (b) represents the total $|e\rangle$ state population evolution resulting from a combined fit of the $|e\rangle$ and the $|g\rangle$ state population evolutions with the relative evolutions from Eqs. (6.13).

and a combined estimate $\beta_{eg} = 3.9(16) \times 10^{-13}\,\mathrm{cm}^3/\mathrm{s}$ is obtained. We note again that e-g pair losses measured in a bulk ensemble involve collision processes in both the symmetric and anti-symmetric inter-orbital channels, and β_{eg} should therefore be interpreted as an effective in-trap loss rate coefficient.

Influence of tight confinement

Spin-exchange and inelastic loss rates which were measured in ensembles trapped in a vertical optical lattice can be influenced by the the tight confinement in the vertical direction [331, 332]. Both the elastic and the inelastic scattering properties of the gas in a tight confined geometry are found to depend exclusively on the dimensionless parameters $\mathcal{E}/(\hbar\omega_0)$ and a/a_{ho} [331], where ω_0 and a_{ho} are the confinement frequency and harmonic oscillator length in the tightly confined direction, and $\mathcal{E} = \hbar^2 k^2/m$ is the kinetic energy of relative motion of the colliding atoms (which is on the order of E_F at ultracold temperatures). For our vertical lattice potential, $\omega_0 \equiv \omega_{z,\mathrm{lat}} = 2\pi \cdot 28.1(3)\,\mathrm{kHz}$ for a depth $V_z = 50\,E_r$ and $a_{\mathrm{ho}} = \sqrt{\hbar/(m\omega_{z,\mathrm{lat}})} \simeq 870\,a_0$. For our temperatures well below the tight confinement frequency $k_B T \lesssim 0.1\hbar\omega_{z,\mathrm{lat}}$, the gas enters a regime usually termed as quasi-two-dimensional (quasi-2D), where amongst the available states along the tightly confined direction only the harmonic oscillator ground state is significantly occupied.

The elastic and inelastic collision rates in the quasi-2D regime significantly deviate from their 3D counterparts when the associated scattering length is large, i.e. $a \gtrsim a_{\mathrm{ho}}$ [331]. We are interested in estimating the effect of the lattice confinement on the measured inelastic rates, and in particular on the ratio between the inelastic rates and the elastic spin-exchange rate. On one hand, the relevant scattering length in the case of β_{ee} is $a_{ee} < a_{\mathrm{ho}}$; we therefore expect nearly no influence of the tight confinement on the mea-

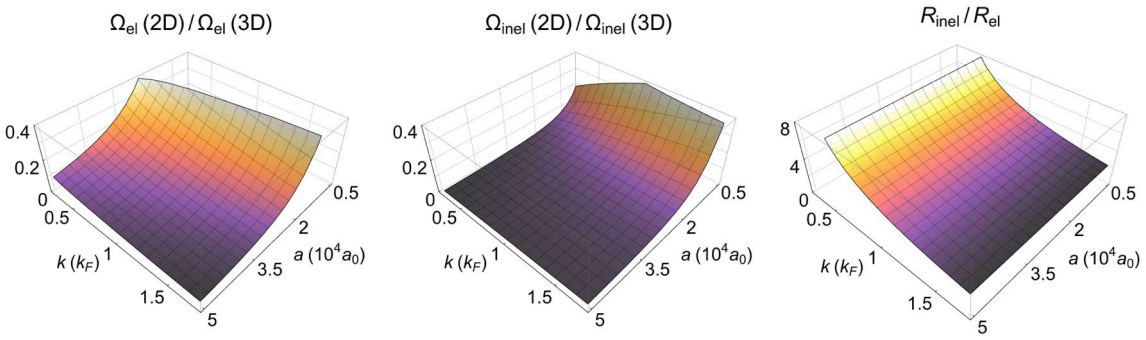

Figure 6.11 – Effects of tight axial confinement on elastic and inelastic atomic collisions: comparison between quasi-2D and 3D collision rates. (a)-(b) The ratio between the quasi-2D and the 3D elastic-inelastic collision rate is plotted as a function of the scattering length a and the average relative momentum k. (c) A comparison among the expected enhancement of inelastic and elastic scattering rates from quasi-2D to 3D.

sured inelastic e-e loss rate. On the other hand, for e-g collisions, we expect a consistent influence of the axial confinement, since $a_{eg}^{+} > a_{\rm ho}$. Let us then determine the expected e-g collision rates in 3D from the ones measured in quasi-2D ensembles, and we assume for the spin-exchange rate coefficient $\gamma_{\rm ex} \sim \gamma_{eg}^{+}$.

The ratio between the e-g elastic collision rate in the tight confined geometry $\Omega_{\rm el}^{2D}$ and its 3D analogue $\Omega_{\rm el}^{3D}$ can be written as [331]

$$\frac{\Omega_{\rm el}^{2D}}{\Omega_{\rm el}^{3D}} = \frac{n_{2D}\,\gamma_{2D}}{n_{3D}\,\gamma_{3D}} \simeq \frac{\langle |f_{00}(k)|^2 \rangle}{8\sqrt{2\pi}\,k\,a}\,\frac{a_{\rm ho}}{a} \tag{6.14}$$

where $\langle \ldots \rangle$ stands for a Fermi-Dirac average, k is the the relative momentum of colliding particles and

$$|f_{00}(k)|^2 = \frac{16\pi^2}{(\sqrt{2\pi}a_{\rm ho}/a - \log(\kappa\,k^2\,a_{\rm ho}^2))^2 + \pi^2} \tag{6.15}$$

is the quasi-2D scattering amplitude [331, 332], with $\kappa \approx 3.5$. Furthermore, n_{2D} (n_{3D}) is the two-dimensional (three-dimensional) gas mean density and γ_{2D} (γ_{3D}) is the elastic collision rate coefficient in two (three) dimensions. A plot of this ratio as a function of k and a is given in Fig. 6.11(a). For a temperature $T = 0.25\,T_F$, $\langle k \rangle \simeq k_F$, and setting $a = a_{eg}^{+} \simeq 3300\,a_0$ yields $\Omega_{\rm el}^{2D}/\Omega_{\rm el}^{3D} \simeq 0.1$.

Moreover, the ratio between the e-g inelastic quasi-2D collision rate $\Omega_{\rm inel}^{2D}$ and the 3D rate $\Omega_{\rm inel}^{3D}$ is given by [331]:

$$\frac{\Omega_{\rm inel}^{2D}}{\Omega_{\rm inel}^{3D}} = \frac{n_{2D}\,\beta_{2D}}{n_{3D}\,\beta_{3D}} \simeq \frac{\langle |f_{00}(k)|^2 \rangle}{(4\pi\,a)^2}\,\sqrt{2\pi}\,a_{\rm ho}^2 \tag{6.16}$$

where β_{2D} (β_{3D}) is the inelastic collision rate coefficient in two (three) dimensions.

This ratio is plotted in Fig. 6.11(b) as a function of k and a, and for $\langle k \rangle \simeq k_F$ and $a = a_{eg}^{+} \simeq 3300\, a_0$ we obtain $\Omega_{\text{inel}}^{2D}/\Omega_{\text{inel}}^{3D} \simeq 0.04$. We can therefore expect a 10-fold and a 25-fold increase of the e-g elastic and inelastic collision rates, respectively, for a 3D ensemble compared to a quasi-2D ensemble at the same density. In Fig. 6.11(c), the ratio between relative enhancement of the inelastic and elastic rate in 3D is plotted, namely:

$$\frac{R_{\text{inel}}}{R_{\text{el}}} = \frac{\Omega_{\text{inel}}^{3D}}{\Omega_{\text{inel}}^{2D}} \frac{\Omega_{\text{el}}^{2D}}{\Omega_{\text{el}}^{3D}} \tag{6.17}$$

We can conclude therefore that, although the e-g rate coefficients for a tightly confined gas need to be corrected in order to obtain their 3D analogues, the elastic to inelastic coefficient ratio is approximately preserved over a wide range of scattering lengths and gas temperatures. The measured ratio $\gamma_{\text{ex}}/\beta_{eg} \sim 30$ is not reduced to less than 10, independently of the effective dimensionality of the system.

6.3.2 On-site atom losses

As the ensemble measurements of e-g inelastic losses are not able to distinguish between the symmetric and the antisymmetric collision channels, we further characterise atom losses of isolated inter-orbital pairs trapped on the sites of a three-dimensional lattice. In this way, the pair can be approximately excited to a pure $|eg^{-}\rangle$ state and the stability of this can be individually verified. An $m_{F,F'} = \pm 5/2$ mixture is loaded into a lattice with $\tilde{V} \simeq 37\, E_r$ and the isolated pairs are selectively excited with a π-pulse resonant to the $|gg\rangle \rightarrow |eg^{\,d}\rangle$ transition in a 7 G magnetic field (see also Fig. 6.3). The ground state atom number is monitored at varying hold time after the excitation, as displayed in Fig. 6.12. A lifetime $\tau_{eg}^{-} \simeq 0.78(2)$ s is determined by an exponential fit to the $|g\rangle$ state population evolution, corresponding to an on-site loss rate $(\tau_{eg}^{-})^{-1} = 1.28(3)$ Hz.

Moreover, this measurement represents an example of the direct detection of the number N_D of doubly occupied sites in the lattice. After the decay process has completely depleted the population of doubly occupied sites, the residual atom number reaches a stationary value N_S. As the e-g decay process only pertains doubly occupied sites, one expects the atoms on singly occupied sites to be left after the decay has stopped. As visible in Fig. 6.12, $N_S \simeq 3.1 \times 10^4$ is found to approximately match $N - 2N_D$, where $N \simeq 4.7 \times 10^4$ is the total atom number prior to the excitation and $N_D \simeq 0.85 \times 10^4$ is the number of atoms excited by the initial clock π-pulse. This clearly indicates that the initial π-pulse and the loss mechanism apply to a similar number of lattice sites, further demonstrating the ability of performing site occupation-selective coherent population transfer in a 3D optical lattice. The on-site pair lifetime can be directly related to the to a two-body loss rate coefficient β_{eg}^{-} by means of the relation [333]:

$$(\tau_{eg}^{-})^{-1} = \beta_{eg}^{-} \int d^3 r\, |w(\mathbf{r})|^4 \tag{6.18}$$

A loss rate coefficient $\beta_{eg}^{-} = 3.0(1) \times 10^{-15}\,\text{cm}^3/\text{s}$ is consequently obtained, which can be

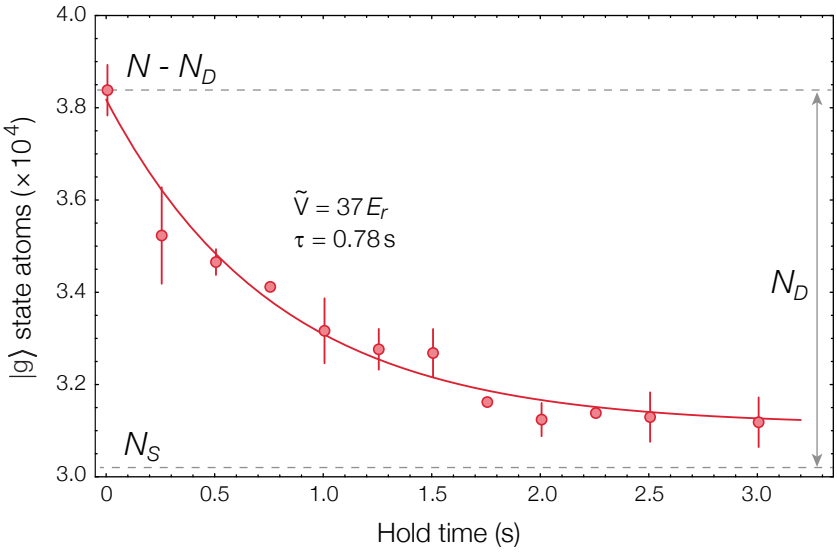

Figure 6.12 – On-site atom losses after the excitation to the $|eg^{\,d}\rangle \simeq |eg^{-}\rangle$ state in a 7 G B-field with a mean lattice depth $\tilde{V} \simeq 37\,E_r$. The ground state atom number prior to the excitation pulse is $N \simeq 4.7 \times 10^4$, i.e. $N_D \simeq 0.85 \times 10^4$ atoms on doubly occupied sites are excited by the π-pulse. A slow exponential decay with a $1/e$ time of $\tau_{eg}^{-} \simeq 0.78(2)$ s is detected (solid line), corresponding in turn to a two-body loss rate coefficient $\beta_{eg}^{-} \simeq 3.0(1) \times 10^{-15}$ cm^3/s. The decay stops when nearly all atoms on doubly occupied sites have been lost. The figure is adapted from Ref. [124].

in turn related to the imaginary part of the a_{eg}^{-} scattering length η_{eg}^{-} by Eq. (1.22):

$$\beta_{eg}^{-} = -\frac{8\pi\hbar}{M}\,\eta_{eg}^{-} \tag{6.19}$$

yielding $\eta_{eg}^{-} \simeq -0.006\,a_0$. The residual $|g\rangle$ state stationary population corresponds to the estimated population of the singly occupied sites: the total atom number loss is in fact equal to the population which is initially excited by the clock π-pulse, evidencing an e-g pair loss process. Furthermore, the reported loss rate coefficient should be seen only as an upper bound, as tunnelling processes are not negligible throughout the long hold time with a lattice depth of $35\,E_r$ in the horizontal directions, and enable additional lossy collision channels such as $|ee\rangle$ state losses.

The direct comparison between the spin-exchange coupling strength V_{ex} and the $|eg^{-}\rangle$ state on-site decay rate confirms further how spin-exchange interactions are by far the dominating process in a three-dimensional lattice, as long as on-site $|ee\rangle$ state losses are prevented by isolating $|e\rangle$ atoms from one another. The remaining inelastic dynamics is thus limited to pair collisions occurring in the nuclear spin singlet state, which was found anyhow to lie at a large energy offset above the ground state of the two-particle system and will then be suppressed in many-body experiments with orbital spin exchange.

The large ratio of elastic to inelastic inter-orbital scattering length is encouraging with regard to the proposed implementation of the Kondo lattice model and its SU(N)-symmetric extension. The large exchange coupling strength V_{ex} found in ^{173}Yb is indeed very desirable. First of all, a strong exchange interaction dominates over the $|g\rangle$ state pair

interaction U_{gg}, characterised by a smaller scattering length. In addition, the exchange coupling and the inelastic collision rates can be reduced by decreasing the spatial overlap between $|g\rangle$ and $|e\rangle$ state wave functions in the lattice, e.g. by means of a state-dependent bi-chromatic lattice along one direction [56, 125]. A large region of the phase diagram of the ferromagnetic Kondo lattice, used for instance to describe colossal magnetoresistive compounds, seems accessible.

Conclusions and outlook

In this thesis, we have shown that quantum gases of fermionic ytterbium in optical lattices are a powerful and versatile system for the investigation of many-body physics with orbital interactions and enlarged symmetries. Owing to a precise control of the nuclear spin and of a novel orbital degree of freedom, obtained by extending the system to include the lowest metastable electronic state besides the ground state, we were able to prepare and study two-orbital degenerate mixtures of different nuclear spin states of ^{173}Yb. Spectroscopic techniques in optical lattices were specifically developed, enabling direct probing of the interactions between different combinations of orbital and spin states.

Our newly developed experimental apparatus for the production, the manipulation and the detection of lattice ultracold gases of ytterbium was described. An all-optical cooling procedure allows to reach degeneracy with both bosonic and fermionic isotopes. By loading the quantum gases into the lowest band of an optical lattice potential, the interaction-dominated regime is accessed. For the experiments presented in this thesis, a state-independent optical lattice was realised by using laser light at the magic wavelength. In addition, state-selective optical potentials can be tailored, exploiting the different dynamic polarisability of the two lowest electronic states of ytterbium. A stable laser setup for addressing the clock transition, connecting the two lowest electronic states of ^{173}Yb, was implemented, empowering the spin-selective, site occupation-selective coherent control of the metastable state population in the optical lattice.

We have shown how the two-orbital SU(N)-symmetric Hubbard model describes the physics of ultracold fermionic alkaline-earth-like gases in optical lattices. It includes an inter-orbital spin-exchange interaction term, providing a key ingredient for the quantum simulation of orbital magnetism phenomena [55]. In particular, by localising one of the two orbital states in a deep optical lattice, the renowned Kondo lattice model can be implemented. Secondly, the strong-coupling limit of the SU(N)-symmetric Hubbard model, namely the SU(N) Heisenberg model, can be realised using ground-state Mott insulators of alkaline-earth-like atoms [54].

We have reported on the discovery of a surprisingly strong spin-exchange coupling between the two orbital states of ^{173}Yb, which nearly saturates the energy gap to the first excited band in the lattice. Exploiting the interaction shift and the differential Zeeman shift of two-particle states on doubly occupied sites of a three-dimensional optical lattice, we were able to spectroscopically investigate the two-orbital interactions in both spin singlet and triplet channels, thereby characterising their scattering properties. We have moreover directly observed the inter-orbital spin-exchange dynamics in a one-dimensional optical lattice, initiated by preparing out-of-equilibrium spin distributions between ensembles in different orbitals. The SU(N) symmetry of all orbital interactions, until now only theoretically predicted, has been directly demonstrated by spectroscopic probing of sev-

eral distinct mixtures of nuclear spin states, and further verified by the observed absence of spin relaxation processes accompanying the spin-exchange dynamics. Finally, inelastic collisions have been investigated, revealing a favourable, large ratio of the elastic to inelastic scattering lengths in each channel.

Outlook

Our findings represent an important step towards the exploration of the two-orbital SU(N)-symmetric Hubbard model and open the route to the cold atom implementation of orbital magnetism and the Kondo lattice model. The realisation of states with strong orbital spin correlations seems within reach, in light of the observed preponderance of elastic interactions over inelastic interactions between the two orbital states and of the versatile state-preparation techniques demonstrated in this thesis. Furthermore, the first direct demonstration of SU(N) symmetry in ^{173}Yb provides exciting prospects for the investigation of SU(N)-symmetric fermionic systems confined to different dimensionalities [53, 73, 156]. SU($N > 2$)-symmetric spin models in optical lattices [55] could also be realised in the future, with the goal of observing the intriguing phases that have been theoretically predicted at varying values of N [54, 62, 163, 227, 232, 239], ranging from magnetically ordered states to spin liquids with long-range correlations.

The deviation of several observables in SU(N)-symmetric Fermi liquids from the spin-1/2 Landau-Fermi liquid behaviour was anticipated [53, 156], due to the enhancement of the repulsion between identical fermions with increasing N, mediated by density fluctuations of atoms in other spin states. Beyond mean-field effects revealing these deviations, e.g. a suppression of the spin susceptibility, could be already measurable in our current experimental conditions [63, 156], with an attainable interaction parameter of ^{173}Yb ground state atoms of $k_F a \simeq 0.15$. In addition, recent numerical calculations suggest that a shallow lattice potential significantly promotes ferromagnetism and phase separation in SU(2) [334, 335] and SU(3) [172] fermionic systems. Our low interaction strengths, compared to $k_F a \approx 1$ for which the SU(2) ferromagnetic instability is predicted in a homogenous system [336], may thus be sufficient for observing a partially polarised state. Investigating experimentally the ferromagnetic tendency of SU(N) fermionic systems at varying N could contribute to advances in the study of the ferromagnetic behaviour of the Hubbard model, considering in particular that the first order character of the ferromagnetic phase transition is expected to be enhanced by a larger N [53, 156]. However, low temperatures well below the tunnel coupling J are necessary to access the strongly correlated spin regime of the Hubbard model. In this respect, alkaline-earth-specific cooling techniques are promising for reaching such temperature regimes in the future [87]. The identification of a clock transition photoassociation resonance and its possible application to tune the ground state scattering length through an optical Feshbach resonance would moreover represent a powerful tool to further explore the physics of SU(N) interacting Fermi systems.

The studies of orbital interactions presented in this work are mostly focused on probing the properties of isolated fermionic atom pairs. Increasing the tunnel coupling of ground state atoms in a state-selective potential will enable the implementation of the Kondo

lattice Hamiltonian. With a view to a high-fidelity preparation of the Kondo lattice, the independent coherent excitation of atoms in the singly and doubly occupied sites of a lattice potential was already shown in this thesis. The separate addressing of the clock transition for the nuclear spin singlet and triplet states will moreover allow to detect on-site spin correlations, with great use for the investigation of many-body states with Kondo screening. Interaction clock spectroscopy could even be used for probing many-body phases of isotope mixtures in optical lattices, owing to the different intra- and inter-species scattering properties. The potential of such probes is currently being extended with the development of high-resolution imaging techniques and of a single two-dimensional gas preparation scheme. By these upgrades, the detection of site occupations and two-body spin states in a spatially resolved fashion will become possible.

Orbital interactions could also be exploited to produce highly-entangled many-body states, which are valuable for measurement-based quantum computation and for atom interferometry. It was recently shown theoretically that highly-entangled multi-particle spin states, namely Dicke states, are generated in alkaline-earth-like fermionic gases as a result of the dissipative evolution driven by strong inelastic *s*-wave collisions between metastable state atoms [337]. Dicke states possess a completely symmetric spin wave function, whose entanglement could be revealed by Ramsey clock spectroscopy [337]. On the other hand, they possess a completely anti-symmetric spatial wave function and do not therefore experience any *s*-wave collision, resulting in a suppression of inelastic losses.
Spin-exchanging processes have been also notably suggested for engineering entangling gates on atomic pairs [83, 115]. SWAP gates have been already implemented using the exchange coupling between distinct vibrational states in a lattice [116] or the superexchange coupling in a superlattice [338]. A precise dynamic control of inter-orbital spin-exchange, attainable by an abrupt B-field switching to initiate and freeze out the spin-exchanging dynamics [176], could be used to prepare on-site two-particle entanglement in both the spin and orbital degrees of freedom. By optical coherent manipulation of atom internal states, in combination with a superlattice potential for the merging and splitting of atom pairs [116, 338], maximally-entangled many-body states could then be created.

As another concrete prospect for quantum simulation, the coherent coupling between the ground and the metastable state in an anti-magic optical lattice can be exploited for realising strong effective magnetic fields and even non-Abelian gauge fields [64]. In such a lattice potential, the two states are confined to the nodes and the anti-nodes of the standing-wave intensity pattern and occupy thus spatially separated lattice sites. Laser-assisted tunnelling between these two sub-lattices can be driven by coherent clock excitation and complex tunnelling phases can be engineered in the process. These phases implement the so-called Peierls phases, analogous to the Aharonov-Bohm phase experienced by a charged particle moving in a magnetic field, and allow to create effective magnetic fluxes on the order of one flux quantum per unit cell [46, 47, 64]. The system can then be described by the famous Harper-Hofstadter Hamiltonian, used to describe the integer quantum Hall effect and chiral edge states. In a similar way, artificial gauge fields in synthetic dimensions could also be engineered by taking advantage of the clock transition for coupling different nuclear spin states [102].

We can also envision applications of the tuneable coherent coupling between delo-

calised and localised states, obtained through occupation-dependent addressing of the clock transition in a state-selective lattice. Sparse or disordered immobile atoms in the metastable state could be prepared in order to explore the physics of single- and multi-component Fermi systems with interacting impurities, in equilibrium and out-of-equilibrium settings [339, 340]. Furthermore, the analogy between localised and delocalised atoms in a lattice with radiation emitters and the radiation field continuum, respectively, could be exploited to simulate and tailor quantum-optical phenomena like superradiance [341]. In conclusion, both the demonstrated coherent control of the electronic degree of freedom and the realisation of inter-orbital spin exchange offer many new possibilities for stimulating experiments.

APPENDIX A

Light shifts and optical potentials

Polarisability of a state and AC-Stark shift

Neutral atoms become polarised in the presence of an oscillating electric field, such as the one generated by a laser beam. The effect of the atom-light interaction leads to the AC-Stark shift of atomic states, which depends on the state-specific dynamic polarisability $\alpha(\omega)$, introduced in Eq. (1.1). The polarisability of an electronic state $|\beta\rangle$ is given to lowest order by summing the contributions of the second-order AC-Stark shift from all other electronic states [97]:

$$\alpha(\beta;\omega) = \sum_{\beta' \neq \beta} \frac{2\,\omega_{\beta'\beta}}{\hbar\,(\omega_{\beta'\beta} - \omega)^2} \left|\langle \beta | \hat{\epsilon} \cdot \mathbf{d} | \beta' \rangle\right|^2 \tag{A.1}$$

where $\mathbf{d} = e\,\mathbf{r}$ is the atomic dipole operator, $\hat{\epsilon}$ is the field polarisation vector and $\omega_{\beta'\beta}$ are the frequencies of the atomic transitions, taken with positive (negative) sign for final states with higher (lower) energy than $|\beta\rangle$.

In the presence of state internal substructure, such as with the Zeeman m_F sublevels of a hyperfine state $|\gamma J\,F\rangle$, the atomic polarisability is generalised to a tensor [97]:

$$\alpha_{\mu\nu}(\gamma J\,F\,m_F;\omega) = \sum_{\gamma J' F' m'_F} \frac{2\omega_{F'F}}{\hbar\,(\omega_{F'F} - \omega)^2} \langle \gamma J\,F\,m_F | d_\mu | \gamma J'\,F'\,m'_F \rangle \langle \gamma J'\,F'\,m'_F | d_\nu | \gamma J\,F\,m_F \rangle \tag{A.2}$$

The AC-Stark shift for an electric field $\mathbf{E}$ is given by:

$$\Delta V(\gamma J\,F\,m_F;\omega) = -\sum_{\mu\nu} \mathrm{Re}\left[\alpha_{\mu\nu}(\gamma J\,F\,m_F;\omega)\right] E_\mu E_\nu \tag{A.3}$$

The polarisability tensor $\alpha_{\mu\nu}$ can be written as the sum of three irreducible spherical tensors of ranks 0, 1 and 2, termed scalar, vector and tensor polarisability, respectively [97]. Since the vector light shift is nulled for a linearly polarised light field and the tensor light shift is orders of magnitude smaller [90], only the scalar light shift is usually relevant for the dipole potentials adopted in this thesis, e.g. the magic optical lattice.

Let us now clarify in more detail the role of state magnetic substructure on dipole potentials and dipole forces. Thanks to the Wigner-Eckart theorem, the dipole matrix element of a given transition $|s\rangle \equiv |\gamma J\,F\,m_F\rangle \rightarrow |s'\rangle \equiv |\gamma J'\,F'\,m'_F\rangle$ can be broken up into two factors:

$$d_{s's} = \langle \gamma' || \mathbf{d} || \gamma \rangle\, \mathcal{A}_{s's} \tag{A.4}$$

The first factor is independent of the state hyperfine and magnetic substructures and is usually called the reduced dipole matrix element, whereas the second factor $\mathcal{A}_{s's}$ is dependent on all quantum numbers, and is related to the Clebsch-Gordan coefficients [15, 117]. Considering for simplicity only linearly or circularly polarised light, $\mathcal{A}_{s's}$ is given by:

$$\begin{aligned}\mathcal{A}_{s's}(m_F,q) = (-1)^{1+L'+S+J+J'+I-m'_F} \\ \times \sqrt{(2J+1)(2J'+1)(2F+1)(2F'+1)} \\ \times \begin{Bmatrix} L' & J' & S \\ J & L & 1 \end{Bmatrix} \begin{Bmatrix} J' & F' & I \\ F & J & 1 \end{Bmatrix} \begin{pmatrix} F & 1 & F' \\ m_F & q & -(m_F+q) \end{pmatrix}\end{aligned} \tag{A.5}$$

where the curly brackets and round brackets arrays denote respectively the $6j$-symbol and the $3j$-symbol [15], and q represents the polarisation of the light so that $m'_F = m_F + q$ ($q = 0$ for linear polarisation aligned to the quantisation axis and $q = \pm 1$ for right- and left-circular polarisations propagating along the quantisation axis). The dependence of $\mathcal{A}_{s's}$ on m_F and q results in different line strengths characterising each of the transitions within the magnetic substructure of a dipole transition (see Fig. A.1).

An explicit form of the total light shift as a function of the quantum numbers of a state $|s\rangle \equiv |\gamma J\, F\, m_F\rangle$ and the light polarisation q is derived:

$$\Delta V(\gamma J\, F\, m_F; \omega, q, \mathbf{r}) = -\frac{I(\mathbf{r})}{\epsilon_0\, c} \sum_{s' \neq s} \frac{\omega_{s's}}{\hbar\,(\omega_{s's} - \omega)^2}\, |d_{s's}|^2 \tag{A.6}$$

where $d_{s's}$ is given by Eqs. (A.4)-(A.5). The light shift depends therefore on the polarisation of the light through $|\mathcal{A}_{s's}|^2$ for each transition.

In order to compute the light shift of a state $|s\rangle$, the reduced dipole matrix elements of the $|s\rangle \to |s'\rangle$ transitions can be directly related to the decay rates of the states $|s'\rangle$ state to the state $|s\rangle$:

$$\Gamma(s' \to s) = \frac{\omega_{s's}^3}{3\pi\hbar\, c^3\, \epsilon_0} \frac{\left|\langle \gamma' || \mathbf{d} || \gamma \rangle\right|^2}{2J'+1} \tag{A.7}$$

The state labels s and s' need to be switched for states $|s'\rangle$ that are lower in energy than $|s\rangle$, causing a sign flip of $\omega_{s's}$. Using this relation to rewrite Eq. (A.6), we obtain:

$$\Delta V(\gamma J\, F\, m_F; \omega, q, \mathbf{r}) = -I(\mathbf{r}) \sum_{s' \neq s} \frac{3\pi\, c^2}{2\omega_{s's}^3} |\mathcal{A}_{s's}(m_F, q)|^2 \left(\frac{\Gamma(s' \to s)}{\omega_{s's} - \omega} + \frac{\Gamma(s' \to s)}{\omega_{s's} + \omega} \right) \tag{A.8}$$

This formula can be used to estimate the light shift of an arbitrary state for any light frequency, provided that the decay channels of the state and to the state are known to some precision (see Fig. 2.1 concerning the most relevant states in ytterbium). Eq. (A.8) yields Eq. (1.3) in the limit of a two-level atom.

Transition strengths of the hyperfine transitions in ytterbium

The transition strengths are defined as the absolute square of the Clebsch-Gordan coefficients $|\mathcal{A}_{s's}(m_F, q)|^2$. All line strengths associated with the hyperfine and magnetic

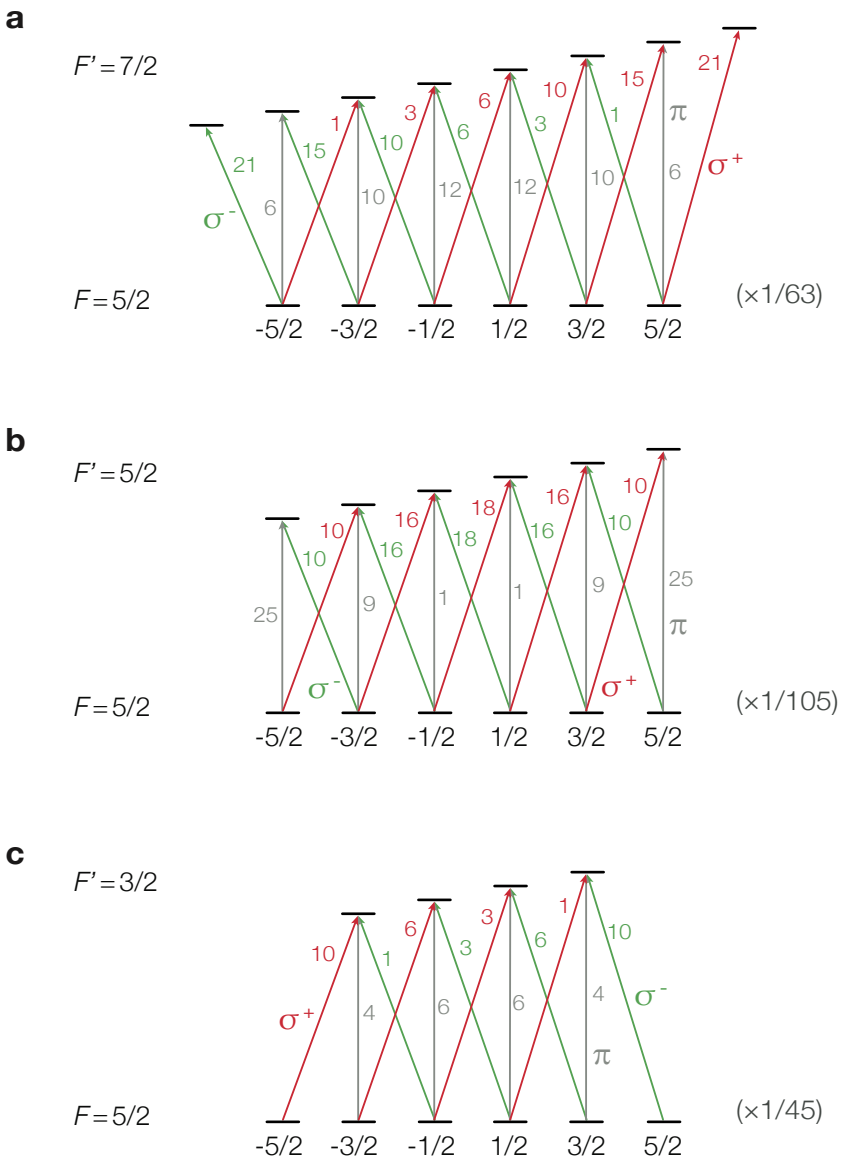

Figure A.1 – Line strengths $|\mathcal{A}_{s's}|^2$ for the different hyperfine $^1S_0 \rightarrow {}^1P_1$ and $^1S_0 \rightarrow {}^3P_1$ transitions. The strengths are normalised to the weakest allowed transition. The line strengths of the $^1S_0 \rightarrow {}^3P_1$ transitions are identical to the ones of the $^1S_0 \rightarrow {}^1P_1$ transitions, since the finite dipole matrix element of the former is entirely induced by the spin-orbit interaction, which mixes the two pure LS-coupling eigenstates (see Eq. (2.4)). Similarly, the line strengths of the $^1S_0(F = 5/2) \rightarrow {}^3P_0(F' = 5/2)$ transition are equal to the ones of the $^1S_0(F = 5/2) \rightarrow {}^3P_1(F' = 5/2)$ transition.

substructure of a dipole transition can be computed through Eq. (A.5). The obtained values for the relevant transitions of ytterbium are reported in Fig. A.1. We note here that the non-squared Clebsch-Gordan coefficient $\mathcal{A}_{s's}$ can be positive or negative, yielding an according transition dipole matrix element. The transition Rabi frequency in Eq. (5.1) can therefore be positive or negative, besides being affected by the magnitude of the coefficient. For instance, opposite Rabi frequencies are found on the clock $^1S_0 \rightarrow {}^3P_0$ π-

transitions for opposite m_F states: $\mathcal{A}_{\text{clock}}(m_F, q=0) = -\mathcal{A}_{\text{clock}}(-m_F, q=0)$.

Dipole traps with Gaussian beams

Optical dipole traps are usually created using Gaussian laser beams. For such a beam propagating along the z-direction, the intensity profile is given by:

$$I(\mathbf{r}) = I_0 \left(\frac{w_0}{w(z)}\right)^2 e^{-2r^2/w^2(z)} \tag{A.9}$$

where w_0 is the beam waist and $w(z) = w_0\sqrt{1+z^2/z_R^2}$, with $z_R = \pi w_0^2/\lambda$ being the Rayleigh range of the beam. Inserting this intensity profile in Eq. (1.3), the potential minimum for a red-detuned beam is found at $\mathbf{r} = 0$, where the intensity equals I_0. The dipole potential in the vicinity of $\mathbf{r} = 0$ is approximately harmonic. Atoms usually occupy only a small region of the trap, experiencing a harmonic potential with frequencies given by:

$$\omega_{x,y} = \sqrt{\frac{4V_0}{M\,w_0^2}}, \qquad \omega_z = \sqrt{\frac{2V_0}{M\,z_R^2}} \tag{A.10}$$

where V_0 is the magnitude of the potential depth at the peak intensity I_0, and the transversal x, y-frequencies are usually on the order of 10 to 100 Hz. The potential is significantly weaker in the axial direction of the laser beam, and single-beam optical traps yield therefore atomic samples with a characteristic cigar shape. In situations where a more isotropic confinement is desirable, two Gaussian beams can be intersected at $\mathbf{r} = 0$. The beams are usually frequency-shifted from each other to prevent unwanted interference at the crossing. Optical traps realised in this way are usually named crossed dipole traps. Elliptic Gaussian beams can also be employed, i.e. beams described by different waists w_{0x}, w_{0y} in the x, y-directions. In this case the resulting harmonic confinement can be made anisotropic, with different frequencies ω_x, ω_y in the two directions. One important effect to consider is gravitational sagging, namely the shift of the potential minimum along the vertical direction due to gravitational force. The influence of gravity increases for weaker dipole traps, and atoms above a certain energy can spill out towards the bottom. This effect is used for evaporative cooling, where the hotter atoms escape the trap by spilling away while the power of the dipole beam providing the vertical confinement is decreased.

Optical lattice potentials with Gaussian beams

In red-detuned lattices, where potential minima coincide with intensity minima, trapped atoms experience a Gaussian confinement potential in the directions orthogonal to the propagation direction of the lattice beam (see Fig. A.2). This confinement potential has the same total depth V_0 as the lattice potential itself and its frequency is given by the beam waist using Eq. (A.10). When multiple lattice beams are crossed, a three-dimensional

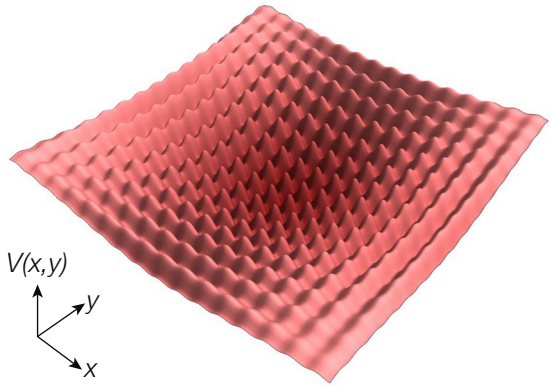

Figure A.2 – Optical lattice potential in the x-y plane. The underlying confining potential results from the Gaussian profile of three retro-reflected orthogonal beams with the same waist size (not to scale).

confining potential is present, which close to its minimum is characterised by the harmonic frequencies:

$$\omega_{\mu,\mathrm{lat}} = \sqrt{\frac{4V_0}{M}\left(\frac{1}{w_{1,\mathrm{lat}}^2}+\frac{1}{w_{2,\mathrm{lat}}^2}\right)} \tag{A.11}$$

where $w_{1,\mathrm{lat}}$ and $w_{2,\mathrm{lat}}$ are the waists of the lattice beams propagating orthogonally to the μ-axis, and we assume for simplicity that all beams have equal intensities. An additional anti-confinement, which however does not compensate the Gaussian confinement, is induced by the the varying lattice depth perpendicular to the propagation direction due to the decrease of the lowest vibrational state energy at each lattice site. In harmonic approximation, its (imaginary) frequency is given by:

$$\omega_{\mu,\mathrm{ac}} = \frac{2\pi\hbar}{M\,\lambda}\sqrt{\frac{1}{w_{1,\mathrm{lat}}^2}+\frac{1}{w_{2,\mathrm{lat}}^2}}\left(\frac{V_0}{E_r}\right)^{1/4} \tag{A.12}$$

By summing this two contribution in quadrature one obtains the total confining potential frequency in the μ-direction: $\omega_{\mu,\mathrm{c}} = \sqrt{\omega_{\mu,\mathrm{lat}}^2 - \omega_{\mu,\mathrm{ac}}^2}$, which in usual experimental configurations is similar to $\omega_{\mu,\mathrm{lat}}$. For blue-detuned lattices, the situation is radically different due to the near absence of the Gaussian confinement (see e.g. [167]).

Motion in a homogenous lattice potential

Let us consider a cubic homogeneous lattice potential, i.e. $V_x(\mathbf{r}) = V_y(\mathbf{r}) = V_z(\mathbf{r}) = V_0$ in Eq. (1.6), consisting of three independent potentials along each direction. The Hamiltonians corresponding to the motion in each spatial direction can be treated separately. For simplicity we will consider here a lattice potential along the x-direction, and the Hamiltonian is given by:

$$\hat{H}_{0x} = \int dx\,\hat{\psi}^\dagger(x)\left(-\frac{\hbar^2}{2M}\frac{\partial^2}{\partial x^2}+V_{\mathrm{lat}}(x)\right)\hat{\psi}(x) \tag{A.13}$$

where $\hat{\psi}^\dagger(x)$ ($\hat{\psi}(x)$) is the field operator that creates (annihilates) a particle at position x. The motion in a combined sinusoidal and harmonic potential which results from crossing Gaussian lattice beams (see Fig. A.2) is briefly discussed in Appendix B.

For a particle moving in a potential with a discrete translational symmetry, the Bloch theorem ensures the possibility of constructing a set of wave functions which are the analogues of plane waves in free space, denominated Bloch states. The energies of Bloch states are grouped in bands separated by band gaps, whose width and separation depend on the lattice depth [117, 118]. Bloch states $\psi_q^{(\ell)}(x)$ are labeled by their quasimomentum q (restricted to the first Brillouin zone, i.e. $-k < q \leq k$) and band-index ℓ. A plot of the Bloch energy bands in one dimension is shown in Fig. A.3, where the width of each band and the gaps between different bands are given as a function of the lattice depth.

As explained in Chapter 5, the bandwidth of the lowest Bloch band and the gap to the first excited band are important in the context of the excitation to the metastable state in an optical lattice. When the clock excitation laser is propagating along the direction of one of the lattice axes, only the corresponding one-dimensional lattice structure is relevant. As quasimomentum is conserved in the directions orthogonal to the clock laser wave vector (it is completely conserved in the Lamb-Dicke regime), only the lattice structure in the wave vector direction counts.

In the Bloch-wave basis, the one-dimensional Hamiltonian takes a diagonal form, and one can write:

$$\hat{H}_{0x} = \sum_{q\,\ell} \mathcal{E}_\ell(q)\, \hat{\psi}_q^{(\ell)\dagger} \hat{\psi}_q^{(\ell)} \tag{A.14}$$

where the Bloch states annihilation and creation operators are defined by

$$\hat{\psi}_q^{(\ell)} = \int dx\, \hat{\psi}(x)\, \psi_q^{(\ell)}(x) \tag{A.15}$$

and $\mathcal{E}_\ell(q)$ is the dispersion relation of the ℓ-th Bloch band. We refrained here from working out the details of the derivation, that can be readily found in the existing literature (e.g. [117, 118]) and in several doctoral thesis.

As in free space maximally localised wave functions can be constructed by Fourier-transform of plane waves, the same procedure can be followed in the presence of the lattice: a basis of maximally localised wave functions within a certain energy band, called Wannier functions, can be constructed by Fourier-transform of Bloch waves. The Wannier function localised around the position x_j of the j-th lattice site can be obtained as [118]:

$$w_{\ell j}(x) \equiv w_\ell(x - x_j) = \frac{1}{\sqrt{L}} \sum_q e^{-iqx_j}\, \psi_q^{(\ell)}(x_j) \tag{A.16}$$

where L is the number of lattice sites[1,2]. Wannier functions are as localised as possible around the individual lattice sites position and are a suitable orthonormal basis to treat

[1] Bloch waves are defined up to an overall phase; however Wannier functions clearly depend on the choice of the phase for each quasimomentum q in the sum. In one dimension, it is known that a certain choice of the phases leads to exponentially localised Wannier functions [342].

[2] Here, we implicitly assumed a system with a finite number of lattice site and quasimomenta; for an infinite system, the sum turns into an integral.

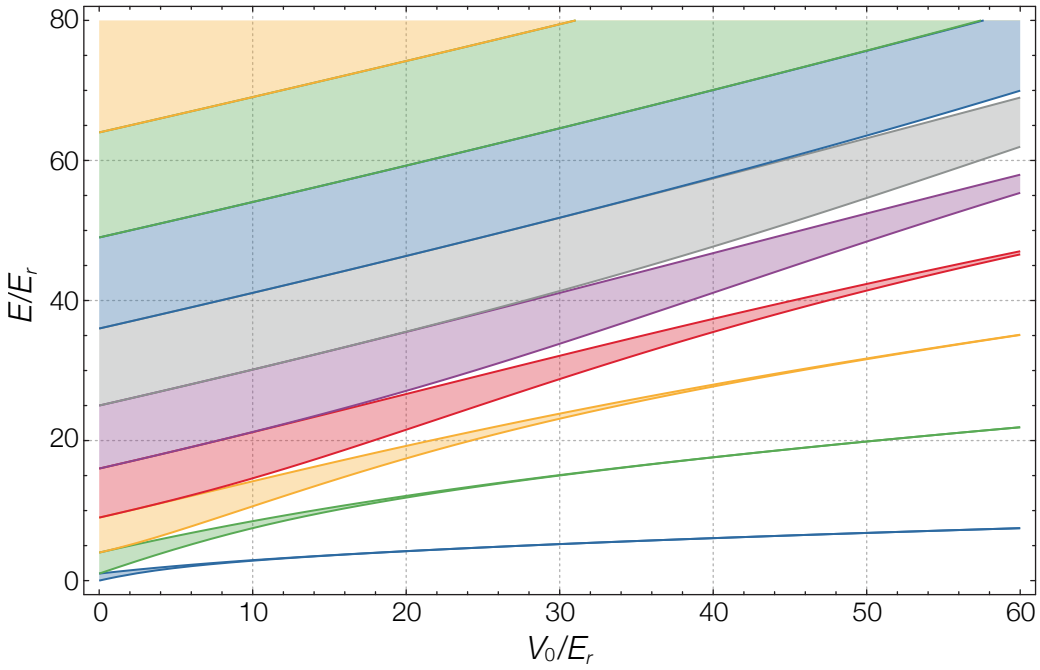

Figure A.3 – Bloch band energies as a function of the lattice potential depth in one dimension. In dimensions $D > 1$, different energy bands overlap at small lattice depth and band gaps open up only at a finite depth.

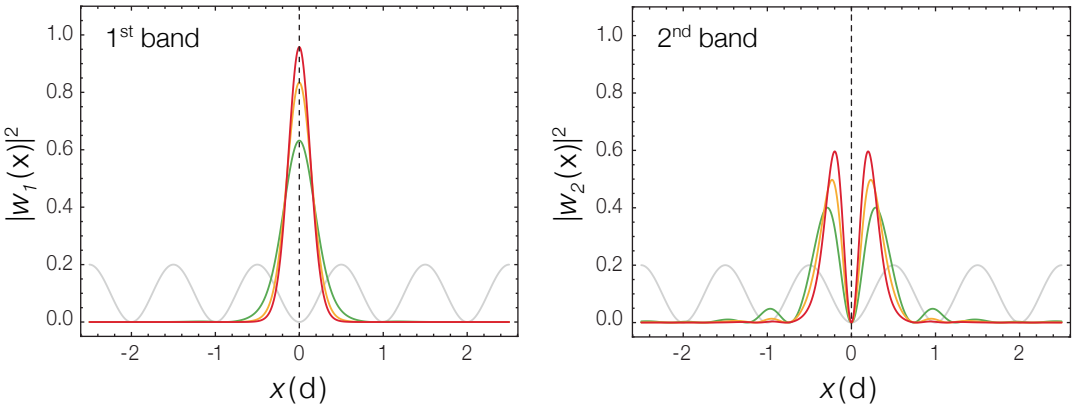

Figure A.4 – Absolute square of the two lowest-band Wannier functions for three different lattice depths: 3 E_r (green), 7 E_r (yellow) and 11 E_r (red). The grey line shows the shape of the lattice potential.

local effects such as contact interactions in a lattice. Plots of of the probability distributions of lowest and first excited Wannier states as a function of position in the lattice are displayed in Fig. A.4. In the Wannier basis, the kinetic energy of the particles is associated with the tunnelling process of a particle from one Wannier state to another. The tunnelling amplitude between two Wannier states is described by the Hamiltonian matrix element between the two states. We can expand the field operators in Eq. (A.13) in terms

of Wannier state operators:

$$\hat{\psi}(x) = \sum_j w_{\ell j}(x)\,\hat{c}_{\ell j} \tag{A.17}$$

where $\hat{c}^\dagger_{\ell j}$ creates an atom in the Wannier function $w_{\ell j}(x)$. The Hamiltonian in Eq. (A.13) can then be written in the Wannier basis:

$$\hat{H}_{0x} = -\sum_\ell \sum_{ij} J^\ell_{ij}\,\hat{c}^\dagger_{\ell i}\hat{c}_{\ell j} \tag{A.18}$$

The tunnel coupling J^ℓ_{ij} between the i-th and the j-th lattice sites in the ℓ-th band is given by:

$$J^\ell_{ij} = \int dx\, w^*_{\ell i}(x)\left(-\frac{\hbar^2}{2M}\frac{\partial^2}{\partial x^2} + V_{\text{lat}}(x)\right) w_{\ell j}(x) \tag{A.19}$$

We note here that Wannier functions in different bands along each direction can be composed to give the three-dimensional Wannier functions:

$$w_{\ell\,\mathbf{n}}(\mathbf{r}) = w_{\ell_x i}(x)\, w_{\ell_y j}(y)\, w_{\ell_z k}(z) \tag{A.20}$$

with $\mathbf{n} = (i, j, k)$, and the above discussion can thus be readily generalised to three dimensions. The Hamiltonian in Eq. (A.18) is simplified in the tight-binding limit, where the description is restricted to the lowest Bloch band ($\ell = 1$) and only the tunnelling between neighbouring lattice sites $\langle i, j\rangle$ is retained:

$$\hat{H}_{0x} = -J \sum_{\langle i,j\rangle} \hat{c}^\dagger_i \hat{c}_j \tag{A.21}$$

where $\hat{c}^\dagger_j$ creates an atom in the Wannier function $w_j(x) \equiv w_{1j}(x)$.

In the tight binding regime, the dispersion relation of the first energy band takes a simple cosinusoidal form: $\mathcal{E}(q) = 2J\cos(qd)$, where $d = \pi/k$ is the lattice period [14]. The bandwidth can therefore be expressed with respect to J: $\Delta\mathcal{E} = 4J$ ($12J$ in a cubic three-dimensional lattice). For any given quasimomentum q, the dispersion relation can be locally approximated to a parabolic one. In this way one can define an effective mass M^*, which helps describing the single-particle dynamics:

$$\frac{1}{M^*} = \frac{1}{\hbar^2}\frac{\partial^2}{\partial q^2}\,\mathcal{E}(q) \tag{A.22}$$

APPENDIX B

Fundamentals of trapped Fermi gases

Thermodynamic quantities

Fermionic atoms, i.e. atoms with an uneven number of neutrons, in the absence of interactions exhibit an ideal Fermi gas behaviour. The occupation of a single-particle eigenstate of the Hamiltonian with energy $\mathcal{E}$ at an equilibrium temperature T is described by the Fermi-Dirac distribution:

$$F(\mathcal{E}) = \frac{1}{e^{\frac{\mathcal{E}-\mu}{k_B T}} + 1} \tag{B.1}$$

where k_B is the Boltzmann constant and μ is the chemical potential of the gas, fixed by the atom number N (see below). We have assumed here that a single component, e.g. spin state, is present in the gas, but all formulas can be generalised to s-component fermions by accounting for multiple state occupation with a factor s in front of $F(\mathcal{E})$. The Fermi energy is defined as the chemical potential at zero temperature, $E_F = \mu(T = 0)$. The Fermi wave number is $k_F = \sqrt{2\,M\,E_F}/\hbar$ and the Fermi temperature is $T_F = E_F - \mathcal{E}_0/k_B$, where $\mathcal{E}_0$ is the energy of the lowest eigenstate. The fugacity $z = \exp(\frac{\mu}{k_B T})$ is often used to parametrise the degree of quantum degeneracy of the gas: for $T \gg T_F$, $z \simeq 0$ and the Fermi-Dirac distribution approaches the Boltzmann distribution, whereas for $T \ll T_F$, $z \to +\infty$ and $F(\mathcal{E}) = \Theta(\mathcal{E} - E_F)$.

For a gas in a three-dimensional (3D) harmonic trap with a potential

$$V_{3\mathrm{D}}(\mathbf{r}) = \frac{1}{2} M \left(\omega_x^2\, x^2 + \omega_y^2\, y^2 + \omega_z^2\, z^2 \right) \tag{B.2}$$

the density of states at energy $\mathcal{E}$ equals

$$g_{3\mathrm{D}}(\mathcal{E}) = \frac{\mathcal{E}^2}{2\hbar^3 \bar{\omega}^3} \tag{B.3}$$

where $\bar{\omega} = (\omega_x\, \omega_y\, \omega_z)^{1/3}$ is the mean trap frequency. The Fermi energy in a the harmonic trap can be obtained by fixing the atom number N:

$$N = \int_0^\infty d\mathcal{E}\, g(\mathcal{E}) F(\mathcal{E}) \underset{T=0}{=} \int_0^\infty d\mathcal{E}\, g(\mathcal{E})\, \Theta(\mathcal{E} - E_F) \tag{B.4}$$

and setting $g(\mathcal{E}) = g_{3\mathrm{D}}(\mathcal{E})$ the Fermi energy equals then $E_F = \hbar\bar{\omega}\,(6N)^{1/3}$.

Using the Fermi-Dirac distribution $F(\mathcal{E})$ and the density of states $g(\mathcal{E})$, several thermodynamic quantities $X(N, T)$ can be readily obtained analytically by performing integrals

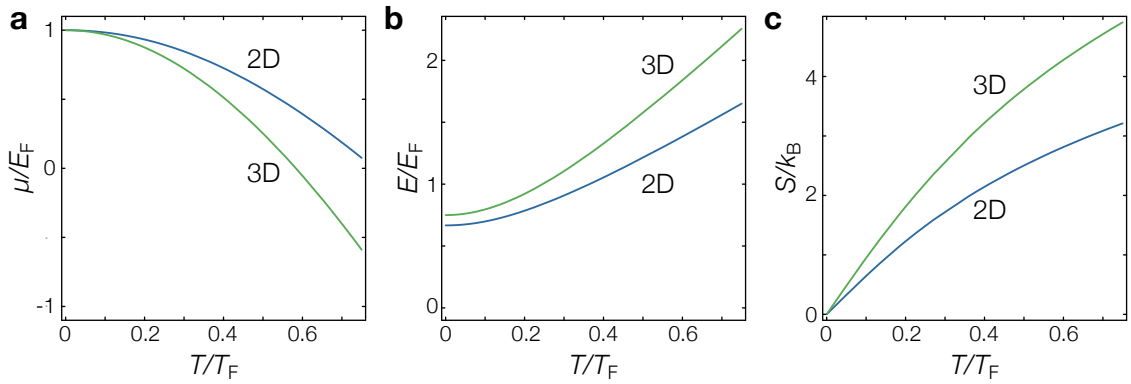

Figure B.1 – Thermodynamic quantities of a spin-polarised (non-interacting) Fermi gas confined in a 2D or 3D harmonic trap, as a function of temperature. (a) Chemical potential. (b) Mean energy per particle. (c) Mean entropy per particle.

with the form:

$$X(N,T) = \int_0^\infty d\mathcal{E}\, C\mathcal{E}^\eta F(\mathcal{E}) = -C\,(k_B T)^{1+\eta}\,\Gamma(1+\eta)\,\mathrm{Li}_{1+\eta}\big(-z(N,T)\big) \tag{B.5}$$

where $\mathrm{Li}_n(x)$ are the polylogarithmic function of order n and $\Gamma(n)$ is the Euler gamma function. In order to compute the quantities X, the fugacity $z(N,T)$ can be obtained by inverting the following relation numerically:

$$N = \int_0^\infty d\mathcal{E}\, g_{3\mathrm{D}}(\mathcal{E}) F(\mathcal{E}) = -\frac{k_B^3 T^3\,\mathrm{Li}_3(-z)}{\hbar^3\bar{\omega}^3} \tag{B.6}$$

The chemical potential is then:

$$\mu(N,T) = k_B T \log\big(z(N,T)\big) \underset{T\to 0}{\simeq} E_F\left(1 - \frac{\pi^2}{3}\frac{T^2}{T_F^2}\right) \tag{B.7}$$

where the low-temperature limit is obtained through a Sommerfeld expansion of the integral. Using Eq. (B.5), the total energy E in a 3D harmonic trap can be obtained:

$$E(N,T) = -\frac{3k_B^4 T^4\,\mathrm{Li}_4(-z)}{\hbar^3\bar{\omega}^3} \underset{T\to 0}{\simeq} \frac{3}{4} N E_F\left(1 + \frac{2\pi^2}{3}\frac{T^2}{T_F^2}\right) \tag{B.8}$$

Using the previous results, the total entropy can be obtained as well [215]:

$$S(N,T) = \frac{E-\mu N}{k_B T} + \int_0^\infty d\mathcal{E}\, g_{3\mathrm{D}}(\mathcal{E}) \log\left(1 + z\,\exp\left(-\frac{\mathcal{E}}{k_B T}\right)\right) \tag{B.9}$$

Such quantities can also be computed for a 2D harmonic trap by simply replacing the 3D trap potential and the density of states with their 2D analogues:

$$\begin{aligned} V_{2\mathrm{D}}(\mathbf{r}) &= \frac{1}{2} M\left(\omega_x^2 x^2 + \omega_y^2 y^2\right) \\ g_{2\mathrm{D}}(\mathcal{E}) &= \frac{\mathcal{E}}{\hbar^2\bar{\omega}^2} \end{aligned} \tag{B.10}$$

Plots of μ, E and S as a function of T in a two- and three-dimensional harmonic trap are displayed in Fig. B.1.

Density and momentum distribution

The real space and momentum distribution of an ideal Fermi gas in a harmonic trap can be obtained exactly by summing over all eigenstate wave functions weighted by the Fermi-Dirac distribution. However, a semi-classical approximation, usually termed Thomas-Fermi approximation or local-density approximation (LDA), is typically used, as it is quite accurate in the limit of large atom number N where many single-particle states are occupied [19, 343]. The number density in phase space is given in LDA by:

$$f(\mathbf{r},\mathbf{p}) = \frac{1}{(2\pi)^3}\frac{1}{e^{\frac{1}{k_B T}\left(\frac{p^2}{2M}+V_{\text{trap}}(\mathbf{r})-\mu\right)}+1} \tag{B.11}$$

The Thomas-Fermi density and momentum distributions are then obtained by integration in momentum space and position space, respectively [343]:

$$\begin{aligned} n(\mathbf{r}) &= \int d\mathbf{p}\, f(\mathbf{r},\mathbf{p}) \\ \tilde{n}(\mathbf{p}) &= \int d\mathbf{r}\, f(\mathbf{r},\mathbf{p}) \end{aligned} \tag{B.12}$$

In a 3D harmonic trap one obtains:

$$\begin{aligned} n(\mathbf{r}) &= -\left(\frac{M k_B T}{2\pi\hbar^2}\right)^{3/2} \mathrm{Li}_{3/2}\left(-z\exp\left(-\frac{V_{3D}(\mathbf{r})}{k_B T}\right)\right) \\ \tilde{n}(\mathbf{p}) &= -\left(\frac{k_B T}{2\pi M\hbar^2\bar{\omega}^2}\right)^{3/2} \mathrm{Li}_{3/2}\left(-z\exp\left(-\frac{p^2}{2M k_B T}\right)\right) \end{aligned} \tag{B.13}$$

whereas in 2D:

$$\begin{aligned} n(\mathbf{r}) &= \frac{M k_B T}{2\pi\hbar^2}\log\left(1+z\exp\left(-\frac{V_{2D}(\mathbf{r})}{k_B T}\right)\right) \\ \tilde{n}(\mathbf{p}) &= \frac{k_B T}{2\pi M\hbar^2\bar{\omega}^2}\log\left(1+z\exp\left(-\frac{p^2}{2M k_B T}\right)\right) \end{aligned} \tag{B.14}$$

We note here that the Thomas-Fermi momentum distribution of an ideal Fermi gas is isotropic, leading to a correspondingly isotropic expansion when the gas is released from a harmonic trap. The column-integrated 3D Thomas-Fermi momentum distribution is used to fit the column density in time-of-flight absorption images, in order to determine the fugacity z of the experimental samples. The associated T/T_F is obtained through the relation in Eq. (B.6): $T/T_F = (-6\,\mathrm{Li}_3(-z))^{-1/3}$.

Interactions

All results given so far hold for non-interacting Fermi gases. However, in the absence of a Feshbach resonance to tune the scattering length to zero, the density and momentum distributions and the thermodynamic quantities of our (multi-spin) experimental samples are always affected by interactions. The relevance of the interactions is determined by the dimensionless interaction parameter $k_F a$ [19]. For ground state ^{173}Yb atoms, the scattering

length is $a \simeq 195\,a_0$, and for typical trapping frequencies in our setup after the evaporation (see Section 2.2.4) and $N \sim 10^5$, the interaction parameter is rather small: $k_F a \simeq 0.1$. For weak repulsive interactions $k_F a \ll 1$, a zero-temperature first-order perturbative expansion in $k_F a$ using a contact potential yields a correction to the energy per particle of approximately $0.3\,k_F a$ [19], which is thus fairly small in our experimental conditions. Moreover, the momentum and density distributions are expected to be very similar to the semi-classical ones [344]. In general, interacting fermions are described by Landau's Fermi-liquid theory [80, 155], as long as no symmetry-breaking phase transition occurs under the influence of interactions. Within Fermi-liquid theory, the low-energy excitation spectrum of the interacting gas is in one-to-one correspondence with the spectrum of an ideal Fermi gas. Although collective modes appear due to interactions, distribution functions and thermodynamic quantities retain a similar shape, since the density of states and the state occupation distribution have the same form as for the ideal Fermi gas [80, 155].

Adiabatic loading from a harmonic dipole trap into a 1D lattice

In order to estimate the density of the 2D gases trapped in each of the vertical optical lattice sites after the adiabatic loading from a harmonic trap (see Section 6.2), we use a model which assumes conservation of total entropy and thermal equilibrium during the transfer. The spatial profile of the Fermi gas in the dipole trap before the loading into the lattice is modelled by the Thomas-Fermi density distribution in Eq. (B.13). After the transfer, the vertical degree of freedom is effectively frozen out by the lattice potential. The sum of entropies and atom numbers of the 2D gases in the vertical lattice are fitted to give the total entropy S_0 and atom number N_0 in the dipole trap, with the chemical

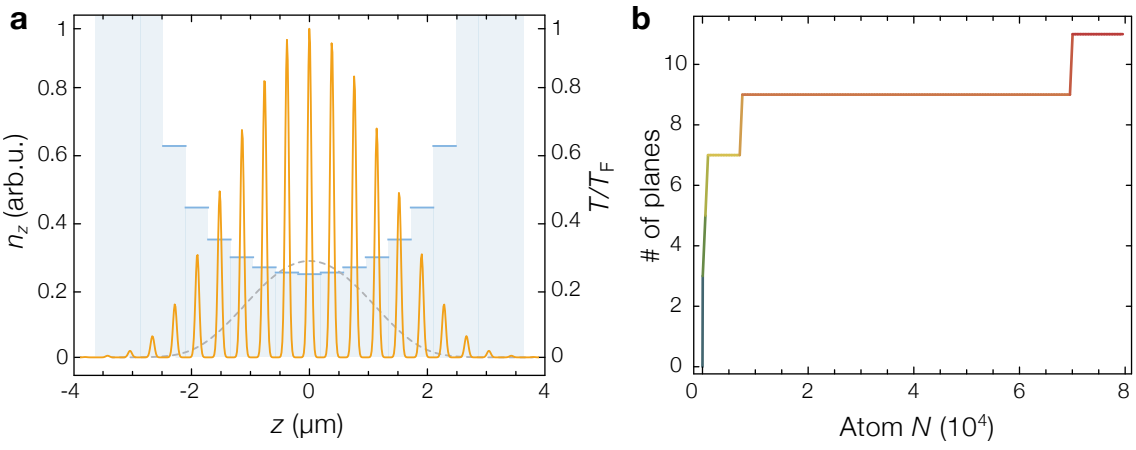

Figure B.2 – Adiabatic transfer of a Fermi gas from the dipole trap into the vertical lattice potential. (a) x-y integrated density profile n_z along the lattice direction, calculated for $N = 2 \times 10^4$ atoms per spin state and $T = 0.2\,T_F$ (before the transfer). The blue bars show the reduced temperature in each vertical lattice site after the transfer. The dashed line represents the x-y integrated density along the lattice direction inside the dipole trap before the transfer. (b) Number of vertical lattice sites (planes) populated by more than 5% of the atom number N as a function of N (per spin state). The temperature in the dipole trap is set to $T = 0.2\,T_F$.

potential μ_0 and the temperature T as free parameters:

$$\begin{cases} S_0 = & \sum_j S_j^{2D}(\mu_j, T) \\ N_0 = & \sum_j N_j^{2D}(\mu_j, T) \end{cases} \tag{B.15}$$

where $\mu_j = \mu_0 - \frac{1}{2} M \omega_z^2 z_j^2$ is the local chemical potential, ω_z is the dipole trap vertical frequency at the moment of the transfer and z_j is the z-coordinate of the centre of the j-th vertical lattice site. The density profile in each lattice site is modelled as a 2D Thomas-Fermi density distribution in the horizontal plane (see Eq. (B.14)) and as the approximately Gaussian vibrational ground state in the lattice direction z:

$$\begin{aligned} n_j(x,y,z) = s \frac{M k_B T}{2\pi\hbar^2} \log\left(1 + \exp\left(\frac{\mu_j}{k_B T}\right) \exp\left(-\frac{M}{2 k_B T}\left(\omega_{x,\mathrm{lat}}^2 x^2 + \omega_{y,\mathrm{lat}}^2 y^2\right)\right)\right) \\ \times \left(\frac{M \omega_{z,\mathrm{lat}}}{\pi\hbar}\right)^{1/2} \exp\left(-\frac{M \omega_{z,\mathrm{lat}}}{\hbar}\left(z - z_j\right)^2\right) \end{aligned} \tag{B.16}$$

where s is the number of spin components and $\omega_{\mu,\mathrm{lat}}$ are the trap frequencies in the vertical lattice. By inserting the measured trap frequencies in the dipole trap and in a vertical lattice depth $V_z = 50\, E_r$, we determine in-plane mean densities between $4 \cdot 10^{13}$ and $8 \cdot 10^{13}$ atoms/cm^3, corresponding to mean in-plane Fermi energies between $E_F = h \cdot 2.1\,\mathrm{kHz}$ and $E_F = h \cdot 3.7\,\mathrm{kHz}$. The atom distribution among different planes as a function of the total atom number N is displayed in Fig. B.2. The gas temperature in the dipole trap does not significantly affect the number of occupied planes and only produces sizeable difference on the edges of the final density distribution.

Motion in a combined harmonic and lattice potential

It was shown in Chapter 1 how local interactions in a lattice can be conveniently represented in the Wannier basis, and for sufficiently deep lattices the tight-binding approximation simplifies the Hamiltonian to the single-band Hubbard model in Eq. 1.34. The Wannier basis is also well-suited to treat the case of a lattice potential with an underlying confinement potential, and we will discuss here the case of harmonic confinement. The harmonic potential (usually resulting from the Gaussian intensity profile of the lattice beams as explained above) breaks the translational symmetry of the periodic lattice potential. However, the spatial variation of the lattice depth is typically very small for the atomic cloud sizes $R < 50\lambda$ used in experiments. Neglecting this variation, the tunnelling coupling is assumed homogenous and equal to J for any pair of neighbouring lattice sites. The tight-binding Hamiltonian for the motion in a one-dimensional combined potential is given by:

$$H_0 = -J \sum_{\langle i,j \rangle} \hat{c}_i^\dagger \hat{c}_j + \sum_i \Omega_i \hat{n}_i \tag{B.17}$$

where $\Omega_i = \frac{1}{2} M \omega_c^2 d^2 i^2$, with $d = \lambda/2$ being the lattice spacing, and the trap centre is located at $i = 0$. The lowest eigenstates of this Hamiltonian are well approximated by harmonic oscillator eigenstates, and the effect of the lattice potential can be included by

replacing the mass M with the effective mass M^* (see Eq. (A.22)). However, the situation is completely different in proximity of the band edge. The level of the band edge is position dependent, due to the onsite offset energies Ω_i, and is therefore reached first in the centre of the trap; the energy bands are effectively curved by the harmonic confinement (see Fig. B.3). Eigenstates with an energy above the central band edge are therefore spatially confined to the sides of the trap, because of Bragg reflection at the upper band edge. In contrast to the case of a translationally invariant potential, where localisation can only be induced by interactions or disorder, atoms in a combined potential become localised on lattice sites k for which the harmonic energy offset exceeds the tunnel coupling $\Omega_k - \Omega_{k-1} > J$. The number of localised atoms increases both with the lattice depth and with the strength of the confinement. In the extreme regime of very deep lattices, with an effectively flat dispersion relation, all eigenstates are completely localised. The experimental consequences of this lattice-induced localisation mechanism in a harmonic trap for fermionic atoms have been the object of several studies [92, 215–217, 291, 292].

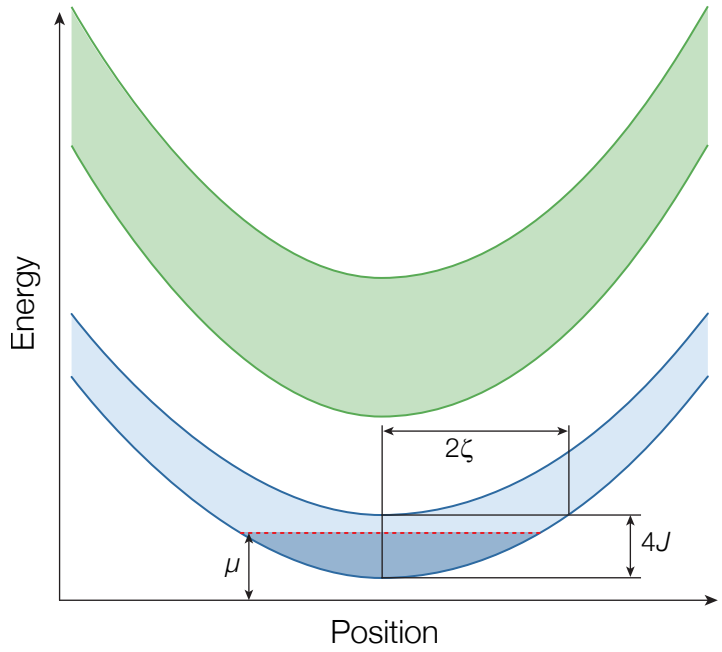

Figure B.3 – Illustration of the energy bands as a function of position for a combined harmonic and sinusoidal potential. The lattice energy bands are curved by the harmonic confinement, leading to a position-dependent filling factor for fermionic atoms.

As the variation of the confinement potential is very small on a lattice spacing scale, the system can be still regarded as locally homogenous. However, the filling factor of the energy bands becomes position-dependent, decreasing towards the trap edges as sketched in Fig. B.3. In the tight-biding limit, the fermion density and the momentum distribution can be expressed in terms of characteristic lengths ζ_μ in each direction, defined through $J = \frac{1}{2} M \omega_\mu^2 \zeta_\mu^2$, such that the filling factor for a given atom number N exclusively depends on $\zeta_x\, \zeta_y\, \zeta_z$ [292]. The filling factor can thus be varied by tuning the atom number N, the

tunnel coupling J and the trap frequencies ω_μ. When fermions interact in such a combined potential, different phases can coexist in the trap due to the radially varying filling factor [31]. Moreover, thermodynamical quantities are different from both their analogues in a homogenous lattice or in a purely harmonic potential [215, 216].

APPENDIX C

Clock laser stability

Short-term laser stability

The clock laser short-term stability could only be characterised by direct precision spectroscopy on cold atomic samples, since laser sources of similar stability were not available for heterodyne detection. As already mentioned in Section 3.4 and 5.1, an (infrared) laser frequency stability of around 20 Hz could be achieved over a time scale of several minutes, most likely not limited by the rigidity of the PDH phase lock but rather by short-term fluctuations of the ULE resonator and of the lock error signal offset, due for instance to light power fluctuations in the lock branch or etaloning. We can evaluate the performance of the lock by analysing the suppression of externally generated perturbations fed into the closed-loop circuit. Such a measurement is shown in Fig. C.1 and can be used to optimise the gain and the corner frequencies of the different integrator stages of the fast PID controller (Toptica FALC 110), used to regulate the laser frequency. For the measure-

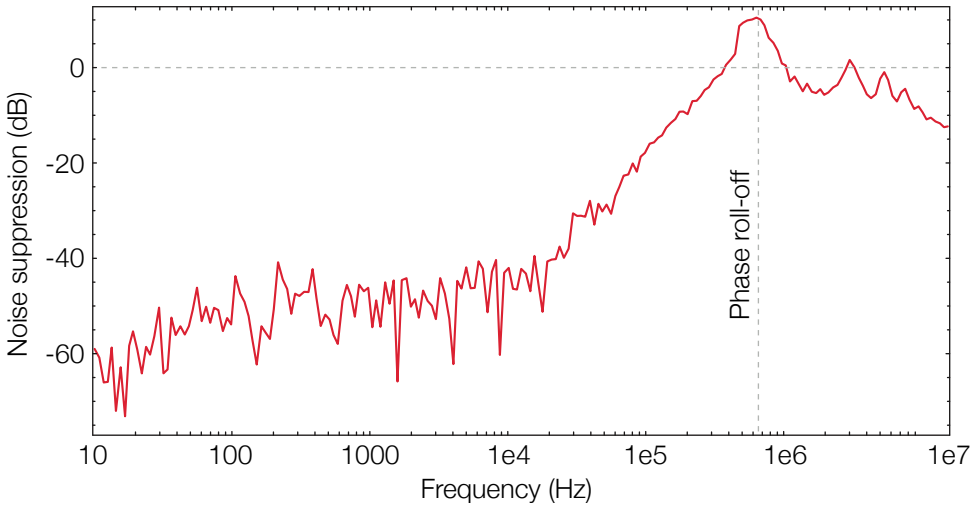

Figure C.1 – Closed-loop frequency noise suppression of the PDH lock to the ULE resonator. The measurement is performed using a network analyser, which injects a small disturbance in the closed loop through a power splitter, and analyses the response of the system in the PDH error signal. A region with large noise suppression extends to approximately 30 kHz, where the noise starts growing to reach the closed-loop pole located for this measurement at approximately 600 KHz. This frequency corresponds to the location of the phase roll-off of the closed-loop transfer function.

ment shown here, a servo bandwidth of above 600 kHz is realised; servo bandwidths as high as 1.1 MHz can be achieved by adjusting the PID fast integrator corner frequency, but a reduced noise suppression is obtained for such high-bandwidth settings. We instead optimised the settings of the feedback loop only to achieve the highest possible noise suppression below 100 kHz, which is the most relevant part of the spectrum affecting the laser linewidth [299].

Fiber-noise cancellation

An additional source of frequency noise are the mechanical and thermal disturbances which couple to the laser in the optical fiber, guiding the light from the laser optical table to the experiment one. A beat note measurement between two light beams following different paths, one of which includes a double passage in the 100 MHz AOM (see Fig. 3.14) and a back-and-forth passage in the optical fiber, is measured by a fast photodiode; the noise spectrum of the beat signal can therefore be analysed, as shown in Fig. C.3. A stable RF source (Abracon AOCJY-A-100MHz-SW OCXO with 1 Hz stability) is used to drive the AOM, preventing long term drifts. In addition, the beat signal may be locked to the stable RF source at double the AOM frequency, in order to narrow its linewidth by cancelling the fiber-induced noise. This is done by means of a phase-locked loop (PLL) and a PI controller; the spectrum of stabilised beat signal, shown in Fig. C.3, is clearly narrower. However, both the free-running and the locked beat signals FWHM are below the 10 Hz resolution of our spectrum analyser. One complication arises considering that the PLL error signal is generated only when the AOM is already powered, deflecting the light on the beam path aligned to the fiber input. The regulation has therefore a lag time before the lock point is found by the PI controller, but the use of a very high proportional gain guarantees a sufficiently quick engagement of the regulation. As the phase lock is properly functioning, it is highly likely that the actual stabilised beat linewidth is at the 1 Hz stability level of the RF source. With the 20 Hz laser stability currently achieved, unfortunately the noise canceller cannot be fully exploited but it could become a necessary resource if lower laser linewidths are achieved in the future.

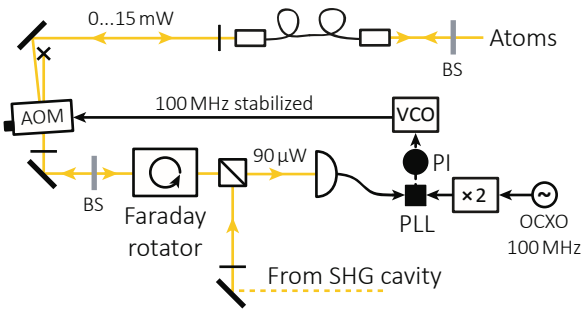

Figure C.2 – A schematic of the fiber-noise canceller. The frequency noise introduced in the optical fiber is detected through the beat note at twice the AOM frequency. The beat signal is stabilised to an 100 MHz OCXO source by means of a PLL circuit and a PI controller regulating a VCO with high modulation bandwidth, which drives then the AOM.

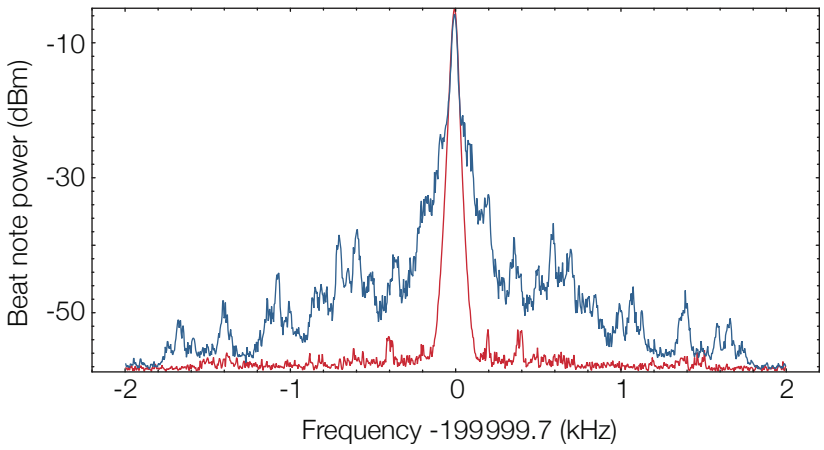

Figure C.3 – Beat signal between the two laser beam paths in the fiber-noise cancellation system. The measurement of the unstabilised beat signal (blue) FWHM is limited by the spectrum analyser resolution (the minimum resolution bandwidth of 10 Hz and a 40 s sweep time are used). A rather broad noise pedestal is however clearly present, extending over 1 kHz in each direction. The stabilised beat signal (red) is evidently narrower, but the dominant low-frequency noise could not be observed using the provided spectrum analyser. For both signals, the FWHM is smaller than 10 Hz and the fiber noise does therefore currently not limit the attainable short-term frequency stability of the clock light.

Long-term laser stability

The long-term stability of the clock laser frequency is dominated by ULE cavity drifts and possibly by PDH error signal drifts. Let us start by discussing possible sources of error signal drifts. Residual amplitude modulation (AM) by the fiber-coupled EOM, generating the PDH sidebands, is affecting the error signal offset and is caused by imperfect polarisation alignment to the EOM crystal axis [297]. It is well-known that birefringence in the crystal varies with temperature, and residual AM can therefore cause a temperature-dependent error signal offset fluctuation. For this reason, the EOM temperature is actively stabilised to 0.1°C, maintaining the residual AM as constant as possible over time. Other sources of unwanted PDH error signal offsets can be present, e.g. amplifiers introducing DC offsets or non-linearities in the feedback loop but they should be negligible compared to other effects. Etaloning between optical elements in the beam path to the ULE resonator can also cause error signal drifts, and could be minimised by replacing the PBS and quarter-wave plate arrangement with a Faraday isolator (see Fig. 3.16). Slow drifts of the resonator length are already stabilised to a high level, with uncontrolled drifts being on the order of only 100 Hz over a day scale. The drift of our cavity is regularly inspected by taking reference spectroscopic measurements. Such measurements are executed using very low-atom number samples of spin-polarised ^{173}Yb, minimising the effect of interactions and residual light shifts in the optical trap. Furthermore, two opposite spin states are probed in an alternated fashion while an external magnetic field is applied, and the centre between the two measured resonances is used as the zero-field transition frequency calibration. A typical several-day drift measurement is displayed in Fig. C.4. The drift is largely dominated by the ageing-related cavity length variation, which produces a linear

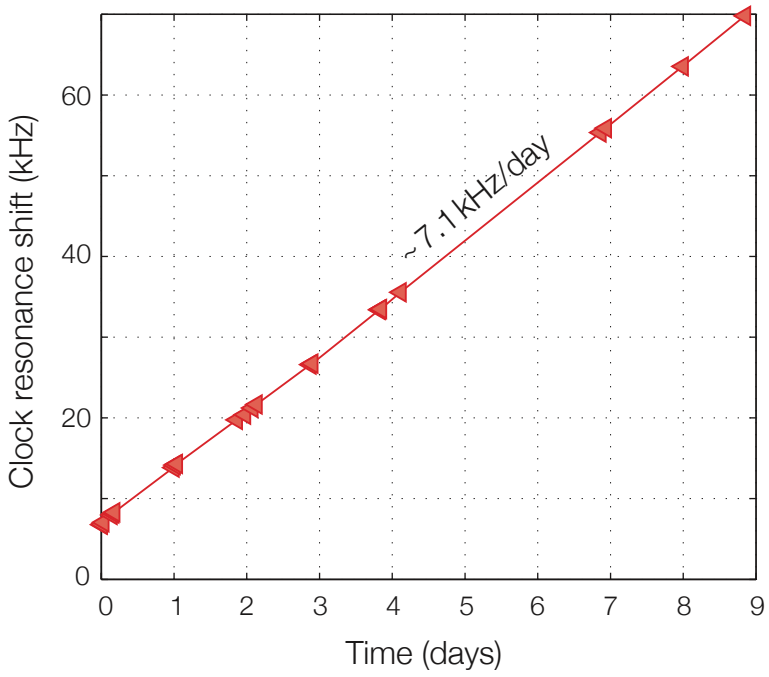

Figure C.4 – Linear drift of the ULE cavity frequency. Since the measured clock atomic resonance shifts linearly up in time, we can conclude that the cavity resonance is drifting up in frequency space, i.e. the resonator is shortening over time. The measured drift rate is +80 mHz/s, corresponding to approximately 2.5 Hz during a full experimental cycle.

and positive cavity frequency shift. This drift rate is constant at approximately 40 mHz/s over several-month scale, although seldom variations on the order of 10% were observed. Any shift of the infrared laser frequency doubles its value when observed as an atomic transition shift, probed by the frequency-doubled light, and we thus observe a resonance shift of approximately 80 mHz/s or 7.1 kHz/day. As the shift accumulated during a single experimental cycle equals roughly 2.5 Hz, it is very important to compensate it in order not to overestimate or underestimate the absorption lines position and widths. We do this by updating the frequency offset between our clock laser and the cavity reference during each experimental cycle, just before the spectroscopy pulse is applied. This offset is generated by the fiber-coupled EOM used for the PDH lock (see Fig. 3.11) and can be remotely controlled through the digital interface of a RF signal generator.

In order to suppress all other thermal and mechanical shifts of the ULE resonator length, the system is thoroughly isolated from the environment. Most importantly, the zero-crossing temperature of the linear thermal expansion coefficient (CTE) was experimentally determined by clock transition spectroscopy. Several measurements were performed at different resonator temperatures, letting the cavity settle during a certain equilibration time (typically a few days) after any regulation temperature change. The results are shown in Fig. C.5: the zero-crossing point of the CTE is found at $T_0 = 26.3(1)°\mathrm{C}$, and a very low residual temperature sensitivity at the minimum is fitted

$$\frac{\Delta\nu(T)}{\nu} \simeq= -4\times10^{-10}\,(T-T_0)^2\,\mathrm{K}^{-2}. \tag{C.1}$$

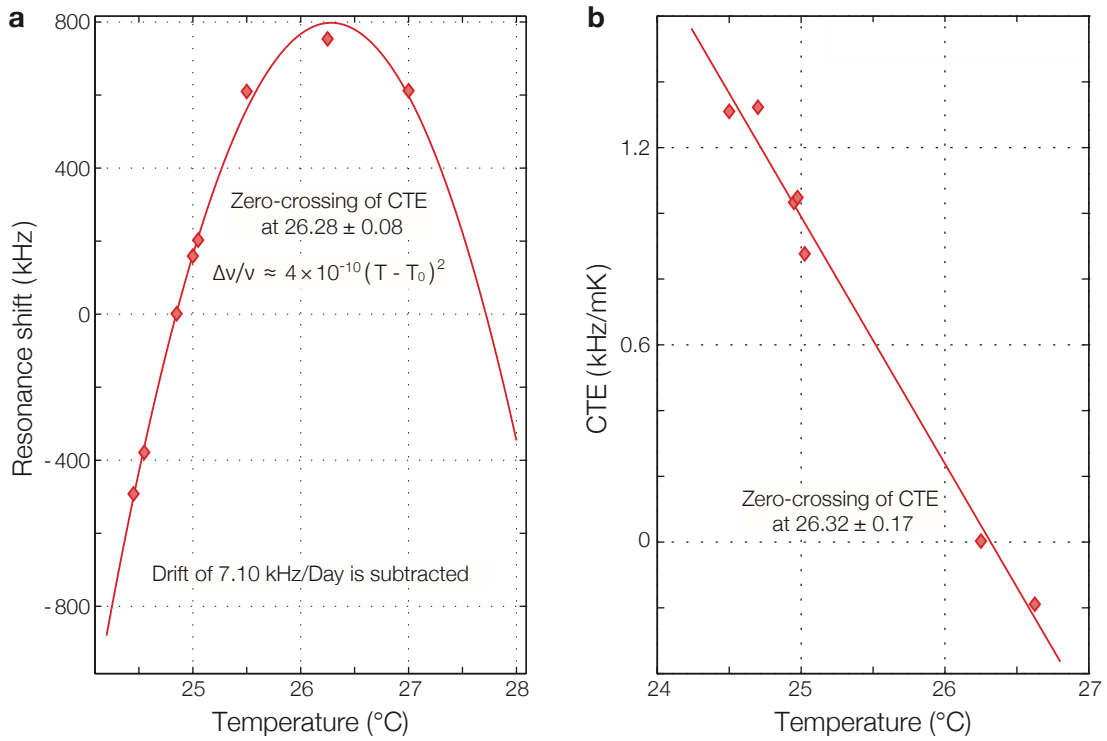

Figure C.5 – Characterization of the ULE cavity thermal expansion. The zero-linear expansion temperature $T_0 = 26.3(1)°C$ is found by spectroscopic characterisation of the thermal frequency shifts. (a) A plot of the measured steady-state frequency shifts at different resonator temperatures. A very low residual temperature sensitivity $\Delta\nu(T)/\nu$ around the zero-crossing temperature of the CTE was measured. (b) Direct estimation of the linear CTE dependence upon temperature. Data points represent the measured frequency shift slopes across several applied temperature steps. A linear fit to the measured frequency sensitivity is used as an alternative way to determine the zero-crossing of the linear CTE.

To give an idea of the realistic frequency stability of the resonator, the CTE equals 2 Hz/mK if the cavity is tuned 0.01°C away from T_0 and 25 Hz/mK if it is tuned 0.1°C away from T_0, which is fairly good in comparison to similar cavities [297]. We can therefore explain the observed 100 Hz absolute long-term stability, given the 5 mK resolution of our temperature controller. A higher-precision controller could improve the long-term stability, although environment temperature fluctuations might then become the dominant cause of slow drifts. In this case, temperature stabilisation of the entire ULE setup enclosure would be beneficial.

Bibliography

[1] H. K. Onnes. *Nobel Lecture: Investigations into the Properties of Substances at Low Temperatures, which Have Led, amongst Other Things, to the Preparation of Liquid Helium* (1913). See page: 1

[2] J. Bardeen, L. Cooper, and J. Schrieffer. *Theory of Superconductivity*. Phys. Rev. **108**, 1175–1204 (1957). See page: 1

[3] A. Damascelli, Z. Hussain, and Z.-X. Shen. *Angle-resolved photoemission studies of the cuprate superconductors*. Rev. Mod. Phys. **75**, 473–541 (2003). See page: 1

[4] P. Lee, N. Nagaosa, and X.-G. Wen. *Doping a Mott insulator: Physics of high-temperature superconductivity*. Rev. Mod. Phys. **78**, 17–85 (2006). See page: 1

[5] J. Hubbard. *Electron Correlations in Narrow Energy Bands*. Proc. R. Soc. A **276**, 238–257 (1963). See page: 1

[6] C. Beenakker. *Search for Majorana Fermions in Superconductors*. Ann. Rev. Cond. Mat. Phys. **4**, 113–136 (2013). See page: 1

[7] A. Stern. *Anyons and the quantum Hall effect - A pedagogical review*. Ann. Phys. **323**, 204–249 (2008). See page: 1

[8] R. P. Feynman. *Simulating physics with computers*. Int. J. Theor. Phys. **21**, 467–488 (1982). See page: 2

[9] I. Buluta and F. Nori. *Quantum Simulators*. Science **326**, 108–111 (2009). See page: 2

[10] A. Aspuru-Guzik and P. Walther. *Photonic quantum simulators*. Nature Phys. **8**, 285–291 (2012).

[11] R. Blatt and C. F. Roos. *Quantum simulations with trapped ions*. Nature Phys. **8**, 277–284 (2012).

[12] I. Bloch, J. Dalibard, and S. Nascimbène. *Quantum simulations with ultracold quantum gases*. Nature Phys. **8**, 267–276 (2012). See pages: 2, 34

[13] A. A. Houck, H. E. Tureci, and J. Koch. *On-chip quantum simulation with superconducting circuits*. Nature Phys. **8**, 292–299 (2012). See page: 2

[14] I. Bloch, J. Dalibard, and W. Zwerger. *Many-body physics with ultracold gases*. Rev. Mod. Phys. **80**, 885–964 (2008). See pages: 2, 3, 14, 17, 108, 109, 182

[15] H. J. Metcalf and P. Van der Straten. *Laser cooling and trapping*. Springer, New York (1999). See pages: 2, 61, 176

[16] M. H. Anderson, J. R. Ensher, M. R. Matthews, C. E. Wieman, and E. A. Cornell. *Observation of Bose-Einstein Condensation in a Dilute Atomic Vapor*. Science **269**, 198–201 (1995). See page: 2

[17] K. Davis, M. Mewes, M. Andrews, N. van Druten, D. Durfee, D. Kurn, and W. Ketterle. *Bose-Einstein Condensation in a Gas of Sodium Atoms*. Phys. Rev. Lett. **75**, 3969–3973 (1995). See page: 2

[18] B. DeMarco and D. S. Jin. *Onset of Fermi Degeneracy in a Trapped Atomic Gas*. Science **285**, 1703–1706 (1999). See page: 2

[19] S. Giorgini, L. P. Pitaevskii, and S. Stringari. *Theory of ultracold atomic Fermi gases*. Rev. Mod. Phys. **80**, 1215–1274 (2008). See pages: 3, 73, 74, 185, 186

[20] C. Chin, R. Grimm, P. Julienne, and E. Tiesinga. *Feshbach resonances in ultracold gases*. Rev. Mod. Phys. **82**, 1225–1286 (2010). See pages: 3, 20, 21, 24, 26, 158

[21] D. Jaksch, C. Bruder, J. I. Cirac, C. W. Gardiner, and P. Zoller. *Cold Bosonic Atoms in Optical Lattices*. Phys. Rev. Lett. **81**, 3108–3111 (1998). See pages: 3, 17

[22] M. Greiner, O. Mandel, T. Esslinger, T. W. Hänsch, and I. Bloch. *Quantum phase transition from a superfluid to a Mott insulator in a gas of ultracold atoms*. Nature **415**, 39–44 (2002). See pages: 3, 76

[23] M. Greiner and S. Fölling. *Condensed-matter physics: Optical lattices*. Nature **453**, 736–738 (2008). See pages: 3, 14, 15

[24] B. Paredes, A. Widera, V. Murg, O. Mandel, S. Fölling, I. Cirac, G. V. Shlyapnikov, T. W. Hänsch, and I. Bloch. *Tonks-Girardeau gas of ultracold atoms in an optical lattice*. Nature **429**, 277–281 (2004). See pages: 3, 15, 151

[25] T. Kinoshita, T. Wenger, and D. S. Weiss. *Observation of a One-Dimensional Tonks-Girardeau Gas*. Science **305**, 1125–1128 (2004). See page: 3

[26] S. Fölling, S. Trotzky, P. Cheinet, M. Feld, R. Saers, A. Widera, T. Müller, and I. Bloch. *Direct observation of second-order atom tunnelling*. Nature **448**, 1029–1032 (2007). See page: 3

[27] S. Trotzky, P. Cheinet, S. Fölling, M. Feld, U. Schnorrberger, A. M. Rey, A. Polkovnikov, E. A. Demler, M. D. Lukin, and I. Bloch. *Time-Resolved Observation and Control of Superexchange Interactions with Ultracold Atoms in Optical Lattices*. Science **319**, 295–299 (2008). See pages: 42, 43

[28] D. Greif, T. Uehlinger, G. Jotzu, L. Tarruell, and T. Esslinger. *Short-Range Quantum Magnetism of Ultracold Fermions in an Optical Lattice*. Science **340**, 1307–1310 (2013). See pages: 3, 42

[29] J. K. Chin, D. E. Miller, Y. Liu, C. Stan, W. Setiawan, C. Sanner, K. Xu, and W. Ketterle. *Evidence for superfluidity of ultracold fermions in an optical lattice*. Nature **443**, 961–964 (2006). See page: 3

[30] M. Köhl, H. Moritz, T. Stöferle, K. Günter, and T. Esslinger. *Fermionic Atoms in a Three Dimensional Optical Lattice: Observing Fermi Surfaces, Dynamics, and Interactions*. Phys. Rev. Lett. **94**, 080403 (2005). See pages: 3, 42, 43, 109

[31] U. Schneider, L. Hackermüller, S. Will, T. Best, I. Bloch, T. A. Costi, R. W. Helmes, D. Rasch, and A. Rosch. *Metallic and Insulating Phases of Repulsively Interacting Fermions in a 3D Optical Lattice*. Science **322**, 1520–1525 (2008). See pages: 3, 41, 42, 43, 44, 77, 189

[32] R. Jördens, N. Strohmaier, K. Günter, H. Moritz, and T. Esslinger. *A Mott insulator of fermionic atoms in an optical lattice*. Nature **455**, 204–207 (2008). See page: 3

[33] C. Becker, P. Soltan-Panahi, J. Kronjäger, S. Dörscher, K. Bongs, and K. Sengstock. *Ultracold quantum gases in triangular optical lattices*. New J. Phys. **12**, 065025 (2010). See pages: 3, 16

[34] P. Soltan-Panahi, J. Struck, P. Hauke, A. Bick, W. Plenkers, G. Meineke, C. Becker, P. Windpassinger, M. Lewenstein, and K. Sengstock. *Multi-component quantum gases in spin-dependent hexagonal lattices*. Nature Phys. **7**, 434–440 (2011).

[35] L. Tarruell, D. Greif, T. Uehlinger, G. Jotzu, and T. Esslinger. *Creating, moving and merging Dirac points with a Fermi gas in a tunable honeycomb lattice*. Nature **483**, 302–305 (2012). See page: 16

[36] G.-B. Jo, J. Guzman, C. K. Thomas, P. Hosur, A. Vishwanath, and D. M. Stamper-Kurn. *Ultracold Atoms in a Tunable Optical Kagome Lattice*. Phys. Rev. Lett. **108**, 045305 (2012). See pages: 3, 16

[37] S. Fölling, F. Gerbier, A. Widera, O. Mandel, T. Gericke, and I. Bloch. *Spatial quantum noise interferometry in expanding ultracold atom clouds*. Nature **434**, 481–484 (2005). See pages: 3, 43

[38] T. Rom, T. Best, D. van Oosten, U. Schneider, S. Fölling, B. Paredes, and I. Bloch. *Free fermion antibunching in a degenerate atomic Fermi gas released from an optical lattice*. Nature **444**, 733–736 (2006). See page: 3

[39] G. K. Campbell, J. Mun, M. Boyd, P. Medley, A. E. Leanhardt, L. G. Marcassa, D. E. Pritchard, and W. Ketterle. *Imaging the Mott Insulator Shells by Using Atomic Clock Shifts*. Science **313**, 649–652 (2006). See pages: 3, 11, 43

[40] S. Fölling, A. Widera, T. Müller, F. Gerbier, and I. Bloch. *Formation of Spatial Shell Structure in the Superfluid to Mott Insulator Transition*. Phys. Rev. Lett. **97**, 060403 (2006). See pages: 11, 43, 153

[41] P. T. Ernst, S. Gotze, J. S. Krauser, K. Pyka, D.-S. Luhmann, D. Pfannkuche, and K. Sengstock. *Probing superfluids in optical lattices by momentum-resolved Bragg spectroscopy*. Nature Phys. **6**, 56–61 (2010). See page: 3

[42] J. F. Sherson, C. Weitenberg, M. Endres, M. Cheneau, I. Bloch, and S. Kuhr. *Single-atom-resolved fluorescence imaging of an atomic Mott insulator*. Nature **467**, 68–72 (2010). See pages: 3, 15

[43] W. S. Bakr, A. Peng, M. E. Tai, R. Ma, J. Simon, J. I. Gillen, S. Fölling, L. Pollet, and M. Greiner. *Probing the Superfluid–to–Mott Insulator Transition at the Single-Atom Level*. Science **329**, 547–550 (2010). See pages: 3, 15

[44] C. Weitenberg, M. Endres, J. F. Sherson, M. Cheneau, P. Schauß, T. Fukuhara, I. Bloch, and S. Kuhr. *Single-spin addressing in an atomic Mott insulator*. Nature **471**, 319–324 (2011). See page: 3

[45] A. Polkovnikov, K. Sengupta, A. Silva, and M. Vengalattore. *Colloquium : Nonequilibrium dynamics of closed interacting quantum systems*. Rev. Mod. Phys. **83**, 863–883 (2011). See page: 3

[46] J. Dalibard, F. Gerbier, G. Juzeliūnas, and P. Öhberg. *Colloquium: Artificial gauge potentials for neutral atoms*. Rev. Mod. Phys. **83**, 1523–1543 (2011). See pages: 3, 12, 19, 173

[47] N. Goldman, G. Juzeliūnas, P. Öhberg, and I. B. Spielman. *Light-induced gauge fields for ultracold atoms*. Rep. Progr. Phys. **77**, 126401 (2014). See pages: 3, 173

[48] T. Lahaye, C. Menotti, L. Santos, M. Lewenstein, and T. Pfau. *The physics of dipolar bosonic quantum gases*. Rep. Progr. Phys. **72**, 126401 (2009). See page: 3

[49] M. Takamoto, F.-L. Hong, R. Higashi, and H. Katori. *An optical lattice clock*. Nature **435**, 321–324 (2005). See pages: 4, 14, 19, 125, 128

[50] B. J. Bloom, T. L. Nicholson, J. R. Williams, S. L. Campbell, M. Bishof, X. Zhang, W. Zhang, S. L. Bromley, and J. Ye. *An optical lattice clock with accuracy and stability at the 10^{-18} level*. Nature **506**, 71–75 (2014). See pages: 4, 11

[51] N. Hinkley, J. A. Sherman, N. B. Phillips, M. Schioppo, N. D. Lemke, K. Beloy, M. Pizzocaro, C. W. Oates, and A. D. Ludlow. *An atomic clock with 10^{-18} instability*. Science **341**, 1215–1218 (2013). See pages: 4, 11, 125

[52] Y. Takasu, K. Maki, K. Komori, T. Takano, K. Honda, M. Kumakura, T. Yabuzaki, and Y. Takahashi. *Spin-Singlet Bose-Einstein Condensation of Two-Electron Atoms*. Phys. Rev. Lett. **91**, 040404 (2003). See pages: 4, 34, 47, 79

[53] M. Cazalilla, A. Ho, and M. Ueda. *Ultracold gases of ytterbium: Ferromagnetism and Mott states in an SU (6) Fermi system*. New J. Phys. **11**, 103033 (2009). See pages: 4, 9, 28, 29, 30, 45, 119, 172

[54] M. Hermele, V. Gurarie, and A. M. Rey. *Mott Insulators of Ultracold Fermionic Alkaline Earth Atoms: Underconstrained Magnetism and Chiral Spin Liquid*. Phys. Rev. Lett. **103**, 135301 (2009). See pages: 10, 45, 46, 171, 172

[55] A. V. Gorshkov, M. Hermele, V. Gurarie, C. Xu, P. S. Julienne, J. Ye, P. Zoller, E. Demler, M. D. Lukin, and A. M. Rey. *Two-orbital SU(N) magnetism with ultracold alkaline-earth atoms*. Nature Phys. **6**, 289–295 (2010). See pages: 4, 5, 9, 10, 11, 19, 20, 27, 28, 30, 31, 32, 34, 37, 39, 42, 43, 45, 46, 119, 120, 143, 171, 172

[56] A. J. Daley, M. M. Boyd, J. Ye, and P. Zoller. *Quantum Computing with alkaline-earth-metal atoms*. Phys. Rev. Lett. **101**, 170504 (2008). See pages: 4, 9, 13, 17, 18, 19, 42, 57, 58, 170

[57] W. Yi, A. J. Daley, G. Pupillo, and P. Zoller. *State-dependent, addressable subwavelength lattices with cold atoms*. New J. Phys. **10**, 073015 (2008). See page: 19

[58] K. Shibata, S. Kato, A. Yamaguchi, S. Uetake, and Y. Takahashi. *A scalable quantum computer with ultranarrow optical transition of ultracold neutral atoms in an optical lattice*. Appl. Phys. B **97**, 753–758 (2009). See pages: 9, 57

[59] A. V. Gorshkov, A. M. Rey, A. J. Daley, M. M. Boyd, J. Ye, P. Zoller, and M. D. Lukin. *Alkaline-earth-metal atoms as few-qubit quantum registers*. Phys. Rev. Lett. **102**, 110503 (2009). See pages: 4, 9, 13, 33, 35, 117

[60] M. Foss-Feig, M. Hermele, and A. M. Rey. *Probing the Kondo lattice model with alkaline-earth-metal atoms*. Phys. Rev. A **81**, 051603(R) (2010). See pages: 4, 5, 9, 10, 19, 34, 42

[61] M. Foss-Feig, M. Hermele, V. Gurarie, and A. M. Rey. *Heavy fermions in an optical lattice*. Phys. Rev. A **82**, 053624 (2010). See pages: 4, 5, 9, 10, 19, 34, 35, 42, 43

[62] M. Hermele and V. Gurarie. *Topological liquids and valence cluster states in two-dimensional SU(N) magnets*. Phys. Rev. B **84**, 174441 (2011). See pages: 4, 35, 45, 46, 172

[63] M. A. Cazalilla and A. M. Rey. *Ultracold Fermi gases with emergent SU(N) symmetry*. Rep. Progr. Phys. **77**, 124401 (2014). See pages: 4, 28, 29, 30, 45, 46, 119, 172

[64] F. Gerbier and J. Dalibard. *Gauge fields for ultracold atoms in optical superlattices*. New J. Phys. **12**, 033007 (2010). See pages: 4, 9, 12, 19, 125, 173

[65] T. Fukuhara, Y. Takasu, M. Kumakura, and Y. Takahashi. *Degenerate Fermi Gases of Ytterbium*. Phys. Rev. Lett. **98**, 030401 (2007). See pages: 4, 34, 47

[66] T. Fukuhara, S. Sugawa, Y. Takasu, and Y. Takahashi. *All-optical formation of quantum degenerate mixtures*. Phys. Rev. A **79**, 021601 (2009). See pages: 48, 53, 59

[67] S. Kraft, F. Vogt, O. Appel, F. Riehle, and U. Sterr. *Bose-Einstein Condensation of Alkaline Earth Atoms:* ^{40}Ca. Phys. Rev. Lett. **103**, 130401 (2009).

[68] S. Stellmer, M. K. Tey, B. Huang, R. Grimm, and F. Schreck. *Bose-Einstein Condensation of Strontium*. Phys. Rev. Lett. **103**, 200401 (2009).

[69] Y. N. M. de Escobar, P. G. Mickelson, M. Yan, B. J. DeSalvo, S. B. Nagel, and T. C. Killian. *Bose-Einstein Condensation of* ^{84}Sr. Phys. Rev. Lett. **103**, 200402 (2009).

[70] B. J. DeSalvo, M. Yan, P. G. Mickelson, Y. N. Martinez de Escobar, and T. C. Killian. *Degenerate Fermi Gas of* ^{87}*Sr*. Phys. Rev. Lett. **105**, 030402 (2010).

[71] S. Taie, Y. Takasu, S. Sugawa, R. Yamazaki, T. Tsujimoto, R. Murakami, and Y. Takahashi. *Realization of a SU(2)×SU(6) system of fermions in a cold atomic gas*. Phys. Rev. Lett. **105**, 190401 (2010). See pages: 4, 34, 47, 48, 54, 59, 111, 116

[72] S. Taie, R. Yamazaki, S. Sugawa, and Y. Takahashi. *An SU(6) Mott insulator of an atomic Fermi gas realized by large-spin Pomeranchuk cooling*. Nature Phys. **8**, 825–830 (2012). See pages: 4, 30, 46, 116, 158

[73] G. Pagano, M. Mancini, G. Cappellini, P. Lombardi, F. Schäfer, H. Hu, X.-J. Liu, J. Catani, C. Sias, M. Inguscio, et al. *A one-dimensional liquid of fermions with tunable spin*. Nature Phys. **10**, 198–201 (2014). See pages: 4, 29, 46, 116, 172

[74] A. Rapp, G. Zaránd, C. Honerkamp, and W. Hofstetter. *Color Superfluidity and "Baryon" Formation in Ultracold Fermions*. Phys. Rev. Lett. **98**, 160405 (2007). See pages: 5, 27, 28, 30

[75] G. R. Stewart. *Heavy-fermion systems*. Rev. Mod. Phys. **56**, 755–787 (1984). See pages: 5, 36, 145

[76] P. Coleman. *Heavy Fermions: Electrons at the Edge of Magnetism. Handbook of Magnetism and Advanced Magnetic Materials*, Volume 1, pages 95–148. Wiley, New York (2007). See pages: 5, 34, 35, 36, 37, 38, 39, 42, 44

[77] P. Gegenwart, Q. Si, and F. Steglich. *Quantum criticality in heavy-fermion metals*. Nature Phys. **4**, 186–197 (2008). See pages: 5, 36, 37, 145

[78] Y. Tokura and N. Nagaosa. *Orbital Physics in Transition-Metal Oxides*. Science **288**, 462–468 (2000). See pages: 5, 36, 37, 45

[79] J. Van den Brink, G. Khaliullin, and D. Khomskii. *Orbital Effects in Manganites*. In *Colossal Magnetoresistive Manganites*, pages 263–301. Springer, Netherlands (2004). See pages: 5, 35, 36, 37

[80] H. v. Löhneysen, A. Rosch, M. Vojta, and P. Wölfle. *Fermi-liquid instabilities at magnetic quantum phase transitions*. Rev. Mod. Phys. **79**, 1015–1075 (2007). See pages: 5, 36, 37, 186

[81] N. D. Mathur, F. M. Grosche, S. R. Julian, I. R. Walker, D. M. Freye, R. K. W. Haselwimmer, and G. G. Lonzarich. *Magnetically mediated superconductivity in heavy fermion compounds*. Nature **394**, 39–43 (1998). See pages: 5, 36, 37

[82] C. Pfleiderer. *Superconducting phases of f-electron compounds*. Rev. Mod. Phys. **81**, 1551–1624 (2009). See pages: 5, 36

[83] D. Hayes, P. Julienne, and I. Deutsch. *Quantum Logic via the Exchange Blockade in Ultracold Collisions*. Phys. Rev. Lett. **98**, 070501 (2007). See pages: 9, 13, 35, 173

[84] N. R. Cooper. *Optical Flux Lattices for Ultracold Atomic Gases*. Phys. Rev. Lett. **106**, 175301 (2011). See pages: 9, 12, 19

[85] D. Banerjee, M. Bögli, M. Dalmonte, E. Rico, P. Stebler, U.-J. Wiese, and P. Zoller. *Atomic quantum simulation of U(N) and SU(N) non-abelian lattice gauge theories*. Phys. Rev. Lett. **110**, 125303 (2013). See pages: 9, 28, 30

[86] C. J. Foot. *Atomic physics*. Oxford University Press, Oxford (2004). See pages: 10, 49, 54, 55, 108, 115

[87] S. Stellmer, R. Grimm, and F. Schreck. *Production of quantum-degenerate strontium gases*. Phys. Rev. A **87**, 013611 (2013). See pages: 10, 46, 47, 70, 172

[88] S. Dörscher. *Creation of ytterbium quantum gases with a compact 2D-/3D-MOT setup*. PhD thesis, University of Hamburg, Hamburg (2013). See pages: 11, 65

[89] A. Derevianko and H. Katori. *Colloquium: Physics of optical lattice clocks*. Rev. Mod. Phys. **83**, 331–347 (2011). See pages: 11, 14, 19

[90] A. D. Ludlow, M. M. Boyd, J. Ye, E. Peik, and P. O. Schmidt. *Optical Atomic Clocks*. Preprint at arxiv.org/abs/1407.3493 (to appear on Rev. Mod. Phys.) (2014). See pages: 11, 13, 19, 52, 59, 125, 175

[91] S. Kato, S. Sugawa, K. Shibata, R. Yamamoto, and Y. Takahashi. *Control of Resonant Interaction between Electronic Ground and Excited States*. Phys. Rev. Lett. **110**, 173201 (2013). See pages: 11, 59

[92] H. Ott, E. de Mirandes, F. Ferlaino, G. Roati, V. Türck, G. Modugno, and M. Inguscio. *Radio Frequency Selective Addressing of Localized Atoms in a Periodic Potential*. Phys. Rev. Lett. **93**, 120407 (2004). See pages: 11, 43, 77, 188

[93] A. Yamaguchi, S. Uetake, S. Kato, H. Ito, and Y. Takahashi. *High-resolution laser spectroscopy of a Bose–Einstein condensate using the ultranarrow magnetic quadrupole transition*. New J. Phys. **12**, 103001 (2010).

[94] M. Bishof, Y. Lin, M. Swallows, A. Gorshkov, J. Ye, and A. Rey. *Resolved Atomic Interaction Sidebands in an Optical Clock Transition*. Phys. Rev. Lett. **106**, 250801 (2011).

[95] M. Yamashita, S. Kato, A. Yamaguchi, S. Sugawa, T. Fukuhara, S. Uetake, and Y. Takahashi. *Strongly interacting array of Bose-Einstein condensates trapped in a one-dimensional optical lattice*. Phys. Rev. A **87**, 041604 (2013). See page: 11

[96] M. M. Boyd, T. Zelevinsky, A. D. Ludlow, S. Blatt, T. Zanon-Willette, S. M. Foreman, and J. Ye. *Nuclear spin effects in optical lattice clocks*. Phys. Rev. A **76**, 022510 (2007). See pages: 11, 12, 27, 31, 33, 52, 54, 125, 135, 136, 143

[97] D. A. Steck. *Quantum and Atom Optics*. Available online at http://steck.us/teaching (Revision 0.10.0, 3 September 2014). See pages: 11, 13, 14, 25, 108, 124, 128, 175

[98] A. Taichenachev, V. Yudin, C. Oates, C. Hoyt, Z. Barber, and L. Hollberg. *Magnetic Field-Induced Spectroscopy of Forbidden Optical Transitions with Application to Lattice-Based Optical Atomic Clocks*. Phys. Rev. Lett. **96**, 083001 (2006). See pages: 12, 57

[99] Z. W. Barber, C. W. Hoyt, C. W. Oates, L. Hollberg, A. V. Taichenachev, and V. I. Yudin. *Direct Excitation of the Forbidden Clock Transition in Neutral* ^{174}Yb *Atoms Confined to an Optical Lattice*. Phys. Rev. Lett. **96**, 083002 (2006). See pages: 12, 57

[100] V. D. Ovsiannikov, V. G. Pal'chikov, A. V. Taichenachev, V. I. Yudin, H. Katori, and M. Takamoto. *Magic-wave-induced* $^1S_0$-$^3P_0$ *transition in even isotopes of alkaline-earth-metal-like atoms*. Phys. Rev. A **75**, 020501 (2007). See pages: 12, 57

[101] Y. J. Lin, K. Jimenez-Garcia, and I. B. Spielman. *Spin-orbit-coupled Bose-Einstein condensates*. Nature **471**, 83–86 (2011). See pages: 12, 117

[102] A. Celi, P. Massignan, J. Ruseckas, N. Goldman, I. B. Spielman, G. Juzeliūnas, and M. Lewenstein. *Synthetic Gauge Fields in Synthetic Dimensions*. Phys. Rev. Lett. **112**, 043001 (2014). See pages: 12, 173

[103] A. D. Cronin, J. Schmiedmayer, and D. E. Pritchard. *Optics and interferometry with atoms and molecules*. Rev. Mod. Phys. **81**, 1051–1129 (2009). See pages: 13, 14

[104] A. Daley, J. Ye, and P. Zoller. *State-dependent lattices for quantum computing with alkaline-earth-metal atoms*. Eur. Phys. J. D **65**, 207–217 (2011). See pages: 13, 19

[105] A. J. Daley. *Quantum computing and quantum simulation with group-II atoms*. Quantum Inf. Process. **10**, 865–884 (2011). See pages: 13, 57

[106] A. Noguchi, Y. Eto, M. Ueda, and M. Kozuma. *Quantum-state tomography of a single nuclear spin qubit of an optically manipulated ytterbium atom*. Phys. Rev. A **84**, 030301 (2011). See page: 13

[107] R. Grimm, M. Weidemüller, and Y. B. Ovchinnikov. *Optical Dipole Traps for Neutral Atoms*. Adv. At. Mol. Opt. Phys. **42**, 95–170 (2000). See pages: 13, 14, 16

[108] S. Chu, J. E. Bjorkholm, A. Ashkin, and A. Cable. *Experimental Observation of Optically Trapped Atoms*. Phys. Rev. Lett. **57**, 314–317 (1986). See page: 14

[109] D. M. Stamper-Kurn, M. R. Andrews, A. P. Chikkatur, S. Inouye, H.-J. Miesner, J. Stenger, and W. Ketterle. *Optical Confinement of a Bose-Einstein Condensate*. Phys. Rev. Lett. **80**, 2027–2030 (1998). See pages: 14, 111

[110] N. L. Smith, W. H. Heathcote, G. Hechenblaikner, E. Nugent, and C. J. Foot. *Quasi-2D confinement of a BEC in a combined optical and magnetic potential*. J. Phys. B **38**, 223 (2005). See page: 14

[111] L. Corman, L. Chomaz, T. Bienaimé, R. Desbuquois, C. Weitenberg, S. Nascimbène, J. Dalibard, and J. Beugnon. *Quench-Induced Supercurrents in an Annular Bose Gas*. Phys. Rev. Lett. **113**, 135302 (2014). See page: 14

[112] A. Gaunt, T. Schmidutz, I. Gotlibovych, R. Smith, and Z. Hadzibabic. *Bose-Einstein Condensation of Atoms in a Uniform Potential*. Phys. Rev. Lett. **110**, 200406 (2013). See page: 14

[113] D. Jaksch, H.-J. Briegel, J. I. Cirac, C. W. Gardiner, and P. Zoller. *Entanglement of Atoms via Cold Controlled Collisions*. Phys. Rev. Lett. **82**, 1975–1978 (1999). See pages: 14, 18

[114] O. Mandel, M. Greiner, A. Widera, T. Rom, T. W. Hänsch, and I. Bloch. *Controlled collisions for multi-particle entanglement of optically trapped atoms*. Nature **425**, 937–940 (2003).

[115] L.-M. Duan, E. Demler, and M. D. Lukin. *Controlling Spin Exchange Interactions of Ultracold Atoms in Optical Lattices*. Phys. Rev. Lett. **91**, 090402 (2003). See pages: 35, 173

[116] M. Anderlini, P. J. Lee, B. L. Brown, J. Sebby-Strabley, W. D. Phillips, and J. V. Porto. *Controlled exchange interaction between pairs of neutral atoms in an optical lattice*. Nature **448**, 452–456 (2007). See pages: 14, 18, 35, 158, 173

[117] J. J. Sakurai and S. F. Tuan. *Modern quantum mechanics*. Addison-Wesley Reading, Massachusetts (1985). See pages: 15, 16, 21, 22, 25, 176, 180

[118] N. Ashcroft and N. Mermin. *Solid State Physics*. Thomson Learning, New York (1976). See pages: 15, 16, 36, 37, 45, 180

[119] T. Stöferle, H. Moritz, C. Schori, M. Köhl, and T. Esslinger. *Transition from a Strongly Interacting 1D Superfluid to a Mott Insulator*. Phys. Rev. Lett. **92**, 130403 (2004). See page: 15

[120] O. Mandel, M. Greiner, A. Widera, T. Rom, T. W. Hänsch, and I. Bloch. *Coherent Transport of Neutral Atoms in Spin-Dependent Optical Lattice Potentials*. Phys. Rev. Lett. **91**, 010407 (2003). See page: 18

[121] Z. W. Barber, J. E. Stalnaker, N. D. Lemke, N. Poli, C. W. Oates, T. M. Fortier, S. A. Diddams, L. Hollberg, C. W. Hoyt, A. V. Taichenachev, and V. I. Yudin. *Optical lattice induced light shifts in an Yb atomic clock*. Phys. Rev. Lett. **100**, 103002 (2008). See pages: 19, 51, 124, 125, 126, 127, 129, 130

[122] N. D. Lemke, A. D. Ludlow, Z. W. Barber, T. M. Fortier, S. A. Diddams, Y. Jiang, S. R. Jefferts, T. P. Heavner, T. E. Parker, and C. W. Oates. *Spin-1/2 Optical Lattice Clock*. Phys. Rev. Lett. **103**, 063001 (2009). See pages: 19, 33, 54, 56, 58, 125, 126, 130, 136

[123] J. McKeever, J. R. Buck, A. D. Boozer, A. Kuzmich, H.-C. Nägerl, D. M. Stamper-Kurn, and H. J. Kimble. *State-Insensitive Cooling and Trapping of Single Atoms in an Optical Cavity*. Phys. Rev. Lett. **90**, 133602 (2003). See page: 19

[124] F. Scazza, C. Hofrichter, M. Höfer, P. C. De Groot, I. Bloch, and S. Fölling. *Observation of two-orbital spin-exchange interactions with ultracold SU(N)-symmetric fermions*. Nature Phys. (2014). See pages: 19, 41, 46, 59, 60, 139, 141, 142, 143, 148, 150, 154, 155, 159, 161, 169

[125] C. Schweizer. *A bi-chromatic optical lattice setup for Kondo-lattice physics with ultracold ytterbium atoms*. Master's thesis, Ludwig-Maximilians-Universität, München (2013). See pages: 19, 42, 89, 96, 106, 170

[126] J. T. Stewart, J. P. Gaebler, and D. S. Jin. *Using photoemission spectroscopy to probe a strongly interacting Fermi gas*. Nature **454**, 744–747 (2008). See page: 19

[127] S. Doniach. *The Kondo lattice and weak antiferromagnetism*. Physica B **91**, 231 – 234 (1977). See pages: 19, 34, 35, 37, 145

[128] K. I. Kugel' and D. I. Khomskiĭ. *Crystal structure and magnetic properties of substances with orbital degeneracy*. J. Exp. Theor. Phys. **37**, 725–730 (1973). See pages: 19, 34, 35, 37, 145

[129] L. J. LeBlanc and J. H. Thywissen. *Species-specific optical lattices*. Phys. Rev. A **75**, 053612 (2007). See page: 20

[130] J. Catani, G. Barontini, G. Lamporesi, F. Rabatti, G. Thalhammer, F. Minardi, S. Stringari, and M. Inguscio. *Entropy Exchange in a Mixture of Ultracold Atoms*. Phys. Rev. Lett. **103**, 140401 (2009). See page: 20

[131] J. Weiner, V. S. Bagnato, S. Zilio, and P. S. Julienne. *Experiments and theory in cold and ultracold collisions*. Rev. Mod. Phys. **71**, 1–85 (1999). See pages: 21, 23, 24, 69, 70

[132] T. D. Lee, K. Huang, and C. N. Yang. *Eigenvalues and eigenfunctions of a Bose system of hard spheres and its low-temperature properties*. Phys. Rev. **106**, 1135–1145 (1957). See page: 22

[133] T. Busch, B. Englert, K. Rzążewski, and M. Wilkens. *Two cold atoms in a harmonic trap*. Found. Phys. **28**, 549–559 (1998). See pages: 23, 151, 158

[134] P. O. Fedichev, M. W. Reynolds, and G. V. Shlyapnikov. *Three-Body Recombination of Ultracold Atoms to a Weakly Bound s Level*. Phys. Rev. Lett. **77**, 2921–2924 (1996). See pages: 23, 70

[135] H. T. C. Stoof, J. M. V. A. Koelman, and B. J. Verhaar. *Spin-exchange and dipole relaxation rates in atomic hydrogen: Rigorous and simplified calculations*. Phys. Rev. B **38**, 4688 (1988). See pages: 24, 162

[136] S. Dürr, J. Garcia-Ripoll, N. Syassen, D. Bauer, M. Lettner, J. Cirac, and G. Rempe. *Lieb-Liniger model of a dissipation-induced Tonks-Girardeau gas*. Phys. Rev. A **79**, 023614 (2009). See pages: 24, 162

[137] N. F. Mott and H. S. W. Massey. *The theory of atomic collisions*, Volume 35. Clarendon Press, Oxford (1965). See page: 24

[138] J. L. Bohn and P. S. Julienne. *Prospects for influencing scattering lengths with far-off-resonant light*. Phys. Rev. A **56**, 1486–1491 (1997). See page: 24

[139] P. O. Fedichev, Y. Kagan, G. V. Shlyapnikov, and J. T. M. Walraven. *Influence of Nearly Resonant Light on the Scattering Length in Low-Temperature Atomic Gases*. Phys. Rev. Lett. **77**, 2913–2916 (1996). See page: 24

[140] R. Ciuryło, E. Tiesinga, and P. S. Julienne. *Optical tuning of the scattering length of cold alkaline-earth-metal atoms*. Phys. Rev. A **71**, 030701 (2005). See pages: 24, 25, 158

[141] K. Enomoto, K. Kasa, M. Kitagawa, and Y. Takahashi. *Optical Feshbach Resonance Using the Intercombination Transition*. Phys. Rev. Lett. **101** (2008). See page: 24

[142] M. Yan, B. J. DeSalvo, B. Ramachandhran, H. Pu, and T. C. Killian. *Controlling Condensate Collapse and Expansion with an Optical Feshbach Resonance*. Phys. Rev. Lett. **110**, 123201 (2013). See page: 24

[143] K. Goyal, I. Reichenbach, and I. Deutsch. *p-Wave optical Feshbach resonances in ^{171}Yb*. Phys. Rev. A **82**, 062704 (2010). See page: 25

[144] R. Yamazaki, S. Taie, S. Sugawa, K. Enomoto, and Y. Takahashi. *Observation of a p-wave optical Feshbach resonance*. Phys. Rev. A **87**, 010704 (2013). See page: 25

[145] R. Yamazaki, S. Taie, S. Sugawa, and Y. Takahashi. *Submicron Spatial Modulation of an Interatomic Interaction in a Bose-Einstein Condensate*. Phys. Rev. Lett. **105**, 050405 (2010). See page: 25

[146] E. Merzbacher. *Quantum mechanics (3rd Edition)*. Wiley, New York (1998). See pages: 25, 28

[147] D. M. Stamper-Kurn and M. Ueda. *Spinor Bose gases: Symmetries, magnetism, and quantum dynamics*. Rev. Mod. Phys. **85**, 1191–1244 (2013). See pages: 26, 27, 160

[148] T.-L. Ho. *Spinor Bose Condensates in Optical Traps*. Phys. Rev. Lett. **81**, 742–745 (1998). See page: 26

[149] S.-K. Yip and T.-L. Ho. *Zero sound modes of dilute Fermi gases with arbitrary spin*. Phys. Rev. A **59**, 4653–4656 (1999). See page: 26

[150] C. Wu, J.-p. Hu, and S.-c. Zhang. *Exact SO(5) Symmetry in the Spin-3/2 Fermionic System*. Phys. Rev. Lett. **91** (2003). See pages: 27, 35

[151] C. Honerkamp and W. Hofstetter. *BCS pairing in Fermi systems with N different hyperfine states*. Phys. Rev. B **70**, 094521 (2004). See page: 30

[152] T. B. Ottenstein, T. Lompe, M. Kohnen, A. N. Wenz, and S. Jochim. *Collisional Stability of a Three-Component Degenerate Fermi Gas*. Phys. Rev. Lett. **101**, 203202 (2008). See page: 27

[153] J. S. Krauser, J. Heinze, N. Flaschner, S. Gotze, O. Jurgensen, D.-S. Luhmann, C. Becker, and K. Sengstock. *Coherent multi-flavour spin dynamics in a fermionic quantum gas*. Nature Phys. **8**, 813–818 (2012). See page: 27

[154] T. Ozawa and G. Baym. *Population imbalance and pairing in the BCS-BEC crossover of three-component ultracold fermions*. Phys. Rev. A **82**, 063615 (2010). See pages: 28, 29

[155] H. Schulz, G. Cuniberti, and P. Pieri. *Field theories for low-dimensional condensed matter systems: spin systems and strongly correlated electrons*, Volume 131, Chapter *Fermi liquids and Luttinger liquids*. Springer, Berlin (2000). See pages: 29, 186

[156] S.-K. Yip, B.-L. Huang, and J.-S. Kao. *Theory of* SU(N) *Fermi liquids*. Phys. Rev. A **89**, 043610 (2014). See pages: 29, 172

[157] S. Nascimbène, N. Navon, K. J. Jiang, F. Chevy, and C. Salomon. *Exploring the thermodynamics of a universal Fermi gas*. Nature **463**, 1057–1060 (2010). See page: 29

[158] B. Fröhlich, M. Feld, E. Vogt, M. Koschorreck, M. Köhl, C. Berthod, and T. Giamarchi. *Two-Dimensional Fermi Liquid with Attractive Interactions*. Phys. Rev. Lett. **109**, 130403 (2012). See page: 29

[159] E. Kuhnle, S. Hoinka, P. Dyke, H. Hu, P. Hannaford, and C. Vale. *Temperature Dependence of the Universal Contact Parameter in a Unitary Fermi Gas*. Phys. Rev. Lett. **106**, 170402 (2011). See page: 29

[160] A. Recati, P. O. Fedichev, W. Zwerger, and P. Zoller. *Fermi one-dimensional quantum gas: Luttinger liquid approach and spin–charge separation*. J. Opt. B **5**, S55 (2003). See page: 29

[161] A. Modawi and A. Leggett. *Some properties of a spin-1 Fermi superfluid: Application to spin-polarized 6Li*. J. Low Temp. Phys. **109**, 625–639 (1997). See page: 29

[162] R. Cherng, G. Refael, and E. Demler. *Superfluidity and Magnetism in Multicomponent Ultracold Fermions*. Phys. Rev. Lett. **99**, 130406 (2007). See page: 29

[163] C. Honerkamp and W. Hofstetter. *Ultracold fermions and the SU(N) Hubbard model*. Phys. Rev. Lett. **92**, 170403 (2004). See pages: 29, 30, 45, 172

[164] A. Rapp, W. Hofstetter, and G. Zaránd. *Trionic phase of ultracold fermions in an optical lattice: A variational study*. Phys. Rev. B **77**, 144520 (2008). See pages: 29, 30

[165] S. Will, T. Best, U. Schneider, L. Hackermüller, D.-S. Lühmann, and I. Bloch. *Time-resolved observation of coherent multi-body interactions in quantum phase revivals*. Nature **465**, 197–201 (2010). See pages: 29, 151

[166] J. B. Marston and I. Affleck. *Large-n limit of the Hubbard-Heisenberg model*. Phys. Rev. B **39**, 11538–11558 (1989). See pages: 30, 35, 45

[167] U. Schneider. *Interacting Fermionic Atoms in Optical Lattices- A Quantum Simulator for Condensed Matter Physics*. PhD thesis, Johannes-Gutenberg-Universität, Mainz (2010). See pages: 30, 77, 179

[168] T. Esslinger. *Fermi-Hubbard Physics with Atoms in an Optical Lattice*. Annu. Rev. Condens. Matter Phys. **1**, 129–152 (2010). See pages: 30, 36, 44

[169] K. R. Hazzard, V. Gurarie, M. Hermele, and A. M. Rey. *High-temperature properties of fermionic alkaline-earth-metal atoms in optical lattices*. Phys. Rev. A **85**, 041604 (2012). See page: 30

[170] E. V. Gorelik and N. Blümer. *Mott transitions in ternary flavor mixtures of ultracold fermions on optical lattices*. Phys. Rev. A **80**, 051602 (2009). See page: 30

[171] I. Affleck and J. B. Marston. *Large-n limit of the Heisenberg-Hubbard model: Implications for high-T_c superconductors*. Phys. Rev. B **37**, 3774–3777 (1988). See pages: 34, 35, 45

[172] A. Rapp and A. Rosch. *Ground-state phase diagram of the repulsive SU(3) Hubbard model in the Gutzwiller approximation*. Phys. Rev. A **83**, 053605 (2011). See page: 172

[173] Z. Cai, H.-H. Hung, L. Wang, and C. Wu. *Quantum magnetic properties of the $SU(2N)$ Hubbard model in the square lattice: A quantum Monte Carlo study*. Phys. Rev. B **88**, 125108 (2013). See pages: 30, 45, 46

[174] S. Capponi, G. Roux, P. Lecheminant, P. Azaria, E. Boulat, and S. White. *Molecular superfluid phase in systems of one-dimensional multicomponent fermionic cold atoms*. Phys. Rev. A **77**, 013624 (2008). See page: 30

[175] O. Boada, A. Celi, J. I. Latorre, and M. Lewenstein. *Quantum Simulation of an Extra Dimension*. Phys. Rev. Lett. **108**, 133001 (2012). See page: 30

[176] G. Cappellini, M. Mancini, G. Pagano, P. Lombardi, L. Livi, M. Siciliani de Cumis, P. Cancio, M. Pizzocaro, D. Calonico, F. Levi, C. Sias, J. Catani, M. Inguscio, and

L. Fallani. *Direct Observation of Coherent Interorbital Spin-Exchange Dynamics*. Phys. Rev. Lett. **113**, 120402 (2014). See pages: 34, 41, 59, 60, 143, 151, 152, 158, 159, 173

[177] A. Hewson. *The Kondo Problem to Heavy Fermions, Cambridge Studies in Magnetism*. Cambridge University Press, Cambridge (1993). See pages: 34, 35, 36, 37, 145

[178] H. Tsunetsugu, M. Sigrist, and K. Ueda. *The ground-state phase diagram of the one-dimensional Kondo lattice model*. Rev. Mod. Phys. **69**, 809–864 (1997). See pages: 34, 35, 39

[179] P. Coleman. *1/N expansion for the Kondo lattice*. Phys. Rev. B **28**, 5255–5262 (1983). See pages: 34, 38, 40, 44

[180] B. Coqblin and J. Schrieffer. *Exchange Interaction in Alloys with Cerium Impurities*. Phys. Rev. **185**, 847–853 (1969). See pages: 34, 40

[181] L.-M. Duan. *Controlling ultracold atoms in multi-band optical lattices for simulation of Kondo physics*. EPL **67**, 721 (2004). See page: 35

[182] B. Paredes, C. Tejedor, and J. I. Cirac. *Fermionic atoms in optical superlattices*. Phys. Rev. A **71**, 063608 (2005). See page: 35

[183] K. I. Kugel' and D. I. Khomskiĭ. *The Jahn-Teller effect and magnetism: transition metal compounds*. Sov. Phys. Usp. **25**, 231–256 (1982). See pages: 35, 37, 145

[184] P. Horsch. *Orbital Physics in Transition-metal Oxides: Magnetism and Optics. Handbook of Magnetism and Advanced Magnetic Materials*, Volume 1, pages 164–202. Wiley, New York (2007). See pages: 35, 36

[185] J. Kondo. *Resistance Minimum in Dilute Magnetic Alloys*. Progr. Theor. Phys. **32**, 37–49 (1964). See pages: 36, 145

[186] F. Steglich, J. Aarts, C. D. Bredl, W. Lieke, D. Meschede, W. Franz, and H. Schäfer. *Superconductivity in the Presence of Strong Pauli Paramagnetism: $CeCu_2Si_2$*. Phys. Rev. Lett. **43**, 1892–1896 (1979). See page: 36

[187] A. Bianchi, R. Movshovich, C. Capan, P. G. Pagliuso, and J. L. Sarrao. *Possible Fulde-Ferrell-Larkin-Ovchinnikov Superconducting State in $CeCoIn_5$*. Phys. Rev. Lett. **91**, 187004 (2003). See page: 36

[188] R. Movshovich, M. Jaime, J. D. Thompson, C. Petrovic, Z. Fisk, P. G. Pagliuso, and J. L. Sarrao. *Unconventional Superconductivity in $CeIrIn_5$ and $CeCoIn_5$: Specific Heat and Thermal Conductivity Studies*. Phys. Rev. Lett. **86**, 5152–5155 (2001).

[189] C. Petrovic, P. G. Pagliuso, M. F. Hundley, R. Movshovich, J. L. Sarrao, J. D. Thompson, Z. Fisk, and P. Monthoux. *Heavy-fermion superconductivity in $CeCoIn_5$ at 2.3 K*. J. Phys. Cond. Mat. **13**, L337 (2001). See page: 36

[190] A. Schröder, G. Aeppli, R. Coldea, M. Adams, O. Stockert, H. v. Löhneysen, E. Bucher, R. Ramazashvili, and P. Coleman. *Onset of antiferromagnetism in heavy-fermion metals*. Nature **407**, 351–355 (2000). See page: 36

[191] H. v. Löhneysen, T. Pietrus, G. Portisch, H. G. Schlager, A. Schröder, M. Sieck, and T. Trappmann. *Non-Fermi-liquid behavior in a heavy-fermion alloy at a magnetic instability*. Phys. Rev. Lett. **72**, 3262–3265 (1994). See pages: 36, 145

[192] G. R. Stewart. *Non-Fermi-liquid behavior in d- and f-electron metals*. Rev. Mod. Phys. **73**, 797–855 (2001). See pages: 36, 145

[193] Q. Si and F. Steglich. *Heavy Fermions and Quantum Phase Transitions*. Science **329**, 1161–1166 (2010). See pages: 36, 37

[194] M. P. Allan, F. Massee, D. K. Morr, J. Van Dyke, A. W. Rost, A. P. Mackenzie, C. Petrovic, and J. C. Davis. *Imaging Cooper pairing of heavy fermions in $CeCoIn_5$*. Nature Phys. **9**, 468–473 (2013). See pages: 36, 43

[195] B. B. Zhou, S. Misra, E. H. da Silva Neto, P. Aynajian, R. E. Baumbach, J. D. Thompson, E. D. Bauer, and A. Yazdani. *Visualizing nodal heavy fermion superconductivity in $CeCoIn_5$*. Nature Phys. **9**, 474–479 (2013). See page: 36

[196] P. W. Anderson. *Localized Magnetic States in Metals*. Phys. Rev. **124**, 41–53 (1961). See pages: 37, 44

[197] J. R. Schrieffer and P. A. Wolff. *Relation between the Anderson and Kondo Hamiltonians*. Phys. Rev. **149**, 491–492 (1966). See page: 37

[198] M. A. Ruderman and C. Kittel. *Indirect Exchange Coupling of Nuclear Magnetic Moments by Conduction Electrons*. Phys. Rev. **96**, 99–102 (1954). See pages: 37, 39, 145

[199] T. Kasuya. *A theory of metallic ferro-and antiferromagnetism on Zener's model*. Progress of theoretical physics **16**, 45–57 (1956).

[200] K. Yosida. *Magnetic Properties of Cu-Mn Alloys*. Phys. Rev. **106**, 893–898 (1957). See pages: 37, 39, 145

[201] P. Coleman, C. Pépin, Q. Si, and R. Ramazashvili. *How do Fermi liquids get heavy and die?* J. Phys. Cond. Mat. **13**, R723 (2001). See pages: 37, 145

[202] M. Z. Asadzadeh, M. Fabrizio, and F. Becca. *Superconductivity from spoiling magnetism in the Kondo lattice model*. Phys. Rev. B **90**, 205113 (2014). See page: 37

[203] O. Bodensiek, R. Žitko, M. Vojta, M. Jarrell, and T. Pruschke. *Unconventional Superconductivity from Local Spin Fluctuations in the Kondo Lattice*. Phys. Rev. Lett. **110**, 146406 (2013). See page: 37

[204] S. Jin, T. H. Tiefel, M. McCormack, R. A. Fastnacht, R. Ramesh, and L. H. Chen. *Thousandfold Change in Resistivity in Magnetoresistive La-Ca-Mn-O Films*. Science **264**, 413–415 (1994). See page: 37

[205] C. N. R. Rao and B. Raveau. *Colossal magnetoresistance, charge ordering and related properties of manganese oxides*. World Scientific, Singapore (1998). See pages: 37, 145

[206] P. Anderson. *New Approach to the Theory of Superexchange Interactions*. Phys. Rev. **115**, 2–13 (1959). See pages: 37, 45

[207] P. W. Anderson. *Local moments and localized states*. Rev. Mod. Phys. **50**, 191–201 (1978). See page: 38

[208] P. Nozières. *A "fermi-liquid" description of the Kondo problem at low temperatures*. J. Low Temp. Phys. **17**, 31–42 (1974). See page: 39

[209] S. Burdin, A. Georges, and D. Grempel. *Coherence Scale of the Kondo Lattice*. Phys. Rev. Lett. **85**, 1048–1051 (2000). See page: 39

[210] M. Oshikawa. *Topological Approach to Luttinger's Theorem and the Fermi Surface of a Kondo Lattice*. Phys. Rev. Lett. **84**, 3370–3373 (2000). See page: 39

[211] P. Coleman, I. Paul, and J. Rech. *Sum rules and Ward identities in the Kondo lattice*. Phys. Rev. B **72**, 094430 (2005). See page: 39

[212] C. Lacroix and M. Cyrot. *Phase diagram of the Kondo lattice*. Phys. Rev. B **20**, 1969–1976 (1979). See page: 39

[213] F. Assaad. *Quantum Monte Carlo Simulations of the Half-Filled Two-Dimensional Kondo Lattice Model*. Phys. Rev. Lett. **83**, 796–799 (1999). See page: 39

[214] X. Zhang, M. Bishof, S. L. Bromley, C. Kraus, M. S. Safronova, P. Zoller, A. M. Rey, and J. Ye. *Spectroscopic observation of SU(N)-symmetric interactions in Sr orbital magnetism*. Science (2014). See pages: 41, 60, 163

[215] M. Köhl. *Thermometry of fermionic atoms in an optical lattice*. Phys. Rev. A **73**, 031601 (2006). See pages: 42, 184, 188, 189

[216] P. B. Blakie, A. Bezett, and P. Buonsante. *Degenerate Fermi gas in a combined harmonic-lattice potential*. Phys. Rev. A **75**, 063609 (2007). See pages: 42, 189

[217] L. Pezzè, L. Pitaevskii, A. Smerzi, S. Stringari, G. Modugno, E. de Mirandes, F. Ferlaino, H. Ott, G. Roati, and M. Inguscio. *Insulating Behavior of a Trapped Ideal Fermi Gas*. Phys. Rev. Lett. **93**, 120401 (2004). See pages: 42, 43, 188

[218] N. Strohmaier, Y. Takasu, K. Günter, R. Jördens, M. Köhl, H. Moritz, and T. Esslinger. *Interaction-Controlled Transport of an Ultracold Fermi Gas*. Phys. Rev. Lett. **99**, 220601 (2007). See page: 42

[219] N. Gemelke, X. Zhang, C.-L. Hung, and C. Chin. *In situ observation of incompressible Mott-insulating domains in ultracold atomic gases*. Nature **460**, 995–998 (2009). See pages: 43, 109

[220] P. Aynajian, E. H. da Silva Neto, A. Gyenis, R. E. Baumbach, J. D. Thompson, Z. Fisk, E. D. Bauer, and A. Yazdani. *Visualizing heavy fermions emerging in a quantum critical Kondo lattice*. Nature **486**, 201–206 (2012). See page: 43

[221] J. Meineke, J.-P. Brantut, D. Stadler, T. Müller, H. Moritz, and T. Esslinger. *Interferometric measurement of local spin fluctuations in a quantum gas*. Nature Phys. **8**, 454–458 (2012). See page: 43

[222] F. F. Assaad. *Depleted Kondo lattices: Quantum Monte Carlo and mean-field calculations*. Phys. Rev. B **65**, 115104 (2002). See page: 43

[223] R. K. Kaul and M. Vojta. *Strongly inhomogeneous phases and non-Fermi-liquid behavior in randomly depleted Kondo lattices*. Phys. Rev. B **75**, 132407 (2007). See pages: 43, 44

[224] T. Yanagisawa and Y. Shimoi. *Ground State of the Kondo-Hubbard Model at Half Filling*. Phys. Rev. Lett. **74**, 4939–4942 (1995). See page: 44

[225] M. Feldbacher, C. Jurecka, F. F. Assaad, and W. Brenig. *Single-hole dynamics in the half-filled two-dimensional Kondo-Hubbard model*. Phys. Rev. B **66**, 045103 (2002). See page: 44

[226] M. Kitagawa, K. Enomoto, K. Kasa, Y. Takahashi, R. Ciuryło, P. Naidon, and P. S. Julienne. *Two-color photoassociation spectroscopy of ytterbium atoms and the precise determinations of s-wave scattering lengths*. Phys. Rev. A **77**, 012719 (2008). See pages: 44, 58, 59, 60, 146, 151

[227] P. Corboz, A. M. Läuchli, K. Penc, M. Troyer, and F. Mila. *Simultaneous Dimerization and SU(4) Symmetry Breaking of 4-Color Fermions on the Square Lattice*. Phys. Rev. Lett. **107**, 215301 (2011). See pages: 45, 46, 172

[228] R. Moessner and J. Chalker. *Properties of a Classical Spin Liquid: The Heisenberg Pyrochlore Antiferromagnet*. Phys. Rev. Lett. **80**, 2929–2932 (1998). See page: 45

[229] Y. Li, M. Ma, D. Shi, and F. Zhang. *SU(4) Theory for Spin Systems with Orbital Degeneracy*. Phys. Rev. Lett. **81**, 3527–3530 (1998). See page: 45

[230] P. Corboz, M. Lajkó, A. Läuchli, K. Penc, and F. Mila. *Spin-Orbital Quantum Liquid on the Honeycomb Lattice*. Phys. Rev. X **2**, 041013 (2012). See page: 45

[231] C. Xu and C. Wu. *Resonating plaquette phases in SU(4) Heisenberg antiferromagnet*. Phys. Rev. B **77**, 134449 (2008). See page: 45

[232] T. Tóth, A. Läuchli, F. Mila, and K. Penc. *Three-Sublattice Ordering of the SU(3) Heisenberg Model of Three-Flavor Fermions on the Square and Cubic Lattices*. Phys. Rev. Lett. **105**, 265301 (2010). See pages: 46, 172

[233] S. Manmana, K. R. Hazzard, G. Chen, A. Feiguin, and A. M. Rey. *SU(N) magnetism in chains of ultracold alkaline-earth-metal atoms: Mott transitions and quantum correlations*. Phys. Rev. A **84**, 043601 (2011). See page: 45

[234] P. Sinkovicz, A. Zamora, E. Szirmai, M. Lewenstein, and G. Szirmai. *Spin liquid phases of alkaline-earth-metal atoms at finite temperature*. Phys. Rev. A **88**, 043619 (2013).

[235] E. Szirmai. *Two-orbital physics of high-spin fermionic alkaline-earth atoms confined in a one-dimensional chain*. Phys. Rev. B **88**, 195432 (2013).

[236] T. Lang, Z. Meng, A. Muramatsu, S. Wessel, and F. Assaad. *Dimerized Solids and Resonating Plaquette Order in* SU(N)*-Dirac Fermions*. Phys. Rev. Lett. **111**, 066401 (2013).

[237] H. Song and M. Hermele. *Mott insulators of ultracold fermionic alkaline earth atoms in three dimensions*. Phys. Rev. B **87**, 144423 (2013).

[238] P. Nataf and F. Mila. *Exact Diagonalization of Heisenberg* SU(N) *Models*. Phys. Rev. Lett. **113**, 127204 (2014). See page: 45

[239] L. Bonnes, K. Hazzard, S. Manmana, A. Rey, and S. Wessel. *Adiabatic Loading of One-Dimensional* SU(N) *Alkaline-Earth-Atom Fermions in Optical Lattices*. Phys. Rev. Lett. **109**, 205305 (2012). See pages: 46, 172

[240] L. Messio and F. Mila. *Entropy Dependence of Correlations in One-Dimensional* SU(N) *Antiferromagnets*. Phys. Rev. Lett. **109**, 205306 (2012). See page: 46

[241] F. Assaad. *Phase diagram of the half-filled two-dimensional* SU(N) *Hubbard-Heisenberg model: A quantum Monte Carlo study*. Phys. Rev. B **71**, 075103 (2005). See page: 46

[242] R. Laughlin. *Anomalous Quantum Hall Effect: An Incompressible Quantum Fluid with Fractionally Charged Excitations*. Phys. Rev. Lett. **50**, 1395–1398 (1983). See page: 46

[243] T.-H. Han, J. S. Helton, S. Chu, D. G. Nocera, J. A. Rodriguez-Rivera, C. Broholm, and Y. S. Lee. *Fractionalized excitations in the spin-liquid state of a kagome-lattice antiferromagnet*. Nature **492**, 406–410 (2012). See page: 46

[244] L. Balents. *Spin liquids in frustrated magnets*. Nature **464**, 199–208 (2010). See page: 46

[245] M. K. Tey, S. Stellmer, R. Grimm, and F. Schreck. *Double-degenerate Bose-Fermi mixture of strontium*. Phys. Rev. A **82**, 011608 (2010). See page: 47

[246] A. H. Hansen, A. Khramov, W. H. Dowd, A. O. Jamison, V. V. Ivanov, and S. Gupta. *Quantum degenerate mixture of ytterbium and lithium atoms*. Phys. Rev. A **84**, 011606 (2011).

[247] S. Sugawa, R. Yamazaki, S. Taie, and Y. Takahashi. *Bose-Einstein condensate in gases of rare atomic species*. Phys. Rev. A **84**, 011610 (2011).

[248] S. Dörscher, A. Thobe, B. Hundt, A. Kochanke, R. Le Targat, P. Windpassinger, C. Becker, and K. Sengstock. *Creation of quantum-degenerate gases of ytterbium in a compact 2D-/3D-magneto-optical trap setup*. Rev. Sci. Instrum. **84**, 043109 (2013). See pages: 47, 61

[249] J. C. G. de Marignac and E. Ador. *Œuvres complètes: Mémoires et critiques 1860-1887*. Eggimann, Genève (18..). See page: 47

[250] C. R. Hammond. *Handbook of chemistry and physics*, Volume 81, Chapter *The elements*. CRC Press, Boca Raton (2000). See page: 48

[251] A. F. Holleman. *Lehrbuch der anorganischen Chemie*. Walter de Gruyter (1995). See page: 48

[252] C. B. Alcock, V. P. Itkin, and M. K. Horrigan. *Vapour pressure equations for the metallic elements: 298-2500K*. Can. Metall. Quart. **23**, 309–313 (1984). See page: 48

[253] R. Maruyama. *Optical trapping of ytterbium atoms*. PhD thesis, University of Washington, Washington (2003). See page: 48

[254] M. Berglund and M. E. Wieser. *Isotopic compositions of the elements 2009 (IUPAC Technical Report)*. Pure Appl. Chem. **83**, 397–410 (2011). See pages: 48, 49

[255] S. Sugawa, K. Inaba, S. Taie, R. Yamazaki, M. Yamashita, and Y. Takahashi. *Interaction and filling-induced quantum phases of dual Mott insulators of bosons and fermions*. Nature Phys. **7**, 642–648 (2011). See pages: 48, 59

[256] M. Borkowski, R. Ciuryło, P. S. Julienne, R. Yamazaki, H. Hara, K. Enomoto, S. Taie, S. Sugawa, Y. Takasu, and Y. Takahashi. *Photoassociative production of ultracold heteronuclear ytterbium molecules*. Phys. Rev. A **84**, 030702 (2011). See page: 48

[257] J. E. Sansonetti, W. C. Martin, and S. Young. *Handbook of basic atomic spectroscopic data*. J. Phys. Chem. Ref. Data **34**, 1559–2260 (2005). See page: 49

[258] Y. Takasu, K. Komori, K. Honda, M. Kumakura, T. Yabuzaki, and Y. Takahashi. *Photoassociation Spectroscopy of Laser-Cooled Ytterbium Atoms*. Phys. Rev. Lett. **93** (2004). See pages: 50, 51, 52

[259] K. Beloy, J. A. Sherman, N. D. Lemke, N. Hinkley, C. W. Oates, and A. D. Ludlow. *Determination of the 5d6s $^3D_1$ state lifetime and blackbody-radiation clock shift in Yb*. Phys. Rev. A **86**, 051404 (2012). See pages: 50, 52, 54

[260] S. G. Porsev and A. Derevianko. *Hyperfine quenching of the metastable $^3P_{0,2}$ states in divalent atoms*. Phys. Rev. A **69**, 042506 (2004). See pages: 50, 51, 56, 57, 128

[261] S. G. Porsev, Y. G. Rakhlina, and M. G. Kozlov. *Electric-dipole amplitudes, lifetimes, and polarizabilities of the low-lying levels of atomic ytterbium*. Phys. Rev. A **60**, 2781–2785 (1999). See pages: 50, 57, 58

[262] J. W. Cho, H.-g. Lee, S. Lee, J. Ahn, W.-K. Lee, D.-H. Yu, S. K. Lee, and C. Y. Park. *Optical repumping of triplet-P states enhances magneto-optical trapping of ytterbium atoms*. Phys. Rev. A **85**, 035401 (2012). See pages: 50, 52, 58

[263] V. A. Dzuba and A. Derevianko. *Dynamic polarizabilities and related properties of clock states of the ytterbium atom*. J. Phys. B **43**, 074011 (2010). See pages: 50, 124, 125

[264] K. Blagoev and V. Komarovskii. *Lifetimes of levels of neutral and singly ionized lanthanide atoms*. At. Data Nuc. Data Tables **56**, 1–40 (1994). See page: 51

[265] S. G. Porsev, A. Derevianko, and E. N. Fortson. *Possibility of an optical clock using the* $6^1S_0 \rightarrow 6^3P_0^o$ *transition in* $^{171,173}Yb$ *atoms held in an optical lattice*. Phys. Rev. A **69**, 021403 (2004). See pages: 51, 56, 135

[266] R. Maruyama, R. H. Wynar, M. V. Romalis, A. Andalkar, M. D. Swallows, C. E. Pearson, and E. N. Fortson. *Investigation of sub-Doppler cooling in an ytterbium magneto-optical trap*. Phys. Rev. A **68**, 011403 (2003). See pages: 51, 68

[267] V. Natarajan. *Proposed search for an electric-dipole moment using laser-cooled* ^{1}71*Yb atoms*. Eur. Phys. J. D **32**, 33–38 (2005). See page: 52

[268] C. J. Bowers, D. Budker, E. D. Commins, D. DeMille, S. J. Freedman, A.-T. Nguyen, S.-Q. Shang, and M. Zolotorev. *Experimental investigation of excited-state lifetimes in atomic ytterbium*. Phys. Rev. A **53**, 3103–3109 (1996). See page: 52

[269] K. Honda, Y. Takahashi, T. Kuwamoto, M. Fujimoto, K. Toyoda, K. Ishikawa, and T. Yabuzaki. *Magneto-optical trapping of Yb atoms and a limit on the branching ratio of the* $^1P_1$ *state*. Phys. Rev. A **59**, R934–R937 (1999). See page: 52

[270] T. Loftus, J. R. Bochinski, R. Shivitz, and T. W. Mossberg. *Power-dependent loss from an ytterbium magneto-optic trap*. Phys. Rev. A **61**, 051401 (2000). See page: 52

[271] D. Das, S. Barthwal, A. Banerjee, and V. Natarajan. *Absolute frequency measurements in Yb with* 0.08 *ppb uncertainty: Isotope shifts and hyperfine structure in the* 399 *nm* $^1S_0 \rightarrow ^1P_1$ *line*. Phys. Rev. A **72**, 032506 (2005). See pages: 53, 54

[272] K. Pandey, A. K. Singh, P. V. K. Kumar, M. V. Suryanarayana, and V. Natarajan. *Isotope shifts and hyperfine structure in the* 555.8 *nm* $^1S_0 \rightarrow ^3P_1$ *line of Yb*. Phys. Rev. A **80**, 022518 (2009). See page: 54

[273] N. Poli, Z. W. Barber, N. D. Lemke, C. W. Oates, L. S. Ma, J. E. Stalnaker, T. M. Fortier, S. A. Diddams, L. Hollberg, J. C. Bergquist, A. Brusch, S. Jefferts, T. Heavner, and T. Parker. *Frequency evaluation of the doubly forbidden* $^1S_0 \rightarrow {}^3P_0$ *transition in bosonic* ^{174}Yb. Phys. Rev. A **77**, 050501 (2008). See pages: 54, 56, 136

[274] C. W. Hoyt, Z. W. Barber, C. W. Oates, T. M. Fortier, S. A. Diddams, and L. Hollberg. *Observation and Absolute Frequency Measurements of the* $^1S_0$-$^3P_0$ *Optical Clock Transition in Neutral Ytterbium*. Phys. Rev. Lett. **95**, 083003 (2005). See pages: 54, 56, 127

[275] J. Migdalek and W. Baylis. *Relativistic transition probabilities and lifetimes of low-lying levels in ytterbium*. J. Phys. B **24**, L99 (1991). See page: 54

[276] S. Stellmer. *Degenerate quantum gases of strontium*. PhD thesis, University of Innsbruck, Innsbruck (2013). See pages: 56, 64, 67, 70

[277] S. Kato, K. Shibata, R. Yamamoto, Y. Yoshikawa, and Y. Takahashi. *Optical magnetic resonance imaging with an ultra-narrow optical transition*. Appl. Phys. B **108**, 31–38 (2012). See pages: 57, 153

[278] A. Yamaguchi. *Metastable State of Ultracold and Quantum Degenerate Ytterbium Atoms: High-Resolution Spectroscopy and Cold Collisions*. PhD thesis, Kyoto University, Kyoto (2008). See page: 58

[279] C. Hofrichter. *In preparation*. PhD thesis, Ludwig-Maximilians-Universität, München (2015). See pages: 58, 127, 136

[280] A. D. Ludlow, N. D. Lemke, J. A. Sherman, C. W. Oates, G. Quéméner, J. von Stecher, and A. M. Rey. *Cold-collision-shift cancellation and inelastic scattering in a Yb optical lattice clock*. Phys. Rev. A **84**, 052724 (2011). See pages: 59, 60, 133, 139, 142, 146, 164

[281] N. D. Lemke, J. von Stecher, J. A. Sherman, A. M. Rey, C. W. Oates, and A. D. Ludlow. *p-Wave cold collisions in an optical lattice clock*. Phys. Rev. Lett. **107**, 103902 (2011). See pages: 59, 60, 133, 146

[282] M. Bishof, M. J. Martin, M. D. Swallows, C. Benko, Y. Lin, G. Quéméner, A. M. Rey, and J. Ye. *Inelastic collisions and density-dependent excitation suppression in a 87-Sr optical lattice clock*. Phys. Rev. A **84**, 052716 (2011). See pages: 60, 139, 142

[283] A. Traverso, R. Chakraborty, Y. Martinez de Escobar, P. Mickelson, S. Nagel, M. Yan, and T. Killian. *Inelastic and elastic collision rates for triplet states of ultracold strontium*. Phys. Rev. A **79**, 060702 (2009). See pages: 60, 164

[284] T. E. Barrett, S. W. Dapore-Schwartz, M. D. Ray, and G. P. Lafyatis. *Slowing atoms with σ^- polarized light*. Phys. Rev. Lett. **67**, 3483–3486 (1991). See page: 61

[285] N. F. Ramsey. *Molecular beams*. Clarendon Press, Oxford (1956). See pages: 63, 81, 82

[286] H. Katori, T. Ido, Y. Isoya, and M. Kuwata-Gonokami. *Magneto-Optical Trapping and Cooling of Strontium Atoms down to the Photon Recoil Temperature*. Phys. Rev. Lett. **82**, 1116–1119 (1999). See page: 64

[287] T. Loftus, T. Ido, A. Ludlow, M. Boyd, and J. Ye. *Narrow Line Cooling: Finite Photon Recoil Dynamics*. Phys. Rev. Lett. **93**, 073003 (2004). See pages: 64, 65

[288] E. A. Curtis, C. W. Oates, and L. Hollberg. *Quenched narrow-line laser cooling of ^{40}Ca to near the photon recoil limit*. Phys. Rev. A **64** (2001). See page: 64

[289] T. Kuwamoto, K. Honda, Y. Takahashi, and T. Yabuzaki. *Magneto-optical trapping of Yb atoms using an intercombination transition*. Phys. Rev. A **60**, R745–R748 (1999). See pages: 65, 67

[290] T. Loftus, T. Ido, M. Boyd, A. Ludlow, and J. Ye. *Narrow line cooling and momentum-space crystals*. Phys. Rev. A **70**, 063413 (2004). See page: 65

[291] L. Viverit, C. Menotti, T. Calarco, and A. Smerzi. *Efficient and Robust Initialization of a Qubit Register with Fermionic Atoms*. Phys. Rev. Lett. **93**, 110401 (2004). See pages: 77, 188

[292] M. Rigol and A. Muramatsu. *Confinement control by optical lattices*. Phys. Rev. A **70**, 043627 (2004). See pages: 77, 188

[293] H. v. Raven. *Aufbau und Charakterisierung eines Triplett-Rückpumpersystems für Ytterbium-173*. Bachelor's thesis, Ludwig-Maximilians-Universität, München (2013). See page: 89

[294] T. Hänsch and B. Couillaud. *Laser frequency stabilization by polarization spectroscopy of a reflecting reference cavity*. Opt. Comm. **35**, 441–444 (1980). See page: 91

[295] M. Tabachnyk. *Aufbau eines Referenzlasers für den 399 nm $^1S_0 \rightarrow {}^1P_1$ Übergang von Ytterbium*. Bachelor's thesis, Ludwig-Maximilians-Universität, München (2012). See page: 91

[296] P. Ketterer. *A stable laser setup for the 578 nm clock transition of ytterbium*. Master's thesis, Ludwig-Maximilians-Universität, München (2012). See pages: 94, 97, 98, 99, 100, 103

[297] J. Alnis, A. Matveev, N. Kolachevsky, T. Udem, and T. W. Hänsch. *Subhertz linewidth diode lasers by stabilization to vibrationally and thermally compensated ultralow-expansion glass Fabry-Pérot cavities*. Phys. Rev. A **77**, 053809 (2008). See pages: 97, 193, 195

[298] L. Ricci, M. Weidemüller, T. Esslinger, A. Hemmerich, C. Zimmermann, V. Vuletic, W. König, and T. Hänsch. *A compact grating-stabilized diode laser system for atomic physics*. Opt. Comm. **117**, 541 – 549 (1995). See page: 97

[299] G. D. Domenico, S. Schilt, and P. Thomann. *Simple approach to the relation between laser frequency noise and laser line shape*. Appl. Opt. **49**, 4801–4807 (2010). See pages: 97, 103, 192

[300] M. Spießl. *Aufbau und charakterisierung eines verdopplungsresonators fuer den ytterbium-uhrenuebergang*. Bachelor's thesis, Ludwig-Maximilians-Universität, München (2011). See page: 98

[301] Z. Barber. *Ytterbium optical lattice clock*. PhD thesis, University of Colorado, Boulder (2007). See pages: 102, 106

[302] A. D. Ludlow, X. Huang, M. Notcutt, T. Zanon-Willette, S. M. Foreman, M. M. Boyd, S. Blatt, and J. Ye. *Compact, thermal-noise-limited optical cavity for diode laser stabilization at 1×10^{-15}*. Opt. Lett. **32**, 641–643 (2007). See page: 102

[303] K. Numata, A. Kemery, and J. Camp. *Thermal-Noise Limit in the Frequency Stabilization of Lasers with Rigid Cavities*. Phys. Rev. Lett. **93**, 250602 (2004). See page: 102

[304] R. Drever, J. Hall, F. Kowalski, J. Hough, G. Ford, A. Munley, and H. Ward. *Laser phase and frequency stabilization using an optical resonator*. Appl. Phys. B **31**, 97–105 (1983). See page: 102

[305] E. D. Black. *An introduction to Pound–Drever–Hall laser frequency stabilization*. Am. J. Phys. **69**, 79–87 (2001). See page: 102

[306] C. Salomon, D. Hils, and J. L. Hall. *Laser stabilization at the millihertz level*. J. Opt. Soc. Am. B **5**, 1576–1587 (1988). See page: 103

[307] A. Kastberg, W. D. Phillips, S. L. Rolston, R. J. C. Spreeuw, and P. S. Jessen. *Adiabatic Cooling of Cesium to 700 nK in an Optical Lattice*. Phys. Rev. Lett. **74**, 1542–1545 (1995). See page: 109

[308] M. Greiner, I. Bloch, O. Mandel, T. W. Hänsch, and T. Esslinger. *Exploring Phase Coherence in a 2D Lattice of Bose-Einstein Condensates*. Phys. Rev. Lett. **87** (2001). See page: 109

[309] W. Gerlach and O. Stern. *Der experimentelle nachweis der richtungsquantelung im magnetfeld*. Z. Physik A **9**, 349–352 (1922). See page: 111

[310] T. Sleator, T. Pfau, V. Balykin, O. Carnal, and J. Mlynek. *Experimental demonstration of the optical Stern-Gerlach effect*. Phys. Rev. Lett. **68**, 1996–1999 (1992). See page: 111

[311] S. Stellmer, R. Grimm, and F. Schreck. *Detection and manipulation of nuclear spin states in fermionic strontium*. Phys. Rev. A **84**, 043611 (2011). See pages: 111, 116, 121

[312] N. R. Cooper and J. Dalibard. *Optical flux lattices for two-photon dressed states*. EPL **95**, 66004 (2011). See page: 117

[313] J. S. Krauser, U. Ebling, N. Fläschner, J. Heinze, K. Sengstock, M. Lewenstein, A. Eckardt, and C. Becker. *Giant spin oscillations in an ultracold Fermi sea*. Science **343**, 157–160 (2014). See pages: 122, 160

[314] U. Ebling, J. S. Krauser, N. Fläschner, K. Sengstock, C. Becker, M. Lewenstein, and A. Eckardt. *Relaxation Dynamics of an Isolated Large-Spin Fermi Gas Far from Equilibrium*. Phys. Rev. X **4**, 021011 (2014). See pages: 122, 160

[315] K. Guo, G. Wang, and A. Ye. *Dipole polarizabilities and magic wavelengths for a Sr and Yb atomic optical lattice clock*. J. Phys. B **43**, 135004 (2010). See page: 124

[316] A. V. Taichenachev, V. I. Yudin, V. D. Ovsiannikov, and V. G. Pal'chikov. *Optical Lattice Polarization Effects on Hyperpolarizability of Atomic Clock Transitions*. Phys. Rev. Lett. **97**, 173601 (2006). See page: 125

[317] D. Leibfried, R. Blatt, C. Monroe, and D. Wineland. *Quantum dynamics of single trapped ions*. Rev. Mod. Phys. **75**, 281–324 (2003). See pages: 128, 131

[318] S. Blatt. *Ultracold Collisions and Fundamental Physics with Strontium*. PhD thesis, University of Colorado, Boulder (2011). See page: 131

[319] A. D. Ludlow. *The strontium optical lattice clock: optical spectroscopy with sub-Hertz accuracy*. PhD thesis, University of Colorado, Boulder (2008). See page: 131

[320] G. K. Campbell, M. M. Boyd, J. W. Thomsen, M. J. Martin, S. Blatt, M. D. Swallows, T. L. Nicholson, T. Fortier, C. W. Oates, S. A. Diddams, et al. *Probing interactions between ultracold fermions*. Science **324**, 360–363 (2009). See pages: 133, 142

[321] K. Gibble. *Decoherence and Collisional Frequency Shifts of Trapped Bosons and Fermions*. Phys. Rev. Lett. **103**, 113202 (2009).

[322] A. M. Rey, A. V. Gorshkov, and C. Rubbo. *Many-Body Treatment of the Collisional Frequency Shift in Fermionic Atoms*. Phys. Rev. Lett. **103**, 260402 (2009). See page: 133

[323] M. D. Swallows, M. Bishof, Y. Lin, S. Blatt, M. J. Martin, A. M. Rey, and J. Ye. *Suppression of collisional shifts in a strongly interacting lattice clock*. Science **331**, 1043–1046 (2011). See page: 142

[324] M. J. Mark, E. Haller, K. Lauber, J. G. Danzl, A. J. Daley, and H.-C. Nägerl. *Precision Measurements on a Tunable Mott Insulator of Ultracold Atoms*. Phys. Rev. Lett. **107**, 175301 (2011). See pages: 151, 157

[325] G. Zürn, F. Serwane, T. Lompe, A. N. Wenz, M. G. Ries, J. E. Bohn, and S. Jochim. *Fermionization of Two Distinguishable Fermions*. Phys. Rev. Lett. **108**, 075303 (2012). See page: 151

[326] M. Köhl, K. Günter, T. Stöferle, H. Moritz, and T. Esslinger. *Strongly interacting atoms and molecules in a 3D optical lattice*. J. Phys. B **39**, S47 (2006). See page: 151

[327] F. Deuretzbacher, K. Plassmeier, D. Pfannkuche, F. Werner, C. Ospelkaus, S. Ospelkaus, K. Sengstock, and K. Bongs. *Heteronuclear molecules in an optical lattice: Theory and experiment*. Phys. Rev. A **77**, 032726 (2008). See pages: 151, 158

[328] J. Mentink and S. Kokkelmans. *Two interacting atoms in an optical lattice site with anharmonic terms*. Phys. Rev. A **79**, 032709 (2009). See pages: 151, 158

[329] C. Gerving, T. Hoang, B. Land, M. Anquez, C. Hamley, and M. Chapman. *Non-equilibrium dynamics of an unstable quantum pendulum explored in a spin-1 Bose-Einstein condensate*. Nature Comm. **3**, 1169 (2012). See page: 160

[330] U. Ebling, A. Eckardt, and M. Lewenstein. *Spin segregation via dynamically induced long-range interactions in a system of ultracold fermions*. Phys. Rev. A **84**, 063607 (2011). See page: 160

[331] D. S. Petrov and G. V. Shlyapnikov. *Interatomic collisions in a tightly confined Bose gas*. Phys. Rev. A **64**, 012706 (2001). See pages: 166, 167

[332] Z. Hadzibabic and J. Dalibard. *Two-dimensional Bose fluids: An atomic physics perspective*. Riv. Nuovo Cimento **34**, 389 (2011). See pages: 166, 167

[333] J. J. García-Ripoll, S. Dürr, N. Syassen, D. M. Bauer, M. Lettner, G. Rempe, and J. I. Cirac. *Dissipation-induced hard-core boson gas in an optical lattice*. New J. Phys. **11**, 013053 (2009). See page: 168

[334] P. N. Ma, S. Pilati, M. Troyer, and X. Dai. *Density functional theory for atomic Fermi gases*. Nature Phys. **8**, 601–605 (2012). See page: 172

[335] S. Pilati, I. Zintchenko, and M. Troyer. *Ferromagnetism of a Repulsive Atomic Fermi Gas in an Optical Lattice: A Quantum Monte Carlo Study*. Phys. Rev. Lett. **112**, 015301 (2014). See page: 172

[336] S. Pilati, G. Bertaina, S. Giorgini, and M. Troyer. *Itinerant Ferromagnetism of a Repulsive Atomic Fermi Gas: A Quantum Monte Carlo Study*. Phys. Rev. Lett. **105**, 030405 (2010). See page: 172

[337] M. Foss-Feig, A. J. Daley, J. K. Thompson, and A. M. Rey. *Steady-State Many-Body Entanglement of Hot Reactive Fermions*. Phys. Rev. Lett. **109**, 230501 (2012). See page: 173

[338] S. Trotzky, Y.-A. Chen, U. Schnorrberger, P. Cheinet, and I. Bloch. *Controlling and Detecting Spin Correlations of Ultracold Atoms in Optical Lattices*. Phys. Rev. Lett. **105**, 265303 (2010). See page: 173

[339] J. Goold, T. Fogarty, N. Lo Gullo, M. Paternostro, and T. Busch. *Orthogonality catastrophe as a consequence of qubit embedding in an ultracold Fermi gas*. Phys. Rev. A **84**, 063632 (2011). See page: 174

[340] M. Knap, A. Shashi, Y. Nishida, A. Imambekov, D. A. Abanin, and E. Demler. *Time-Dependent Impurity in Ultracold Fermions: Orthogonality Catastrophe and Beyond*. Phys. Rev. X **2**, 041020 (2012). See page: 174

[341] C. Navarrete-Benlloch, I. de Vega, D. Porras, and J. I. Cirac. *Simulating quantum-optical phenomena with cold atoms in optical lattices*. New J. Phys. **13**, 023024 (2011). See page: 174

[342] W. Kohn. *Analytic Properties of Bloch Waves and Wannier Functions*. Phys. Rev. **115**, 809–821 (1959). See page: 180

[343] D. A. Butts and D. S. Rokhsar. *Trapped Fermi gases*. Phys. Rev. A **55**, 4346–4350 (1997). See page: 185

[344] G. M. Bruun and K. Burnett. *Interacting Fermi gas in a harmonic trap*. Phys. Rev. A **58**, 2427–2434 (1998). See page: 186

Acknowledgements

I would like to begin by thanking Prof. Immanuel Bloch for giving me the opportunity to work in his research group. It has been a great privilege and pleasure. I admire his positive and encouraging attitude towards research, which he transmitted to the entire group. He became for me the example of how an astonishing scientific knowledge and an authentic talent for conveying this to others can be combined. I also thank Prof. Wilhelm Zwerger for correcting this manuscript, as well as Prof. Harald Weinfurter and Prof. Wolfgang Zinth for being part of my defence committee.

It is only thanks to many great people that our experiment led to some great achievements. The creativity, the devotion and the hard work of the colleagues with whom I shared these years could indeed turn an empty lab into a quantum physics playground. Let me thus especially thank Simon Fölling, for having the brave idea of picking ytterbium in the first place and taking on the challenge. His impressive physics knowledge and intuition are exceptional, and I am greatly indebted to him for teaching me a significant amount of the things I know. A big thanks goes to Christian Hofrichter, Pieter De Groot and Moritz Höfer, with whom I spent so much time trying to figure out new ideas and solutions to the puzzles of the daily lab life. The entire team's genuine passion for research and dedication have been extremely valuable. We enjoyed lots of discussions and pleasant moments, inside and outside the lab, that I will always remember with joy. It was equally a pleasure to work with Luis Riegger and Diogo Rio Fernandes, who recently joined our team, and to whom I wish a great time in the group. Let me also acknowledge all the students and interns who did a great job in our lab: Philip Ketterer, Christian Schweizer, Emily Davis, Maxim Tabachnyk, Martin Spießl, Hendrik Von Raven and QinQin Yu.

A special thanks goes to the rest of the Bloch group, both at LMU and at MPQ, including the ones who are already elsewhere, for creating such a stimulating intellectual and social atmosphere. I am grateful to all of them for always being so friendly, kind and helpful. I will remember with a big smile all the time spent together: the chats and the drinks, the visits to Ringberg, Bad Honnef and Venice, the bike tours, the barbecues at the Isar and the other countless amusing occasions. Sharing the office with Monika Aidelsburger was truly a pleasure, as well as frequently discussing with Marcos Atala next door or bothering the Fermi teams upstairs with physics or technical questions. Particular yummy thanks to Martin Boll and Niko Bucheim for their amazing dinners and to Lucia Duca for her inimitable Tiramisú.

I would also like to thank the group secretaries, especially Ildiko Kecskesi and Zhora Hauck at LMU for their precious help. Without them, every sort of matter or problem would have just been much harder to deal with. The work, the patience - and the sense of humour - of Bodo Hecker and Jürgen Aust have been fundamental to keep our experiment running and advancing, together with the efforts of all technicians and the staff at the LMU machine shop.

During these years I have met so many amazing people, physicists and non-physicists, and the list keeps getting longer. Let me just mention my close friends and Frana's mates in Munich: Luca, Luigi and Niccolò. A warm thanks goes to my whole family, giving me unconditional trust and support: my parents Anna and Claudio and my little sister Margherita, my grandparents Dino and Olga, my uncles Fabrizio and Giuseppe. Finally, let me thank Nicoletta, who has always been there for me, no matter if we were close together or far apart. I dedicate this thesis to you. Keep at it, you are almost through the PhD yourself!